EBM Experimental Biology and Medicine

Volume 250 | Issue 2

Experimental Biology and Medicine

Editor in Chief

Nicola Conran
University of Campinas,
Brazil

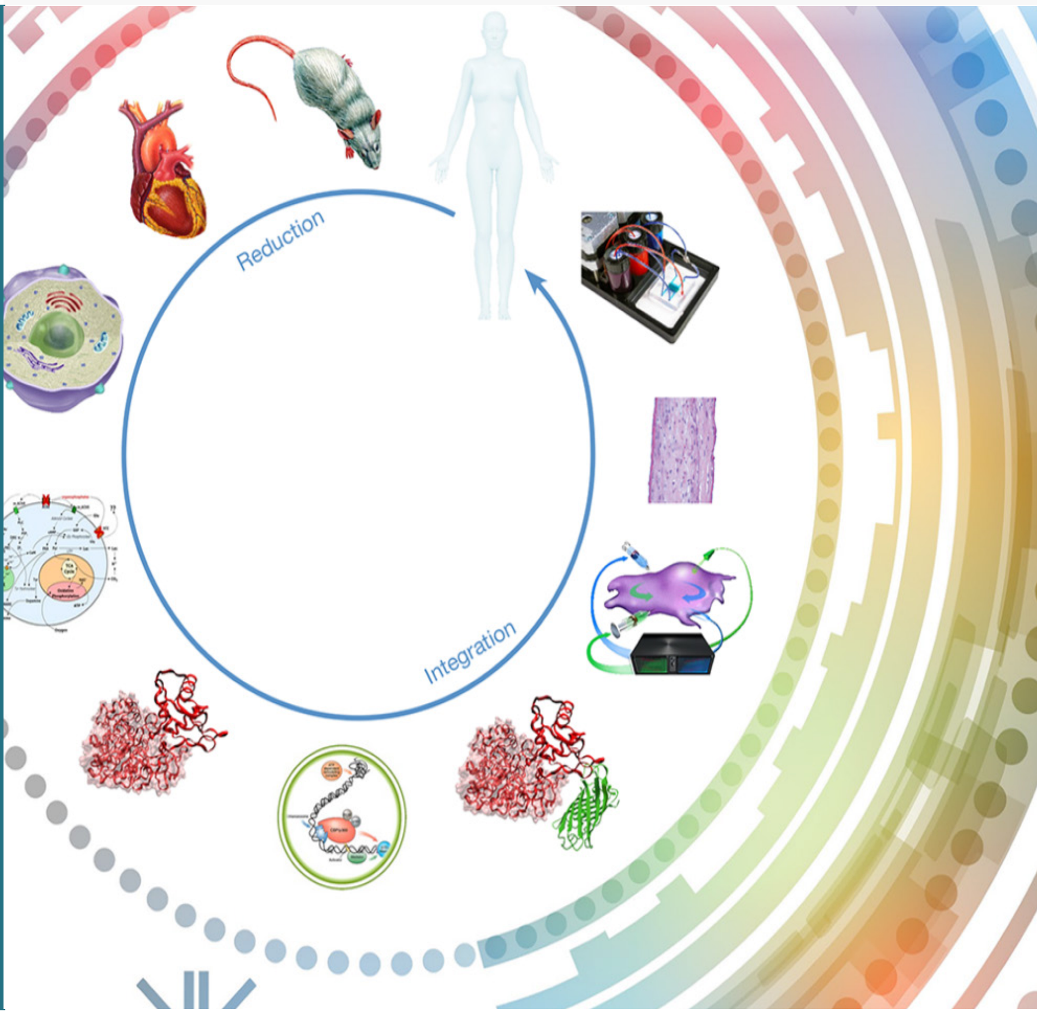

ISBN 978-2-8325-6086-0
DOI 10.3389/978-2-8325-6086-0

frontiers | Publishing Partnerships

Society for Experimental Biology and Medicine
3220 N Street NW, #179
Washington DC 20007, USA
Executive Director – ed@sebm.org
Assistant to Editor-in-Chief – bzimmer@sebm.org

www.sebm.org

Editorial Board

EDITOR IN CHIEF
Nicola Conran
University of Campinas

DEPUTY EDITOR
Sulev Kõks
Murdoch University

GLOBAL EDITORS

Africa
Gordon Awandare
University of Ghana

Asia
Shaw-Jenq Tsai
National Cheng Kung University

Europe
Farzin Farzaneh
King's College London

Americas
Nicola Conran
University of Campinas

Australia/Oceana
Sulev Kõks
Murdoch University

Anatomy/Pathology

Associate Editor

Ian Zagon
Penn State University College of Medicine

William Banks
Alexander V. Ljubimov
Patricia J. McLaughlin
Artur Pasternak

Artifical Intelligence/Machine Learning Applications to Biomedical Research

Associate Editor

Huixiao Hong
US Food and Drug Administration

Xiaohui Fan
Ping Gong
Ruili Huang
Jie Liu
Fred Prior
Paul Rogers
Tieliu Shi
Wei Shi
Wenming Xiao

Biochemistry and Molecular Biology

Associate Editor

Muriel A. Lambert
Rutgers New Jersey Medical School

Brian D Adams
Bin Guo
J. Patrick O'connor

Bioimaging

Associate Editor

Shuliang Jiao
Florida International University

Kamran Avanaki
Zygmunt Gryczynski
Xinmai Yang
Xincheng Yao
Baohong Yuan
Weizhao Zhao

Biomedical Engineering

Associate Editor

F. Kurtis Kasper
University of Texas Health Science Center at Houston

Angela Pannier

Bionanoscience

Associate Editor

Juan Melendez
University of Albany

Nathaniel Cady
Hassan A. Elfawal
Jonathan F Lovell
Ya-Ping Sun
Maria Tomassone
Siyang Zheng

Cell and Developmental Biology

Associate Editor

Lidiane Torres
Albert Einstein College of Medicine

David Dean
Leszek Kotula
Harold I Saavedra
Yigang Wang
Warren Zimmer

Clinical Trials

Giuseppe Pizzorno
Daniel Vaena

Endocrinology and Nutrition

Co Associate Editors

Clint Allred and Keith Erikson
University of North Carolina Greensboro

Demin Cai
Sam Dagogo-Jack
Weiqun Wang
Malcolm Watford
Chia-Shan Wu

Environmental Health/Biomarkers/Precision Medicine

Associate Editor

William Slikker, Jr.
Retired

Gary Steven Friedman
Donald Johann
Igor Pogribny

Genomics, Proteomics, and Bioinformatics

Associate Editor

Sulev Kõks
Murdoch University

Mark Geraci
Paul Potter
John P Quinn
Giovanni Stracquadanio

Immunology/Microbiolog/Virology

Co Associate Editors

Flávio Guimarães Da Fonseca
Federal University of Minas Gerais

Renata Sesti-Costa
State University of Campinas

Andrea Doria
Farzin Farzaneh
Kam Hui
Francois Villinger

Mechanisms of Aging

Associate Editor

Shigemi Matsuyama
Case Western Reserve University

Ricki Colman
Aolin Allen Hsu
Akihiro Ikeda
Masaru Miyagi
Vincent Monnier

Neuroscience

Associate Editor

Michael Neal Lehman
Kent State University

Lique M. Coolen
Terrence Deak
Max L Fletcher
Sandra Mooney
Gregg Stanwood
Richard M Xu

Pharmacology/Toxicology

Associate Editor

Santosh Kumar
University of Tennessee Health Science Center

Guzel Bikbova
Pawel Brzuzan
Laetitia Dou
Jianxiong Jiang
Youngmi Jung
Li-Fu Li
Jonathan Shannahan
Manish Tripathi
Chaowu Xiao
Wuxiang Xie
Qihe Xu

Physiology and Pathophysiology

Associate Editor

Robert T. Mallet
University of North Texas Health Science Center

Rong Ma
Gabor Tigyi
Shaw-Jenq Tsai
Samuel Verges
Lei Xi
Chunyu Zeng

Population Health

Associate Editor

Ashish Joshi
School of Public Health, University of Memphis

Stem Cell Biology

Associate Editor

Jian Feng
State University of New York at Buffalo

Vania Broccoli
Jose Cibelli
Guoping Fan
Antonis Hatzopoulos
Dan S. Kaufman
Chun-Li Zhang

Structural Biology

Associate Editor

Tom Thompson
University of Cincinnati

Andrew P. Hinck
James Horn
Rhett Kovall
Vincent Luca
Rick Page

Synthetic Biology

Tara Deans
Ahmad Khalil
Aditya M. Kunjapur
Kevin Solomon

Systems Biology and Microphysiological Systems

Salman Khetani	Andre Levchenko
Deok-Ho Kim	

Translational Research

Associate Editor

Chia-Ching (Josh) Wu
National Cheng Kung University

Jing An	Chulso Moon
Pan Pan Chong	Esther Obeng
Hyacinth Idu Hyacinth	Athena Starland-Davenport
Monica M. Jablonski	

EBM eBook Copyright Statement

The copyright in the text of individual articles in this eBook is the property of their respective authors or their respective institutions or funders. The copyright in graphics and images within each article may be subject to copyright of other parties. In both cases this is subject to a license granted to Frontiers.

The compilation of articles constituting this eBook is the property of Frontiers.

Each article within this eBook, and the eBook itself, are published under the most recent version of the Creative Commons CC-BY licence. The version current at the date of publication of this eBook is CC-BY 4.0. If the CC-BY licence is updated, the licence granted by Frontiers is automatically updated to the new version.

When exercising any right under the CC-BY licence, Frontiers must be attributed as the original publisher of the article or eBook, as applicable.

Authors have the responsibility of ensuring that any graphics or other materials which are the property of others may be included in the CC-BY licence, but this should be checked before relying on the CC-BY licence to reproduce those materials. Any copyright notices relating to those materials must be complied with.

Copyright and source acknowledgement notices may not be removed and must be displayed in any copy, derivative work or partial copy which includes the elements in question.

All copyright, and all rights therein, are protected by national and international copyright laws. The above represents a summary only. For further information please read Frontiers' Conditions for Website Use and Copyright Statement, and the applicable CC-BY licence.

ISSN 1535-3699
ISBN 978-2-8325-6086-0
DOI 10.3389/978-2-8325-6086-0

2025 | Volume 250 | Issue 2 | ISSN 1535-3699

Table of contents

Anatomy/Pathology

Original Research 07 Impaired fracture healing is associated with callus chondro-osseous junction abnormalities in periostin-null and osteopontin-null mice
Marc Teitelbaum, Maya D. Culbertson, Charlene Wetterstrand and J. Patrick O'Connor

Cell and Developmental Biology

Original Research 26 Baseline gene expression in BALB/c and C57BL/6 peritoneal macrophages influences but does not dictate their functional phenotypes
Carlos M. Restrepo, Alejandro Llanes, Lizzi Herrera, Esteban Ellis, Iliana Quintero and Patricia L. Fernández

Immunology/Microbiology/Virology

Highlight

Original Research 40 scRNA-seq reveals elevated interferon responses and TNF-α signaling via NFkB in monocytes in children with uncomplicated malaria
Collins M. Morang'a, Riley S. Drake, Vincent N. Miao, Nancy K. Nyakoe, Dominic S. Y. Amuzu, Vincent Appiah, Yaw Aniweh, Yaw Bediako, Saikou Y. Bah, Alex K. Shalek, Gordon A. Awandare, Thomas D. Otto and Lucas Amenga-Etego

Immunology/Microbiology/Virology

Brief Communication 56 Functional mass spectrometry indicates anti-protease and complement activity increase with COVID-19 severity
Douglas D. Fraser, Swapan Roy, Matt Kuruc, Maritza Quintero, Logan R. Van Nynatten, Gediminas Cepinskas, Haiyan Zheng, Amenah Soherwardy and Devjit Roy

Physiology and Pathophysiology

Original Research 66 A study on the differences in the gut microbiota and metabolism between male and female mice in different stress periods
Yajun Qiao, Juan Guo, Qi Xiao, Jianv Wang, Xingfang Zhang, Xinxin Liang, Lixin Wei, Hongtao Bi and Tingting Gao

Translational Research

Highlight

Mini Review

83 Is platelet-rich plasma better than steroids as epidural drug of choice in lumbar disc disease with radiculopathy? Meta-analysis of randomized controlled trials
Sathish Muthu, Vibhu Krishnan Viswanathan and Prakash Gangadaran

Corrigendum

93 Corrigendum: Decreased PPP1R3G in pre-eclampsia impairs human trophoblast invasion and migration via Akt/MMP-9 signaling pathway
Huimin Shi, Renyu Kong, Xu Miao, Lingshan Gou, Xin Yin, Yuning Ding, Xiliang Cao, Qingyong Meng, Maosheng Gu and Feng Suo

Experimental Biology and Medicine

TYPE Original Research
PUBLISHED 22 January 2025
DOI 10.3389/ebm.2024.10066

OPEN ACCESS

*CORRESPONDENCE
J. Patrick O'Connor,
✉ oconnojp@njms.rutgers.edu

RECEIVED 05 December 2023
ACCEPTED 22 August 2024
PUBLISHED 22 January 2025

CITATION
Teitelbaum M, Culbertson MD, Wetterstrand C and O'Connor JP (2025) Impaired fracture healing is associated with callus chondro-osseous junction abnormalities in periostin-null and osteopontin-null mice.
Exp. Biol. Med. 249:10066.
doi: 10.3389/ebm.2024.10066

Impaired fracture healing is associated with callus chondro-osseous junction abnormalities in periostin-null and osteopontin-null mice

Marc Teitelbaum[1,2], Maya D. Culbertson[1], Charlene Wetterstrand[1] and J. Patrick O'Connor[1,2]*

[1]Department of Orthopaedics, Rutgers-New Jersey Medical School, Newark, NJ, United States,
[2]Rutgers-School of Graduate Studies, Newark Health Sciences Campus, Newark, NJ, United States

Abstract

Periostin and osteopontin are matricellular proteins abundantly expressed in bone fracture callus. Null mutation of either the periostin (*Postn*) gene or the osteopontin (*Spp1*) gene can impair bone fracture healing. However, the cell and molecular pathways affected by loss of POSTN or SPP1 which lead to impaired fracture healing are not well understood. To identify potential pathways, a detailed radiological, histological, and immunohistochemical analysis of femur fracture healing in *Postn*-null (*Postn*KO), *Spp1*-null (*Spp1*KO), and normal (WT) mice was performed. Apparent changes in specific protein levels identified by immunohistochemistry were confirmed by mRNA quantitation. Comparisons between the *Postn*KO and *Spp1*KO fracture calluses were confounded by interactions between the two genes; loss of *Postn* reduced *Spp1* expression and loss of *Spp1* reduced *Postn* expression. Consequently, alterations in fracture healing between mice heterozygous for the *Postn*-null allele (*Postn*HET) as well as the *Postn*KO and *Spp1*KO mice were similar. Calluses from *Postn*HET, *Postn*KO, and *Spp1*KO mice all had dysmorphic chondro-osseous junctions and reduced numbers of osteoclasts. The dysmorphic chondro-osseous junctions in the *Postn*HET, *Postn*KO, and *Spp1*KO calluses were associated with reduced numbers of MMP-13 expressing hypertrophic chondrocytes, consistent with delayed cartilage resolution. Unlike collagen X expressing callus chondrocytes, chondrocytes only expressed MMP-13 when localized to the chondro-osseous junction or after traversing the chondro-osseous junction. Cyclooxygenase-2 (COX-2) expression also appeared to be reduced in osteoclasts from the *Postn*HET, *Postn*KO, and *Spp1*KO calluses, including in those osteoclasts localized at the chondro-osseous junction. The results indicate that POSTN and SPP1 are necessary for normal chondro-osseous junction formation and that signaling from the chondro-osseous junction, possibly from COX-2 expressing osteoclasts, regulates callus vasculogenesis and chondrocyte hypertrophy necessary for endochondral ossification during fracture healing.

KEYWORDS

periostin, osteopontin, endochondral ossification, chondro-osseous junction, fracture healing, osteoclast, cyclooxygenase-2

Impact statement

Impaired healing in *Postn*-null and *Spp1*-null mice provided evidence for a regulatory role of the callus chondro-osseous junction in bone fracture healing. Delayed callus cartilage resolution and reduced callus vasculogenesis in *Postn*-null and *Spp1*-null calluses were associated with abnormal chondro-osseous junction morphology, reduced transition of chondrocytes into MMP13 expressing hypertrophic chondrocytes, and reduced COX-2 expression in chondro-osseous junction osteoclasts. The results indicate that the chondro-osseous junction is not just the site at which callus cartilage is resorbed prior to bone formation but that the chondro-osseous junction has a critical regulatory role in endochondral ossification. Loss of *Postn* or *Spp1* reduced expression of the other gene, suggesting that expression of these matricellular proteins is coordinated during fracture healing and that *Postn* and *Spp1* are important for normal chondro-osseous functioning. The results advance our understanding of matricellular proteins in bone regeneration and identify new roles for the chondro-osseous junction in endochondral ossification.

Introduction

Bone fractures normally heal through tissue regeneration [1]. Immediately after fracture, a hematoma forms at the site which is accompanied by local tissue hypoxia as factors are released from degranulating platelets and from damaged nerves located on or within the bone [2–4]. An inflammatory response quickly follows and the fracture site is rapidly populated with myeloid and other cells that have migrated to or proliferated at the fracture site to form the presumptive callus [5]. New bone is then directly made by periosteal cells to form buttresses of bone ringing the external, peripheral edges of the callus. Within the now well-defined external callus, cells differentiate into chondrocytes and a chondro-osseous junction is formed between the bony peripheral edges of the callus and callus chondrocytes. Osteoclasts localize at the chondro-osseous junction to form a margin at which endochondral bone formation initiates [6].

Endochondral ossification is characterized by chondrocyte hypertrophy adjacent to the chondro-osseous junction, destruction of the hypertrophic chondrocytes and associated extra-cellular matrix, vasculogenesis, and osteoblast-mediated bone formation [7, 8]. Vasculogenesis is necessary for endochondral ossification during fetal bone development, bone growth, and fracture healing [9, 10]. The osteoclasts at the chondro-osseous junction, sometimes called chondroclasts, are thought to destroy the hypertrophic cartilage matrix and enable vasculogenesis necessary for fracture healing [11]. As healing progresses, the two chondro-osseous junctions, one proximal and one distal to the fracture, advance from the callus peripheries as endochondral ossification continues. Eventually, the chondro-osseous junctions converge to bridge the fracture with new bone. Bony bridging of the fracture results in a significant increase in bone structural mechanics. The external callus decreases in size as woven bone within the callus undergoes osteoclast-mediated remodeling into more mechanically stable lamellar bone until the fracture is fully healed.

The molecules and mechanisms necessary to regulate the temporal and spatially overlapping physiological, cellular, and molecular processes governing fracture healing are not well defined [12–14]. While the roles of certain cytokines, lipid mediators, and growth factors in fracture healing have been studied extensively [13], the roles of non-structural extracellular matrix proteins, or matricellular proteins, in bone fracture healing are less clear. Matricellular proteins interact with other extracellular matrix components, growth factors, and cell surface receptors to affect cell signaling, cell-cell interactions, and the local tissue environment [15, 16]. As such, matricellular proteins may act to coordinate the cellular and molecular processes involved in fracture healing.

Periostin (POSTN) and osteopontin (SPP1) are matricellular proteins expressed in the fracture callus and loss of *Spp1* or *Postn* in mice leads to fracture healing deficits [17–20]. Mice that are homozygous for a targeted null mutation of *Postn* are viable and fertile, though with notable phenotypes including reduced bone quality [21]. Mice that are homozygous for a targeted null mutation of *Spp1* are also viable and fertile [22]. *Postn* and *Spp1* are associated with multiple physiological processes that can affect fracture healing including inflammation, chondrogenesis, osteogenesis, vasculogenesis, and osteoclastogenesis [19, 23–29].

Spp1 mRNA and POSTN are localized in hypertrophic chondrocytes at the callus chondro-osseous junction and

TABLE 1 Study oligodeoxynucleotide primers.

Genotyping primers			
Gene allele	**Designation**	**Forward**	**Reverse**
Spp1^{tm1Blh}	*Spp1*KO	GCCTGAAGAACGAGATCAGC	GTCTGGAGAACATGGGTGCT
Spp1	WT	GGGTGCAGGCTGTAAAGCTA	GTCTGGAGAACATGGGTGCT
Postn$^{tm1.1(KOMP)Vlcg}$	*Postn*KO	CGGTCGCTACCATTACCAGT	CAGTTCCTACCCCACAGGAG
Postn	WT	CATCCTAAATACCCTCCAGTGC	GGACTTCATCAATCAGGTGGA
RTqPCR Primers			
Gene	**Protein**	**Forward**	**Reverse**
Actb	ß-actin	GGGCTATGCTCTCCCTCACG	AGACGAACATAGCACAGCTTCTCTT
Mmp-13	Matrix Metallopeptidase 13	GAGTGCCTGATGTGGGTGAAT	CCAGAAGGTCCATCAAATGGGT
Acp5	Tartrate-resistant Acid Phosphatase 5	GGTTCCAGGAGACCTTTGAG	TTCCAGCCAGCACATACC
Ctsk	Cathepsin-K	AGGCAGCTAAATGCAGAGGGTACA	AGCTTGCATCGATGGACACAG AGA
Acan	Aggrecan	CATGAGAGAGGCGAATGGAA	TGATCTCGTAGCGATCTTTCTTCT
Pecam1	CD-31	CCAAAGCCAGTAGCATCATGGTC	GGATGGTGAAGTTGGCTACAGG
Ptgs2	Cyclooxygenase-2	GGGCAGGAAGTCTTTGGTC	GGTAACCGCTCAGGTGTTG
B2m	ß-2-microglobulin	CTGCTACGTAACACAGTTCCACCC	CATGATGCTTGATCACATGTCTCG
Postn	Periostin	CCTGCCCTTATATGCTCTGCT	AAACATGGTCAATAGGCATCACT
Spp1	Osteopontin	GCAGCCATGAGTCAAGTCAGC	GCCTCTTCTTTAGTTGACC
Bglap	Osteocalcin	CCATGAGGACCATCTTTCTGC	CAGGTCCTAAATAGTGATACC

SPP1 and POSTN are integrin αvß3 ligands [20, 30–32]. Osteoclasts abundantly express integrin αvß3 and are localized at the callus chondro-osseous junction [33, 34]. The proximity of hypertrophic chondrocytes expressing SPP1 and POSTN and osteoclasts expressing integrin αvß3 at the callus chondro-osseous junction suggests that *Spp1* or *Postn* can affect fracture healing by regulating events at the chondro-osseous junction. To test this hypothesis, we undertook a detailed analysis of the morphological events that occur during femur fracture healing in normal mice and mice deficient in *Postn* or *Spp1*. Our analysis indicates that *Postn* and *Spp1* are necessary for formation of a normal callus chondro-osseous junction and that reductions in callus vasculogenesis and chondrocyte hypertrophy in *Postn* or *Spp1* deficient mice are associated with reduced osteoclast cyclooxygenase-2 (COX-2) expression.

Materials and methods

Animal models

Mice with a targeted null mutation in the periostin gene (*Postn*$^{tm1.1(KOMP)Vlcg}$) were purchased from Jackson Laboratory (Stock #024186, Bar Harbor, ME). Homozygous *Postn*$^{tm1.1(KOMP)Vlcg}$ null mice (*Postn*KO) are viable and fertile but with reduced mechanical integrity in connective tissues [35, 36]. The *Postn*$^{tm1.1(KOMP)Vlcg}$ mice were bred with C57BL/6 mice to produce normal (WT), *Postn*$^{tm1.1(KOMP)Vlcg}$ heterozygous (*Postn*HET), and *Postn*KO mice.

Mice with a targeted null mutation in the osteopontin gene (*Spp1*^{tm1Blh}) were purchased from Jackson Laboratory (Stock #004936, Bar Harbor, ME) [22]. The *Spp1*^{tm1Blh} null mice (*Spp1*KO) have a C57BL/6 genetic background and were maintained by homozygous null breeding to produce *Spp1*KO mice. Mice were genotyped via allele-specific PCR amplification of DNA extracted from tail clip biopsies (Table 1). Immunohistochemistry was conducted to confirm loss of *Postn* and *Spp1* protein expression in the fracture calluses of homozygous null mice. Six to fourteen mice were used for each genotype at each time point of which at least 3 were males. All animal procedures were approved by the Rutgers-New Jersey Medical School Institutional Animal Care and Use Committee (IACUC; protocol #201800006).

Fracture procedure and radiography

Male and female mice aged 15 weeks were anesthetized by intraperitoneal injection of ketamine and xylazine (0.1 and 0.01 mg/g body weight, respectively) prior to retrograde insertion of 0.01-inch diameter stainless steel pin in the right femoral canal to stabilize the impending fracture. At 16 weeks of age, the mice were anesthetized again and underwent a closed, diaphyseal fracture of the right femur using a custom-made, three-point controlled impact device (BBC Specialty Automotive Center, Linden, NJ) as described previously [37]. For all genotypes, male mice weighed significantly more than the females.

C57BL/6 and *Spp1*KO mice had significantly higher body weights than *Postn*KO mice. C57BL/6 mice weighed 23.17 ± 3.70 g (mean ± SD), *Spp1*KO 24.42 ± 3.23 g (mean ± SD), *Postn*KO 21.28 ± 3.19 g (mean ± SD) and *Postn*HET 22.47 ± 3.89 g (mean ± SD). Ventral-dorsal radiographs of the mice were made using an XPERT80 digital radiography cabinet (KUBTEC, Stratford, CT) with exposure settings of 65 kV, 90 μA, and 8 s immediately after fracture and then at 7, 10, 14, 21, and 28 days after fracture (dpf) or until the endpoint (see Supplementary Figure S1). Fixed femurs (see below) were stored in 70% ethanol prior to high-resolution computerized tomography (μCT) scanning. Specimens were scanned using a Bruker Skyscan 1275 system (Micro Photonics Inc., Allentown, PA) at 73 kVp, with an intensity of 133 μA, a voxel size of 12 μm isotropic, and with a 0.5 mm aluminum filter. Scanner images were reconstructed (NRecon), analyzed (CTan), and viewed (CTvol) using software from the manufacturer (Bruker, Kontich, Belgium). A detailed description of the method used to measure fracture callus volume and fracture callus bone (calcified tissue) volume can be found in the Supplementary Material (see Supplementary Figure S2).

Histology

After euthanasia, femurs were resected and then fixed in an aqueous solution of bronopol (3% w/v), diazolidinyl urea (3% w/v), zinc sulfate hepta-hydrate (1.2% w/v), sodium citrate (0.29% w/v), ascorbic acid (0.025% w/v), and 20% (v/v) ethanol for 2 days at room temperature. The specimens were then either immediately decalcified in 0.5 M disodium EDTA for 2 weeks at 4°C or analyzed by μCT before decalcification. The decalcified specimens were embedded in paraffin, cut into 5 μm thick longitudinal sections parallel to the intramedullary canal in the dorsal-ventral plane, and mounted onto TruBond 380 glass slides (Newcomer Supply, Middleton, WI). Mounted sections were deparaffinized using three changes of xylene and rehydrated in a graded ethanol series. Osteoclasts were detected by tartrate-resistant acid phosphatase (TRAP) staining with a hematoxylin counterstain. Cartilage was visualized by safranin-O staining with fast green and hematoxylin counterstaining. Bone was visualized using aniline blue staining with Biebrich scarlet-acid fuchsin and hematoxylin counterstaining (Masson's trichrome staining). Sections were cover-slipped with Cytoseal mounting medium (Fisher Scientific, Waltham, MA). Unless otherwise indicated, stains and reagents were from Sigma-Aldrich (St. Louis, MO).

Immunohistochemistry (IHC)

Antibodies used are listed in Table 2. Tissue sections were deparaffinized and rehydrated as described above before antigen retrieval in 10 mM sodium citrate pH 6.0 buffer (70–80°C, 1 h) for COX-2, CD31, POSTN, SPP1, F4/80 and Cathepsin K (CTSK) detection, or in phosphate-buffered saline (PBS) with 25 mg/mL testicular hyaluronidase (37°C for 1 h; Worthington Biochemical Corporation, Lakewood, NJ) for MMP-13 and Collagen X detection. Endogenous peroxidases were quenched with 3% H_2O_2 in PBS (30 min at room temperature) followed by non-specific epitope blocking with SuperBlock (room temperature for 1 h; ThermoFisher, Waltham, MA). After washing with PBS, 150 μL of primary antibody diluted in Antibody Diluent pH7.4 (IHC World, Woodstock, MD) was applied to each histological section and incubated overnight in a humidified chamber at 4°C. See Table 2 for antibody dilutions. Following several washes in PBS, sections were incubated in POLINK-2 Plus Rabbit polymeric HRP secondary antibody per the manufacturer's instructions (IHC World) and then washed with PBS before colorimetric detection using diaminobenzidine (GBI Labs, Bothell, WA). Sections were counterstained with methyl green to detect cell nuclei.

Histology and immunohistochemistry image collection and analysis

Digital images of callus fracture sections were captured using an Olympus BX53 microscope and DP73 camera (Olympus Corporation of America, Center Valley, PA). Cartilage and bone areas were measured for each specimen using OsteoMeasure Software (OsteoMetrics Inc., Decatur, GA)

TABLE 2 Study rabbit antibodies.

Antibody target	Company	Catalog number	Type	Dilution	Antigen retrieval
CTSK (cathepsin K)	Novus Biologicals	NBP1-45460	PAb	1:100	10 mM sodium citrate, 1 h, 75°C
CD-31	Cell Signaling	77699	MAb	1:500	10 mM sodium citrate, 1 h, 75°C
Collagen X	abcam	ab260040	MAb	1:1,000	25 mg/mL hyaluronidase, 1 h, 37°C
COX-2	Cayman	160,126	PAb	1:700	10 mM sodium citrate, 1 h, 75°C
F4/80	Cell Signaling	70076	MAb	1:1,000	10 mM sodium citrate, 1 h, 75°C
MMP-13	abcam	ab219620	MAb	1:100	25 mg/mL hyaluronidase, 1 h, 37°C
SPP1 (osteopontin)	Novus Biologicals	NB600-1043	PAb	1:50	10 mM sodium citrate, 1 h, 75°C
POSTN (periostin)	Sino Biological	50450-RP02	PAb	1:5,000	10 mM sodium citrate, 1 h, 75°C

from safranin-O and trichrome stained sections, respectively, and normalized as a percentage of total callus area. TRAP positive cells were manually counted using OsteoMeasure and divided by callus area to generate the density of TRAP positive cells per mm^2. Similar procedures for image collection and analysis were conducted with the IHC samples to determine COX-2, Cathepsin K (CTSK), MMP-13, CD31, Collagen X (COL10A1), and F4/80 positive areas or cell numbers in the callus. Examples showing how MMP-13 expressing chondrocytes and vascular lumens surrounded by CD31 expressing cells were counted are shown in Supplementary Figure S3. A comparison between using TRAP staining and IHC detection of CTSK to count callus osteoclasts showed a high degree of correlation (R^2 = 0.91, see Supplementary Figure S4).

Fracture callus RNA isolation, cDNA synthesis, and qPCR

Fracture calluses were resected at 14 days after fracture (dpf) from at least 3 male and 3 female mice of each genotype. Calluses were flash-frozen in liquid nitrogen and stored at −80°C until RNA extraction [38]. Briefly, each callus was homogenized in Trizol Reagent (1 mL per 50 to 100 mg callus weight) using a Precellys 24 Omni Bead Homogenizer (Bertin Technologies SAS; Montigny-le-Bretonneux, France). After Trizol extraction, the RNA was further purified using a Qiagen RNeasy mini kit as per the manufacturer's instructions (Qiagen, Hilden, Germany). RNA concentration and integrity were determined by absorbance and agarose gel electrophoresis, respectively.

Target mRNA levels were measured using RT-qPCR as follows. cDNA was prepared from each RNA preparation using an Applied Biosystems High-Capacity cDNA kit (Waltham, MA). The cDNA from 0.1 μg of total RNA along with 1 μM of each primer were used in each 25 μL qPCR reaction (SYBR Green PCR Master Mix, Applied Biosystems 4309155). Amplifications were performed using a Bio-Rad Laboratories CFX96 Real-Time System (Hercules, CA). At least 3 qPCR reactions were performed with each cDNA preparation for every target mRNA and the mean threshold cycle (Ct) value was used for further comparisons. At least 6 callus RNA preparations (3 male and 3 female) were measured for each genotype and for each target mRNA. Target mRNA levels were normalized to corresponding β-actin mRNA Ct values. Relative gene expression was determined using the $2^{-\Delta\Delta CT}$ method [39].

Statistical analyses

Statistical analyses were performed using OriginPro 2022b (OriginLab Corp., Northhampton, MA). Callus histomorphometry data, including the number of TRAP positive+ cells, cartilage area, bone area, and all immunohistochemistry gene quantifications were analyzed by 3-way ANOVA using genotype, days post-fracture (dpf) and gender as independent variables. Post-hoc tests utilized Tukey or Holm-Sidak corrections to identify significant differences between groups. Detailed information regarding the statistical analyses is shown in the Supplementary Material.

Results

Loss of *Postn* or *Spp1* affects fracture callus formation and remodeling

μCT was performed on femurs resected at 14, 21, and 28 days post-fracture (dpf) to visualize and quantify morphological differences in the facture calluses between wild type (WT), *Postn*HET, *Postn*KO, and *Spp1*KO genotypes (see Supplementary Figure S1 for digital radiographs). Longitudinal sections from reconstructed μCT volumes are shown for each time point and genotype in Figure 1. Healing appeared to proceed normally in the WT control C57BL/6 mice (Figures 1A–C) with apparent bridging

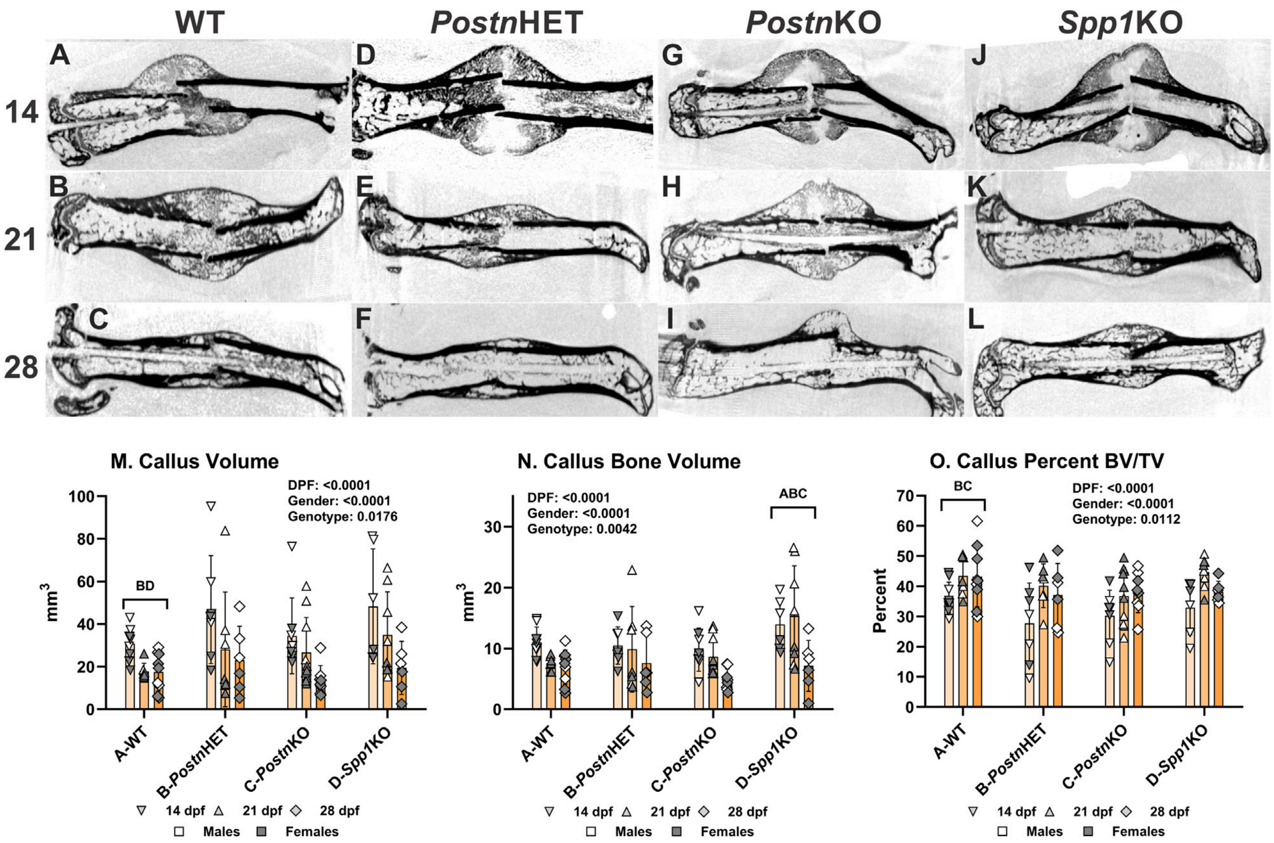

FIGURE 1
μCT Analysis of Fracture Callus Bone in *Postn* and *Spp1* Deficient Mice. Fractured mouse femurs were collected from C57BL/6 (WT), *Postn*$^{+/-}$ (*Postn*HET), *Postn* $^{-/-}$ (*Postn*KO), and *Spp1*$^{-/-}$ (*Spp1*KO) mice and imaged by μCT scanning. Shown are representative images from the reconstructed fractured femur scans at 14, 21, and 28 dpf for WT **(A–C)**, *Postn*HET **(D–F)**, *Postn*KO **(G–I)**, and *Spp1*KO mice **(J–L)**, respectively. Callus total volume [TV, panel **(M)**], bone volume [BV, panel **(N)**] and normalized bone volume [BV/TV, panel **(O)**] were determined from μCT imaging data collected from at least three female and three male mice of each genotype and at each time point. The effects of time after fracture, gender, and genotype were determined by 3-way ANOVA and P-values are reported [insets, panels **(M–O)**]. Significant differences between genotypes ($p < 0.05$) are noted in each graph.

at 14 dpf, definitive bridging by 21 dpf, and callus remodeling evident at 28 dpf [37]. Healing also appeared to proceed reasonably well in the *Postn*HET mice with definitive bridging by 21 dpf and evident callus remodeling at 28 dpf, though at 14 dpf less calcified tissue was evident in the external callus (Figures 1D–F). The external fracture callus in the *Postn*KO and *Spp1*KO mice at 14 dpf appeared to have central areas devoid of calcified tissue (Figures 1G, J). By 21 dpf, the *Postn*KO and *Spp1*KO calluses appeared to bridge the fracture (Figures 1H, K). Callus remodeling was evident at 28 dpf in the *Postn*KO and *Spp1*KO mouse fracture calluses (Figures 1I, L). However, less bone was evident in the 28 dpf *Postn*KO callus and the extent of callus remodeling appeared reduced for both genotypes.

The μCT data were also used to quantify total callus volume (TV) and callus bone (calcified tissue) volume (BV). As expected, TV, BV, and BV/TV varied with time after fracture for all genotypes showing a general pattern of decreasing callus TV (means of 39, 27, and 18 mm^3 at 14, 21, and 28 dpf) and BV (means of 11, 10, and 6.5 mm^3 at 14, 21, and 28 dpf) but increasing BV/TV from 14 dpf (means of 32, 41, and 39% at 14, 21, and 28 dpf; Figures 1M–O). In addition, male mice also had significantly larger calluses (TV; means of 37 vs. 19 mm^3) and more callus bone (BV; means of 11.5 vs. 7.4 mm^3), though normalized callus bone volume (BV/TV) was in general greater in the female mice (means of 34% vs. 41%; see Supplementary Material). Across all time points and both genders, callus TV was significantly greater in the *Postn*HET (33.1 mm^3) and *Spp1*KO (34.3 mm^3) as compared to the WT (22.4 mm^3) and *Postn*KO (25.1 mm^3) mice. Consistent with the overall callus volume, BV was significantly greater in the *Spp1*KO mice (12.5 mm^3) and lowest in the *Postn*KO mice (7.8 mm^3), though differences between WT (8.6 mm^3), *Postn*HET (9.4 mm^3), and *Postn*KO were not significant. In contrast, BV/TV across all time points and both genders was significantly lower in the *Postn*HET (34.9%) and *Postn*KO (35.1%) mice as compared to the WT

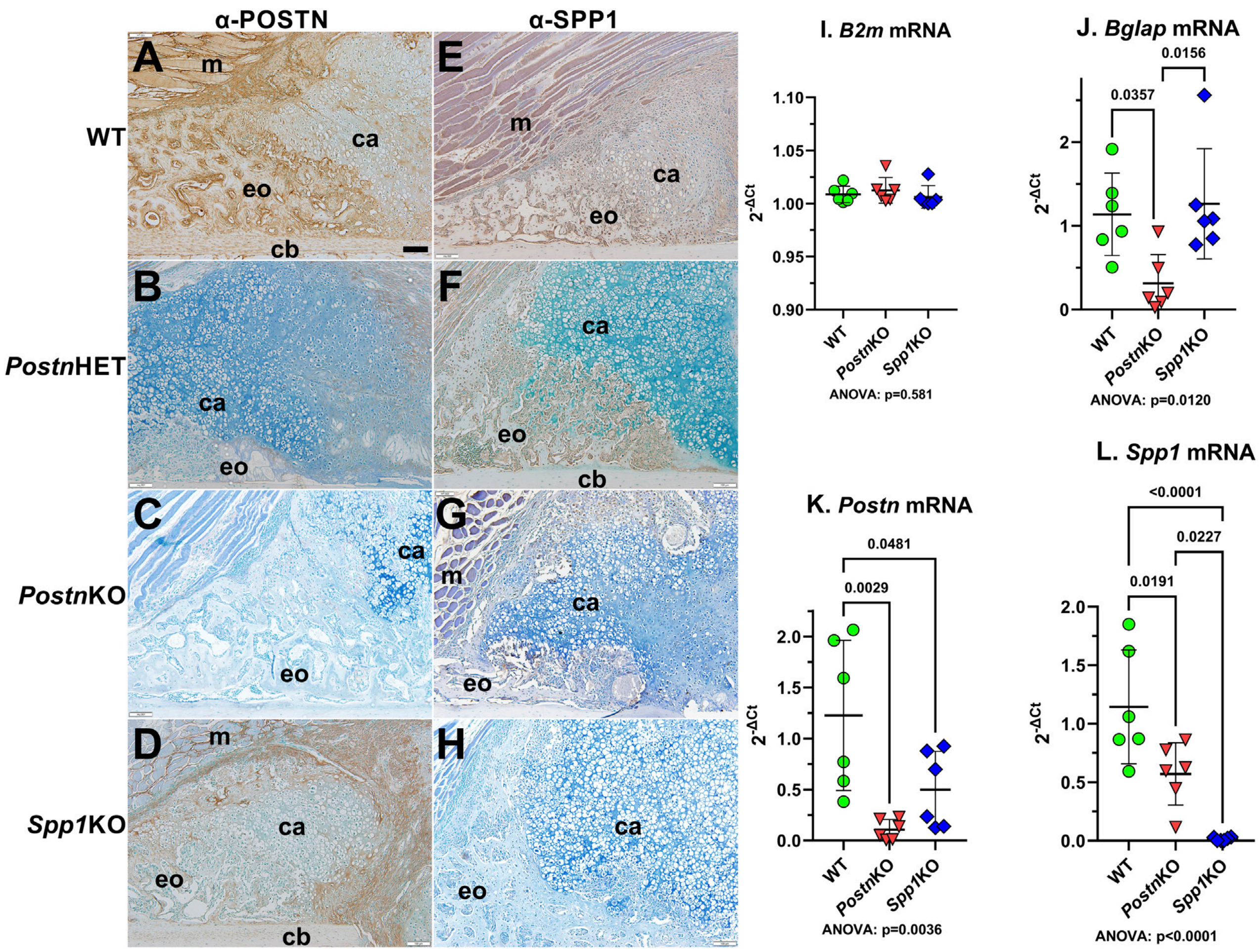

FIGURE 2
Immunohistochemical Detection of POSTN and SPP1 in normal and *Postn* or *Spp1* deficient mouse femur fracture calluses. Mouse femurs collected at 10 dpf were used to detect POSTN **(A–D)** or SPP1 **(E–H)** in WT **(A, E)**, *Postn*HET **(B, F)**, *Postn*KO **(C, G)** or *Spp1*KO **(D, H)** calluses. The images show approximately one-quarter of the fracture callus and are oriented with the femur cortical bone at the bottom and fracture site in the bottom right corner. Muscle (m), cartilage (ca), cortical bone (cb), and areas of apparent new bone formation (eo) are labeled. POSTN and SPP1 were readily detected in the WT mouse calluses [**(A, E)**, respectively]. POSTN expression appeared reduced in the *Postn*HET callus **(B)**, while SPP1 expression appeared to be near normal levels **(F)**. POSTN expression was not detected in the *Postn*KO callus **(C)** which also appeared to have reduced levels of SPP1 though with some expression evident in callus chondrocytes **(G)**. POSTN appeared less abundant in the *Spp1*KO callus **(D)** as compared to WT **(A)** but was still readily detected. As expected, SPP1 was not detected in the *Spp1*KO callus **(H)**. RTqPCR quantitation of control ß2 microglobulin [*B2m*; **(I)**], osteocalcin [*Bglap*; **(J)**], *Postn* **(K)**, and *Spp1* **(L)** mRNA levels in callus RNA prepared from three male and three female WT, *Postn*KO, or *Spp1*KO mice at 14 dpf paralleled the immunohistochemical detection results. *Postn* and *Spp1* mRNA levels appeared absent from their corresponding KO callus RNA preparations. *Postn* mRNA was also significantly reduced in the *Spp1*KO callus RNA while *Spp1* mRNA was significantly reduced in the *Postn*KO callus RNA. ANOVA and post-hoc P values are shown in **(I, J, K, L)**. Scale bar equals 100 μm **(A)**.

mice (40.8%), though no statistical difference was detected for the *Spp1*KO mice (39.2%).

SPP1 and POSTN expression in normal, *Postn*-deficient, and *Spp1*-deficient fracture calluses

Immunohistochemistry was performed on 10 dpf calluses to confirm normal expression of POSTN and SPP1 in WT mice and loss of POSTN and SPP1 expression in *Postn*KO and *Spp1*KO mice, respectively (Figure 2).

POSTN was broadly expressed throughout the WT callus (Figure 2A). POSTN levels appeared higher in osteoblast-rich areas and along the chondro-osseous junction with apparent lower levels in callus chondrocytes. POSTN expression levels appeared to be reduced in the *Postn*HET callus with POSTN localization limited to fibroblasts and newly differentiated chondrocytes at the center of the callus and to chondrocytes near the chondro-osseous junction (Figure 2B). As expected,

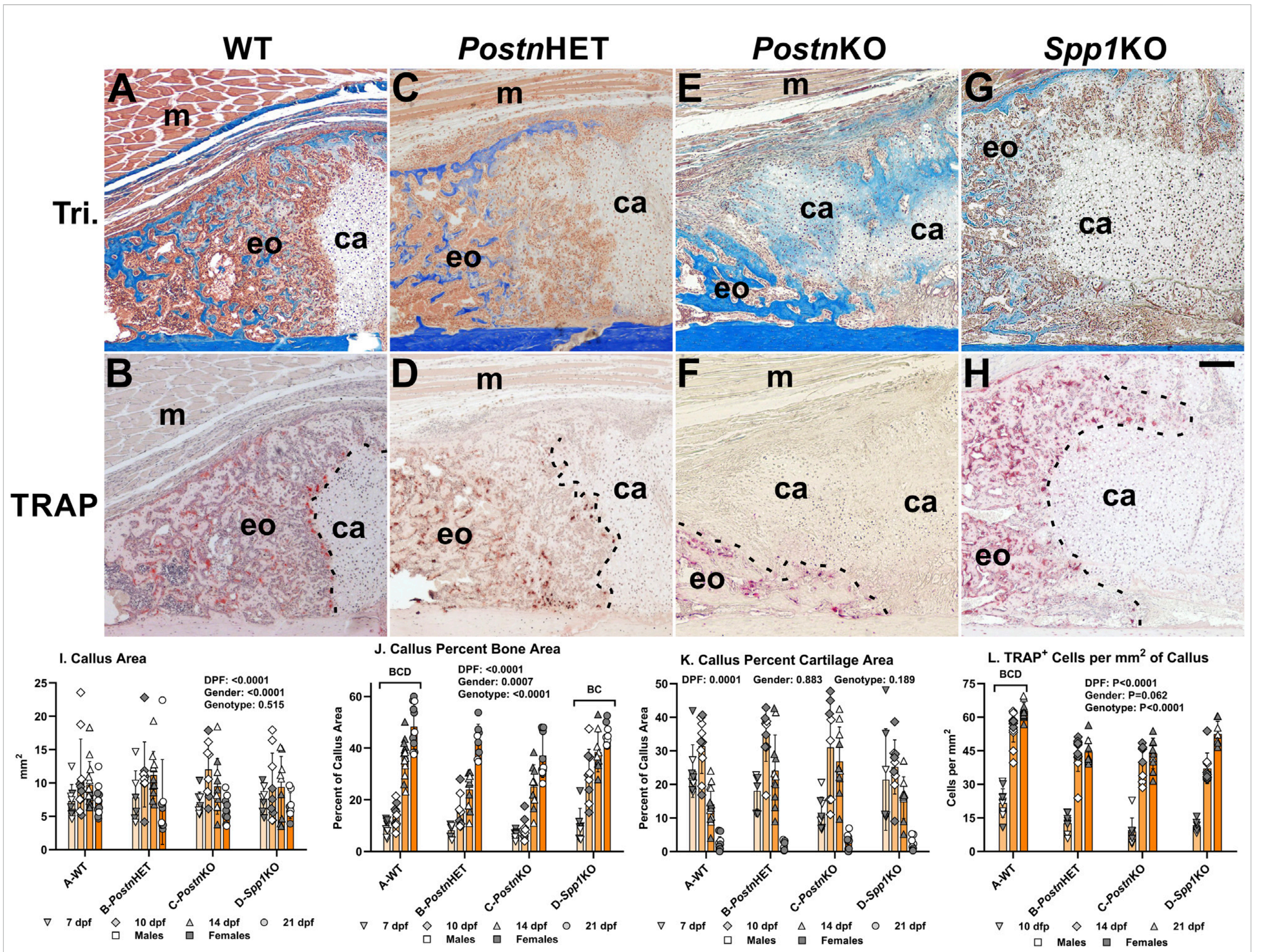

FIGURE 3
Histomorphometric Analysis of *Postn* and *Spp1* Deficient Mouse Fracture Calluses. Longitudinal sections from 14 dpf mouse femur fracture calluses stained with Masson's trichrome **(A, C, E, G)** or for tartrate resistant acid phosphatase (TRAP) activity **(B, D, F, H)** are shown from WT **(A, B)**, *Postn*HET **(C, D)**, *Postn*KO **(E, F)**, and *Spp11*KO mice **(G, H)**. The images show approximately one-quarter of the fracture callus and are oriented with the femur cortical bone at the bottom and fracture site in the bottom right corner. Muscle (m), cartilage (ca), and areas of apparent new bone formation (eo) are labeled. The chondro-osseous junction is highlighted with a dashed line in panels **(B, D, F, H)**. Femur fracture calluses were used to measure callus area **(I)**, normalized callus bone area **(J)**, and normalized callus cartilage area **(K)** at 7, 10, 14, and 21 dpf. Cartilage was identified by safranin-O staining (not shown). Tartrate resistant acid phosphatase (TRAP) staining was used to identify and count callus TRAP$^+$ cells at 10, 14, and 21 dpf **(L)**. The effect of time after fracture, gender, and genotype were determined by 3-way ANOVA and P-values are noted [insets, **(I, J, K, L)**]. Differences between genotypes are noted in each graph. Scale bar equals 100 μm **(H)**.

POSTN was absent in the *Postn*KO callus (Figure 2C). POSTN expression was detected in the *Spp1*KO callus though at an apparent reduced level as compared to WT (Figure 2D).

SPP1 was also broadly expressed throughout the WT fracture callus with SPP1 localized in callus osteoblasts and chondrocytes (Figure 2E). As expected, SPP1 expression appeared absent in the *Spp1*KO callus (Figure 2H). SPP1 levels appeared reduced in the *Postn*HET callus with expression in osteoblasts and in a subset of chondrocytes at or near the chondro-osseous junction (Figure 2F). SPP1 expression in the *Postn*KO callus appeared to be even further reduced as compared to the *Postn*HET callus (Figure 2G).

Postn and *Spp1* mRNA levels were measured in total RNA prepared from 14 dpf WT, *Postn*KO, and *Spp1*KO calluses by RTqPCR. As expected, ß-2-microglobulin (B2m) mRNA levels were similar between calluses from all genotypes (Figure 2I), while *Postn* and *Spp1* mRNA levels were significantly reduced in the *Postn*KO and *Spp1*KO calluses, respectively (Figures 2K, L). Similar to the IHC results, *Spp1* mRNA and *Postn* mRNA levels were significantly lower than WT levels in the *Postn*KO and *Spp1*KO calluses, respectively. We also noted that osteocalcin (*Bglap*) mRNA levels were reduced in the *Postn*KO mouse calluses (Figure 2J), which was consistent with the reduced callus BV/TV (Figure 1O) and reduced callus bone area (Figure 3J) in *Postn* deficient mice.

Loss of *Postn* or *Spp1* affects fracture callus morphology

Masson's trichrome staining was performed on tissue sections of fracture calluses collected at 7, 10, 14, and 21 dpf to visualize morphological differences between mouse genotypes during the healing process. Images from one quadrant of the external fracture callus of a WT, *Postn*HET, *Postn*KO, and *Spp1*KO mouse at 14 dpf are shown in Figures 3A, C, E, G, respectively. External callus bone tissue and cartilage were identified based on staining and morphology and quantified at each time point as shown in Figures 3I–K. Similarly, TRAP staining was performed on serial sections to identify osteoclasts in the fracture calluses (Figures 3B, D, F, H). At 14 dpf, the external callus of the WT mouse has apparent newly formed bone, is highly cellularized, and has a clearly demarcated chondro-osseous junction that is lined with osteoclasts (TRAP$^+$ cells; Figures 3A, B). While the 14 dpf *Postn*HET callus also appears to have a considerable amount of new bone and is highly cellularized, the chondro-osseous junction is neither distinct nor abundantly populated with osteoclasts (Figures 3C, D). The *Postn*KO mouse callus appears to have less new bone, more cartilage, and a poorly defined chondro-osseous junction (Figure 3E, F). The *Spp1*KO mouse callus appears to have amounts of new bone and cartilage that are comparable to the WT callus (Figures 3G, H). Similar to the *Postn*HET and *Postn*KO chondro-osseous junctions though, the *Spp1*KO chondro-osseous junction also appears to have fewer osteoclasts and displays an abnormal morphology.

Callus area, percent bone area, percent cartilage area, and density of TRAP$^+$ cells were quantified at each time point and for each genotype as shown in Figures 3I–L. As expected, callus area was dependent upon time after fracture and gender but was not dependent upon genotype.

For all genotypes, callus percent bone area increased with time after fracture (Figure 3J) while callus percent cartilage area peaked at 10 dpf before declining (Figure 3K). Callus percent bone area was dependent upon time after fracture, gender, and genotype with WT significantly different from all other genotypes and *Spp1*KO different from *Postn*HET and *Postn*KO. In contrast, callus percent cartilage area was only dependent upon on time after fracture and not gender or genotype. The density of osteoclasts (TRAP$^+$ cells/mm^2) was dependent upon time after fracture and genotype, but not gender (Figure 3L). Osteoclast density rapidly increased between 10 and 14 dpf for all genotypes but overall osteoclast density was greater in the WT mouse fracture calluses than in the *Postn*HET, *Postn*KO, or *Spp1*KO mouse calluses.

Loss of *Postn* or *Spp1* alters chondrocyte hypertrophy

The effects of *Postn* and *Spp1* null mutations on callus chondrocyte hypertrophy were assessed by immunohistochemical (IHC) detection and quantification of Collagen X (COL10A1) and Matrix Metallopeptidase-13 (MMP13). Serial sections from mouse fracture calluses collected at 7, 10, or 14 dpf were stained with Safranin-O to detect cartilage (Figures 4A, D, G, J, see also Figure 3K) or used for IHC detection of collagen X (Figures 4B, E, H, K) or MMP-13 (Figures 4C, F, I, L). Safranin-O stained areas appeared to roughly correlate with callus areas expressing collagen X. In contrast, callus cells expressing MMP-13 were generally not evident in callus cartilage areas stained with Safanin-O. Instead, cells expressing MMP-13 also appeared to express collagen X and were localized in areas of newly forming bone.

The percentage of callus cartilage area that expressed collagen X was determined at 7, 10, and 14 dpf (Figure 4M). Callus area expressing collagen X was dependent upon time after fracture and mouse genotype, but not gender. Across all time points, the percent of callus area that stained for COL10A1 by IHC was significantly lower for the *Postn*KO (21%) and *Spp1*KO (21%) mouse calluses as compared to WT (29%; $p < 0.009$).

Callus chondrocytes were counted at 10 and 14 dpf (Figure 4N) and compared to the number of callus chondrocytes expressing MMP-13, and thus presumably undergoing hypertrophy (Figure 4O). The number of callus chondrocytes was significantly reduced in the *Postn*KO and *Spp1*KO mouse calluses as compared to WT ($p = 0.039$). The number of callus chondrocytes also decreased between 10 dpf to 14 dpf by 33% in WT, 34% in *Postn*HET, 23% in *Postn*KO, and 29% in *Spp1*KO calluses. Conversely, the percentage of callus chondrocytes expressing MMP-13 increased between 10 and 14 dpf for all genotypes ($p < 0.0001$), even though the percentage of MMP-13 expressing chondrocytes was significantly lower in the *Postn*HET, *Postn*KO, and *Spp1*KO mouse calluses as compared to WT ($p < 0.0001$).

Fracture callus vascularization is reduced by loss of *Postn* or *Spp1*

Neovascularization of fracture calluses collected at 7, 10, and 14 dpf was assessed in WT, *Postn*HET, *Postn*KO, and *Spp1*KO mice by immunohistochemical (IHC) detection of CD31 (Figure 5). CD31 is encoded by *Pecam1* and is expressed by vascular endothelial cells [40]. At 10 and 14 dpf, blood vessels expressing CD31 were abundant in areas of the WT fracture callus that had or were undergoing endochondral ossification but were absent in the cartilage (Figures 5A, B). Blood vessels were similarly abundant in the *Postn*HET fracture calluses at 10 and 14 dpf (Figures 5C, D).

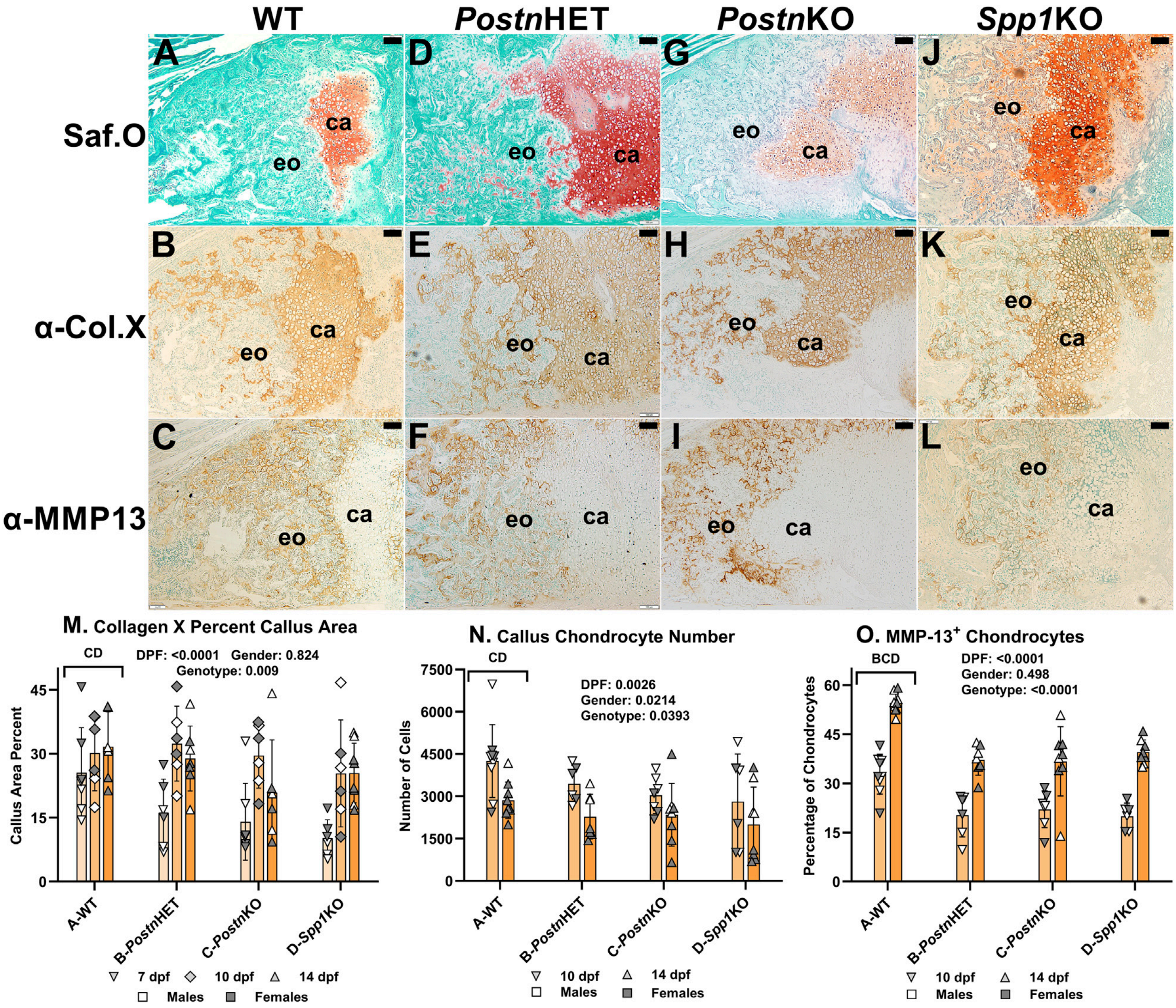

FIGURE 4
Immunohistochemical Analysis of Chondrocyte Hypertrophy in *Postn* and *Spp1* Deficient Mouse Fracture Calluses. Longitudinal sections from 14 dpf mouse femur fracture calluses were stained with safranin-O and fast green **(A, D, G, J)** or used to detect Collagen X **(B, E, H, K)** and MMP-13 **(C, F, I, L)** by immunohistochemistry. Specimens were from WT **(A–C)**, *Postn*HET **(D–F)**, *Postn*KO **(G–I)** and *Spp1*KO **(J–L)** mice. Areas of callus cartilage (ca) and endochondral ossification (eo) are noted. Collagen X expression (brown) was prominently detected around callus cartilage chondrocytes but also around chondrocytes in areas of endochondral bone formation for all genotypes. In contrast, MMP-13 expression (brown) was detected around chondrocytes in areas of endochondral ossification but rarely around chondrocytes in the callus cartilage. Quantitative analysis found reduced collagen X staining area, numbers of chondrocytes, and MMP-13$^+$ chondrocytes in *Postn*KO and *Spp1*KO mouse calluses **(M–O)**. The number of MMP-13$^+$ chondrocytes also was significantly reduced in the *Postn*HET specimens as compared to WT **(O)**. The effects of time after fracture, gender, and genotype were determined by 3-way ANOVA and P-values are shown in each graph [insets, **(M–O)**]. Scale bars equal 100 μm.

However, fewer blood vessels were apparent in the 10 and 14 dpf fracture calluses of the *Postn*KO and *Spp1*KO mice (Figures 5E–H). CD31$^+$ lumens in the fracture callus, and therefore presumptive blood vessels, were counted at 7, 10, and 14 dpf for all mouse genotypes and normalized to callus area (Figure 5I). Blood vessel density was dependent upon time after fracture, gender, and genotype. For all genotypes, the number of callus CD31$^+$ lumens increased with time after fracture. However, the rate of increase appeared greater in the WT and *Postn*HET calluses, leading to a relative paucity of new blood vessels in the *Postn*KO and *Spp1*KO fracture calluses. The reduced density of CD31$^+$ lumens in fracture calluses of male mice was consistent with previously observed sexual dimorphism in vasculogenesis associated with wound healing [41–43]. Quantification of the new blood vessels lumen area found an apparent time-dependent increase in lumen area but no effect of gender or genotype was detected (Figure 5J).

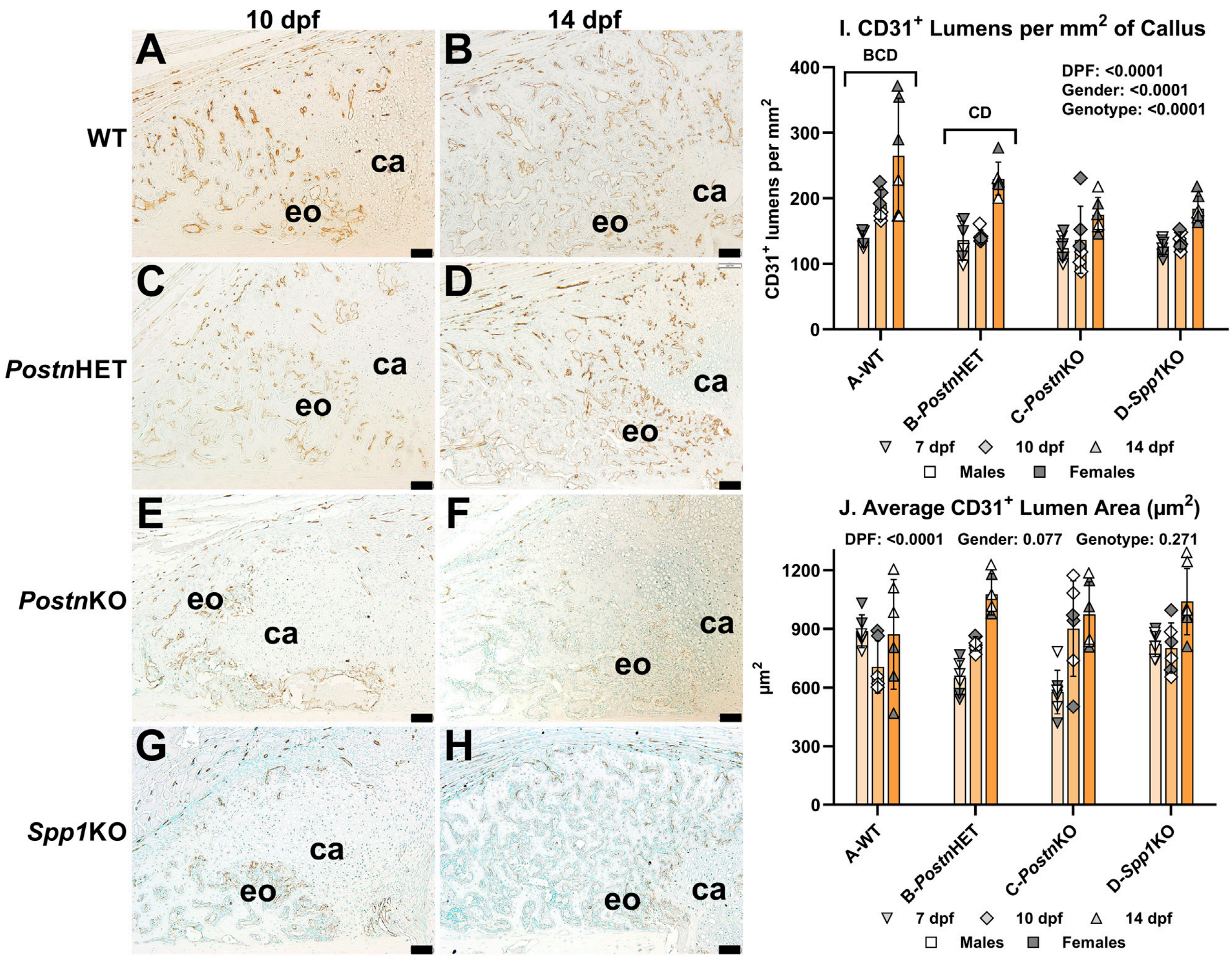

FIGURE 5
Immunohistochemical Assessment of Fracture Callus Vasculogenesis in *Postn* and *Spp1* Deficient Mice. Endothelial cells were identified in femur fracture callus longitudinal sections by immunohistochemical staining for CD31 (*Pecam1*) at 7 (not shown), 10 **(A, C, E, G)**, and 14 dpf **(B, D, F, H)** and from WT **(A, B)**, *Postn*HET **(C, D)**, *Postn*KO **(E, F)** and *Spp1*KO mice **(G, H)**. Avascular callus cartilage (ca) and vascularized areas of endochondral bone formation (eo) are shown. Quantitative analysis of vascular lumens surrounded by $CD31^+$ cells found a reduced density of lumens in the *Postn*HET, *Postn*KO, and *Spp1*KO specimens as compared to WT **(I)**. The reduced lumen density in the *Postn*HET, *Postn*KO, and *Spp1*KO calluses was not associated with changes in mean lumen area **(J)**. The effect of time after fracture, gender, and genotype were determined by 3-way ANOVA and P-values are shown in each graph [insets, **(I, J)**]. Scale bars equal 100 μm.

Effects of *Postn* or *Spp1* disruption on callus macrophages and osteoclasts

Fracture callus distribution of macrophages and osteoclasts was determined by immunohistochemical detection of F4/80 and cathepsin K (CTSK), respectively (Figure 6). At 14 dpf, $F4/80^+$ cells were detected in calluses from all genotypes (Figures 6A, C, E, G). The $F4/80^+$ cells appeared to be absent from callus cartilage but enriched in areas of newly formed bone. Osteoclasts detected by CTSK expression were evident along the callus chondro-osseous junction and within areas of newly formed bone (Figures 6B, D, F, H). Relative to WT mouse calluses, IHC detection of CTSK appeared to be reduced in the *Postn*HET and *Postn*KO mouse calluses and further reduced in the *Spp1*KO mouse callus. Interestingly, $F4/80^+$ cells were rarely observed in the region adjacent to the chondro-osseous junction.

The $F4/80^+$ and $CTSK^+$ cells in fracture calluses collected at 7, 10, and 14 dpf were counted for each mouse genotype and normalized to callus area. The density of $F4/80^+$ cells was dependent upon time after fracture and genotype, but not gender (Figure 6I). The density of $F4/80^+$ cells increased with time after fracture for all genotypes, but the density of $F4/80^+$ cells was reduced in the *Postn*KO and *Spp1*KO mouse calluses. Similarly, the density of $CTSK^+$ osteoclasts was dependent upon on time after fracture and genotype but not gender (Figure 6J). The density of osteoclasts increased with time

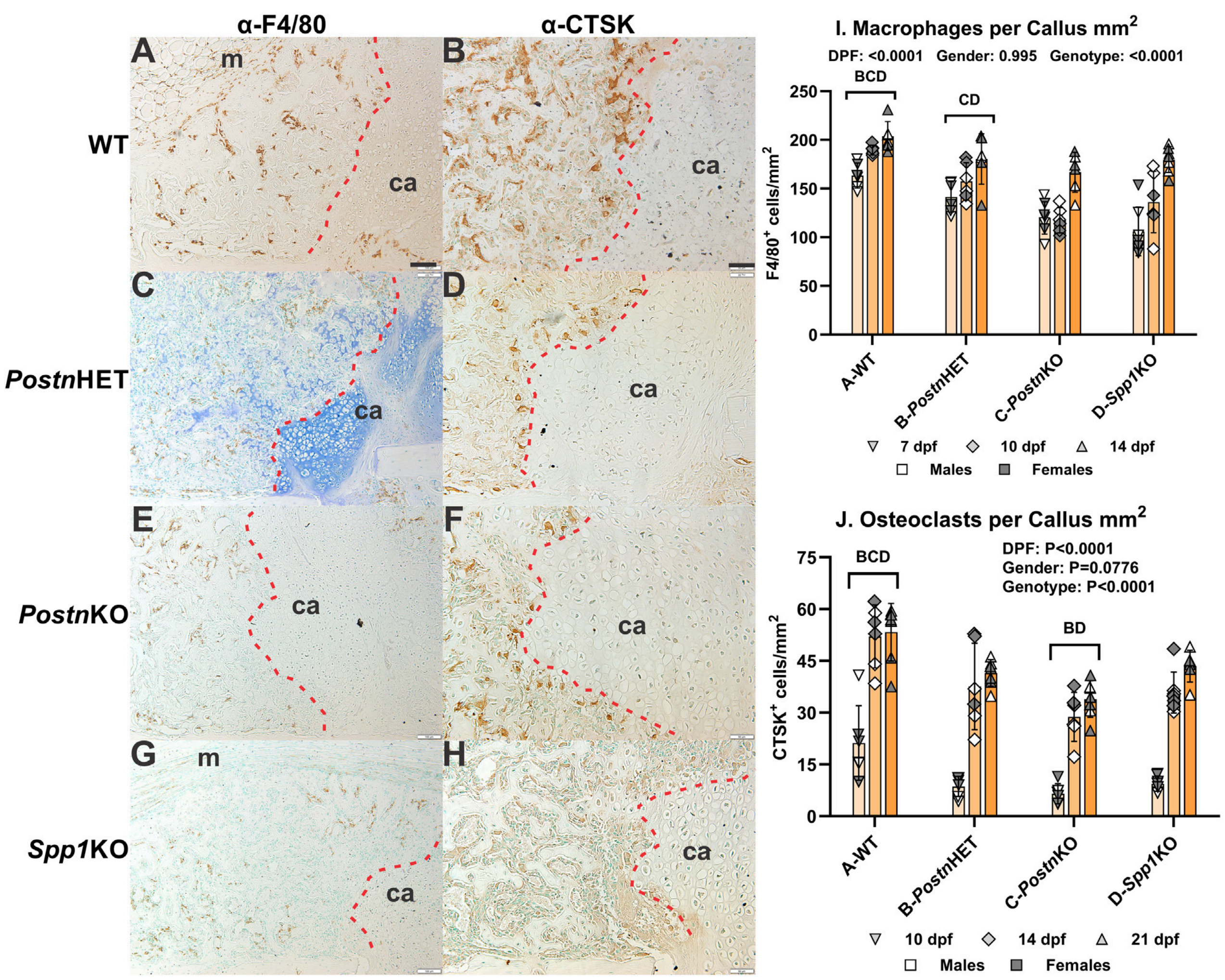

FIGURE 6
Effects of *Postn* or *Spp1* Deficiency on Callus Macrophages and Osteoclasts. Immunohistochemistry was used to identify macrophages expressing F4/80 [*Adgre1*; **(A, C, E, G)**] or osteoclasts expressing cathepsin K [*Ctsk*; **(B, D, F, H)**] in 7 (not shown), 10 (not shown), 14 (AH), and 21 dpf (not shown) fracture calluses of WT **(A, B)**, *Postn*HET **(C, D)**, *Postn*KO **(E, F)**, and *Spp1*KO mice **(G, H)**. Callus cartilage (ca) and muscle surrounding the callus (m) are noted. The chondro-osseous junction is highlighted with a dashed red line. F4/80 expressing macrophages were detected in areas of endochondral bone formation but were less abundant at the chondro-osseous junction and rare in the callus cartilage. CTSK expressing osteoclasts were also observed in areas of endochondral bone formation, localized at the chondro-osseous junction, and absent from callus cartilage. Quantitative analyses found significant reductions in macrophage **(I)** and osteoclast **(J)** density for all tested genotypes as compared to WT. The effects of time after fracture, gender, and genotype were determined by 3-way ANOVA and Pvalues are shown in each graph [insets, **(I, J)**]. Scale bar equals 100 μm for F4/80 **(A)** and 50 μm for CTSK **(B)** immunostaining.

after fracture for all genotypes. Osteoclast density at all time points was highest in the WT mouse calluses and lowest in the *Postn*KO mouse calluses.

Loss of *Postn* or *Spp1* reduces osteoclast COX-2 expression

Fracture callus cells expressing COX-2 were detected by IHC (Figure 7). In 14 dpf WT fracture calluses, COX-2 expression was easily detectable in osteoblasts, some chondrocytes, and osteoclasts, including those at the chondro-osseous junction (Figure 7A). Strong COX-2 expression was evident in osteoblasts and some chondrocytes of the *Postn*HET and *Postn*KO mouse calluses (Figures 7B, C). COX-2 expression was evident but comparatively reduced in osteoclasts of the *Postn*HET and *Postn*KO mouse calluses as compared to the osteoclasts and osteoblasts in the WT mouse calluses and the osteoblasts in the *Postn*HET and *Postn*KO mouse calluses. In the *Spp1*KO mouse calluses, COX-2 expression was evident in osteoblasts and some chondrocytes but osteoclast COX-2 expression was markedly faint in comparison to callus

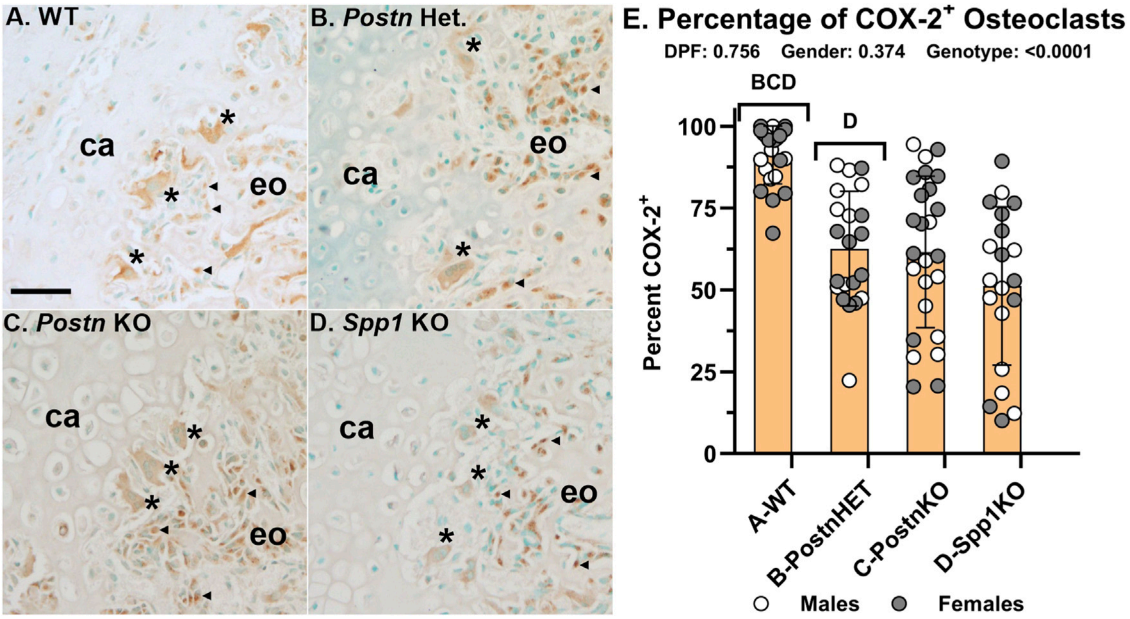

FIGURE 7
COX-2 Expression is Reduced in Fracture Callus Osteoclasts of *Postn* and *Spp1* Deficient Mice. COX-2 (*Ptgs2*) expression was detected in fracture callus cells by immunohistochemistry. Shown are sections from callus specimens along the chondro-osseous junction collected at 14 dpf for WT **(A)**, *Postn*HET **(B)**, *Postn*KO **(C)**, and *Spp1*KO mice **(D)**. Relative expression of COX-2 in apparent callus osteoblasts (◀) and osteoclasts (*) from WT mice appeared similar **(A)**. In contrast, osteoclast COX-2 expression relative to osteoblast expression appeared lower in the *Postn*HET specimens **(B)**, lower still in the *Postn*KO specimens **(C)**, and weak in the *Spp1*KO specimens **(D)**. The number of osteoclasts that appeared to express COX-2 were compared to the number of TRAP expressing osteoclasts as a percentage **(E)**. Similar to the apparent reduction in osteoclast COX-2 expression, the percentage of COX-2 expressing osteoclasts was reduced in the *Postn* and *Spp1* deficient mouse fracture callus specimens collected at 10, 14, and 21 dpf. The effect of genotype on osteoclast COX-2 expression was significant, but not those of time after fracture or gender as determined by 3-way ANOVA. P-values are shown [inset, **(E)**]. Callus cartilage (ca) and areas of endochondral ossification (eo) are shown. Scale bars equal 20 μm **(A)**.

osteoclasts from the WT, *Postn*HET, and *Postn*KO mice (Figure 7D).

Callus osteoclasts and COX-2 expressing osteoclasts were counted at 10, 14, and 21 dpf from WT, *Postn*HET, *Postn*KO, and *Spp1*KO mice (Figure 7E). The percentage of osteoclasts expressing COX-2 was not dependent upon time after fracture or gender. However, the percentage of osteoclasts expressing COX-2 was reduced in the *Postn*HET (63%), *Postn*KO (62%), and *Spp1*KO (51%) calluses as compared to calluses from WT mice (91%).

Changes in callus mRNA levels associated with loss of *Postn* or *Spp1*

Total RNA was isolated from 14 dpf calluses of WT, *Postn*KO, and *Spp1*KO mice and target mRNA levels were measured by RT-qPCR. Chondrogenesis and chondrocyte hypertrophy were assessed by measuring Aggrecan (*Acan*) and MMP-13 (*Mmp13*) mRNA levels, respectively. *Acan* mRNA levels were similar between WT, *Postn*KO and *Spp1*KO mouse calluses, though *Acan* mRNA levels were greater in *Postn*KO calluses than *Spp1*KO calluses (Figure 8A). In contrast and similar to the IHC results (Figure 4), *Mmp13* mRNA levels were significantly reduced in the *Postn*KO and *Spp1*KO mouse calluses as compared to WT (Figure 8B). Vasculogenesis was assessed by measuring CD31 (*Pecam1*) mRNA levels and similar to the IHC results (Figure 5), *Pecam1* mRNA levels were significantly reduced in the *Spp1*KO mice, though not in the *Postn*KO mouse calluses (P = 0.13; Figure 8C). Osteoclast activity was assessed by measuring Cathepsin K (*Ctsk*) and Tartrate Resistant Acid Phosphatase (*Acp5*) mRNA levels. While IHC results showed significant reductions in TRAP⁺ cell density (Figure 3) and CTSK⁺ cell density (Figure 6), only mRNA levels for *Acp5* were significantly lower in the *Spp1*KO mouse calluses (Figures 8D, E). COX-2 (*Ptgs2*) mRNA levels were also measured and were significantly reduced in both the *Postn*KO and *Spp1*KO mouse calluses as compared to WT calluses (Figure 8F).

Discussion

In control experiments to confirm reduced target mRNA and protein expression in the *Postn*KO and *Spp1*KO mouse calluses (Figure 2), we observed that loss of *Postn* reduced

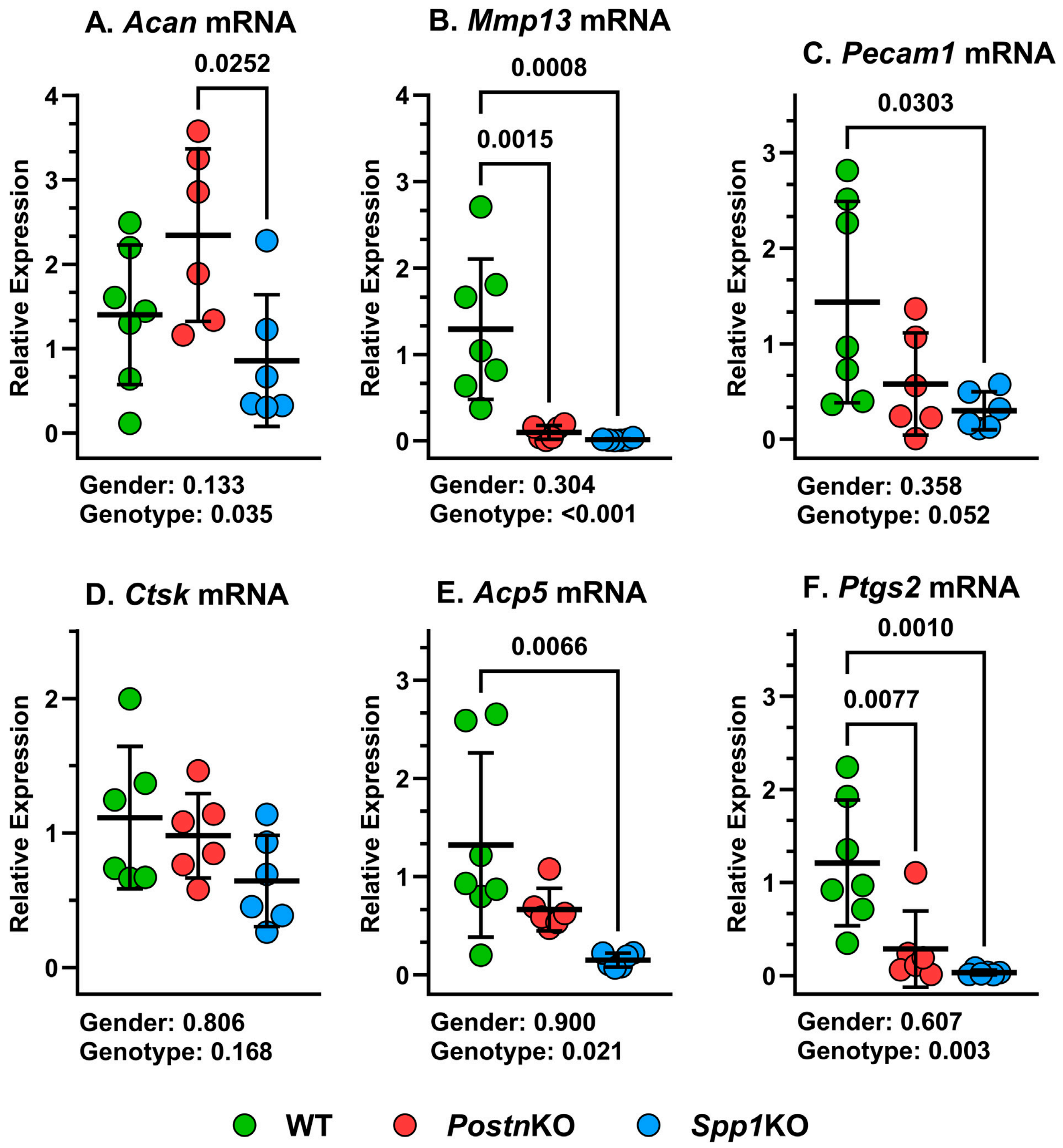

FIGURE 8
Loss of *Postn* and *Spp1* alters callus gene expression at 14 dpf. RNA was prepared from mouse calluses collected at 14 dpf from at least three male and three female mice of each genotype. mRNA levels for **(A)** *Acan*, **(B)** *MMP13*, **(C)** *Pecam1*, **(D)** *Ctsk*, **(E)** *Acp5*, and **(F)** *Ptgs2* were determined by RTqPCR and normalized to *Actb* (ß-actin) mRNA levels using the $2^{-\Delta CT}$ method. mRNA levels were compared between genotypes and gender using 2-way ANOVA and post-hoc analyses. P values are shown beneath each graph.

Spp1 expression and conversely, loss of *Spp1* reduced *Postn* expression. *Postn* and *Spp1* expression were also reduced in the *Postn*HET mouse fracture calluses; consistent with *Postn* affecting *Spp1* expression (Figure 2). Rios et al. also observed reduced POSTN levels in *Postn*HET newborn mouse protein extracts, indicating no compensatory expression from the remaining, normal *Postn* allele [21]. Whether the mutual effects of *Postn* on *Spp1* expression and *Spp1* on *Postn* expression relate to signaling functions associated with these matricellular proteins, a temporal change in fracture healing gene expression associated with impaired healing, or a combination of these effects will require additional investigation. Therefore, ascribing any fracture healing effect to *Postn* versus *Spp1* in this study is limited by the mutual gene expression effects of *Postn* and *Spp1* on each other.

Null mutations in *Postn* or *Spp1* produced similar, negative effects on mouse femur fracture healing. Notably, resolution of callus cartilage by endochondral ossification appeared delayed in the mutant mice as indicated by radiographic imaging, increased callus volume, and reduced callus bone area (Figures 1, 3). The underlying cellular effects of lost *Postn* or *Spp1* in the fracture callus also appeared similar. Callus chondrocyte hypertrophy was abnormal as evidenced by the reduced number and proportion of MMP-13 expressing chondrocytes and *Mmp13* expression in the *Postn*KO and *Spp1*KO mouse calluses (Figures 4, 8). Null mutations in *Postn* or *Spp1* also altered the morphology of the chondro-osseous junction and reduced the overall number of callus osteoclasts (Figures 3, 6, 7). The abnormal morphology of the chondro-osseous junction is particularly evident in the *Postn*HET callus shown in Figures 3C, D in which the transition zone was enlarged between the callus cartilage and the area of new bone formation. The paucity of TRAP$^+$ osteoclasts at the chondro-osseous junction was also evident in the *Postn*KO and *Spp1*KO calluses (Figure 3). The apparent altered healing in the *Postn*HET, *Postn*KO, and *Spp1*KO calluses was accompanied by reduced callus vascularization (Figure 5). Thus, *Postn* and *Spp1* appear to have multiple roles during fracture healing including promoting chondrocyte hypertrophy and callus vascularization, which are both necessary for normal fracture healing [8, 10].

In this study, the stabilized femur fractures in the *Postn*KO mice showed delayed healing with apparent bony bridging of the callus by 28 dpf rather than by 21 dpf (Figure 1). The *Postn*KO mouse calluses also had significant reductions in BV/TV, bone area, chondrocyte number, Type X collagen stained area, number of chondrocytes expressing MMP-13, callus vascularity, and osteocalcin expression (Figures 1–5). Similarly, Duchamp de Lageneste et al. found that fracture callus cartilage and bone area were reduced in *Postn*KO mice [20]. However, and in contrast to the stabilized femur fractures used in the present study, the un-stabilized tibia fractures used by Duchamp de Lageneste et al. failed to heal after 28 days in the *Postn*KO mice [20].

Femur fractures in the *Spp1*KO mice also showed delayed healing with apparent bony bridging by 21 dpf as compared to 14 dpf in the wild-type C57BL/6 mice (Figure 1). The *Spp1*KO mouse fracture also had reduced bone area, chondrocytes, TRAP$^+$ cells, Type X collagen staining area, MMP-13 expressing chondrocytes, and callus vascularity similar to the *Postn*KO mice (Figures 3–5). Using the same stabilized femur fracture model, Duvall et al. also found that fracture healing was delayed in *Spp1*KO mice and was characterized by reduced callus vascularization at 7 dpf, reduced callus size at 7 and 14 dpf, and reduced callus mechanical properties at 28 dpf, but with a larger callus at 56 dpf. The larger callus in the *Spp1*KO mice at 56 dpf was interpreted as impaired remodeling of the callus though no differences in expression of RANKL, TRAP, Cathepsin K, or OPG were detected in calluses at earlier time points. The current analysis found that callus vascularity was similarly reduced in the *Spp1*KO mice (Figure 5) but, in contrast, that callus osteoclast density was also reduced (Figure 6).

Hypertrophic chondrocytes express Type X Collagen (COL10A1) and MMP-13 [44]. Chondrocyte COL10A1 expression was evident in the fracture calluses of WT, *Postn*HET, *Postn*KO, and *Spp1*KO mice (Figure 4). Indeed, most rounded chondrocytes within the callus were surrounded by COL10A1 suggesting that once differentiated, fracture callus chondrocytes rapidly begin expressing *Col10a1*. In contrast, most, if not all, callus chondrocytes only expressed MMP-13 once the chondrocyte encountered or traversed the chondro-osseous junction. This observation suggests that a signaling event occurs with chondrocytes at the chondro-osseous junction to induce MMP-13 expression (Figure 4C). Furthermore, loss of POSTN or SPP1 appears to impair *Mmp13* induction as evident by the reduced proportion of MMP-13$^+$ chondrocytes (Figure 4) and reduced callus *Mmp13* expression (Figure 8), likely contributing to impaired bone formation (Figures 1, 3).

In the WT, *Postn*HET, *Postn*KO, and *Spp1*KO mouse calluses, the chondro-osseous junction is lined with TRAP$^+$ and CTSK$^+$ osteoclasts (Figures 3, 6). The localization of osteoclasts at the chondro-osseous junction suggests that osteoclasts may mediate the hypertrophic transition from COL10A1$^+$, MMP-13$^-$ chondrocytes to COL10A1$^+$, MMP-13$^+$ chondrocytes as the chondro-osseous junction encounters and then traverses callus cartilage. Indeed, the osteoclast secretome has been shown to induce MMP-13 expression in cultured chondrocytes [45]. Culturing osteoclasts on a cartilage substratum or co-culturing osteoclasts with chondrocytes can alter osteoclast activity and promote osteoclast MMP-8 expression [46]. In the present study, loss of *Postn* or *Spp1* reduced callus osteoclast density (Figures 3, 6) as well as the proportion of osteoclasts scored positive for COX-2 expression via IHC from 91% in WT calluses to 62% in *Postn*KO and 51% in *Spp1*KO calluses (Figure 7). Loss of *Postn* or *Spp1* also reduced overall levels of callus COX-2 mRNA (Figure 8). This suggests that as callus chondrocytes encounter the chondro-osseous junction, prostaglandins produced via COX-2 in the chondro-osseous junction osteoclasts help promote *Mmp13* expression in the chondrocytes. Prostaglandins produced via COX-2 can regulate chondrocyte *Mmp13* expression [47]. For instance, prostaglandin E_2 signaling via the EP2 receptor was reported to inhibit *Mmp13* expression [48], while prostaglandin E_2 signaling via the EP4 receptor was reported to promote

Mmp13 expression [49]. COX-2 expression is also associated with increased MMP-13 expression in other systems [50, 51]. Determining whether COX-2 expressed in osteoclasts at the chondro-osseous junction is directly or indirectly regulating callus chondrocyte hypertrophy will require additional experimentation.

MMP-13 appears to be a focal point for both osteoclastogenesis and chondrocyte hypertrophy. Treating osteoclast precursors with exogenous MMP-13 promoted osteoclastogenesis *in vitro* independent of MMP-13 proteolytic activity [52]. Hypertrophic chondrocytes expressing *Mmp13* mRNA were found in close proximity to TRAP$^+$ osteoclasts in mouse rib fracture calluses [53]. Genetic ablation of *Mmp13* delayed resolution of callus cartilage in mouse tibia fracture calluses and in adolescent mouse growth plates [54, 55]. The expanded hypertrophic zone in the *Mmp13* deficient mouse growth plates was characterized by an increased number of hypertrophic cell layers expressing *Spp1* at the chondro-osseous junction. Similar deficiencies in endochondral ossification between the *Mmp13* deficient mice and the *Postn*HET, *Postn*KO, and *Spp1*KO mice as described here suggests that loss of *Postn* or *Spp1* is affecting callus endochondral ossification, at least in part, through reduced chondrocyte *Mmp13* expression. In support of this conclusion, Xu et al. found that exogenous addition of SPP1, especially phosphorylated SPP1, can induce *Mmp13* expression in cultured human chondrocytes while Attur et al. found that mouse articular chondrocytes lacking *Postn* exhibited reduced *Mmp13* expression in an arthritis model [56, 57].

Neovascularization of the fracture callus is critical for healing and the number of blood vessels (CD31$^+$ lumens) was significantly reduced in the *Postn*HET, *Postn*KO, and *Spp1*KO mouse calluses (Figure 5). A prior study also found callus vascularization was deficient in *Spp1* null mice [19]. Loss of *Postn* or *Spp1* reduced callus *Ptgs2* (COX-2) and *Mmp13* mRNA levels (Figure 8) and specifically reduced COX-2 expression in osteoclasts (Figure 7) and MMP-13 expression in chondrocytes (Figure 4). Loss of *Mmp13* impairs growth plate endochondral ossification and chondrocyte MMP-13 expression is associated with angiogenesis during endochondral ossification [7, 55, 58]. COX-2 is also associated with angiogenesis in several systems including tumor growth [59, 60]. COX-2 activity is a rate limiting step in the production of prostaglandins which directly stimulate angiogenesis [61, 62]. For example, prostaglandin E_2 was found to induce *Mmp13* expression in mouse calvaria cell cultures and promote angiogenesis [63]. Thus, reduced expression of COX-2 in the *Postn*HET, *Postn*KO, and *Spp1*KO calluses could have directly impaired neovascularization of the fracture callus via reduced prostaglandin synthesis (Figure 5) and affected MMP-13 expression in callus chondrocytes (Figures 3, 7).

The decrease in callus osteoclasts in the *Postn* and *Spp1* deficient mice was also accompanied by a reduction in callus F4/80$^+$ macrophages (Figure 6). Loss of SPP1 or POSTN could have affected inflammation during the early stages of fracture healing leading to reduced monocyte infiltration of the callus. Unfortunately, inflammation and the early stages of healing were not investigated in the *Postn*HET, *Postn*KO, or *Spp1*KO mice. The available IHC data, however, suggests that the F4/80$^+$ macrophages are preferentially located in areas of newly formed bone and bone marrow, scarce at the chondro-osseous junction, and absent from callus cartilage (Figure 6). Thus, the available results indicate that the reduction in F4/80$^+$ macrophages is a function of reduced bone and bone marrow formation in the external callus and likely is not causative for the reduction in callus osteoclasts. Still, other macrophage or monocyte populations that do not express F4/80 may have been affected by loss of POSTN or SPP1 leading to the reduction in callus osteoclasts [64].

The mechanisms through which POSTN and SPP1 affect osteoclast COX-2 expression, chondrocyte hypertrophy, and callus neovascularization will require further investigation. As matricellular proteins, POSTN and SPP1 localize in the extracellular matrix to provide signaling cues rather than a structural function within the extracellular matrix [26, 65]. POSTN was widely distributed throughout the fracture callus with apparent greater staining in areas rich with osteoblasts and around chondrocytes at the chondro-osseous junction (Figure 2A). SPP1 also localized at areas rich in osteoblasts and was evident in callus chondrocytes including chondrocytes at the chondro-osseous junction (Figure 2E), consistent with *Spp1* expression in hypertrophic chondrocytes [66]. In the *Postn*HET, and particularly the *Postn*KO fracture calluses, SPP1 expression was reduced but localized to chondrocytes near the chondro-osseous junction (Figures 2F, G).

Both POSTN and SPP1 are integrin ligands and both chondrocytes and osteoclast express integrins, suggesting that local levels of POSTN and SPP1 can alter chondrocyte and osteoclast functions via integrin mediated signaling [31, 32, 34, 67]. For instance, SPP1 signaling via integrin αvß3 can affect osteoclast activity [31, 68, 69]. SPP1 and POSTN also can induce chondrocyte MMP13 expression, though the signaling pathways employed are less clear [56, 70, 71]. In cancer models, SPP1 can induce COX-2 expression, promote matrix metallopeptidase expression, and promote angiogenesis [72, 73]. This suggests that *Spp1* or *Postn* expression in chondrocytes at the chondro-osseous junction may have a similar role by inducing COX-2 expression in osteoclasts, promoting *Mmp13* expression, and promoting angiogenesis. The precise mechanism through which SPP1, POSTN, or other matricellular proteins spatially coordinate events in the fracture callus or at the chondro-osseous junction to control chondrocyte hypertrophy, osteoclast gene expression, and vasculogenesis to enable endochondral bone formation will require a deeper understanding of the cell signaling events involved.

Author contributions

MT performed experiments, aided in experimental design and methods, collected and analyzed data, and helped prepare the manuscript. MC performed experiments, maintained mouse colonies, and aided with manuscript preparation. CW collected and analyzed data. JO'C developed the study, aided in experimental design and methods, performed data analysis, and prepared the manuscript. All authors contributed to the article and approved the submitted version.

Data availability

The original contributions presented in the study are included in the article/Supplementary Material, further inquiries can be directed to the corresponding author.

Ethics statement

The animal study was approved by the Institutional Animal Care and Use Committee-Rutgers University. The study was conducted in accordance with the local legislation and institutional requirements.

Funding

The author(s) declare financial support was received for the research, authorship, and/or publication of this article. This work was supported by the National Institute of Arthritis and Musculoskeletal and Skin Diseases of the National Institutes of Health (grant number R01AR069044); the Rutgers-New Jersey Medical School Department of Orthopaedics; the Fred F. Buechel, M.D., Chair for Joint Replacement at New Jersey Medical School; and the Fred F. Behrens, M.D. Endowed Chair in Orthopedic Trauma Education.

Acknowledgments

The authors thank Joel Pierre and Luke Fritzky from the Rutgers-New Jersey Medical School Cellular Imaging and Histology Core for their help in preparing the many histological samples used in the reported experiments.

Conflict of interest

The author(s) declared no potential conflicts of interest with respect to the research, authorship, and/or publication of this article.

Supplementary material

The Supplementary Material for this article can be found online at: https://www.ebm-journal.org/articles/10.3389/ebm.2024.10066/full#supplementary-material

References

1. Schenk RK. Biology of fracture repair. In: Browner BD, Jupiter JB, Levine AM, Trafton PG, editors. *Skeletal Trauma*. Philadelphia: W.B. Saunders Company (1992). p. 31–75.

2. Brighton CT, Krebs AG. Oxygen tension of healing fractures in the rabbit. *The J Bone and Joint Surg* (1972) **54**:323–32. doi:10.2106/00004623-197254020-00010

3. Shiu HT, Leung PC, Ko CH. The roles of cellular and molecular components of a hematoma at early stage of bone healing. *J Tissue Eng Regen Med* (2018) **12**: e1911–e1925. doi:10.1002/term.2622

4. Apel PJ, Crane D, Northam CN, Callahan M, Smith TL, Teasdall RD. Effect of selective sensory denervation on fracture-healing: an experimental study of rats. *The J Bone Joint Surgery-American Volume* (2009) **91**:2886–95. doi:10.2106/jbjs.h.01878

5. Ono T, Takayanagi H. Osteoimmunology in bone fracture healing. *Curr Osteoporos Rep* (2017) **15**:367–75. doi:10.1007/s11914-017-0381-0

6. Lin HN, O'Connor JP. Osteoclast depletion with clodronate liposomes delays fracture healing in mice. *J Orthop Res* (2017) **35**:1699–706. doi:10.1002/jor.23440

7. Kojima T, Hasegawa T, de Freitas PH, Yamamoto T, Sasaki M, Horiuchi K, et al. Histochemical aspects of the vascular invasion at the erosion zone of the epiphyseal cartilage in MMP-9-deficient mice. *Biomed Res* (2013) **34**:119–28. doi:10.2220/biomedres.34.119

8. Hu DP, Ferro F, Yang F, Taylor AJ, Chang W, Miclau T, et al. Cartilage to bone transformation during fracture healing is coordinated by the invading vasculature and induction of the core pluripotency genes. *Development* (2017) **144**:221–34. doi:10.1242/dev.130807

9. Gerber HP, Vu TH, Ryan AM, Kowalski J, Werb Z, Ferrara N. VEGF couples hypertrophic cartilage remodeling, ossification and angiogenesis during endochondral bone formation. *Nat Med* (1999) **5**:623–8. doi:10.1038/9467

10. Hausman MR, Schaffler MB, Majeska RJ. Prevention of fracture healing in rats by an inhibitor of angiogenesis. *Bone* (2001) **29**:560–4. doi:10.1016/s8756-3282(01)00608-1

11. Odgren PR, Witwicka H, Reyes-Gutierrez P. The cast of clasts: catabolism and vascular invasion during bone growth, repair, and disease by osteoclasts, chondroclasts, and septoclasts. *Connect Tissue Res* (2016) **57**:161–74. doi:10.3109/03008207.2016.1140752

12. Lin HN, Cottrell J, O'Connor JP. Variation in lipid mediator and cytokine levels during mouse femur fracture healing. *J Orthop Res* (2016) **34**:1883–93. doi:10.1002/jor.23213

13. Bahney CS, Zondervan RL, Allison P, Theologis A, Ashley JW, Ahn J, et al. Cellular biology of fracture healing. *J Orthopaedic Res* (2019) **37**:35–50. doi:10.1002/jor.24170

14. Malhan D, Schmidt-Bleek K, Duda GN, El Khassawna T. Landscape of well- coordinated fracture healing in a mouse model using molecular and cellular analysis. *Int J Mol Sci* (2023) **24**:3569. doi:10.3390/ijms24043569

15. Bornstein P, Sage EH. Matricellular proteins: extracellular modulators of cell function. *Curr Opin Cell Biol* (2002) **14**:608–16. doi:10.1016/s0955-0674(02)00361-7

16. Bonnet N, Garnero P, Ferrari S. Periostin action in bone. *Mol Cell Endocrinol* (2016) **432**:75–82. doi:10.1016/j.mce.2015.12.014

17. Hirakawa K, Hirota S, Ikeda T, Yamaguchi A, Takemura T, Nagoshi J, et al. Localization of the mRNA for bone matrix proteins during fracture healing as determined by *in situ* hybridization. *J Bone Mineral Res* (1994) **9**:1551–7. doi:10.1002/jbmr.5650091007

18. Nakazawa T, Nakajima A, Seki N, Okawa A, Kato M, Moriya H, et al. Gene expression of periostin in the early stage of fracture healing detected by cDNA microarray analysis. *J Orthopaedic Res* (2004) **22**:520–5. doi:10.1016/j.orthres.2003.10.007

19. Duvall CL, Taylor WR, Weiss D, Wojtowicz AM, Guldberg RE. Impaired angiogenesis, early callus formation, and late stage remodeling in fracture healing of osteopontin-deficient mice. *J Bone Mineral Res* (2007) **22**:286–97. doi:10.1359/jbmr.061103

20. Duchamp de Lageneste O, Julien A, Abou-Khalil R, Frangi G, Carvalho C, Cagnard N, et al. Periosteum contains skeletal stem cells with high bone regenerative potential controlled by Periostin. *Nat Commun* (2018) **9**:773. doi:10.1038/s41467-018-03124-z

21. Rios H, Koushik SV, Wang H, Wang J, Zhou HM, Lindsley A, et al. Periostin null mice exhibit dwarfism, incisor enamel defects, and an early-onset periodontal disease-like phenotype. *Mol Cell Biol* (2005) **25**:11131–44. doi:10.1128/mcb.25.24.11131-11144.2005

22. Liaw L, Birk DE, Ballas CB, Whitsitt JS, Davidson JM, Hogan BL. Altered wound healing in mice lacking a functional osteopontin gene (spp1). *J Clin Invest* (1998) **101**:1468–78. doi:10.1172/jci2131

23. Icer MA, Gezmen-Karadag M. The multiple functions and mechanisms of osteopontin. *Clin Biochem* (2018) **59**:17–24. doi:10.1016/j.clinbiochem.2018.07.003

24. Reinholt FP, Hultenby K, Oldberg A, Heinegard D. Osteopontin--a possible anchor of osteoclasts to bone. *Proc Natl Acad Sci U S A* (1990) **87**:4473–5. doi:10.1073/pnas.87.12.4473

25. Ishijima M, Rittling SR, Yamashita T, Tsuji K, Kurosawa H, Nifuji A, et al. Enhancement of osteoclastic bone resorption and suppression of osteoblastic bone formation in response to reduced mechanical stress do not occur in the absence of osteopontin. *The J Exp Med Exp Med* (2001) **193**:399–404. doi:10.1084/jem.193.3.399

26. Duchamp de Lageneste O, Colnot C. Periostin in bone regeneration. *Adv Exp Med Biol* (2019) **1132**:49–61. doi:10.1007/978-981-13-6657-4_6

27. Clark D, Doelling J, Hu D, Miclau T, Nakamura M, Marcucio R. Age-related decrease in periostin expression may be associated with attenuated fracture healing in old mice. *J Orthopaedic Res Res* (2023) **41**:1022–32. doi:10.1002/jor.25439

28. Ishihara S, Usumi-Fujita R, Kasahara Y, Oishi S, Shibata K, Shimizu Y, et al. Periostin splice variants affect craniofacial growth by influencing chondrocyte hypertrophy. *J Bone Miner Metab* (2023) **41**:171–81. doi:10.1007/s00774-023-01409-y

29. Merle B, Garnero P. The multiple facets of periostin in bone metabolism. *Osteoporos Int Int* (2012) **23**:1199–212. doi:10.1007/s00198-011-1892-7

30. Nakase T, Sugimoto M, Sato M, Kaneko M, Tomita T, Sugamoto K, et al. Switch of osteonectin and osteopontin mRNA expression in the process of cartilage-to-bone transition during fracture repair. *Acta Histochem* (1998) **100**:287–95. doi:10.1016/s0065-1281(98)80015-9

31. Miyauchi A, Alvarez J, Greenfield EM, Teti A, Grano M, Colucci S, et al. Recognition of osteopontin and related peptides by an alpha v beta 3 integrin stimulates immediate cell signals in osteoclasts. *J Biol Chem* (1991) **266**:20369–74. doi:10.1016/s0021-9258(18)54932-2

32. Gillan L, Matei D, Fishman DA, Gerbin CS, Karlan BY, Chang DD. Periostin secreted by epithelial ovarian carcinoma is a ligand for alpha(V)beta(3) and alpha(V)beta(5) integrins and promotes cell motility. *Cancer Res* (2002) **62**:5358–64.

33. Lin HN, O'Connor JP. Immunohistochemical localization of key arachidonic acid metabolism enzymes during fracture healing in mice. *PLoS One* (2014) **9**:e88423. doi:10.1371/journal.pone.0088423

34. Nesbitt S, Nesbit A, Helfrich M, Horton M. Biochemical characterization of human osteoclast integrins. Osteoclasts express alpha v beta 3, alpha 2 beta 1, and alpha v beta 1 integrins. *J Biol Chem* (1993) **268**:16737–45. doi:10.1016/s0021-9258(19)85479-0

35. Oka T, Xu J, Kaiser RA, Melendez J, Hambleton M, Sargent MA, et al. Genetic manipulation of periostin expression reveals a role in cardiac hypertrophy and ventricular remodeling. *Circ Res* (2007) **101**:313–21. doi:10.1161/circresaha.107.149047

36. Norris RA, Damon B, Mironov V, Kasyanov V, Ramamurthi A, Moreno-Rodriguez R, et al. Periostin regulates collagen fibrillogenesis and the biomechanical properties of connective tissues. *J Cell Biochem* (2007) **101**:695–711. doi:10.1002/jcb.21224

37. Manigrasso MB, O'Connor JP. Characterization of a closed femur fracture model in mice. *J Orthop Trauma* (2004) **18**:687–95. doi:10.1097/00005131-200411000-00006

38. Cottrell JA, Lin HN, O'Connor JP. Method for measuring lipid mediators, proteins, and messenger RNAs from a single tissue specimen. *Anal Biochem* (2015) **469**:34–42. doi:10.1016/j.ab.2014.10.004

39. Schmittgen TD, Zakrajsek BA. Effect of experimental treatment on housekeeping gene expression: validation by real-time, quantitative RT-PCR. *J Biochem Biophysical Methods* (2000) **46**:69–81. doi:10.1016/s0165-022x(00)00129-9

40. Qin X, Xi Y, Jiang Q, Chen C, Yang G. Type H vessels in osteogenesis, homeostasis, and related disorders. *Differentiation* (2023) **134**:20–30. doi:10.1016/j.diff.2023.09.005

41. Lam Y, Lecce L, Bursill C, Ng M. The role of sex steroids in angiogenesis. In: Mehta JL, Mathur P, Dhalla NS, editors. *Biochemical basis and therapeutic implications of angiogenesis*. Cham: Springer International Publishing (2017). p. 445–71.

42. Gilliver SC, Ruckshanthi JP, Hardman MJ, Nakayama T, Ashcroft GS. Sex dimorphism in wound healing: the roles of sex steroids and macrophage migration inhibitory factor. *Endocrinology* (2008) **149**:5747–57. doi:10.1210/en.2008-0355

43. Blankenhorn EP, Troutman S, Clark LD, Zhang XM, Chen P, Heber-Katz E. Sexually dimorphic genes regulate healing and regeneration in MRL mice. *Mamm Genome* (2003) **14**:250–60. doi:10.1007/s00335-002-2222-3

44. D'Angelo M, Yan Z, Nooreyazdan M, Pacifici M, Sarment DS, Billings PC, et al. MMP-13 is induced during chondrocyte hypertrophy. *J Cell Biochem* (2000) **77**:678–93. doi:10.1002/(sici)1097-4644(20000615)77:4<678::aid-jcb15>3.0.co;2-p

45. Cherifi C, Latourte A, Vettorazzi S, Tuckermann J, Provot S, Ea HK, et al. Inhibition of sphingosine 1phosphate protects mice against chondrocyte catabolism and osteoarthritis. *Osteoarthritis and Cartilage Cartilage* (2021) **29**:1335–45. doi:10.1016/j.joca.2021.06.001

46. Larrouture QC, Cribbs AP, Rao SR, Philpott M, Snelling SJ, Knowles HJ. Loss of mutual protection between human osteoclasts and chondrocytes in damaged joints initiates osteoclastmediated cartilage degradation by MMPs. *Sci Rep* (2021) **11**:22708. doi:10.1038/s41598-021-02246-7

47. Clark CA, Schwarz EM, Zhang X, Ziran NM, Drissi H, O'Keefe RJ, et al. Differential regulation of EP receptor isoforms during chondrogenesis and chondrocyte maturation. *Biochem Biophysical Res Commun* (2005) **328**:764–76. doi:10.1016/j.bbrc.2004.11.074

48. Sato T, Konomi K, Fujii R, Aono H, Aratani S, Yagishita N, et al. Prostaglandin EP2 receptor signalling inhibits the expression of matrix metalloproteinase 13 in human osteoarthritic chondrocytes. *Ann Rheum Dis* (2011) **70**:221–6. doi:10.1136/ard.2009.118620

49. Attur M, Al-Mussawir HE, Patel J, Kitay A, Dave M, Palmer G, et al. Prostaglandin E2 exerts catabolic effects in osteoarthritis cartilage: evidence for signaling via the EP4 receptor. *The J Immunol* (2008) **181**:5082–8. doi:10.4049/jimmunol.181.7.5082

50. Ren J, Liu J, Sui X. Correlation of COX-2 and MMP-13 expressions with gastric cancer and their effects on prognosis. *J Buon* (2019) **24**:187–93.

51. Chen YJ, Chan DC, Lan KC, Wang CC, Chen CM, Chao SC, et al. PPARγ is involved in the hyperglycemia-induced inflammatory responses and collagen degradation in human chondrocytes and diabetic mouse cartilages. *J Orthopaedic Res* (2015) **33**:373–81. doi:10.1002/jor.22770

52. Fu J, Li S, Feng R, Ma H, Sabeh F, Roodman GD, et al. Multiple myeloma-derived MMP-13 mediates osteoclast fusogenesis and osteolytic disease. *J Clin Invest* (2016) **126**:1759–72. doi:10.1172/jci80276

53. Yamagiwa H, Tokunaga K, Hayami T, Hatano H, Uchida M, Endo N, et al. Expression of metalloproteinase-13 (Collagenase-3) is induced during fracture healing in mice. *Bone* (1999) **25**:197–203. doi:10.1016/s8756-3282(99)00157-x

54. Behonick DJ, Xing Z, Lieu S, Buckley JM, Lotz JC, Marcucio RS, et al. Role of matrix metalloproteinase 13 in both endochondral and intramembranous ossification during skeletal regeneration. *PLoS ONE* (2007) **2**:e1150. doi:10.1371/journal.pone.0001150

55. Stickens D, Behonick DJ, Ortega N, Heyer B, Hartenstein B, Yu Y, et al. Altered endochondral bone development in matrix metalloproteinase 13-deficient mice. *Development* (2004) **131**:5883–95. doi:10.1242/dev.01461

56. Xu M, Zhang L, Zhao L, Gao S, Han R, Su D, et al. Phosphorylation of osteopontin in osteoarthritis degenerative cartilage and its effect on matrix metalloprotease 13. *Rheumatol Int* (2013) **33**:1313–9. doi:10.1007/s00296-012-2548-4

57. Attur M, Duan X, Cai L, Han T, Zhang W, Tycksen ED, et al. Periostin loss-of-function protects mice from post-traumatic and agerelated osteoarthritis. *Arthritis Res Ther* (2021) **23**:104. doi:10.1186/s13075-021-02477-z

58. Kosaki N, Takaishi H, Kamekura S, Kimura T, Okada Y, Minqi L, et al. Impaired bone fracture healing in matrix metalloproteinase-13 deficient mice. *Biochem Biophysical Res Commun* (2007) **354**:846–51. doi:10.1016/j.bbrc.2006.12.234

59. Tsujii M, Kawano S, Tsuji S, Sawaoka H, Hori M, DuBois RN. Cyclooxygenase regulates angiogenesis induced by colon cancer cells. *Cell* (1998) **93**:705–16. doi:10.1016/s0092-8674(00)81433-6

60. Toomey D, Murphy J, Conlon K. COX-2, VEGF and tumour angiogenesis. *The Surgeon* (2009) **7**:174–80. doi:10.1016/s1479-666x(09)80042-5

61. Form DM, Auerbach R. PGE2 and angiogenesis. *Exp Biol Med Exp Biol Med Soc Exp Biol Med* (1983) **172**:214–8. doi:10.3181/00379727-172-41548

62. Vane JR, Bakhle YS, Botting RM. Cyclooxygenases 1 and 2. *Annu Rev Pharmacol Toxicol Toxicol* (1998) **38**:97–120. doi:10.1146/annurev.pharmtox.38.1.97

63. Miyaura C, Inada M, Suzawa T, Sugimoto Y, Ushikubi F, Ichikawa A, et al. Impaired bone resorption to prostaglandin E2 in prostaglandin E receptor EP4-knockout mice. *J Biol Chem* (2000) **275**:19819–23. doi:10.1074/jbc.m002079200

64. Frade BB, Dias RB, Gemini Piperni S, Bonfim DC. The role of macrophages in fracture healing: a narrative review of the recent updates and therapeutic perspectives. *Stem Cell Investig* (2023) **10**:4. doi:10.21037/sci-2022-038

65. Alford AI, Hankenson KD. Matricellular proteins: extracellular modulators of bone development, remodeling, and regeneration. *Bone* (2006) **38**:749–57. doi:10.1016/j.bone.2005.11.017

66. Chen Z, Yue SX, Zhou G, Greenfield EM, Murakami S. ERK1 and ERK2 regulate chondrocyte terminal differentiation during endochondral bone formation. *J Bone Mineral Res* (2015) **30**:765–74. doi:10.1002/jbmr.2409

67. Prein C, Beier F. ECM signaling in cartilage development and endochondral ossification. *Curr Top Dev Biol* (2019) **133**:25–47. doi:10.1016/bs.ctdb.2018.11.003

68. Franzen A, Hultenby K, Reinholt FP, Onnerfjord P, Heinegard D. Altered osteoclast development and function in osteopontin deficient mice. *J Orthopaedic Res* (2008) **26**:721–8. doi:10.1002/jor.20544

69. Ross FP, Chappel J, Alvarez JI, Sander D, Butler WT, Farach-Carson MC, et al. Interactions between the bone matrix proteins osteopontin and bone sialoprotein and the osteoclast integrin alpha v beta 3 potentiate bone resorption. *J Biol Chem* (1993) **268**:9901–7. doi:10.1016/s0021-9258(18)98430-9

70. Attur M, Yang Q, Shimada K, Tachida Y, Nagase H, Mignatti P, et al. Elevated expression of periostin in human osteoarthritic cartilage and its potential role in matrix degradation via matrix metalloproteinase-13. *Faseb j* (2015) **29**:4107–21. doi:10.1096/fj.15-272427

71. Han T, Mignatti P, Abramson SB, Attur M. Periostin interaction with discoidin domain receptor-1 (DDR1) promotes cartilage degeneration. *PLoS One* (2020) **15**:e0231501. doi:10.1371/journal.pone.0231501

72. Jain S, Chakraborty G, Kundu GC. The crucial role of cyclooxygenase-2 in osteopontin-induced protein kinase C α/c-Src/IκB kinase α/β–Dependent prostate tumor progression and angiogenesis. *Cancer Res* (2006) **66**:6638–48. doi:10.1158/0008-5472.can-06-0661

73. Kale S, Raja R, Thorat D, Soundararajan G, Patil TV, Kundu GC. Osteopontin signaling upregulates cyclooxygenase-2 expression in tumor-associated macrophages leading to enhanced angiogenesis and melanoma growth via α9β1 integrin. *Oncogene* (2014) **33**:2295–306. doi:10.1038/onc.2013.184

EBM Experimental Biology and Medicine

TYPE Original Research
PUBLISHED 03 January 2025
DOI 10.3389/ebm.2024.10377

OPEN ACCESS

*CORRESPONDENCE
Patricia L. Fernández,
pllanes@indicasat.org.pa

RECEIVED 10 September 2024
ACCEPTED 09 December 2024
PUBLISHED 03 January 2025

CITATION
Restrepo CM, Llanes A, Herrera L, Ellis E, Quintero I and Fernández PL (2025) Baseline gene expression in BALB/c and C57BL/6 peritoneal macrophages influences but does not dictate their functional phenotypes.
Exp. Biol. Med. 249:10377.
doi: 10.3389/ebm.2024.10377

Baseline gene expression in BALB/c and C57BL/6 peritoneal macrophages influences but does not dictate their functional phenotypes

Carlos M. Restrepo[1,2], Alejandro Llanes[1,2], Lizzi Herrera[3], Esteban Ellis[1,4,5], Iliana Quintero[1] and Patricia L. Fernández[1,2]*

[1]Centro de Biología Celular y Molecular de Enfermedades, Instituto de Investigaciones Científicas y Servicios de Alta Tecnología (INDICASAT AIP), Panama City, Panama, [2]Sistema Nacional de Investigación (SNI), Secretaría Nacional de Ciencia Tecnología e Innovación (SENACYT), Panama City, Panama, [3]Bioterio, Instituto de Investigaciones Científicas y Servicios de Alta Tecnología (INDICASAT AIP), Panama City, Panama, [4]Departamento de Biotecnología, Facultad de Ciencias de la Salud, Universidad Latina de Panamá, Panama City, Panama, [5]Facultad de Ciencia y Tecnología, Universidad Tecnológica de Panamá, Panama City, Panama

Abstract

Macrophages are effector cells of the immune system and essential modulators of immune responses. Different functional phenotypes of macrophages with specific roles in the response to stimuli have been described. The C57BL/6 and BALB/c mouse strains tend to selectively display distinct macrophage activation states in response to pathogens, namely, the M1 and M2 phenotypes, respectively. Herein we used RNA-Seq and differential expression analysis to characterize the baseline gene expression pattern of unstimulated resident peritoneal macrophages from C57BL/6 and BALB/c mice. Our aim is to determine if there is a possible predisposition of these mouse strains to any activation phenotype and how this may affect the interpretation of results in studies concerning their interaction with pathogens. We found differences in basal gene expression patterns of BALB/c and C57BL/6 mice, which were further confirmed using RT-PCR for a subset of relevant genes. Despite these differences, our data suggest that baseline gene expression patterns of both mouse strains do not appear to determine by itself a specific macrophage phenotype.

KEYWORDS

macrophages, RNA-seq, BALB/c, C57BL/6, pathogen

Impact statement

In this study, we used RNA-Seq to analyze the baseline gene expression profiles of peritoneal macrophages from C57BL/6 and BALB/c mice, which are known for their Th1- and Th2-biased immune responses, respectively. Our goal was to understand how these baseline patterns influence the interpretation of gene expression changes in other studies where pathogen interaction is considered. We found that, while there are significant differences in the basal gene expression profiles between BALB/c and C57BL/6 peritoneal macrophages, these differences do not dictate the macrophage activation phenotype. Therefore, baseline gene expression in resident peritoneal macrophages should not influence the interpretation of transcriptomic analyses conducted in response to pathogen infection. This finding is crucial for analysing the results of studies comparing gene expression patterns in resident peritoneal macrophages during pathogen challenges. This research underscores important considerations for studying the mechanisms that shape resident peritoneal macrophage phenotypes in response to intracellular pathogens.

Introduction

Macrophages are cells from the innate immune system that are essential in the elimination of pathogens and the initiation of the immune response. Tissue resident macrophages adapt to their microenvironment and exhibit specific functions essential to maintain tissue homeostasis. Distinct transcriptional regulators determine tissue-specific transcription programs in resident macrophages [1]. Macrophages are usually in a naïve phenotype, which is altered depending on environmental signals. Two main activated states of macrophages have been proposed, the classically activated subtype (M1), which shows a pro-inflammatory and microbicidal profile, and the alternative activated subtype (M2), which is associated with an anti-inflammatory response and tissue repair and homeostasis [2]. Various M2 subsets have been described, induced by the exposure of naïve macrophages to different cytokines, all of which have immunosuppressive features [3]. Polarization into either of these activated states results in the alteration of cell surface marker expression and inflammatory-related factors. The M1 macrophages are characterized by overexpression of the surface markers CD80, CD86 and CD16/32, and actively produce pro-inflammatory cytokines such as the tumour necrosis factor alpha (TNF-α), interleukin 6 (IL-6) and IL-12 [4]. Meanwhile, M2 macrophages have been shown to express higher levels of mannose receptor (CD206), arginase-1, and the anti-inflammatory cytokine IL-10 [4]. Currently, new knowledge in areas such as proteomics and transcriptomics has revealed a more complex scenario within this classification that requires further studies.

Activated lymphocytes can modulate the differentiation states of macrophages through the profile of cytokines that they secret, thus controlling the type of immune response to specific stimuli. For example, Th1 cytokines like TNF-α and interferon gamma (IFN-γ) promote the development of the M1 phenotype, while promotion of the M2 phenotype is directed by Th2 cytokines, usually IL-4 and IL-13 [5]. However, other factors that are not characterized in the context of Th1 Th2 responses elicit similar macrophage phenotypes [6]. Although there are discrepancies between *in vivo* and *in vitro* studies regarding the expression of markers that characterize these phenotypes [7], *in vitro* studies have shed light on the mechanisms involved in the differential response of macrophages to several stimuli.

Laboratory mouse strains C57BL/6 and BALB/c respectively display Th1-biased and Th2-biased immune responses, thus making them interesting models for studying the mechanisms involved in the heterogeneity of macrophage activation. For instance, macrophages isolated from C57BL/6 tend to show higher levels of nitric oxide (NO) production in comparison to BALB/c-derived macrophages after stimulation with IFN-γ and LPS [2, 8, 9]. These innate differences between the two mouse strains have been also reflected in the higher resistance of C57BL/6 against infections to different pathogens such as *Mycobacterium tuberculosis*, *Pasteurella pneumotropica*, *Chlamydia* and *Leishmania* spp. [10–13]. Furthermore, studies on murine macrophage infection with *Leishmania* species have shown that macrophages from Th1-biased strains are more easily activated than those from Th2-biased strains [14, 15]. However, it has also been shown that infection with *Leishmania* can increase the ability of macrophages to stimulate a Th2 response [16]. In fact, a quite heterogeneous range of responses and patterns of gene expression have been reported when studying the immune response of C57BL/6 and BALB/c to different *Leishmania* species [17–22].

During the last few years, our group has been working in characterizing the immune response of BALB/c and C57BL/6 mice to the infection with *Leishmania panamensis* [23, 24]. Our results have shown that BALB/c-infected mice are more susceptible to the infection than C57BL/6, exhibiting higher inflammation and parasite loads at the inoculation site [24]. In a study conducted *in vitro*, we observed that infection of C57BL/6 macrophages with *L. panamensis* induced a pro-inflammatory gene expression pattern associated with a classic M1 phenotype, whereas BALB/c macrophages showed gene expression patterns intermediate between M1 and M2 [23]. In this study, we compared the baseline gene expression patterns from uninfected BALB/c and C57BL/6 macrophages, used as controls in the previous study. Our main goal is to assess if there is a possible predisposition of these mouse strains to the M1 or M2 phenotype, which may in turn affect the interpretation of changes in gene expression patterns associated with the interaction with pathogens such as *Leishmania* spp.

Materials and methods

Institutional ethics committee statement and laboratory animal handling

All experimental procedures involving mice were approved by the Institutional Animal Care and Use Committee of

INDICASAT (protocol number IACUC-14-002, approved on 30 May 2014, and renewed on 29 July 2019). All procedures were performed following international and institutional regulations for the ethical handling of laboratory animals. Animals were maintained in Specific Pathogen Free (SPF) conditions at INDICASAT's animal facility with free access to food and water, a constant temperature of 24°C and a 12-hour light/dark cycle.

Murine macrophage isolation

Resident peritoneal macrophages were obtained from female BALB/c and C57BL/6 mice, by peritoneal washing with chilled Roswell Park Memorial Institute (RPMI) (Gibco, Gaithersburg, MD, United States). A density of 1×10^6 cells per well in 24-well plates were seeded in RPMI with 10% fetal bovine serum, penicillin/streptomycin (100 U/mL/100 μg/mL). Cells were incubated for 2 h at 37°C and 5% CO_2. After removing non-adherent cells by washing with RPMI medium, adherent macrophages were incubated for 24 h more at 37°C and 5% CO_2. Peritoneal macrophages were processed independently for each mouse strain and each experiment was performed in triplicate.

Flow cytometry

After 24 h of culture, cells were harvested, washed with phosphate-buffered saline (PBS), and blocked with 1% BSA for 15 min. After washing, cells were incubated with 5 μg/mL of anti-mouse CD11b FITC, CD80 APC, CD86 PE-Cy5, MRC1 (CD206) APC, MHC-II PE (eBioscience, San Diego, CA, United States) and/or anti-mouse F4/80 PE (Abcam, Cambridge, United Kingdom) diluted in 1% BSA, for 30 min at 4°C. Following two sequential washes, cells were resuspended in PBS for flow cytometry analysis. Events were acquired with a CyFlow cytometer, and the data were analyzed using FloMax software (PARTEC, Münster, Germany) and FlowJo v10.10 (Becton, Dickinson and Company, East Rutherford, NJ, United States). Statistical calculations of mean, standard error of the mean (SEM), one-way ANOVA followed by Sidak's multiple comparison test were performed using GraphPad Prism version 10.2.3 (GraphPad Inc., La Jolla, CA, United States). Differences between groups were considered significant if $P < 0.05$ (****$P < 0.0001$).

RNA isolation and transcriptome sequencing

Macrophage total RNA was purified using Trizol (Invitrogen, Carlsbad, CA, United States) and chloroform separation. Integrity and purity of the RNA samples were evaluated using the Agilent RNA 6000 Nano kit on a 2100 Bioanalyzer system (Agilent Technologies, Santa Clara, CA, United States). RNA concentration was estimated by fluorometry using Picogreen (Invitrogen, Carlsbad, CA, United States) and a Victor 3 multilabel plate reader (PerkinElmer, Waltham, MA, United States). The TruSeq RNA v2 sample preparation kit (Illumina, San Diego, CA, United States) was used for generating libraries of complementary DNA (cDNA) fragments from polyadenylated [poly(A)] RNA. A NovaSeq 6000 sequencer (Illumina, San Diego, CA, United States) was used to sequence cDNA libraries, yielding a total of 100 million 150-bp paired-end reads per sample.

Mapping and transcript abundance estimation

Alignment of the cDNA-derived reads to the mouse reference genome was performed using HISAT2 (version 2.1.0) [25], following the implemented default parameters for paired-end and non-strand-specific RNA-Seq data. The mouse reference genome (mm10, build name GRCm38) was retrieved from the UCSC Genome Browser.[1] FeatureCounts (version 1.6.3) [26] was used to estimate transcript abundance from read alignments. Those gene features having a single count across all samples or counts equal to zero were classified as suspected non-expressed genes and further removed before subsequent analyses.

Data quality assessment and differential expression analysis

For visualization of sample-to-sample distances, gene counts were normalized to correct for differences in sequencing depth. The normalized counts were subsequently transformed to logarithms to the base 2 and the variance stabilizing transformation (VST) algorithm was used to stabilize the variance across the mean [27]. The transformed data was used for calculating all pairwise Euclidean distances and the resulting relationships were visualized by using principal component analysis (PCA).

The DESeq2 R package (version 1.38.1) [28] was used for conducting differential expression analysis on raw counts. C57BL/6-derived counts were taken as the reference for determining the relative difference in basal expression. Therefore, DESeq2 results are interpreted as higher or lower expression levels in BALB/c with respect to C57BL/6.

---

[1] http://genome.ucsc.edu/

Differentially expressed genes were defined as those having a logarithm to the base 2 of fold change (*log*2FC) of at least 0.5 and a Benjamini- Hochberg (BH) multiple-testing adjusted *P*-value of < 0.05. The overall results of the differential expression analysis were visualized using volcano and log ratio and mean average (MA) plots.

Functional enrichment analysis

The ClusterProfile R package (version 3.12.0) [29] was used for identification of signaling and metabolic pathways defined in the Kyoto Encyclopedia of Genes and Genomes (KEGG) database. A cut-off *P*-value of 0.05 was used to identify KEGG pathways overrepresented in the differentially expressed genes. Two independent lists of genes with higher and lower expression in BALB/c with respect to C57BL/6 were separately used as input files. The non-redundant list of genes contained in all identified enriched KEGG pathways except for those describing pathogen- or disease-specific pathways was extracted. Differences in basal gene expression levels between mouse strains in the non-redundant list of genes were visualized as an expression plot and a heatmap based on the RNA-Seq counts normalized by size factor and variance stabilizing transformation (VST).

Quantitative PCR

For quantitative real time (RT)-PCR, 1 μg of total RNA was first reverse-transcribed using the High-Capacity cDNA reverse transcription kit (Applied Biosystems, Waltham, MA, United States). Subsequently, RT-PCR was performed on a QuantStudio 5 thermocycler (Applied Biosystems, Waltham, MA, United States) using SYBR Green PCR Master Mix (Applied Biosystems, Waltham, MA, United States). Cycling conditions consisted of an initial hold at 95°C (10 min) and 40 cycles of 95°C (15 s), and 60°C (60 s). The housekeeping gene encoding hypoxanthine phosphoribosyltransferase (*hprt*) was used as endogenous control for data normalization. Analyses of relative gene expression of *Tnf*, *Il10*, *Il4ra*, *Mrc1*, *Ccl5*, *Fcgr1*, *iNos*, *Sod3* and *Il4* were performed by the $2^{(-\Delta\Delta CT)}$ method. Briefly, cycle threshold (CT) values of the target genes and *hprt* were obtained, and ΔCT values were calculated by substracting the CT values of *hprt* from CT values of the target genes for each sample. The ΔΔCT was calculated using C57BL/6 as reference and substracting its ΔCT from the ΔCT of the BALB/c sample. The relative gene expression of each target gene was then determined using the formula $2^{(-\Delta\Delta CT)}$. The primer sequences used are listed in Supplementary Table S1. Statistical calculations of mean and SEM for fold differences of all target genes from 4 independent experiments were performed using GraphPad Prism version 10-2.3 (GraphPad Inc., La Jolla, CA, United States).

Results

RNA sequencing and data quality assessment

To characterize differences in basal expression between BALB/c and C57BL/6, RNA-Seq and differential expression analysis were conducted in unstimulated peritoneal resident macrophages cultured in triplicate. The proportion of macrophages in peritoneal lavages was determined by the percentage of CD11b and F4/80 double positive cells, which was 33.2 ± 3.1% for BALB/c and 41.7 ± 3.0% for C57BL/6 (Supplementary Figure S1). From the double positive population, the proportions of $F4/80^{Low}CD11b^{Low}$ and $F4/80^{High}CD11b^{High}$ were respectively, 43.2 ± 0.7% and 47.0 ± 1.1% for BALB/c and 30.4 ± 2.5% and 61.3 ± 2.6% for C57BL/6 (Supplementary Figure S1). Total RNA was purified from cells of both mouse strains at 24 h of culture. Sequencing of poly(A)-enriched RNA generated ~120 million paired-end reads 150-bp long per sample. Sequence data of this project can be retrieved from the Sequence Read Archive (SRA) through BioProject PRJNA656921, accession numbers SRX10075500, SRX10075501 and SRX10075504 for BALB/c samples, and SRX10075508, SRX10075509 and SRX10075510 for C57BL/6 samples. On average, 98% of reads from each mapped unambiguously to the mouse reference genome.

In order to evaluate if our samples from each mouse strain are reasonably different, a principal component analysis (PCA) based on Euclidean distances was performed. For sample distances estimation, data was previously transformed by means of the variance stabilizing transformation (VST) algorithm [27], to correct for sample distance and variance overestimation resulting from calculating [25] the logarithm of small counts. The PCA analysis explained 99% of the total variance and showed a clustering pattern that clearly separates samples according to mouse strain (Supplementary Figure S2).

Differential expression analysis and pathway enrichment analysis

For differential expression analysis, the C57BL/6 strain was considered as the reference state. Therefore, our results should be interpreted as higher or lower basal expression levels for genes from BALB/c with respect to C57BL/6, instead of the up- or downregulation of such genes. Altogether, we found 615 differentially expressed (DE) genes between BALB/c and C57BL/6 unstimulated macrophages. From these genes, 266 showed a higher relative basal expression level in BALB/c with respect to C57BL/6 macrophages, whereas 349 showed lower relative basal expression (Figure 1; Supplementary Figure S3; Supplementary Table S2).

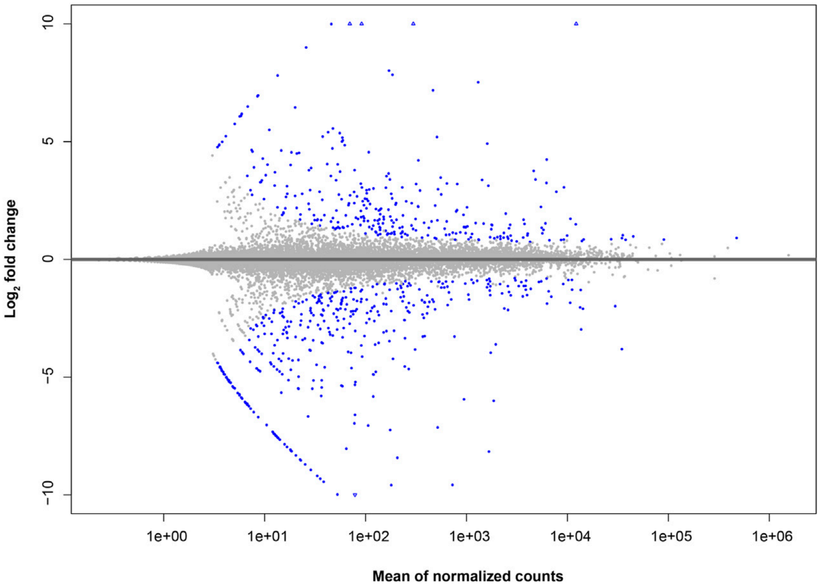

FIGURE 1
MA-plot of gene expression differences in macrophages of BALB/c in comparison to C57BL/6. The log2 fold change for BALB/c against C57BL/6 samples (*y* axis) is plotted against the average of normalized counts (*x* axis). Each gene is represented with a dot. Genes with significant fold difference between mouse strains (BH multiple testing adjusted *P*-value <0.05) are shown in blue.

Additionally, we performed a pathway enrichment analysis to identify KEGG pathways enriched by genes with higher and lower basal expression in BALB/c with respect to C57BL/6. In total, 38 KEGG pathways were found to be enriched, 30 and 8 when considering genes with higher and lower basal expression in BALB/c, respectively (Supplementary Table S3). Since we were interested in intrinsic differences between unstimulated macrophages from the two mouse strains, pathogen- or disease-specific pathways (26 in total) were not considered for subsequent analyses. Pathways associated with antigen processing and presentation, cellular senescence and apoptosis, cell adhesion, processing within the lysosome, and metabolism of amino acids were all enriched by genes with higher basal expression in BALB/c with respect to C57BL/6 (Table 1). Conversely, pathways found to be enriched by genes with lower basal expression in BALB/c with respect to C57BL/6 were mainly associated with cytokine-cytokine receptor interaction and hematopoietic cell lineage differentiation (Table 2). In general, pathway enrichment analysis showed that, of all the genes with basal differences in expression between the two mouse strains, 42 appear to be associated with cellular and immune functions that could shed light on macrophage activation patterns (Figure 2; Supplementary Figure S4).

Interestingly, pathways related to the phagosome and mechanisms of antigen processing and presentation were found to be enriched by genes encoding non-classical MHC class I (MHC-Ib) H-2Q molecules, loci 4, 6 and 10 *(H2-Q4*, *H2-Q6* and *H2-Q10*), and their basal expression levels were 2 to 5-fold higher in BALB/c than C57BL/6 (Table 1). Among genes found to have higher basal expression in BALB/c are those encoding cathepsins E, G, L, S, F and D (*Ctse*, *Ctseg*, *Ctsl*, *Ctss*, *Ctsf*, *Ctsd*), arylsulfatase B (*Arsb*) and *N*-sulfoglucosamine sulfohydrolase (*Sgsh*), all of which are associated with lysosomal degradation, ranging from 2 to 10-fold in the case of *Ctse*. Other genes associated with arginine and proline metabolism, including those encoding arginase type II (*Arg2*) and L-arginine:glycine amidinotransferase (*Gatm*) showed basal expression levels of 4.7 and 30 times higher in BALB/c with respect to C57BL/6, respectively. Additional genes with higher expression in BALB/c included those encoding proteins associated with cellular senescence and apoptosis, such as mitogen-activated protein kinases 11/p38 MAPK-β (*Mapk11*) and MAPK3/Extracellular signal-regulated kinase (ERK) 1 (*Mapk3*), with expression levels approximately two times higher, as well as the apoptosis-activating serine protease granzyme B (*Gzmb*), with 6.7-fold expression in BALB/c.

Conversely, genes with lower basal expression in BALB/c were mostly associated with cytokine-cytokine receptor interaction and with the phagosome, showing expression levels that ranged from 0.52 to 0.16 times those of C57BL/6

TABLE 1 Genes with higher basal expression in BALB/c relative to C57BL/6 macrophages along with their assigned KEGG pathways.

Gene	Product	Fold change
Phagosome/Antigen processing and presentation (mmu04145/mmu04612)[a]		
H2-Bl	Histocompatibility 2, blastocyst	185.60
H2-T-ps	Histocompatibility 2, T region locus, pseudogene	8.82
H2-Q10	Histocompatibility 2, Q region locus 10	5.37
Clec7a	C-type lectin domain family 7, member a	3.24
H2-Q6	Histocompatibility 2, Q region locus 6	2.41
H2-Q4	Histocompatibility 2, Q region locus 4	2.03
Cellular senescence (mmu04218)		
Mapk11	Mitogen-activated protein kinase 11/p38 MAPK-β	2.19
Mapk3	Mitogen-activated protein kinase 3/ERK-1	1.77
Lysosome (mmu04142)		
Ctse	Cathepsin E	10.44
Ctsg	Cathepsin G	8.10
Ctsl	Cathepsin L	3.12
Ctss	Cathepsin S	2.91
Arsb	Arylsulfatase B	2.62
Ctsf	Cathepsin F	2.46
Sgsh	N-sulfoglucosamine sulfohydrolase (sulfamidase)	1.92
Ctsd	Cathepsin D	1.90
Neutrophil extracellular trap formation (mmu04613)		
H2bc18	H2B clustered histone 18	101.15
H2bc13	H2B clustered histone 13	17.54
Ctsg	Cathepsin G	8.10
H2bc11	H2B clustered histone 11	4.33
H2bc12	H2B clustered histone 12	3.60
Clec7a	C-type lectin domain family 7, member a	3.24
Plcb2	Phospholipase C, beta 2	3.21
Mapk11	Mitogen-activated protein kinase 11	2.19
Mapk3	Mitogen-activated protein kinase 3	1.77
Cell adhesion molecules (mmu04514)		
F11r	F11 receptor	2.30
Arginine and proline metabolism (mmu00330)		
Gatm	Glycine amidinotransferase (L-arginine:glycine amidinotransferase)	30.32
Arg2	Arginase type II	4.72
Maoa	Monoamine oxidase A	2.61
Got1	Glutamic-oxaloacetic transaminase 1, soluble	1.76

(Continued on following page)

TABLE 1 (*Continued*) Genes with higher basal expression in BALB/c relative to C57BL/6 macrophages along with their assigned KEGG pathways.

Gene	Product	Fold change
Apoptosis (mmu04210)		
Gzmb	Granzyme B	6.69
Tyrosine metabolism (mmu00350)		
Fah	Fumarylacetoacetate hydrolase	2.50

[a]KEGG pathways database accession numbers are indicated next to the pathway name.

TABLE 2 Genes with lower basal expression in BALB/c relative to C57BL/6 macrophages along with their assigned KEGG pathways.

Gene	Product	Fold change
Cytokine-cytokine receptor interaction (mmu04060)[a]		
Il10	Interleukin 10	0.16
Ccr6	Chemokine (C-C motif) receptor 6	0.28
Il4ra	Interleukin 4 receptor, alpha	0.30
Cxcr6	Chemokine (C-X-C motif) receptor 6	0.31
Ccl5	Chemokine (C-C motif) ligand 5	0.37
Il13ra1	Interleukin 13 receptor, alpha 1	0.44
Ccr5	Chemokine (C-C motif) receptor 5	0.44
Phagosome (mmu04145)		
Msr1	Macrophage scavenger receptor 1	0.05
H2-Eb2	Histocompatibility 2, class II antigen E beta2	0.08
C3	Complement component 3	0.31
Fcgr1	Fc receptor, IgG, high affinity I	0.48
Mrc1	Mannose receptor, C type 1	0.53
Hematopoietic cell lineage (mmu04640)		
Csf3r	Colony stimulating factor 3 receptor (granulocyte)	0.16
Fcgr1	Fc receptor, IgG, high affinity I	0.48

[a]KEGG pathways database accession numbers are indicated next to the pathway name.

(Table 2). Genes associated with these pathways include those encoding interleukin 10 (*Il10*), chemokine (C-C motif) ligand 5 (*Ccl5*), chemokine (C-C motif) receptors 5 (*Ccr5*) and 6 (*Ccr6*), chemokine (C-X-C motif) receptor 6 (*Cxcr6*), α subunits of IL-4 and IL-13 receptors (*Il4ra* and *Il13ra1*), mannose receptor C-type 1 (*Mrc1*), and the high-affinity Fc-gamma receptor (*Fcgr1*). Additionally, genes encoding enzymes involved in the regulation of oxidative stress such as glutathione reductase (*Gsr*), superoxide dismutase 3 (SOD3) (*Sod3*), and glutathione-S transferase mu 2 (*Gstm2*) also had a lower basal expression in BALB/c showing respectively expression levels of 0.39, 0.29 and 0.02 times those of C57BL/6 (Supplementary Table S2).

Relative gene expression and cytometry analyses

To confirm the transcriptomic findings discussed above, we used RT-PCR to compare the relative expression of a subset of genes on BALB/c cells respective to C57BL/6. We examined genes *Il10*, *Il4ra*, *Mrc1*, *Ccl5*, *Fcgr1* and *Sod3*, all of which exhibited differential expression in the transcriptomic analysis. Consistent with the results obtained in differential expression analysis, cells from BALB/c mice showed a lower expression of *Il10*, *Il4ra*, *Mrc1* and *Fcgr1* in the non-activated condition, when compared to cells from C57BL/6 mice (Figures 3A, B). Meanwhile, *Sod3* was not detected in the examined samples (Figure 3B).

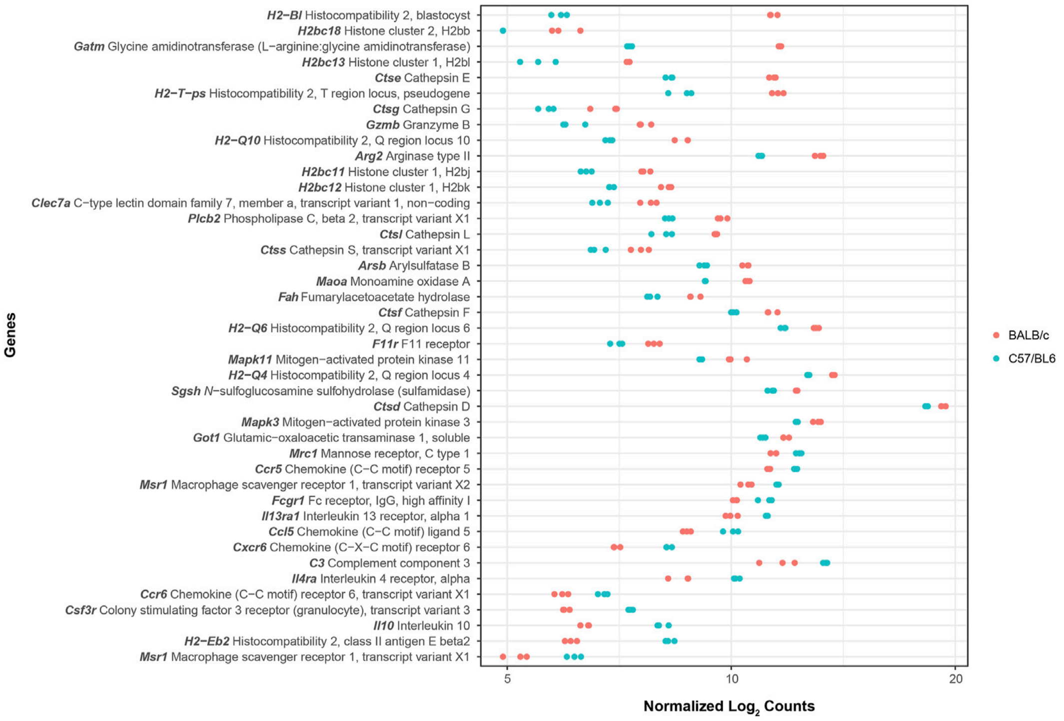

FIGURE 2
Expression plot of genes in selected enriched KEGG pathways. The plot displays differences in basal gene expression levels between BALB/c (pink) and C57BL/6 (cyan) macrophages for the non-redundant list of genes contained in all identified enriched KEGG pathways except for those describing pathogen- or disease-specific pathways. Data represents $\log_2$ RNA-Seq counts normalized by size factor and variance stabilizing transformation (VST).

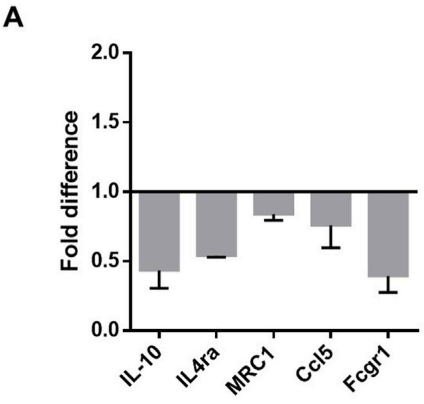

B

Gene	Fold difference
Il10	0.43 ± 0.13
Il4ra	0.54 ± 0.01
Mrc1	0.84 ± 0.04
Ccl5	0.76 ± 0.16
Fcgr1	0.39 ± 0.12
Sod	No detected

FIGURE 3
Relative gene expression of selected genes on BALB/c respective to C57BL/6. Adherent cells obtained from peritoneal lavage were cultured for 24 h. Total RNA was obtained and mRNA for *Il10*, *Il4ra*, *Mrc1*, *Ccl5*, *Fcgr1* and *Sod3* determined by quantitative real-time (RT)- PCR. **(A)** Graph shows results normalized to *hprt* expression and are presented as the fold difference of mRNA expression on BALB/c relative to C57BL/6. **(B)** Table shows the results represented by mean ± SEM. Results were obtained from four independent experiments performed in duplicates.

Additionally, we also used RT-PCR to evaluate the relative expression of genes *Tnf*, *iNos*, and *Il4*, which are relevant to the M1 or M2 macrophage phenotypes, although they were not found to be differentially expressed in the transcriptomic analysis. Interestingly, we observed slight differences in the relative expression of these genes between BALB/c and C57BL/6 cells. *Tnf* showed increased expression in BALB/c compared to C57BL/6, while *iNos* and *Il4* exhibited a slight

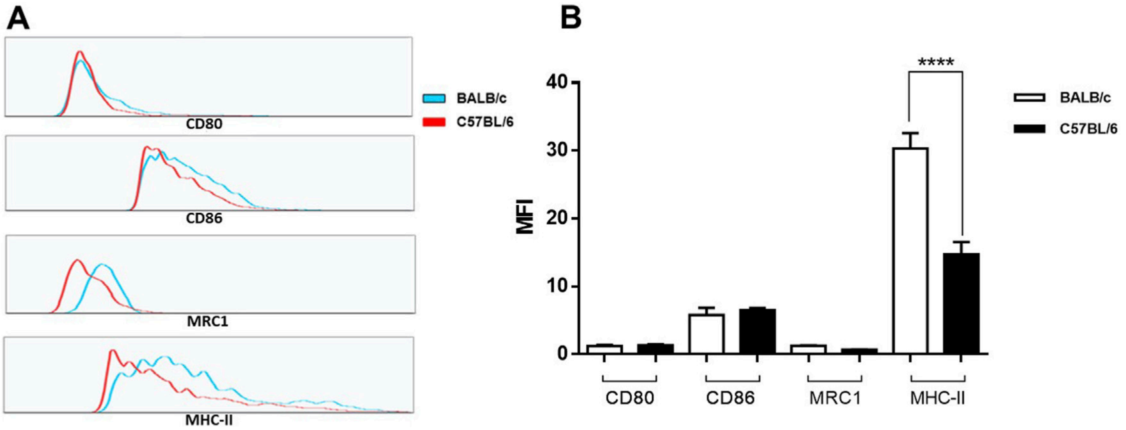

FIGURE 4
Cell surface marker expression of CD80, CD86, MRC1 and MHC II in unstimulated peritoneal cells from BALB/c and C57BL/6 mice. Adherent cells obtained from peritoneal lavage were culture for 24 h. Surface expression of CD11b, CD80, CD86, MRC1 and MHC-II was analyzed by flow cytometry. Representative histograms **(A)** and bar plots for the mean fluorescence intensity (MFI) **(B)** of each marker on CD11b$^+$ positive cells. Bar plots represent mean ± SEM from peritoneal lavages seeded in duplicates from two independent experiments. ****, $p < 0.0001$.

decreased in BALB/c (Supplementary Figure S5). These discrepancies between results from RNA-Seq and RT-PCR are likely associated with inherent features of each methodology and differences in their detection limits [30]. These results suggested that there is not an evident predisposition for the M1 or M2 phenotypes in the cells of these mouse strains.

Moreover, to investigate if there was a marker expression pattern indicative of a predisposition towards any specific macrophage phenotypes, we examined the cell surfaces markers expression of CD80, CD86, MRC1 and MHC II in unstimulated peritoneal cells from BALB/c and C57BL/6 mice. CD80 and CD86 are essential for antigen presentation and activation of T cells and are considered M1 phenotype markers [31–33]. Meanwhile, MRC1 is a classical M2 cellular marker [34]. In the CD11b population we did not observe significant differences in the mean fluorescence intensity (MFI) for CD80 or CD86 markers (Figure 4; Supplementary Table S4). These genes were not identified as differentially expressed by the RNA-Seq analysis between cells from BALB/c and C57BL/6 mice. No significant differences in the expression levels of MRC1 were also found between CD11b$^+$ BALB/c and C57BL/6 peritoneal cells (Figure 4; Supplementary Table S4). Despite the lower gene expression levels of MRC1 in BALB/c cells compared to C57BL/6, we were unable to detect these differences at the protein level. In the case of MHC II, recognized as a marker for both phenotypes [34] BALB/c cells exhibited significant higher expression than C57BL/6 cells (Figure 4B).

Discussion

C57BL/6 and BALB/c mice are known to mount opposite T-cell polarization responses that influence a different phenotype of macrophage programs [35]. *In vivo*, C57BL/6 displays a predominant Th1 response to intracellular pathogens, whereas BALB/c displays a Th2 response [36–38]. It has been suggested that BALB/c mice have specific allelic variants of genes encoding immune-related molecules that promote Th2 responses [39, 40]. Available data indicates that macrophages derived from C57BL/6 or BALB/c mice exhibit distinct activation pathways in response to the same stimuli, ultimately steering a characteristic response of the M1 and M2 phenotypes, respectively [2, 8, 9]. We have studied herein the baseline gene expression patterns of resident peritoneal macrophages from BALB/c and C57BL/6 mice to provide insights into whether the cells of these mouse strains might exhibit a predisposition to any of the macrophage phenotypes. Ultimately, we are interested in understanding if this baseline gene expression could affect the interpretation of results concerning differential gene expression analysis in further presence of pathogens colonizing macrophages.

Our results showed a lower basal expression of M2-related genes, such as IL-4Rα, in BALB/c macrophages. IL-4Rα can bind IL-4 and IL-13, promoting the expression of M2-associated genes. In the absence of this receptor both IL-4- and IL-13-mediated functions are compromised [41]. *In vivo*, IL-4Rα deficiency in macrophages has been shown to reduce the number of M2 macrophages in the liver in a pathogen-free mouse model of induced fibrosis [42]. An IL-4Rα-independent mechanism of Th2 differentiation has also been observed in IL-4Rα-deficient BALB/c mice after infection with *L. major* [43]. Meanwhile, *in vitro*, Th2 differentiation appears to be affected by the absence of IL-4Rα [43]. In macrophages, the IL-4 produced by these cells acts in an autocrine manner through the IL-4Rα receptor; however, IL-4 does not appear to be relevant for the *in vitro* differentiation of the M2 phenotype under type II activation [44]. We have previously observed an upregulation of the gene encoding IL-4 in BALB/c resident peritoneal macrophages in response to infection with *L. panamensis*, but no changes were found in IL-4Rα expression levels [23]. Since the expression of IL-4Rα is known to be very low in macrophages [44], the lower basal expression of this receptor found here in resting BALB/c cells is not likely to determine the phenotype of macrophages in response to *in vitro* intracellular pathogens.

We also observed a lower basal expression for the M2-related marker, the type 1 mannose receptor C (MRC1), in unstimulated BALB/c cells relative to C57BL/6 cells. MRC1 appears to be an essential regulator of glycoprotein homeostasis [45]. It has been observed that the lack of MRC1 is related to the upregulation of pro-inflammatory cytokines in endotoxemia models [46]. Additionally, MRC1 expressed on M2 macrophages has been implicated as a mediator of the infection with virulent strains of some pathogens, such as *Mycobacterium tuberculosis* and *Leishmania*, increasing the severity of the disease [47, 48]. The lower basal expression of this and other M2-related genes observed here for BALB/c, associated with a higher basal expression in C57BL/6, is consistent with a previous study where increased M2-related marker expression was reported for C57BL/6 resident peritoneal macrophages in the absence of specific stimulation [49]. It has been suggested that tissue microenvironment favors MRC1 expression in tissue resident macrophages in both, mice and humans [50, 51]. At the protein level, however, no differences in the surface expression of MRC1 was observed between peritoneal cells of BALB/c and C57BL/6 mice. These findings are consistent with other studies demonstrating that, in unstimulated human PBMC-derived macrophages, the expression levels of MRC1 do not follow the pattern observed in the MRC1 marker gene expression [33]. These results collectively suggest that these mouse strains do not show a predisposition for either macrophage phenotype.

Although a higher basal expression of genes encoding cathepsins and other lysosomal enzymes was observed here in BALB/c cells relative to C57BL/6, previous data showed downregulation or no changes in the expression of these genes in response to *L. panamensis* infection [23]. Cathepsins are involved in antigen processing and thus influence immune responses [52, 53]. Cathepsin L, which was found to be increased at the basal level in BALB/c cells, seems to be involved in the generation of a Th1 response against *Leishmania* [54]. We also observed a higher basal expression of cathepsin D in BALB/c cells. The role of cathepsin D in the modulation of immune response is not well understood; however, it has been shown that the inhibition of cathepsin D during *L. major* infection affects both Th1 and Th2 responses [55]. Thus, BALB/c macrophages appear to be genetically prepared to generate a response favoring the resolution of *Leishmania* infection, nevertheless, these cells tend to show an inability to efficiently respond to infection during host-parasite interaction. Indeed, BALB/c cells expressed similar levels of cell surface markers characteristic of the M1 phenotype, such as CD80 and CD86, to those expressed by C57BL/6 cells. Moreover, surface expression levels of MHC II were higher in BALB/c than in C57BL/6 $CD11b^{+}$ peritoneal cells. Since overexpression of MHC II is found in both M1 and M2 phenotypes [34], these results support the idea that BALB/c is well-equipped to respond to inflammatory stimuli. However, there seems to be no evident predisposition for any of the macrophage phenotypes in the cells of both mouse strains in their basal state.

Interestingly, BALB/c showed a higher basal expression of genes encoding non-classical MHC class I (MHC-Ib) molecules H2-Q4 (Qb-1), H2-Q6 and H2-Q10. Although, no specific role has been defined for H2-Q4 (Qb-1) and H2-Q6 [56], H2-Q10 has been recently identified as a ligand of the inhibitory Ly49C receptor, suggesting that it may act as a regulator of NK cell activation [57]. Additionally, H2-Q10 has been found to have high affinity for CD8αα, thus possibly playing a role in the control of liver-resident CD8αα γδT cells [58]. Moreover, H2-Q10 stabilizes the expression of the MHC-1b molecule H2-T23 (Qa-1b), the murine homolog of HLA-E. This fact suggests that H2-Q10 may have additional immune-modulating effects. Specifically, antigen presentation through Qa-1b has been shown to induce an upregulation of the inhibitory NK receptors CD94/NKG2A in secondary infections with *Listeria monocytogenes*. This leads to reduced apoptosis of cytotoxic T-lymphocytes and a prolonged cytotoxic response [59]. As recent data has demonstrated that H2-Q10 has multiple roles that are relevant to the regulation of immunity, further research is required to determine if the higher basal expression of H2Q molecules in BALB/c mice macrophages may contribute to the response to infections with intracellular pathogens.

Among the genes with a lower basal expression in BALB/c, which indicates a higher expression in C57BL/6 is the high-affinity Fc-gamma receptor, which is important for taking opsonized pathogens. It has been previously reported that thioglycolate-elicited macrophages from C57BL/6 mice also express higher basal levels of this receptor [60]. Other genes found to have a higher basal expression level in C57BL/6 were those encoding pro-inflammatory chemokines and chemokines receptors. Although the gene encoding the IL-10 anti-inflammatory cytokine was also found to have a higher basal expression, which was confirmed by RT-PCR. Despite the higher expression of both anti- and pro-inflammatory genes, it has been previously shown that macrophages from C57BL/6 mice infected with *Leishmania* exhibit a gene expression pattern consistent with an M1 phenotype and have lower levels of intracellular amastigotes than BALB/c cells [23]. These findings suggest that C57BL/6 macrophages are intrinsically prepared to battle infections with intracellular pathogens such as *Leishmania*.

Although not found to be associated with any specific KEGG pathway, genes encoding enzymes involved in antioxidant programs such as superoxide dismutase 3 (SOD3), glutathione reductase and glutathione-S transferases also showed high expression in C57BL/6 compared to BALB/c. SOD3 is an important antioxidant enzyme, which prevents the formation of peroxynitrite ($ONOO^-$) through superoxide (O_2^-) -mediated inactivation of NO [61, 62]. Glutathione reductase, on the other hand, preserves the pool of reduced glutathione, which significantly contributes to regulating reactive oxygen species within the cells [63]. Intracellular glutathione levels in antigen-presenting cells influence the pattern of Th1/Th2 cytokines [64]. It has been shown that the induction of glutathione reductase in response to *L. major* infection in C57BL/6 bone marrow-derived macrophages is several times greater than in BALB/c cells [65]. Higher gene expression and protein levels of antioxidant systems in C57BL/6 compared to BALB/c have also been observed at the basal level in bone marrow-derived macrophages [66]. Since higher levels of NO are produced by cells from C57BL/6 animals compared to BALB/c in response to *L. panamensis* infection [23], the results presented herein support the idea that C57BL/6 cells might be better prepared to counteract the negative effects of oxidative stress associated with infection than BALB/c cells.

Since we were working with tissue-resident cell populations, it is important to highlight the role of the microenvironment in the pattern of gene expression and the function of macrophages. Tissue-resident macrophages have a specific genetic signature and can be distinguished by specific gene expression patterns. The tissue microenvironment is essential for establishing macrophage identity [1, 67]. Macrophages populate tissues very early in the embryonic process and it has been suggested that tissue-resident macrophages originate from precursors present in the yolk sac [68–71]. Despite their common origin, these macrophages develop independently, acquiring specialized functions according to the local microenvironment [72–74]. It has been shown that macrophage populations from different organs express unique mRNA transcripts that allow them to perform specialized local functions [1]. However, evidence have shown that mouse resident peritoneal macrophages change their gene expression pattern when transferred to the lungs, assimilating the pattern of the local macrophage population [67]. These data indicate that the tissue microenvironment has the potential to reprogram differentiated macrophages.

It has been shown that *ex vivo* culture of tissue resident macrophages influences the gene expression pattern and activation status of these cells [67, 75, 76]. The transition of macrophages from the peritoneal cavity to culture medium enriched with M-CSF and/or TGF-β results in marked changes in gene expression [75]. Furthermore, the transfer of alveolar macrophages (AM) from the lung microenvironment of ovalbumin-sensitized rats to *ex vivo* culture and their subsequent reintroduction into AM-depleted sensitized rats results in an increase in Th1 cytokines in bronchoalveolar lavage and a reduction in the alveolar hyperresponsiveness [67]. Together these data indicate the importance of the tissue microenvironment in cell activation status and highlight the effect of *ex vivo* culture on cellular responses. Although unstimulated macrophages were culture for 24 h before RNA-Seq analysis in this study, the pattern of gene expression was markedly different from that obtained in response to infection under the same experimental conditions in a previous study [23]. This emphasizes the importance of considering the basal pattern of gene expression for the subsequent analysis of the changes induced in the presence of a stimulus in an *ex vivo* experimental setting.

We also analyzed the proportion of $F4/80^{high}CD11b^{high}$ and $F4/80^{low}CD11b^{low}$ in peritoneal lavages of C57BL/6 and BALB/c. $F4/80^{high}CD11b^{high}$ cells have been identified as large peritoneal macrophages (LPM) and $F4/80^{low}CD11b^{low}$ cells as small peritoneal macrophages (SPM) [76]. Evidence shows that both populations of macrophages coexist in the peritoneal cavity and although they show strong similarities in gene expression pattern [75] they are functionally different [76]. Thus, the differences in the basal pattern of gene expression observed herein might not be influenced by differences in the proportion of these two populations between C57BL/6 and BALB/c cells. However, it has been shown that adhesion to culture dishes induces morphological, phenotypic, and functional modifications of LPM and SPM [76, 77]. This reinforces the need to consider the basal patterns of gene expression when performing differential expression analyses in response to stimuli.

We observed that BALB/c peritoneal cells exhibit a higher mean fluorescence intensity of MHC II compared to C57BL/6 cells. Previous studies have indicated that SPM express elevated levels of MHC II [73, 76] and the numbers of this subset of cells increase in response to inflammatory conditions [78]. The differences in the expression of MHC II observed herein could be related to the varying proportions of SPM and LPM present in both mouse strains [76]. Furthermore, it has been reported that the levels of MHC II expression are dependent on the cell cycle [79]. It has been observed in BMDMs that cell cycle regulators could modulate the basal or activated transcription of genes not directly associated with cell cycle progression [80]. Macrophages arrested in the G_1 phase of the cell cycle exhibit higher basal expression levels of MHC II; however, they do not increase MHC II expression in response to IFN-γ stimulation [79]. We could speculate that the cell populations analyzed from BALB/c and C57BL/6 mice may have been in different phases of the cell cycle, affecting the basal expression of MHC II. Nevertheless, additional subsets of $MHC\ II^+$ cells have been identified in the peritoneal cavity [81], thus these differences might be also associated with specific cell populations. It has also been suggested that the expression level of certain haplotypes of MHC II molecules in macrophages could promote

Th1 differentiation. It has been shown that Th1 bias appears to be influenced by the presence of the I-A^b allele [82] Interestingly, this allele is expressed by C57BL/6 mice, while BALB/c express the I-A^d allele. The latter emphasizes the need of further studies to characterize in depth resident peritoneal cell populations in these mouse strains.

One limitation of this study is that resident peritoneal cells are a heterogeneous population, thus, we cannot rule out the possible contribution of cells other than macrophages in the observed gene expression patterns. However, the higher proportion of cells in our samples were F4/80$^+$CD11b$^+$, which are macrophages. Moreover, as tissue resident macrophages could harbour diverse populations of macrophages exhibiting a range of activation states [73, 75], this could contribute to a gene expression pattern that mixes markers for different activation phenotypes. Furthermore, several studies use resident peritoneal cells to understand the mechanisms involved in a variety of disease models where macrophages play an essential role. Hence, the results shown here are relevant for the interpretation of gene expression patterns analysis in the resident peritoneal macrophage population under a pathogen challenge. The impact of baseline gene expression of different tissue-macrophages for the understanding of disease pathogenesis requires further studies.

Globally, the gene expression pattern of uninfected C57BL/6 macrophages exhibited significant differences to that of BALB/c macrophages. Our results suggest that macrophages from each mice strain have a specific basal gene expression pattern, which probably influences, but does not appear to determine by itself, the phenotype in response to pathogens. The final phenotype may be influenced also by post-transcriptional modifications, which in turn could be modulated by the pathogens [83]. This study highlights important aspects to consider when studying the mechanisms involved in the development of resident peritoneal macrophage phenotypes in response to intracellular pathogens.

Author contributions

PF and CR conceived and designed the manuscript; CR, AL, EE, LH, and IQ performed the experiments, acquired and analyzed the data; CR, PF, and AL formally interpreted the data; CR, AL, and EE curated the RNA-Seq data; CR and PF wrote the manuscript; CR, AL, and PF reviewed, edited and final approved the manuscript; PF supervised and administered the project; PF, LH, and CR acquired the funding for the project. All authors contributed to the article and approved the submitted version.

Data availability

The datasets presented in this study can be found in online repositories. The names of the repository/repositories and accession number(s) can be found below: https://www.ncbi.nlm.nih.gov/sra/SRX10075500; https://www.ncbi.nlm.nih.gov/sra/SRX10075501; https://www.ncbi.nlm.nih.gov/sra/SRX10075504; https://www.ncbi.nlm.nih.gov/sra/SRX10075508; https://www.ncbi.nlm.nih.gov/sra/SRX10075509; https://www.ncbi.nlm.nih.gov/sra/SRX10075510.

Ethics statement

The animal study was approved by Comité Institucional de Cuidado y Uso de Animales (protocol code CICUA-14-002) Instituto de Investigaciones Científicas y Servicios de Alta Tecnología. The study was conducted in accordance with the local legislation and institutional requirements.

Funding

The author(s) declare that financial support was received for the research, authorship, and/or publication of this article. This work was supported by the Secretaría Nacional de Ciencia, Tecnología e Innovación (SENACYT), Panamá (grant number NI-03-2017); and Sistema Nacional de Investigación (SNI), Panamá (grant numbers SNI-008-2022, SNI- 043-2023, SNI-170-2021).

Acknowledgments

The authors are very grateful to Secretaría Nacional de Ciencia, Tecnología e Innovación (SENACYT) and Sistema Nacional de Investigación (SNI) for financial support to this project.

Conflict of interest

The author(s) declared no potential conflicts of interest with respect to the research, authorship, and/or publication of this article.

Supplementary material

The Supplementary Material for this article can be found online at: https://www.ebm-journal.org/articles/10.3389/ebm.2024.10377/full#supplementary-material

References

1. Gautier EL, Shay T, Miller J, Greter M, Jakubzick C, Ivanov S, et al. Gene-expression profiles and transcriptional regulatory pathways that underlie the identity and diversity of mouse tissue macrophages. *Nat Immunol* (2012) **13**: 1118–28. doi:10.1038/ni.2419

2. Mills CD, Kincaid K, Alt JM, Heilman MJ, Hill AM. M-1/M-2 macrophages and the Th1/Th2 paradigm. *The J Immunol* (2000) **164**:6166–73. doi:10.4049/jimmunol.164.12.6166

3. Mantovani A, Sica A, Sozzani S, Allavena P, Vecchi A, Locati M. The chemokine system in diverse forms of macrophage activation and polarization. *Trends Immunol* (2004) **25**:677–86. doi:10.1016/j.it.2004.09.015

4. Yunna C, Mengru H, Lei W, Weidong C. Macrophage M1/M2 polarization. *Eur J Pharmacol* (2020) **877**:173090. doi:10.1016/j.ejphar.2020.173090

5. Arango DG, Descoteaux A. Macrophage cytokines: involvement in immunity and infectious diseases. *Front Immunol* **5**. doi:10.3389/fimmu.2014.00491

6. Verreck FAW, de Boer T, Langenberg DML, Hoeve MA, Kramer M, Vaisberg E, et al. Human IL-23-producing type 1 macrophages promote but IL-10-producing type 2 macrophages subvert immunity to *(myco)bacteria*. *Proc Natl Acad Sci U S A* (2004) **101**:4560–5. doi:10.1073/pnas.0400983101

7. Orecchioni M, Ghosheh Y, Pramod AB, Ley K. Macrophage polarization: different gene signatures in M1(LPS+) vs. Classically and M2(LPS–) vs. Alternatively activated macrophages. *Front Immunol* (2019) **10**:1084. doi:10.3389/fimmu.2019.01084

8. Soudi S, Zavaran-Hosseini A, Muhammad Hassan Z, Soleimani M, Jamshidi Adegani F, Hashemi SM. Comparative study of the effect of LPS on the function of BALB/c and C57BL/6 peritoneal macrophages. *Cell J* (2013) **15**:45–54.

9. Santos JL, Andrade AA, Dias AAM, Bonjardim CA, Reis LFL, Teixeira SMR, et al. Differential sensitivity of C57BL/6 (M-1) and BALB/c (M-2) macrophages to the stimuli of IFN-γ/LPS for the production of NO: correlation with iNOS mRNA and protein expression. *J Interferon and Cytokine Res* (2006) **26**:682–8. doi:10.1089/jir.2006.26.682

10. Reiner SL, Locksley RM. The regulation of immunity to *Leishmania major*. *Annu Rev Immunol* (1995) **13**:151–77. doi:10.1146/annurev.iy.13.040195.001055

11. Lipoldová M, Demant P. Genetic susceptibility to infectious disease: lessons from mouse models of leishmaniasis. *Nat Rev Genet* (2006) **7**:294–305. doi:10.1038/nrg1832

12. Fornefett J, Krause J, Klose K, Fingas F, Hassert R, Benga L, et al. Comparative analysis of humoral immune responses and pathologies of BALB/c and C57BL/6 wildtype mice experimentally infected with a highly virulent *Rodentibacter pneumotropicus* (*Pasteurella pneumotropica*) strain. *BMC Microbiol* (2018) **18**: 45. doi:10.1186/s12866-018-1186-8

13. Bertolini TB, de Souza AI, Gembre AF, Piñeros AR, Prado Rd Q, Silva JS, et al. Genetic background affects the expansion of macrophage subsets in the lungs of *Mycobacterium tuberculosis*-infected hosts. *Immunology* (2016) **148**:102–13. doi:10.1111/imm.12591

14. Oswald IP, Afroun S, Bray D, Petit J-F, Lemaire G. Low response of BALB/c macrophages to priming and activating signals. *J Leukoc Biol* (1992) **52**:315–22. doi:10.1002/jlb.52.3.315

15. Dileepan KN, Page JC, Li Y, Stechschulte DJ. Direct activation of murine peritoneal macrophages for nitric oxide production and tumor cell killing by interferon-γ. *J Interferon and Cytokine Res* (1995) **15**:387–94. doi:10.1089/jir.1995.15.387

16. Chakkalath HR, Titus RG. *Leishmania major*-parasitized macrophages augment Th2-type T cell activation. *The J Immunol* (1994) **153**:4378–87. doi:10.4049/jimmunol.153.10.4378

17. Gregory DJ, Sladek R, Olivier M, Matlashewski G. Comparison of the effects of *Leishmania major* or *Leishmania donovani* infection on macrophage gene expression. *Infect Immun* (2008) **76**:1186–92. doi:10.1128/iai.01320-07

18. Shadab M, Das S, Banerjee A, Sinha R, Asad M, Kamran M, et al. RNA-seq revealed expression of many novel genes associated with *Leishmania donovani* persistence and clearance in the host macrophage. *Front Cel Infect Microbiol* (2019) **9**:17. doi:10.3389/fcimb.2019.00017

19. Rodriguez NE, Chang HK, Wilson ME. Novel program of macrophage gene expression induced by phagocytosis of *Leishmania chagasi*. *Infect Immun* (2004) **72**: 2111–22. doi:10.1128/iai.72.4.2111-2122.2004

20. Ehrlich A, Castilho TM, Goldsmith-Pestana K, Chae W-J, Bothwell ALM, Sparwasser T, et al. The immunotherapeutic role of regulatory T cells in *Leishmania* (*Viannia) panamensis* infection. *J Immunol* (2014) **193**:2961–70. doi:10.4049/jimmunol.1400728

21. Rocha FJS, Schleicher U, Mattner J, Alber G, Bogdan C. Cytokines, signaling pathways, and effector molecules required for the control of *Leishmania* (*Viannia*) *braziliensis* in mice. *Infect Immun* (2007) **75**:3823–32. doi:10.1128/iai.01335-06

22. Castilho TM, Goldsmith-Pestana K, Lozano C, Valderrama L, Saravia NG, McMahon-Pratt D. Murine model of chronic *L.* (*Viannia) panamensis* infection: role of IL-13 in disease. *Eur J Immunol* (2010) **40**:2816–29. doi:10.1002/eji.201040384

23. Restrepo CM, Llanes A, Herrera L, Ellis E, Lleonart R, Fernández PL. Gene expression patterns associated with *Leishmania panamensis* infection in macrophages from BALB/c and C57BL/6 mice. *Plos Negl Trop Dis* (2021) **15**: e0009225. doi:10.1371/journal.pntd.0009225

24. Herrera L, Llanes A, Álvarez J, Degracia K, Restrepo CM, Rivera R, et al. Antileishmanial activity of a new chloroquine analog in an animal model of *Leishmania panamensis* infection. *Int J Parasitol Drugs Drug Resist* (2020) **14**: 56–61. doi:10.1016/j.ijpddr.2020.08.002

25. Kim D, Langmead B, Salzberg SL. HISAT: a fast spliced aligner with low memory requirements. *Nat Methods* (2015) **12**:357–60. doi:10.1038/nmeth.3317

26. Liao Y, Smyth GK, Shi W. featureCounts: an efficient general purpose program for assigning sequence reads to genomic features. *Bioinformatics* (2014) **30**:923–30. doi:10.1093/bioinformatics/btt656

27. Anders S, Huber W. Differential expression analysis for sequence count data. *Genome Biol* (2010) **11**:R106. doi:10.1186/gb-2010-11-10-r106

28. Love MI, Huber W, Anders S. Moderated estimation of fold change and dispersion for RNA-seq data with DESeq2. *Genome Biol* (2014) **15**:550. doi:10.1186/s13059-014-0550-8

29. Yu G, Wang L-G, Han Y, He Q-Y (2012). clusterProfiler: an R package for comparing biological themes among gene clusters, *OMICS*, **16**: 284–7. doi:10.1089/omi.2011.0118

30. Rachinger N, Fischer S, Böhme I, Linck-Paulus L, Kuphal S, Kappelmann-Fenzl M, et al. Loss of gene information: discrepancies between RNA sequencing, cDNA microarray, and qRT-PCR. *Int J Mol Sci* (2021) **22**:9349. doi:10.3390/ijms22179349

31. Zhou Y, Yoshida S, Kubo Y, Yoshimura T, Kobayashi Y, Nakama T, et al. Different distributions of M1 and M2 macrophages in a mouse model of laser-induced choroidal neovascularization. *Mol Med Rep* (2017) **15**:3949–56. doi:10.3892/mmr.2017.6491

32. Jaguin M, Houlbert N, Fardel O, Lecureur V. Polarization profiles of human M-CSF-generated macrophages and comparison of M1-markers in classically activated macrophages from GM-CSF and M-CSF origin. *Cell Immunol* (2013) **281**:51–61. doi:10.1016/j.cellimm.2013.01.010

33. Hickman E, Smyth T, Cobos-Uribe C, Immormino R, Rebuli ME, Moran T, et al. Expanded characterization of *in vitro* polarized M0, M1, and M2 human monocyte-derived macrophages: bioenergetic and secreted mediator profiles. *PLoS One* (2023) **18**:e0279037. doi:10.1371/journal.pone.0279037

34. Martinez FO, Gordon S. The M1 and M2 paradigm of macrophage activation: time for reassessment. *F1000prime Rep* (2014) **6**:13. doi:10.12703/p6-13

35. Watanabe H, Numata K, Ito T, Takagi K, Matsukawa A. Innate immune response in Th1- and Th2-dominant mouse strains. *Shock* (2004) **22**:460–6. doi:10.1097/01.shk.0000142249.08135.e9

36. Scott P, Natovitz P, Coffman RL, Pearce E, Sher A. Immunoregulation of cutaneous leishmaniasis. T cell lines that transfer protective immunity or exacerbation belong to different T helper subsets and respond to distinct parasite antigens. *The J Exp Med* (1988) **168**:1675–84. doi:10.1084/jem.168.5.1675

37. Heinzel FP, Sadick MD, Holaday BJ, Coffman RL, Locksley RM. Reciprocal expression of interferon gamma or interleukin 4 during the resolution or progression of murine leishmaniasis. Evidence for expansion of distinct helper T cell subsets. *The J Exp Med* (1989) **169**:59–72. doi:10.1084/jem.169.1.59

38. Hsieh CS, Macatonia SE, O'Garra A, Murphy KM. T cell genetic background determines default T helper phenotype development *in vitro*. *The J Exp Med* (1995) **181**:713–21. doi:10.1084/jem.181.2.713

39. Beebe AM, Mauze S, Schork NJ, Coffman RL. Serial backcross mapping of multiple loci associated with resistance to *Leishmania major* in mice. *Immunity* (1997) **6**:551–7. doi:10.1016/s1074-7613(00)80343-x

40. Knight JM, Lee S-H, Roberts L, Smith CW, Weiss ST, Kheradmand F, et al. CD11a polymorphisms regulate TH2 cell homing and TH2-related disease. *J Allergy Clin Immunol* (2014) **133**:189–97.e8. doi:10.1016/j.jaci.2013.03.049

41. Classen A, Lloberas J, Celada A. *Macrophage activation: classical vs. Alternative* (2009). p. 29–43.

42. Weng S-Y, Wang X, Vijayan S, Tang Y, Kim YO, Padberg K, et al. IL-4 receptor alpha signaling through macrophages differentially regulates liver fibrosis progression and reversal. *EBioMedicine* (2018) **29**:92–103. doi:10.1016/j.ebiom.2018.01.028

43. Mohrs M, Holscher C, Brombacher F. Interleukin-4 receptor alpha-deficient BALB/c mice show an unimpaired T helper 2 polarization in response to *Leishmania major* infection. *Infect Immun* (2000) **68**:1773–80. doi:10.1128/iai.68.4.1773-1780.2000

44. La Flamme AC, Kharkrang M, Stone S, Mirmoeini S, Chuluundorj D, Kyle R. Type II-activated murine macrophages produce IL-4. *PLoS One* (2012) **7**:e46989. doi:10.1371/journal.pone.0046989

45. Lee SJ, Evers S, Roeder D, Parlow AF, Risteli J, Risteli L, et al. Mannose receptor-mediated regulation of serum glycoprotein homeostasis. *Science (1979)* (2002) **295**:1898–901. doi:10.1126/science.1069540

46. Kambara K, Ohashi W, Tomita K, Takashina M, Fujisaka S, Hayashi R, et al. *In vivo* depletion of CD206+ M2 macrophages exaggerates lung injury in endotoxemic mice. *The Am J Pathol* (2015) **185**:162–71. doi:10.1016/j.ajpath.2014.09.005

47. Schlesinger LS. Macrophage phagocytosis of virulent but not attenuated strains of *Mycobacterium tuberculosis* is mediated by mannose receptors in addition to complement receptors. *The J Immunol* (1993) **150**:2920–30. doi:10.4049/jimmunol.150.7.2920

48. Lee SH, Charmoy M, Romano A, Paun A, Chaves MM, Cope FO, et al. Mannose receptor high, M2 dermal macrophages mediate nonhealing *Leishmania major* infection in a Th1 immune environment. *J Exp Med* (2018) **215**:357–75. doi:10.1084/jem.20171389

49. Breda J, Banerjee A, Jayachandran R, Pieters J, Zavolan M. A novel approach to single-cell analysis reveals intrinsic differences in immune marker expression in unstimulated BALB/c and C57BL/6 macrophages. *FEBS Lett* (2022) **596**:2630–43. doi:10.1002/1873-3468.14478

50. Dupasquier M, Stoitzner P, Wan H, Cerqueira D, van Oudenaren A, Voerman JSA, et al. The dermal microenvironment induces the expression of the alternative activation marker CD301/mMGL in mononuclear phagocytes, independent of IL-4/IL-13 signaling. *J Leukoc Biol* (2006) **80**:838–49. doi:10.1189/jlb.1005564

51. Bellón T, Martínez V, Lucendo B, del Peso G, Castro MJ, Aroeira LS, et al. Alternative activation of macrophages in human peritoneum: implications for peritoneal fibrosis. *Nephrol Dial Transplant* (2011) **26**:2995–3005. doi:10.1093/ndt/gfq771

52. Nakagawa TY, Rudensky AY. The role of lysosomal proteinases in MHC class Il-mediated antigen processing and presentation. *Immunological Rev* (1999) **172**:121–9. doi:10.1111/j.1600-065x.1999.tb01361.x

53. Cresswell P. Proteases, processing, and thymic selection. *Science* (1998) **280**:394–5. doi:10.1126/science.280.5362.394

54. Zhang T, Maekawa Y, Sakai T, Nakano Y, Ishii K, Hisaeda H, et al. Treatment with cathepsin L inhibitor potentiates Th2-type immune response in *Leishmania major*-infected BALB/c mice. *Int Immunol* (2001) **13**:975–82. doi:10.1093/intimm/13.8.975

55. Zhang T, Maekawa Y, Yasutomo K, Ishikawa H, Fawzy Nashed B, Dainichi T, et al. Pepstatin A-sensitive aspartic proteases in lysosome are involved in degradation of the invariant chain and antigen-processing in antigen presenting cells of mice infected with *Leishmania major*. *Biochem Biophysical Res Commun* (2000) **276**:693–701. doi:10.1006/bbrc.2000.3538

56. Palmer MJ, Frelinger JA. Widespread transcription of a Qa region gene in adult mice. *The J Exp Med* (1987) **166**:95–108. doi:10.1084/jem.166.1.95

57. Sullivan LC, Berry R, Sosnin N, Widjaja JML, Deuss FA, Balaji GR, et al. Recognition of the major histocompatibility complex (MHC) class ib molecule H2-Q10 by the natural killer cell receptor Ly49C. *J Biol Chem* (2016) **291**:18740–52. doi:10.1074/jbc.m116.737130

58. Goodall KJ, Nguyen A, Matsumoto A, McMullen JR, Eckle SB, Bertolino P, et al. Multiple receptors converge on H2-Q10 to regulate NK and γδT-cell development. *Immunol Cel Biol* (2019) **97**:326–39. doi:10.1111/imcb.12222

59. Gunturi A, Berg RE, Forman J. Preferential survival of CD8 T and NK cells expressing high levels of CD94. *The J Immunol* (2003) **170**:1737–45. doi:10.4049/jimmunol.170.4.1737

60. Probst CM, Silva RA, B Menezes JP, Almeida TF, Gomes IN, Dallabona AC, et al. A comparison of two distinct murine macrophage gene expression profiles in response to *Leishmania amazonensis* infection. *BMC Microbiol* (2012) **12**:22. doi:10.1186/1471-2180-12-22

61. Sah SK, Agrahari G, Kim T-Y. Insights into superoxide dismutase 3 in regulating biological and functional properties of mesenchymal stem cells. *Cell Biosci* (2020) **10**:22. doi:10.1186/s13578-020-00386-3

62. Fukai T, Ushio-Fukai M. Superoxide dismutases: role in redox signaling, vascular function, and diseases. *Antioxid and Redox Signaling* (2011) **15**:1583–606. doi:10.1089/ars.2011.3999

63. Couto N, Wood J, Barber J. The role of glutathione reductase and related enzymes on cellular redox homoeostasis network. *Free Radic Biol Med* (2016) **95**:27–42. doi:10.1016/j.freeradbiomed.2016.02.028

64. Peterson JD, Herzenberg LA, Vasquez K, Waltenbaugh C. Glutathione levels in antigen-presenting cells modulate Th1 versus Th2 response patterns. *Proc Natl Acad Sci U S A* (1998) **95**:3071–6. doi:10.1073/pnas.95.6.3071

65. Bichiou H, Rabhi S, Ben Hamda C, Bouabid C, Belghith M, Piquemal D, et al. *Leishmania* parasites differently regulate antioxidant genes in macrophages derived from resistant and susceptible mice. *Front Cel Infect Microbiol* (2021) **11**:748738. doi:10.3389/fcimb.2021.748738

66. Depke M, Breitbach K, Dinh Hoang Dang K, Brinkmann L, Salazar MG, Dhople VM, et al. Bone marrow-derived macrophages from BALB/c and C57BL/6 mice fundamentally differ in their respiratory chain complex proteins, lysosomal enzymes and components of antioxidant stress systems. *J Proteomics* (2014) **103**:72–86. doi:10.1016/j.jprot.2014.03.027

67. Lavin Y, Winter D, Blecher-Gonen R, David E, Keren-Shaul H, Merad M, et al. Tissue-resident macrophage enhancer landscapes are shaped by the local microenvironment. *Cell* (2014) **159**:1312–26. doi:10.1016/j.cell.2014.11.018

68. Ginhoux F, Greter M, Leboeuf M, Nandi S, See P, Gokhan S, et al. Fate mapping analysis reveals that adult microglia derive from primitive macrophages. *Science* (2010) **330**:841–5. doi:10.1126/science.1194637

69. Schulz C, Perdiguero EG, Chorro L, Szabo-Rogers H, Cagnard N, Kierdorf K, et al. A lineage of myeloid cells independent of Myb and hematopoietic stem cells. *Science* (2012) **336**:86–90. doi:10.1126/science.1219179

70. Yona S, Kim K-W, Wolf Y, Mildner A, Varol D, Breker M, et al. Fate mapping reveals origins and dynamics of monocytes and tissue macrophages under homeostasis. *Immunity* (2013) **38**:1073–9. doi:10.1016/j.immuni.2013.05.008

71. Takahashi K. Development and differentiation of macrophages and related cells: historical review and current concepts. *J Clin Exp Hematopathology* (2001) **41**:1–31. doi:10.3960/jslrt.41.1

72. Kohyama M, Ise W, Edelson BT, Wilker PR, Hildner K, Mejia C, et al. Role for Spi-C in the development of red pulp macrophages and splenic iron homeostasis. *Nature* (2009) **457**:318–21. doi:10.1038/nature07472

73. Okabe Y, Medzhitov R. Tissue-specific signals control reversible program of localization and functional polarization of macrophages. *Cell* (2014) **157**:832–44. doi:10.1016/j.cell.2014.04.016

74. Butovsky O, Jedrychowski MP, Moore CS, Cialic R, Lanser AJ, Gabriely G, et al. Identification of a unique TGF-β-dependent molecular and functional signature in microglia. *Nat Neurosci* (2014) **17**:131–43. doi:10.1038/nn.3599

75. Gosselin D, Link VM, Romanoski CE, Fonseca GJ, Eichenfield DZ, Spann NJ, et al. Environment drives selection and function of enhancers controlling tissue-specific macrophage identities. *Cell* (2014) **159**:1327–40. doi:10.1016/j.cell.2014.11.023

76. Ghosn EEB, Cassado AA, Govoni GR, Fukuhara T, Yang Y, Monack DM, et al. Two physically, functionally, and developmentally distinct peritoneal macrophage subsets. *Proc Natl Acad Sci U S A* (2010) **107**:2568–73. doi:10.1073/pnas.0915000107

77. Cassado A, de Albuquerque JAT, Sardinha LR, Buzzo Cd L, Faustino L, Nascimento R, et al. Cellular renewal and improvement of local cell effector activity in peritoneal cavity in response to infectious stimuli. *PLoS One* (2011) **6**:e22141. doi:10.1371/journal.pone.0022141

78. Kim K-W, Williams JW, Wang Y-T, Ivanov S, Gilfillan S, Colonna M, et al. MHC II+ resident peritoneal and pleural macrophages rely on IRF4 for development from circulating monocytes. *J Exp Med* (2016) **213**:1951–9. doi:10.1084/jem.20160486

79. Xaus J, Comalada M, Barrachina M, Herrero C, Goñalons E, Soler C, et al. The expression of MHC class II genes in macrophages is cell cycle dependent. *The J Immunol* (2000) **165**:6364–71. doi:10.4049/jimmunol.165.11.6364

80. Sánchez I, Dynlacht BD. Transcriptional control of the cell cycle. *Curr Opin Cel Biol* (1996) **8**:318–24. doi:10.1016/s0955-0674(96)80004-4

81. Sohn M, Na HY, Ryu SH, Choi W, In H, Shin HS, et al. Two distinct subsets are identified from the peritoneal myeloid mononuclear cells expressing both CD11c and CD115. *Immune Netw* (2019) **19**:e15. doi:10.4110/in.2019.19.e15

82. Baumgart M, Moos V, Schuhbauer D, Müller B. Differential expression of major histocompatibility complex class II genes on murine macrophages associated with T cell cytokine profile and protective/suppressive effects. *Proc Natl Acad Sci* (1998) **95**:6936–40. doi:10.1073/pnas.95.12.6936

83. Wilkins-Rodríguez AA, Escalona-Montaño AR, Aguirre-García M, Becker I, Gutiérrez-Kobeh L. Regulation of the expression of nitric oxide synthase by *Leishmania mexicana* amastigotes in murine dendritic cells. *Exp Parasitol* (2010) **126**:426–34. doi:10.1016/j.exppara.2010.07.014

Experimental Biology and Medicine

TYPE Original Research
PUBLISHED 03 January 2025
DOI 10.3389/ebm.2024.10233

OPEN ACCESS

*CORRESPONDENCE
Thomas D. Otto,
thomasdan.otto@glasgow.ac.uk
Lucas Amenga-Etego,
lamengaetego@ug.edu.gh

RECEIVED 10 May 2024
ACCEPTED 05 December 2024
PUBLISHED 03 January 2025

CITATION
Morang'a CM, Drake RS, Miao VN, Nyakoe NK, Amuzu DSY, Appiah V, Aniweh Y, Bediako Y, Bah SY, Shalek AK, Awandare GA, Otto TD and Amenga-Etego L (2025) scRNA-seq reveals elevated interferon responses and TNF-α signaling via NFkB in monocytes in children with uncomplicated malaria. *Exp. Biol. Med.* 249:10233. doi: 10.3389/ebm.2024.10233

scRNA-seq reveals elevated interferon responses and TNF-α signaling via NFkB in monocytes in children with uncomplicated malaria

Collins M. Morang'a[1], Riley S. Drake[2,3,4,5], Vincent N. Miao[2,3,4,5], Nancy K. Nyakoe[1], Dominic S. Y. Amuzu[1], Vincent Appiah[1], Yaw Aniweh[1], Yaw Bediako[1], Saikou Y. Bah[6], Alex K. Shalek[2,3,4,5], Gordon A. Awandare[1], Thomas D. Otto[6]* and Lucas Amenga-Etego[1]*

[1]West African Centre for Cell Biology of Infectious Pathogens (WACCBIP), Department of Biochemistry, Cell and Molecular Biology, University of Ghana, Accra, Ghana, [2]Program in Health Sciences and Technology, Harvard Medical School and Massachusetts Institute of Technology, Boston, MA, United States, [3]Institute for Medical Engineering and Science (IMES), Department of Chemistry, Koch Institute for Integrative Cancer Research, Massachusetts Institute of Technology (MIT), Cambridge, MA, United States, [4]Ragon Institute of Massachusetts General Hospital (MGH), Massachusetts Institute of Technology (MIT) and Harvard, Cambridge, MA, United States, [5]Broad Institute of Massachusetts Institute of Technology (MIT) and Harvard, Cambridge, MA, United States, [6]School of Infection and Immunity, Medical, Veterinary, and Life Sciences (MVLS), University of Glasgow, Glasgow, United Kingdom

Abstract

Malaria causes significant morbidity and mortality worldwide, disproportionately impacting sub-Saharan Africa. Disease phenotypes associated with *Plasmodium falciparum* infection can vary widely, from asymptomatic to life-threatening. To date, prevention efforts, particularly those related to vaccine development, have been hindered by an incomplete understanding of which factors impact host immune responses resulting in these divergent outcomes. Here, we conducted a field study of 224 individuals to determine host-parasite factors associated with symptomatic malaria "patients" compared to asymptomatic malaria-positive "controls" at both the community and healthy facility levels. We further performed comprehensive immune profiling to obtain deeper insights into differences in response between the pair. First, we determined the relationship between host age and parasite density in patients (n = 134/224) compared to controls (n = 90/224). Then, we applied single-cell RNA sequencing to compare the immunological phenotypes of 18,176 peripheral blood mononuclear cells isolated from a subset of the participants (n = 11/224), matched on age, sex, and parasite density. Patients had higher parasite densities compared to the controls, although the levels had a negative correlation with age in both groups, suggesting that they are key indicators of disease pathogenesis. On average, patients were characterized by a higher fractional abundance of monocytes and an upregulation of innate immune responses, including those to type I and type

II interferons and tumor necrosis factor-alpha signaling via NFκB. Further, in the patients, we identified more putative interactions between antigen-presenting cells and proliferating CD4 T cells, and naïve CD8 T cells driven by MHC-I and MHC-II signaling pathways, respectively. Together, these findings highlight transcriptional differences between immune cell subsets associated with disease phenotypes that may help guide the development of improved malaria vaccines and new therapeutic interventions.

KEYWORDS

uncomplicated malaria, *Plasmodium falciparum*, scRNA-Sequencing, immune responses, cell-cell interactions, TNF-α signaling via NFκB, monocytes

Impact statement

Nearly 50% of the world population is at risk of *Plasmodium* infection, although sub-Saharan Africa carries the greatest share of global burden of malaria. In 2022, the WHO reported 249 million cases, and children under 5 years were the most vulnerable group accounting for 80% of the deaths in Africa. Advances in understanding the molecular basis of pathogenesis at the single-cell level can fuel the development of new therapeutics and malaria vaccines. Previous studies have focused on studying gene expression in bulk heterogeneous cell populations of blood, brain, liver, or spleen tissues, but here, we describe the gene expression in single cells of peripheral blood mononuclear cells. We provide details into the abundance of cell types, genes expressed in each cell subset, and signaling pathways that are associated with malaria. Such information can be used to help design and develop well-targeted malaria therapeutics and vaccines.

Introduction

In 2022, global estimates of malaria cases and deaths have increased to 249 million cases and 608,000 deaths [1]. However, the development of an effective vaccine to address this global health threat remains challenging due to an incomplete understanding of the parasite's biology and limited knowledge of which host factors influence clinical responses to infection.

In malaria-endemic communities, individuals may harbor malaria infections with mild to no symptoms warranting treatment, here referred to as healthy community controls. Such infections may be cleared naturally or progress to uncomplicated malaria, where symptoms become profound enough to necessitate medical intervention. Instructive factors include environmental exposures, transmission intensity, host and parasite genetics, host-pathogen interactions, and host immune responses [2–5]. Illustratively, upregulation of interferon responses and p53 gene expression can attenuate inflammation and protect children from fever [6]; and, when comparing children with asymptomatic and severe malaria, the genes most upregulated in severe cases are related to immunoglobin production and interferon signaling [7]. As reviewed previously, studies have postulated that interferons can orchestrate immune regulatory networks to dampen inflammatory responses and restrict humoral immunity, thus playing a critical role as a wedge that determines protection versus permissiveness to malaria infection [8, 9].

Similarly, it has been shown that the number and phenotype of cells responding to infection can vary with exposure to *Plasmodium* [10]. For example, Africans, who tend to have higher levels of exposure, have been shown to exhibit metabolic and platelet activation during malaria infection as compared to typically infection-naïve Europeans [10]. Similarly, children who experience high cumulative malaria episodes show upregulation of interferon-inducible genes and immunoregulatory cytokines, suggesting an immune modification to prevent immunopathology and severe outcomes during new infections [11]. Beyond differences in exposure and infection history, the strain responsible for each infection can also alter immune response dynamics and disease pathogenesis [12, 13].

Since so many factors can influence host response dynamics to infection (e.g., exposure, the timing of infection), some studies have implemented tightly regulated models of malarial infection, such as controlled human-malaria infections (CHMI). CHMI studies have identified several pathways, including toll-like receptor signaling [14], platelet activation [10], interferon signaling [10, 15, 16], and B-cell receptor signaling, that are involved in immunological modulation of *Plasmodium falciparum* infections [6]. Although CHMI enables more controlled examinations of host-pathogen dynamics post-malaria infection, clinically relevant differences can arise between responses seen in CHMI and natural exposure due to unresolved immunopathological mechanisms elicited during *P. falciparum* infection [10]. Thus, studies involving natural cohorts provide a better avenue to understand variability in immune responses developed through repeated exposure and how they influence disease phenotypes. Besides, immunity to malaria develops very slowly through repeated infections and can wane quickly if individuals leave malaria-endemic areas, suggesting that continuous natural exposure to malaria antigens is important for the development of long-term immunity [11]. Collectively, these studies demonstrate the importance of obtaining a more comprehensive understanding of the host and pathogen factors that influence immune responses to inform the development of new therapeutic approaches and improved vaccines.

To date, most genomic analyses of immunological responses to malarial infection have been performed in heterogeneous cell populations of blood, brain, liver, or spleen tissues [17]. The majority of these studies have been conducted in children and the studies show that symptomatic infections, as mentioned above, are characterized by upregulated expression of genes involved in interferon signaling, antigen presentation, neutrophil-associated signatures, and B cell modules relative to healthy controls [17]. Adults, meanwhile, present slightly varying responses: symptomatic Malian adults, compared to naïve individuals, had upregulated B cell receptor signaling but more modest upregulation of interferon responses, while symptomatic Cameroonian adults showed marked induction of genes related to interleukins and apoptosis compared to presymptomatic individuals [18, 19]. These inconsistencies may be related to patient history/exposure or differences in cellular composition influencing clinical course through a combination of direct and indirect responses. The emergence of single-cell transcriptomics provides a unique opportunity to examine the sources of this variability [20] by profiling abundance and transcriptomic variation across immune cell populations in individuals with high malaria exposure but divergent clinical phenotypes. Moreover, by examining the expression of ligands, receptors, and genes involved in intercellular signaling, we can identify the critical mediators of immune responses and the pathogenesis of malaria for subsequent validation [21].

Here, we present a comparative analysis of peripheral blood mononuclear cells (PBMCs) phenotypes in children from two related surveys conducted in 2019. An active case detection of *P. falciparum* infections at the community level (controls) and passive case detection at the health facility level for patients with uncomplicated malaria (patients) in an endemic area in northern Ghana. Our data describe in unprecedented detail, cell subsets and signaling pathways associated with disease severity to provide new insights into the immune response mechanisms that influence the course of *P. falciparum* infections in young children.

Materials and methods

Study design and sample collection

In 2019, we conducted a cross-sectional active case detection survey in the Kassena-Nankana Municipality of the Upper East Region of Ghana, to recruit children with uncomplicated malaria and controls with *P. falciparum* infections. About 1000 community members were screened for malaria infection using a CareStart™ PfHRP2-based malaria Rapid Diagnostic Test (RDT, Access Bio, NY, United States). Positive cases in the community were defined as "controls" since these individuals hadn't sought treatment within the past 2 weeks. Similarly, a passive case detection of uncomplicated malaria cases was carried out using the same mRDTs to screen individuals presenting at the Navrongo War Memorial Hospital outpatient department. Individuals who tested positive for malaria and who provided written informed consent were recruited into the study and defined as "patients". Five milliliters (mL) of whole blood was collected for PBMC isolation and thick and thin blood smears were for parasite identification and quantification using microscopy. Linear regression analysis was used to determine the relationship between parasite density and age in patients and controls using R software (version 4.2.1).

Of the 224 individuals recruited in both arms of the study, five control participants and six patients were selected for single-cell transcriptomic analysis. Due to the observed clear differences in clinical presentation between the groups driven by fever, headache, and parasite density, the 11 children selected for single-cell analysis had close similarity in these factors. PBMCs were isolated in ACD tubes and spun at 2,000 revolutions per minute (rpm) for 10 min, and the leukocyte layer was transferred to 15 mL. The leukocytes were mixed with phosphate-buffered saline (PBS) and layered on 3 mL of lymphoprep in a 15 mL falcon tube. The layered cells were spun for 30 min at 800 g without breaks and harvested carefully by taking the buffy layer into another falcon tube. The PBMCs were washed twice with PBS and stored in freezing media. During thawing, complete media (RP10) with 20% Fetal Bovine Serum (FBS) was prepared by diluting 20 mL of FBS in 80 mL of Roswellpark Memorial Institute (RPMI) media [22]. PBMCs were removed from Liquid Nitrogen to the −80°C freezer and then thawed during each experiment. Thawing was done by placing the vial in a clean water bath at 37°C until a small crystal of frozen cells was visible. The tubes were cleaned with 70% ethanol, and the contents were transferred to 10 mL of RP10 gently to minimize stressing the cells. The cells were centrifuged at 500 g for 10 min and resuspended in RP10. Cell viability was estimated using Hemocytometer and PBMCs were used after 1 h of resting in the incubator at 37°C.

Seq-Well scRNA-Seq workflow

Seq-Well scRNA-Seq S^3 workflow was performed according to the published methods [23, 24]. In brief, 5×10^5 PBMCs from each patient were dispensed into a single array containing barcoded mRNA capture beads. The arrays were sealed with a Polycarbonate Track Etch (PCTE) membrane (pore size of 0.01 μM), allowing cells to remain separated through the lysis and hybridization steps. mRNA transcripts were hybridized and recovered for reverse transcription using the Maxima H Minus Reverse Transcriptase in the first strand synthesis step. Exonuclease (I) was used to remove excess primers and mRNA was captured via poly-T priming of the poly-A mRNA. The captured mRNA underwent first-strand synthesis to generate single-stranded cDNA while bound to the beads. Enzymes with terminal transferase were used to create 3' overhangs and three cytosines. The overhangs are used in template switching, whereby a SMART sequence is appended to the overhang on both ends of the cDNA molecule during the first strand synthesis. Some templates fail to switch, resulting in loss of the mRNA; hence they are chemically denatured using 0.1M NaOH with random octamer with the SMART sequence in 5' orientation, and a second strand is synthesized. Whole transcriptome amplification of the cDNA was performed using the KAPA HiFi PCR master mix (Kapa Biosystems). Libraries were pooled and purified using AgenCourt AMPure XP Beads. The quality of the library was assessed using Agilent Tape Station with D5000 High Sensitivity tapes and reagents. Samples were barcoded as described in the Nextera XT DNA (Illumina, United States) segmentation method. Tagmentation was important because, after cDNA amplification and clean-up, there are usually very long cDNA molecules that need to be fragmented to be sequenced by Illumina. The Nextera XT DNA tagmentation method is effective and allows for the addition of adaptors and multiplex indexes at both ends of each fragment [24]. Finally, the amplified library was purified using SPRI beads, pooled, and sequenced using the NextSeq500 kit (Illumina, United States). Paired-end sequencing was performed with a read structure of 20 bp read one, 50 bp read two, and 8 bp index one as recommended for Seq-Well. The targeted sequencing depth was 100 million reads for all samples.

Processing sequencing reads

The raw data were converted to demultiplexed FastQ files using bcl2fastq (Version 5, Terra Workspace) using the Nextera XT indices and then aligned to the hg19 human genome using STAR aligner (Version 2.7.9) within the Broad Institute DropSeq workflow (Version 11, Terra Workspace). The data was cleaned using Cell Bender (V 0.2.0) with default settings, to remove ambient RNA [25]. The raw expression matrices and sample information were loaded into the open-source statistical software R (R version 4.2.1). An array with 45,691 gene features for 22,819 cells described data collected across 11 samples. The data were filtered to include only features expressed in more than 20 cells, and the resultant matrix described 18,303 gene features across 22,819 cells. A Seurat (Version 4.0) object was created, and the metadata was added to it to identify the participants [26]. Cell cycle scoring was performed and computation of the percentage of mitochondria genes before integration. The object from each participant was transformed individually within the object using SCTransform followed by the selection of integration features, finding the anchors, and finally combined integration. Principal component analysis was performed to reduce the dimensionality of the data to identify clusters of cells with similar transcriptomic profiles. Clusters and cluster resolution were determined using FindNeighbors and a customized FindClusters function that showed that the best resolution was 0.523, with an average silhouette score of: 0.2 and 11 clusters. One cluster showed no cluster-specific genes and was removed as multiplets, leaving 18,176 cells. The remaining clusters were re-clustered and re-embedded, resulting in 10 clusters with a resolution of 0.292, and an average silhouette score of: 0.301. The average number of transcripts and expressed genes were evaluated per cluster using half violin and boxplots. The clusters were projected to a two-dimensional space using the Uniform Manifold Approximation and Projection (UMAP) [27] algorithm in Seurat.

Reference-based mapping

Immune cell subsets were identified using common cell markers to identify the Mono, T cells, B cells, NK cells, DC, and other immune cell populations. Uniform Manifold Approximation and Projection for Dimensional Reduction (UMAP) was used to embed the cell populations and color code based on the expression of surface markers. The clustered PBMC dataset in this study (query) was mapped to a reference CITE-Seq dataset of 162,000 PBMCS measured with 228 antibodies [26]. The query data were projected into the same dimensional space as the reference dataset, thus separating the cells into the cell types present in the reference dataset. The method first projected the reference data transformation onto the query data, followed by the application of KNN-based identification of mutual nearest neighbors (anchors) between the reference and query. On an L2-normalized dimensional space, the reference data transferred continuous data onto the query data to annotate the scRNA data based on a weighted vote classifier. For visualization, reference-based UMAP embedding was used, considering that all the immune cell populations are well represented.

Analyzing differences in samples

Cluster/sample composition was calculated to determine the proportion of cells per cluster and per cell type. Cell subsets that were significantly different between patient and control groups were identified by computing Dirichlet Regression using the DirichReg function in DirichletReg Package in R [28]. Differentially expressed (DE) genes were computed using the FindMarkers function on Seurat (Version 4.0), which we used to determine differentially expressed genes in the patient and control groups using MAST with significance at ($P< 0.05$) and log fold change of > 0.2. Control 4 was not included in the DE analysis due to different levels of cytokine module scores compared to the other control participants (Supplementary Figure S1E). DE genes were visualized using volcano-like plots and heatmaps to compare all the cell types between patients and controls. The fgsea (R-package) was used to analyze the pre-ranked gene set enrichment analysis (GSEA). Module scores for HLA genes, ISG, NFκB target genes, and cytokines were analyzed using the AddModuleScore function in the Seurat R package, and it calculates the normalized average expression of our ISG gene list for each single cell across cell types. Statistical differences in module scores between the patients and control groups for each cell subset were computed using the Wilcoxon sign-rank test with Bonferroni correction. *The difference between groups was considered statistically significant at P-value < 0.05.* Boxplots were used to visualize the module scores for each cell, denoting the median and interquartile range.

Cell-to-cell interaction using CellChat

CellChat (Version 1.1.1) was used to quantitatively infer and analyze cell-to-cell communication networks [21]. Statistically significant intercellular communication between cell groups was identified using permutation tests, and interactions with a significance level of less than 0.05 were considered significant [21]. Heatmaps were used to visualize each signaling pathway and their cell-cell communications, highlighting the number of interactions, the sources (ligands) of the interactions, and the receivers (receptors) of the interactions. The relative contribution of each ligand-receptor pair to the overall signaling was shown in bar plots. The relative contribution provides a measure of a particular ligand-receptor interaction in a particular cell-cell signaling network. This measure demonstrates the importance or significance of the interaction in mediating cell communication between the cell types and potential functional relationships. It is calculated by comparing the expression levels of different cell receptor and ligand genes between the cell types while accounting for all the possible interaction pairs within a signaling network.

Results

Clinical characteristics of study participants

In this study, we defined "controls" as healthy individuals who tested *Plasmodium* positive by rapid diagnostic test (RDT) in the community. We defined "patients" as individuals with uncomplicated malaria who visited the health facility from the same community, tested *Plasmodium* positive by RDT, and were treated on an outpatient basis. All samples were collected from the same region, the Upper East region of Ghana which is a high transmission area. Overall, 224 individuals were surveyed, including 40% (90/224) of the participants who were community healthy controls and 60% (134/224) of the participants who were patients with uncomplicated malaria (Figure 1A; Supplementary Table S1). Although most participants were children between 1 and 15 years, there was no significant difference between the median age of patients compared to the controls (Wilcoxon rank-sum test, $P = 0.74$) (Supplementary Table S1). However, there was a significant difference in the median parasite density of patients compared to the controls (Wilcoxon rank-sum test, $P < 0.001$) (Supplementary Table S1). Further, the study sought to determine if the patients had higher parasite densities than the controls regardless of age. In general, there was a negative correlation between parasite density and age regardless of phenotype up to age 25 years (Figure 1B). Under 3 years, the patients tended to have lower parasite densities, but these were still higher than their control counterparts. After about age 10 parasite densities fell gradually and plateaued around age 25 but with high variability between the groups (Figure 1B). The correlation between parasite density and malaria patients was statistically significant (Pearson $R^2 = -0.38$, $P < 0.001$), but the correlation between parasite density and age was not statistically significant in the control group (Figure 1B).

Profiling pediatric malaria immune-cell populations using single-cell analysis

In order to examine global differences in cellular composition, gene expression, and intercellular communication between the two groups, we matched individuals based on age (aged 4–8 years), sex, and parasite density for both patients and controls and performed single-cell RNA-seq (scRNA-seq) (Figure 1A; Supplementary Table S2). There was no significant difference in median parasite density between patients and controls in the matched individuals (Wilcoxon rank-sum test, $P > 0.71$) (Supplementary Table S2). In total, we generated 18,176 high-quality single-cell profiles across eleven children with *P. falciparum* infections, allowing us to ascertain differences in expression patterns of immune response genes that might influence disease pathogenesis. Each sample was profiled using Seq-Well S^3, a portable, simple massively parallel scRNA-Seq method [24]. The resulting data were filtered to remove cells based on the fractional abundance of mitochondrial genes (<30%) and transcripts expressing in <20 cells. After variable gene selection, dimensionality reduction, clustering, cluster removal, and reclustering (*Methods*), we retained 18,303 transcripts and identified 10 distinct cell subsets in the 18,176 cells, across the two groups of children (Figure 1C; Supplementary Figure S1A).

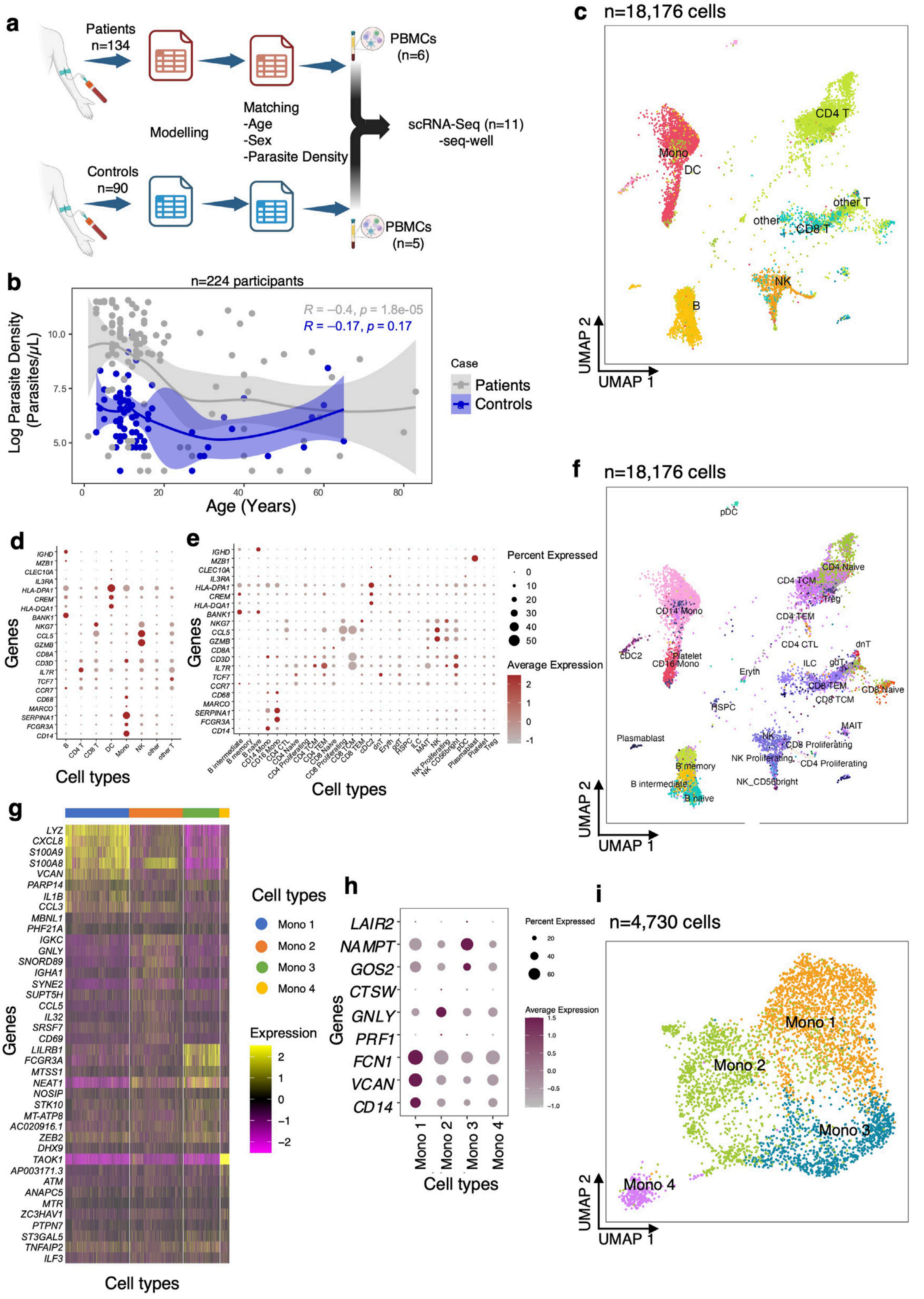

FIGURE 1
Analysis of scRNA-Seq data from uncomplicated malaria patients and community healthy controls. **(A)** Experimental flow showing that PBMCs were collected from eleven individuals out of 224 for scRNA-Sequencing, based on the modeling. **(B)** Regression analysis between parasite density and age for patients (grey) and controls (blue). **(C)** Uniform manifold approximation and projection (UMAP) plot of 22,819 cells from eleven

(Continued)

FIGURE 1 (Continued)
participants colored by identities of 10 cell clusters: mainly B cells, T cells, and Mono. **(D)** Expression levels of cluster-defining marker genes organized by color intensity to show the average expression of the marker in that particular cell type and the proportion of cells with non-zero expression shown by the size of the dot. **(E)** Markers used to annotate the subclusters to various cell subsets showing average expression and fraction of cells expressing the marker. **(F)** Reference mapped dataset showing the predicted subclusters of B, CD4 T, CD8 T, NK, Mono, and DC cell subsets. Reference-defined cell subsets were generated from CITE-seq reference of 162,000 PBMCS measured using 228 antibodies [26]. **(G)** UMAP of re-clustered and re-embedded Mono showing four subclusters of the CD14 and CD16 Mono. **(H)** Markers used to identify monocyte subclusters. **(I)** Mono top 10 highly expressed genes in each subcluster.

We manually annotated these 10 clusters using known RNA marker genes to identify B cells, CD4 T cells, CD8 T cells, natural killer (NK) cells, monocytes (Mono), and dendritic cells (DC) (Supplementary Figures S1B, C). To identify and enumerate cell subsets in our dataset at higher resolution, we opted to map our query dataset to an annotated multimodal reference dataset of PBMCs. First, we confirmed that all the cell subsets identified using manual annotation were present in the resultant UMAP (Supplementary Figure S1D). As expected, our reference mapped dataset recapitulated all PBMC subsets, including B, CD4 T cells, CD8 T cells, NK cells, Mono, and DC (these subsets are used throughout the work; Figures 1C, D). We identified several subclusters, such as intermediate, memory, and naïve B cells; naïve, proliferating, effector memory and central memory CD8 and CD4 T cells; proliferating $CD56^+$ NK cells; $CD14^+$ and $CD16^+$ monocytes (Mono); plasmacytoid (pDC) and conventional (cDC) dendritic cells, and other cell subsets (Figures 1E, F). Since the reference dataset has only annotated two Mono clusters ($CD14^+$ and $CD16^+$), we hypothesized that there might be additional transcriptional heterogeneity describing actively responding Mono subpopulations. Therefore, further sub-clustering was done which resolved the Mono into 3 large subpopulations (Mono 1, Mono 2, Mono 3) and 1 small cluster (Mono 4) (Figures 1G–I) based on previously reported markers [29]. Taken together, these data distinguish nearly all distinct cell subsets that were present in PBMCs of children in both the patients and controls.

Differences in relative cellular composition between the groups

Next, we asked whether there were significant differences in the relative proportions of cell types between the patients and the control group. We found that relative cell proportions of the major cell subsets (B, CD4 T, CD8 T, NK, Mono, and DC) varied between individuals in each group (Figures 2A, B; Supplementary Table S3). The patients exhibited elevated levels of circulating Mono while the controls had higher proportions of circulating B cells (Dirichlet-multinomial regression, $P < 0.01$; Figure 2A; Supplementary Table S3). Further analysis of the B cell subsets showed that the abundance of naïve and intermediate B cells was significantly reduced in the patient group compared to the control group (Dirichlet-multinomial regression, $P < 0.05$; Figure 2B; Supplementary Table S3). We also found a significant expansion of both $CD14^+$ and $CD16^+$ Mono subsets in patients compared to the control group (Dirichlet-multinomial regression, $P < 0.01$; Figure 2B; Supplementary Table S3). Although there is evident variation in cellular proportions of T lymphocytes among all the individuals (Figures 2A, B), we did not observe any significant difference in proportions of either CD4 or CD8 T cells between the groups (Dirichlet-multinomial regression, $P > 0.05$; Figure 2B; Supplementary Table S3). However, the proportions of naïve and central memory CD4 T cells were significantly higher in the patients compared to the control group (Dirichlet-multinomial regression, $P < 0.01$; Figure 2B; Supplementary Table S3). NK cell frequency was also higher in patients suggesting that they may play a role in disease progression (Dirichlet-multinomial regression, $P > 0.05$; Figure 2B; Supplementary Table S3). Among NK cells, the proliferating and $CD56^+$ subsets were higher in patients compared to controls, but these differences were not statistically significant (Dirichlet-multinomial regression, $P > 0.05$; Figure 2B; Supplementary Table S3). Overall, the minor subsets of T cells and other cell types with low frequencies did not show differences in proportions between the groups but the main cell subsets had significant differences in proportions between patients and controls.

Comparative analysis of inflammatory responses in children with malaria

Having identified shifts in the composition of circulating immune cells between the patients and controls, we next asked whether gene expression differed within each immune cell subset between the two groups. Comparing patients to controls, we observed the largest transcriptional changes (measured by pairwise DE across cell types with adjusted P-value < 0.05 and log fold change > 0.2) within B cells and Mono (Figure 2C; Supplementary Table S4). Apart from B cell function genes, there was a general trend toward upregulation of inflammatory genes in B and T cells in patients relative to the control group, including *S100A8, CXCL8,* and *S100A9* (Figure 2C). Significant transcriptional changes were also observed in Mono, with genes such as *IFITM3, FCER1G,* and *CCL4* being upregulated in patients compared to the control group (Figure 2C). Patients were also associated with the upregulation of Major

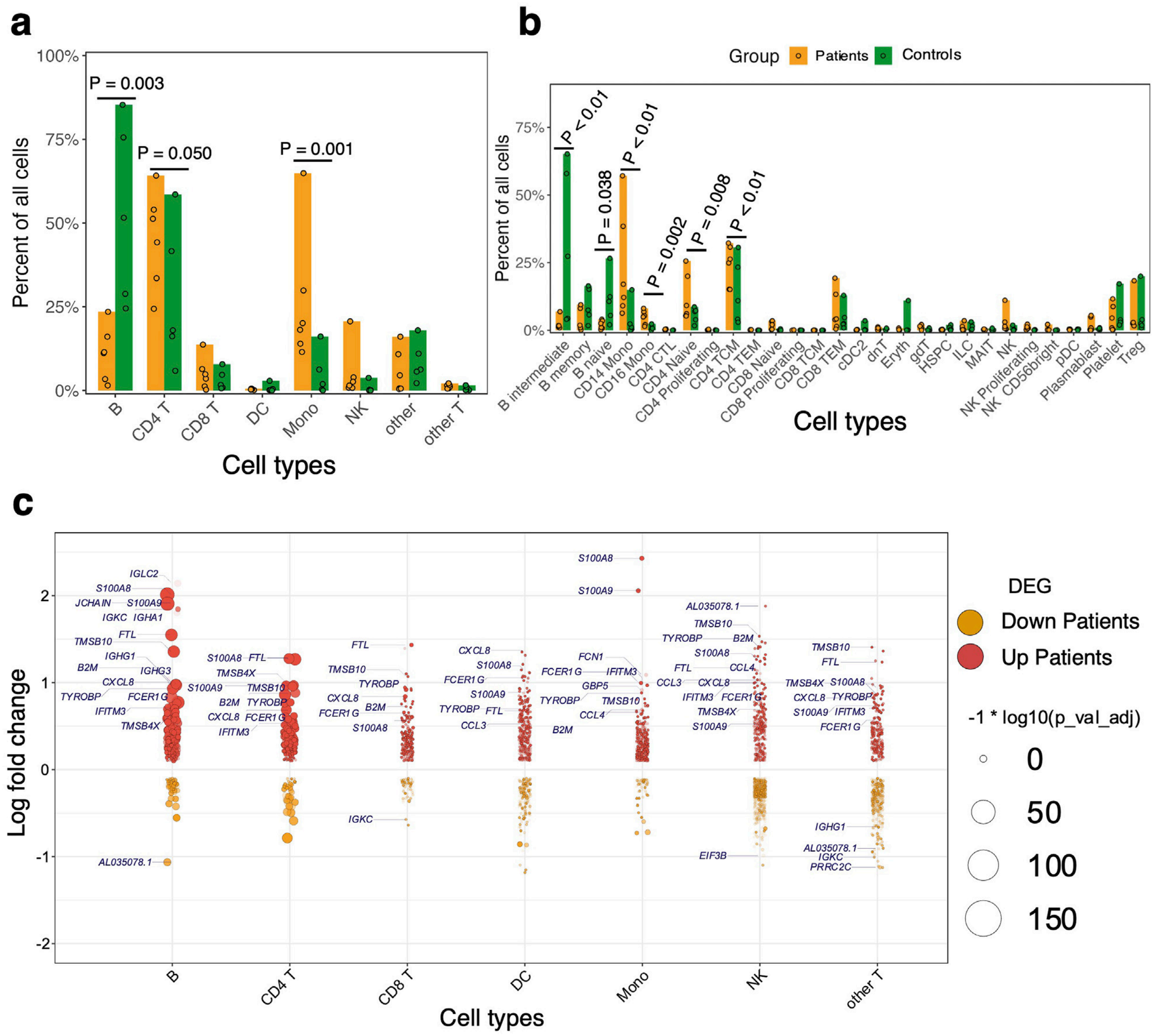

FIGURE 2
Profiling of immune cells from patients compared to the controls. **(A)** Relative cell proportions of the major cell subsets within patients and control groups. Statistical tests were conducted using the Dirichlet Multinomial Regression in the DirichletReg package in R [28]. The dots represent individual proportions while the color scheme represents the patients and control groups. **(B)** Relative proportions of minor cell subsets compared between patients and controls. Cell proportions per group and P-value are shown in Supplementary Table S1. **(C)** Violin-like plots showing genes that are differentially expressed between patients and controls. The x-axis shows the Log_2 fold change against the cell subsets (y-axis) – i.e., B cells, Mono, CD4 T cells, CD8 T cells, other T cells, dendritic cells (DC), and natural killer (NK) cells. The color scheme is based on the upregulated (up patients) and downregulated (down patients) genes in patients and the size of the point represents the adjusted *P*-value. The frequency shows the number of comparisons in which the gene is significantly expressed in the cell subset.

Histocompatibility Complex I (MHC-I) genes such as *HLA-A* and *HLA-C* which are involved in antigen presentation in Mono (Figure 2C). In CD4 and CD8 T cells, there was increased expression of some inflammatory factor signaling genes such as *CXCL8* and *NFKBIA* in patients relative to the control group, suggesting direct sensing of parasite products during clinical presentation (Figure 2C). Using gene set enrichment analyses (GSEA), we found that the patients had robust induction of several innate immune response pathways such as tumor necrosis factor-alpha (TNF-α) signaling via NF-κB, TGF-β signaling, IL6-JAK-STAT pathway, complement, IL2-STAT5 signaling, inflammatory response, interferon-α response (IFN-α), and interferon-γ response (IFN-γ) (Figure 3A; Supplementary Table S5). We observed that although each cell

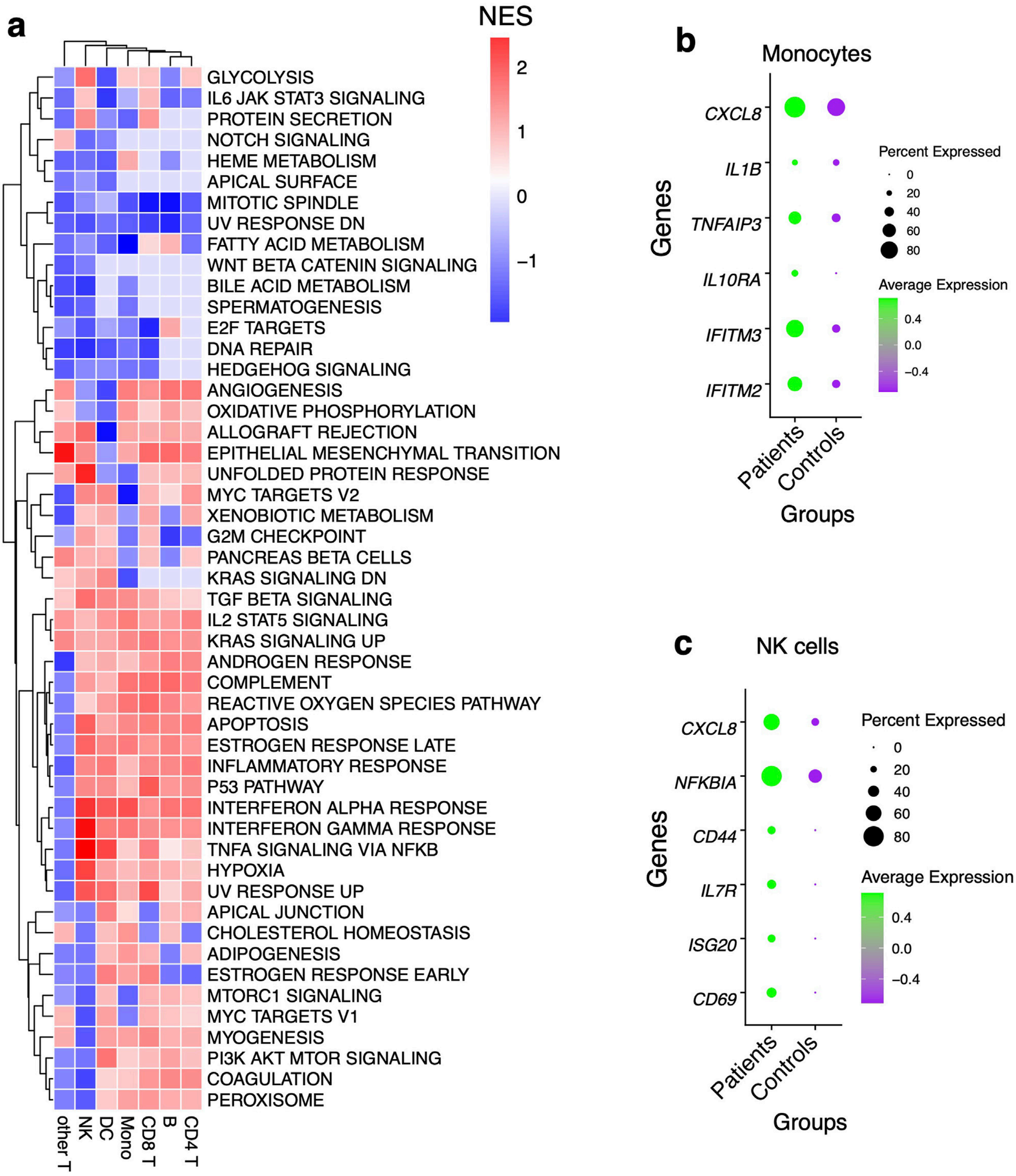

FIGURE 3
Pathway analysis using gene set enrichment method **(A)** Pathway analysis using an immunologic signature gene set enrichment analysis (GSEA) and the color scheme is based on the normalized enrichment score of genes DEG in patients. **(B)** Dot plots showing some of the leading-edge genes in IFN-γ and IFN-α response, TNF-α signaling via NFκB and inflammatory response pathways in Mono and, **(C)** NK cells. Dot size represents the fraction of cell subsets expressing a given gene. The dot color indicates scaled average expression by gene column.

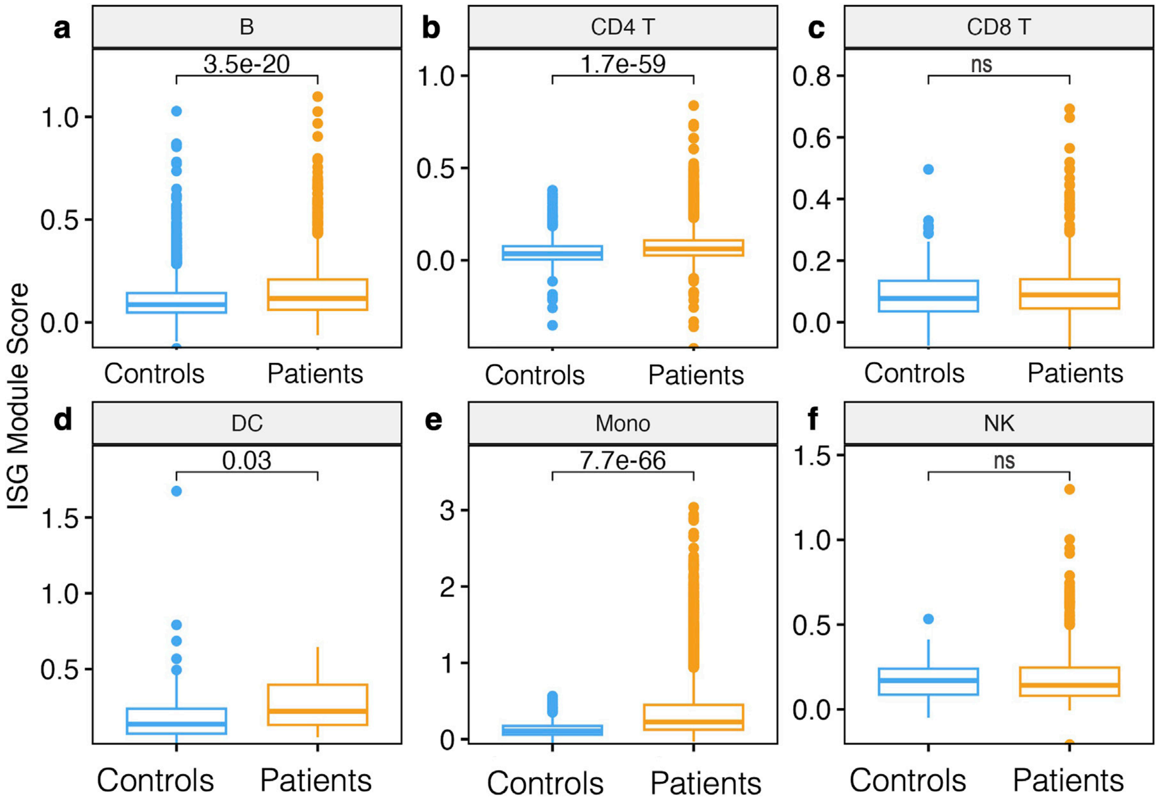

FIGURE 4
Module score analysis of innate immune gene modules. **(A)** Boxplot showing the median and interquartile ranges of interferon-stimulated gene (ISG) module scores per cell subset compared between patients and controls in **(A)** B cells, **(B)** CD4 T cells, **(C)** CD8 T cells, **(D)** DC **(E)** Mono, and **(F)** NK cells. Module scores are computed using the AddModuleScore function in the Seurat R package, which effectively looks at the normalized average expression of our ISG gene list for each single cell across cell types. Statistical significance between the patients and controls of each cell subset was computed using the Wilcoxon sign-rank test with Bonferroni correction (*P-value < 0.05)*. Nonsignificant differences are indicated by ns.

type was enriched in one or more of these pathways, there was a unique molecular signature of the genes involved in each. Upregulation of IFN-γ and IFN-α response pathways in Mono were characterized by increased expression of genes such as *IFITM2*, *IFITM3*, *IL10RA*, and *TNFAIP3*, while in NK cells they were typified by genes such as *NFKBIA*, *CD69*, and *ISG20* (Figures 3B, C; Supplementary Table S5). Mono and natural killer cells upregulated TNF-α signaling via the NF-κB pathway with the induction of genes related to this pathway such as *IL1B* and *TNFAIP3* for Mono, and *IL7R*, *CD44*, and *NFKBIA* for NK cells (Figures 3B, C; Supplementary Table S6). Inflammatory responses in Mono were characterized by *IL10RA, IL1B*, and *CXCL8* while in NK cells they were driven by *CD69*, *IL7R*, *CXCL8*, and *NFKBIA* among others (Figures 3B, C; Supplementary Table S5). Thus, the enrichment of unique genes for each cell subset for similar pathways suggests a specific but concerted contribution of each cell subset toward the innate immune response in patients.

Relative enrichment of ISGs gene modules in monocytes of patients relative to controls

Since IFN genes were significantly upregulated in Mono patients relative to the control group, we next sought to determine if entire gene modules were enriched. Interferon stimulated genes (ISGs) modules scores were significantly higher in B cells, DC, CD4 T cells, and Mono in patients compared to the control group (*Wilcoxon, adjusted P < 0.05 for all comparisons*, Figures 4A, B, D, E); however, there were no significant differences in ISG module scores in CD8 T cells and NK cells (Figures 4C, F). Further examination of intra- and inter-individual variation in these module scores revealed substantial intra-individual variation in cells from the same participant and between cells of the same type from different participants (Supplementary Figure S1E). Overall, our data show that Mono plays a significant role in defining malaria patients compared to control participants from the same community through induction of the ISGs gene modules.

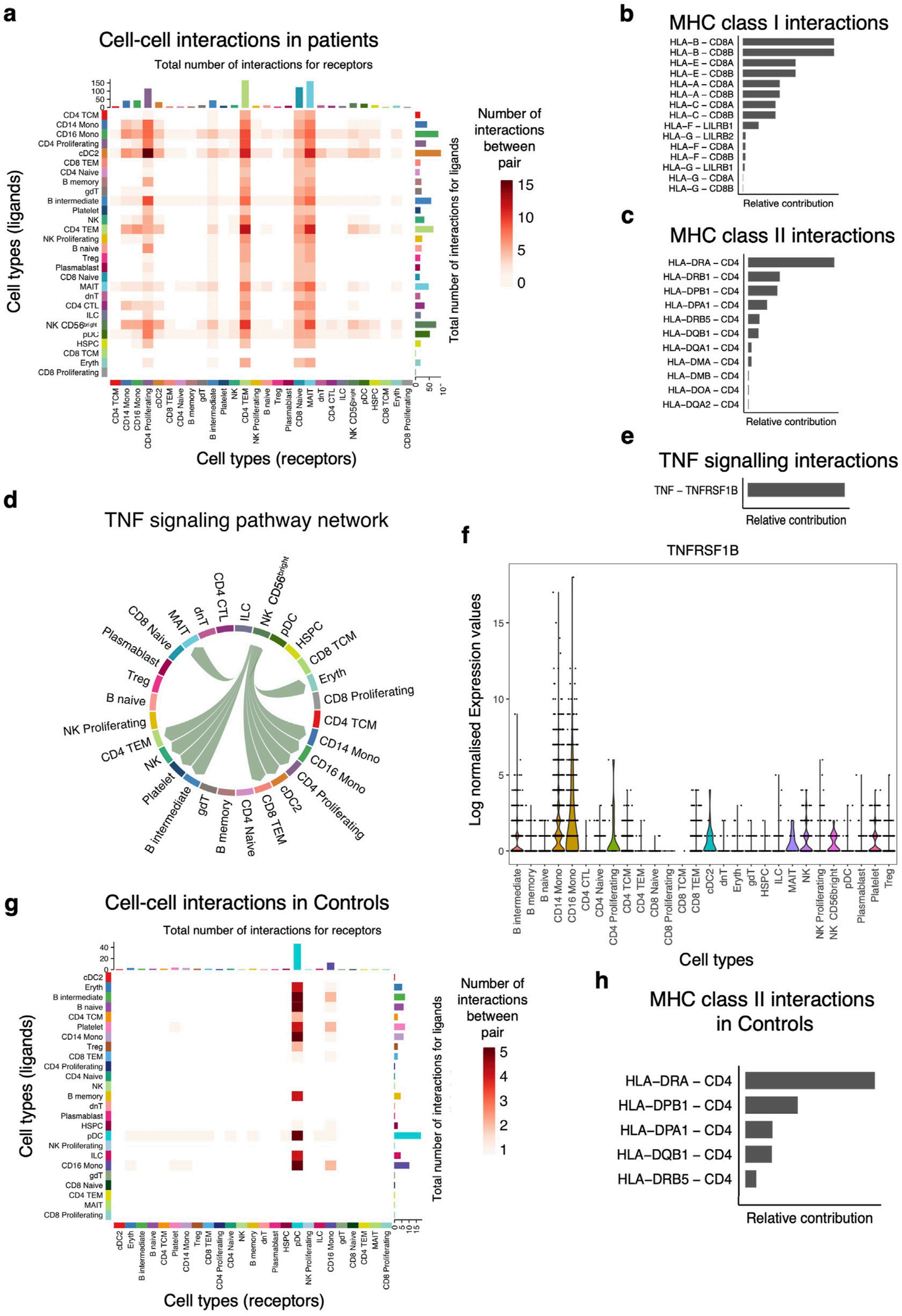

FIGURE 5

Primary innate immune cells dominate the cell-to-cell interactions with other cell subsets. **(A)** Heatmap showing the number of interactions between the PBMCs cell subsets. The y-axis shows the signal senders, and the x-axis shows the signal receivers. **(B)** Relative contribution of ligand-receptor pairs in patients within the MHC class I signaling pathway and **(C)** MHC class II signaling networks, respectively. A higher relative contribution

(Continued)

FIGURE 5 (Continued)
indicates the magnitude of the contribution of the ligand-receptor and its significant role in the MHC I or II signaling networks. **(D)** Cell communications through the TNF signaling pathway and the arrows indicate signal sender to receiver. **(E)** Relative contribution of the TNF-TNFRSF1B ligand-receptor pair towards the TNF signaling pathway. **(F)** Violin plots showing the expression levels of the TNFRSF1B in the Seurat object for the cell subclusters. **(G)** Heatmap comparison showing the overall signaling between all cell subclusters and the number of interactions. **(H)** Relative contribution of MHC class II signaling pathway in the control group.

Role of MHC-I and MHC-II signaling pathways in cell-to-cell interactions

Next, we used our single-cell data to infer putative axes of cell-to-cell communication using signaling ligands, cofactors, and receptors. First, we discerned cell-to-cell interactions in the patients and found that the number of interactions (ligand-receptor) originating from primary innate immune cells such as DC and Mono were greater than those originating from non-antigen presenting cells (Supplementary Table S6). However, our data show very few inferred cellular communication networks in the control group (Supplementary Table S7). This analysis suggests a role for Mono as antigen-presenting cells in orchestrating pro-inflammatory responses by interacting with proliferating CD4 T cells, intermediate B cells, effector memory T cells, and naïve CD8 T cells in the patient group (Figure 5A). Conventional DC also produced factors that interact with proliferating and effector memory CD4 T cells respectively, suggesting a concerted effort by antigen-presenting cells to activate the immune response in patients (Figure 5A). Communication probabilities indicated that MHC-I and MHC-II play a role in these interactions among other pathways. The most significant receptor-ligand pairs for HLA-A, HLA-B, HLA-C, HLA-E, HLA-G, and HLA-F ligands for MHC class I include CD8A, CD8B, LILRB2, and LILRB1 (Figure 5B). The leading intercellular ligand-receptor pairs with CD4 T cells as signal receivers were distinct HLA genes, with the highest relative contribution being driven by HLA-DRA and HLA-DRB1 (Figure 5C). The other minor signaling pathways that were important in patients include MIF, RESISTIN, ANNEXIN, GALECTIN, ADGRE5, APP, CD22, CD45, SELPLG, CD99, CLEC, and TNF signaling networks. For the TNF signaling pathway, the CD56$^+$ NK cells were shown to be interacting with Mono and also with proliferating CD4 T cells, effector memory CD4 and CD8 T cells, and cDC (Figure 5D). This cell communication network was mediated by *TNF* in the sender cells and *TNFRSF1B* in the receiver subsets (Figure 5E), and this corroborates the DE results (Figure 5G). We examined the expression levels of *TNFRSF1B* across all the cell subsets and found that indeed it was expressed in all the receiver cells (Figure 5F). Only the pDC and CD16 Mono showed cell-to-cell interactions with naïve and intermediate B cells and might be playing a role in B cell activation and development in the control group through MHC class II molecules (Figures 5G, H). Therefore, exposure of innate immune cells to parasite ligands may potentially activate intracellular signaling cascades through cell-to-cell interactions to induce rapid expression of a variety of innate immune genes.

Discussion

Here, we recruited 224 participants from Navrongo, a high malaria transmission area with seasonal fluctuations [30]. Interestingly, most of the participants indicated that they use long-lasting insecticide-treated mosquito nets (LLINs), which helps to explain the low frequency of infections; after screening 1,000 individuals in the community, <10% of them were positive for *P. falciparum* as community healthy controls, suggesting a reduction in the malaria infection reservoir. The National Malaria Elimination Program (NMEP) distributes LLINs as part of strategy interventions, including community-based seasonal malaria chemoprevention initiatives for children under 5 years to reduce the malaria burden in this area [30]. The ability of insecticide-treated nets (ITNs) to interrupt malaria transmission has been shown in large-scale studies, which demonstrated that modern housing and ITNs could reduce malaria infections by 1% and 16%, respectively [31]. Further, we investigated the relationship between age and parasite density and found that parasite densities tended to decrease with age, but the levels were generally higher in patients compared to controls in this high transmission intensity area [5]. Immunity to malaria, though partial, depends on exposure levels, or cumulative infection episodes, as a function of transmission intensity among other factors [5, 11]. This relationship naturally results in an association between age and the maturation of the immune response to malaria. Thus, older children have been shown to have fewer occurrences of malarial fevers compared to younger children, demonstrating the impact of immune acquisition through repeated exposures [12]. Thus, an inverse relationship between age and parasite density is expected, because older children can immunologically inhibit, parasite growth and expansion compared to younger children.

To better understand cellular responses driving these divergent clinical phenotypes, we performed scRNA-seq on PBMC samples from eleven of the 224 individuals among the two groups, controlling for group variability driven by age, fever, and parasite density. This enabled us to identify a potential role for interferon responses and TNF-α signaling via NFκB in Mono during the clinical manifestation of pediatric malaria infection. We also found differences in the fractional abundances of PBMC cell subsets, with patients characterized by a proportional increase in Mono while controls had a higher proportion of circulating B cells. We showed cellular level variations in the expression of innate immune modules within and between individuals as well as between clinical phenotypes. Further, we identified a role for Mono and other innate immune cells through MHC-I and MHC-II molecules in driving cell-to-cell interactions with CD8 and CD4 T cells, respectively. Together, our work recontextualizes the function of the innate immune cells in malaria, demonstrates how variable their responses can be, and links specific acute phase response signaling pathways to clinical presentation.

Differential gene expression comparing patients and controls across cell types revealed a significant upregulation of genes associated with innate immunity in different cell types. We show that CCL3 and CCL4 (also known as macrophage inflammatory protein MIP-1α and MIP-1β respectively) were upregulated in Mono of patients, suggesting their possible role in modulating clinical disease [32]. CXCL8, the most potent human neutrophil attracting/activation chemokine [33] was also highly upregulated in B cells, CD4, and CD8 T cells. Other studies have shown that circulating levels of CXCL8 and CCL4 correlated with parasite density, and when found in the cerebrospinal fluid they can predict cerebral malaria mortality [13, 34–36]. Furthermore, the adaptive immune cell subsets (B cells and T cells) in the patient group expressed two alarmins (S100A8 and S100A9) that are known to form calprotein heterodimer, an endogenous TLR4 ligand; this could suggest a possible role in silencing hyperinflammation [37]. We also show significant expression of FCER1G in B cells, Mono, and DC in patients, which is induced by IFN-γ and encodes for a gamma chain of the FC receptor and it is suggested to play an important role in controlling parasitemia [6]. Collectively, our data imply that both adaptive and innate immune cells cooperatively play a role during the pathogenesis of malaria in patients when compared to healthy controls.

We showed that several immune-related pathways are activated by *Plasmodium* infection and disease including the TNF-a signaling via NFκB pathway, IFN-α/γ responses, IL2-STAT5 signaling, and inflammatory response pathway in patients. Since the parasite life cycle involves repeated red cell invasion and rupture, the release of pyrogenic cytokines that drive these pathways such as interleukins, interferons, and TNF in Mono and NK cells, can signify pathophysiological events occurring in malaria patients [13, 38]. These observations could also mean that children who were patients were sampled quite early during the onset of the disease progression trajectory [12]. Our data are consistent with those previously described by integrating whole blood transcriptomics, flow cytometry, and plasma cytokine analysis [6], and our results further identify the cell subsets in which these pathways were more enriched. We show that each of the cell subsets has a unique signature of genes enriched in these immunogenic pathways with minimal sharing. Several studies have shown similar innate immune response pathways in individuals with malaria such as whole blood transcriptomics of the Fulani of West Africa [39], children repeatedly exposed to malaria [6, 11], controlled human malaria infection (CHMI) studies [16], and even mice models [37]. We have now confirmed some of these observations and demonstrated that in the patient state, robust upregulation of certain genes in specific cell subsets is associated with systemic inflammatory responses. Innate immune cells, such as Mono, DC, and NK cells, appear to be most reactive in patients, probably due to continuous exposure in a high transmission area as suggested by other studies [7, 37, 40].

By collating gene modules of interferon-stimulated genes (ISGs), we show that there is a differential expression between patients and controls across different cell subsets. ISGs are normally produced as a function of interferon responses (IFNs) [8], which we observe to be enriched in patients. IFNs are produced primarily by DC to activate ISGs in other cells [41], and we observed that B cells, T cells, Mono, and DC have higher ISG module scores in patients compared to controls. Notably, our data show that each cell or cell subset responds differently upon IFN activation with varying transcriptional responses of an ISG module between individuals. This variability was also observed for cytokine modules, NF-κB target modules, and HLA modules. Similarly, a previous CHMI study observed striking inter-individual variation in immune cell composition and immune responses, demonstrating that an individual can have a unique immune fingerprint [10]. Thus, the variations in immune responses that we observed could be attributed to the complexity of the *P. falciparum* life cycle with several developmental erythrocytic stages, duration of infections, intensity of infection in each individual, genetic factors, genetic variation in immune response genes among other factors [12, 42]. These findings on inter-individual variability in immune responses could provide insights when considering the design and evaluation of interventions that target host immunity in the control of malaria.

Our scRNA-Seq data enabled us to quantitatively infer and analyze cell-to-cell communication networks across all the innate and adaptive immune cells [21]. This analysis enabled us to uncover coordinated interactions between innate and adaptive immune cells through various ligands. The cell-to-cell interactions in patients were driven by MHC class I and II signaling pathways, whereby antigen-presenting cells were shown to have more interactions with proliferating CD4 and naive CD8 T cells. The importance of HLA genes has long been demonstrated by Hill and colleagues who associated HLA-Bw53 antigen and DRB1*1302–DQB1*0501 haplotype to independently protect against severe malaria in West Africa [43]. Thus, our observations on cell-cell interaction involving HLA molecules and T cells support the importance of these molecules during *P. falciparum* infection and disease progression, consistent with the observed varying degrees of interactions in patients compared to control groups. We also showed that within the patient group, there are contrasting interactions between various HLA I and HLA II molecules with CD8 or CD4 T cell receptors, respectively, which could be related to their tight regulation and antigen-presenting ability [44, 45]. Activation of CD4 and CD8 T cells has been correlated with protective immunity to malaria, and they can differentiate into several functionally distinct subsets in the presence of various cytokines [46]. It was not surprising that we identified different fractional abundances of CD4 and CD8 T cell subsets in patients compared to the control group of children, but we demonstrate that ultimately this results in varying degrees of interactions with Mono or DC.

Future work should seek to identify the mechanisms that result in these variations and their impact in orchestrating phagocytic and humoral responses as this critical knowledge gap will be important in developing T cell-based malaria vaccines.

Conclusion

Overall, by using scRNA-seq on PBMCs obtained from patients and controls in a high transmission area, this work sheds light on the interplay between peripheral immune cells during uncomplicated malaria, uncovering the genes and immune pathways in specific cell types that might play a significant role in defining the outcomes of infection. Data presented here demonstrate that the patients with uncomplicated malaria were characterized by the presence of inflammatory response signatures in specific cell types compared to the control group. The results could also suggest that in the control group, a muted innate immune response or disease tolerance mechanism plays a role in enabling children to harbor malaria parasites in high malaria transmission areas without developing uncomplicated malaria [47]. The findings are relevant for guiding the development of malaria vaccines, as it is challenging to develop vaccines that build long lasting immunity, especially in the context of pathophysiologic complexity and mechanisms of immune acquisition through different cell types.

Author contributions

GA, TO, LA-A, YB, and AS contributed to design and conceptualization; CM, LA-A, DA, YA, and NN contributed to sample collection and processing. VM, RD, and CM contributed to performing Seq-Well experiments; CM performed the data analysis and drafted the manuscript. VM, VA, SB, NN, TO, LA-A, and AS contributed to data analysis and drafting of the manuscript. All authors contributed to the article and approved the submitted version.

Data availability

All data generated or analyzed during this study are included in this published article and its Supplementary Material. The scRNA-Seq data are available at https://cellatlas-cxg.mvls.gla.ac.uk/PBMC.Pediatric.Malaria.Ghana/.

Ethics statement

The studies involving humans were approved by Noguchi Memorial Institute of Medical Research, University of Ghana (IRB 0000908) and Ghana Health Service (GHS-ERC 008/02/19). The studies were conducted in accordance with the local legislation and institutional requirements. Written informed consent for participation in this study was provided by the participants' legal guardians/next of kin.

Funding

The author(s) declare that financial support was received for the research, authorship, and/or publication of this article. The study was funded by a DELTAS Africa grant (DEL-15-007: GA). The DELTAS Africa Initiative is an independent funding scheme of the African Academy of Sciences (AAS)'s Alliance for Accelerating Excellence in Science in Africa (AESA) and supported by the New Partnership for Africa's Development Planning and Coordinating Agency (NEPAD Agency) with funding from the Wellcome Trust (107755/Z/15/Z: GA) and the UK government. TO was supported by the Wellcome Trust (104111/Z/14/Z & A). LA-A was supported by the Human Hereditary for Health in Africa (H3Africa), PAMGEN grant (H3AFull/17/008). The study was also supported by the Ragon Institute of MGH, MIT, and Harvard (AS). The funders had no role in the study design and interpretation of the results.

Acknowledgments

We acknowledge the study participants for contributing to the study, and the staff of Navrongo Health Research Centre, who provided support for this study. We are grateful to Felix Ansah, Jersley Chirawurah, Francis Dzabeng, and Jonas Kengne, for their contributions to the data collection and critical review of the work. All data were stored and analyzed on the University of Ghana's high-performance computing system (Zuputo).

Conflict of interest

AS reports compensation for consulting and/or SAB membership from Honeycomb Biotechnologies, Cellarity, Ochre Bio, FL86, Relation Therapeutics, Senda Biosciences, Bio-Rad Laboratories, IntrECate biotherapeutics, and Dahlia Biosciences unrelated to this work.

The remaining author(s) declared no potential conflicts of interest with respect to the research, authorship, and/or publication of this article.

Author disclaimer

The views expressed in this publication are those of the author(s) and not necessarily those of AAS, NEPAD Agency, Wellcome Trust, or the UK government.

Supplementary material

The Supplementary Material for this article can be found online at: https://www.ebm-journal.org/articles/10.3389/ebm.2024.10233/full#supplementary-material

References

1. WHO. *World malaria report 2022*. Geneva: World Health Organisation (2022).

2. Babiker HA, Gadalla AAH, Ranford-Cartwright LC. The role of asymptomatic *P. falciparum* parasitaemia in the evolution of antimalarial drug resistance in areas of seasonal transmission. *Drug Resist Updates* (2013) **16**:1–9. doi:10.1016/j.drup.2013.02.001

3. Bousema T, Okell L, Felger I, Drakeley C. Asymptomatic malaria infections: detectability, transmissibility and public health relevance. *Nat Rev Microbiol* (2014) **12**:833–40. doi:10.1038/nrmicro3364

4. Nyarko PB, Claessens A. Understanding host–pathogen–vector interactions with chronic asymptomatic malaria infections. *Trends Parasitol* (2021) **37**:195–204. doi:10.1016/j.pt.2020.09.017

5. Ademolue TW, Aniweh Y, Kusi KA, Awandare GA. Patterns of inflammatory responses and parasite tolerance vary with malaria transmission intensity. *Malar J* (2017) **16**:145. doi:10.1186/s12936-017-1796-x

6. Tran TM, Guha R, Portugal S, Skinner J, Ongoiba A, Bhardwaj J, et al. A molecular signature in blood reveals a role for p53 in regulating malaria-induced inflammation. *Immunity* (2019) **51**:750–65.e10. doi:10.1016/j.immuni.2019.08.009

7. Boldt ABW, van Tong H, Grobusch MP, Kalmbach Y, Dzeing Ella A, Kombila M, et al. The blood transcriptome of childhood malaria. *EBioMedicine* (2019) **40**: 614–25. doi:10.1016/j.ebiom.2018.12.055

8. Mooney JP, Wassmer SC, Hafalla JC. Type I interferon in malaria: a balancing act. *Trends Parasitol* (2017) **33**:257–60. doi:10.1016/j.pt.2016.12.010

9. Sebina I, Haque A. Effects of type I interferons in malaria. *Immunology* (2018) **155**:176–85. doi:10.1111/imm.12971

10. de Jong SE, van Unen V, Manurung MD, Stam KA, Goeman JJ, Jochems SP, et al. Systems analysis and controlled malaria infection in Europeans and Africans elucidate naturally acquired immunity. *Nat Immunol* (2021) **22**:654–65. doi:10.1038/s41590-021-00911-7

11. Bediako Y, Adams R, Reid AJ, Valletta JJ, Ndungu FM, Sodenkamp J, et al. Repeated clinical malaria episodes are associated with modification of the immune system in children. *BMC Med* (2019) **17**:60. doi:10.1186/s12916-019-1292-y

12. Crompton PD, Moebius J, Portugal S, Waisberg M, Hart G, Garver LS, et al. Malaria immunity in man and mosquito: insights into unsolved mysteries of a deadly infectious disease. *Annu Rev Immunol* (2014) **32**:157–87. doi:10.1146/annurev-immunol-032713-120220

13. Ioannidis LJ, Nie CQ, Hansen DS. The role of chemokines in severe malaria: more than meets the eye. *Parasitology* (2014) **141**:602–13. doi:10.1017/s0031182013001984

14. Kazmin D, Nakaya HI, Lee EK, Johnson MJ, Van Der Most R, Van Den Berg RA, et al. Systems analysis of protective immune responses to RTS,S malaria vaccination in humans. *Proc Natl Acad Sci* (2017) **114**:2425–30. doi:10.1073/pnas.1621489114

15. Milne K, Ivens A, Reid AJ, Lotkowska ME, O'toole A, Sankaranarayanan G, et al. Mapping immune variation and var gene switching in naive hosts infected with plasmodium falciparum. *eLife* (2021) **10**:e62800–31. doi:10.7554/elife.62800

16. Loughland JR, Woodberry T, Field M, Andrew DW, SheelaNair A, Dooley NL, et al. Transcriptional profiling and immunophenotyping show sustained activation of blood monocytes in subpatent Plasmodium falciparum infection. *Clin Translational Immunol* (2020) **9**:e1144. doi:10.1002/cti2.1144

17. Lee HJ, Georgiadou A, Otto TD, Levin M, Coin LJ, Conway DJ, et al. Transcriptomic studies of malaria: a paradigm for investigation of systemic host-pathogen interactions. *Microbiol Mol Biol Rev* (2018) **82**:e00071-17. doi:10.1128/mmbr.00071-17

18. Tran TM, Jones MB, Ongoiba A, Bijker EM, Schats R, Venepally P, et al. Transcriptomic evidence for modulation of host inflammatory responses during febrile *Plasmodium falciparum* malaria. *Scientific Rep* (2016) **6**:31291–12. doi:10.1038/srep31291

19. Ockenhouse CF, Hu WC, Kester KE, Cummings JF, Stewart A, Heppner DG, et al. Common and divergent immune response signaling pathways discovered in peripheral blood mononuclear cell gene expression patterns in presymptomatic and clinically apparent malaria. *Infect Immun* (2006) **74**:5561–73. doi:10.1128/iai.00408-06

20. Hie B, Peters J, Nyquist SK, Shalek AK, Berger B, Bryson BD. Computational methods for single-cell RNA sequencing. *Annu Rev Biomed Data Sci* (2020) **3**: 339–64. doi:10.1146/annurev-biodatasci-012220-100601

21. Jin S, Guerrero-Juarez CF, Zhang L, Chang I, Ramos R, Kuan CH, et al. Inference and analysis of cell-cell communication using CellChat. *Nat Commun* (2021) **12**:1088–20. doi:10.1038/s41467-021-21246-9

22. Hønge BL, Petersen MS, Olesen R, Møller BK, Erikstrup C. Optimizing recovery of frozen human peripheral blood mononuclear cells for flow cytometry. *PLoS ONE* (2017) **12**:e0187440–17. doi:10.1371/journal.pone.0187440

23. Gierahn TM, Wadsworth MH, Hughes TK, Bryson BD, Butler A, Satija R, et al. Seq-Well: portable, low-cost rna sequencing of single cells at high throughput. *Nat Methods* (2017) **14**:395–8. doi:10.1038/nmeth.4179

24. Hughes TK, Wadsworth MH, Gierahn TM, Do T, Weiss D, Andrade PR, et al. Second-strand synthesis-based massively parallel scRNA-seq reveals cellular states and molecular features of human inflammatory skin pathologies. *Immunity* (2020) **53**:878–94.e7. doi:10.1016/j.immuni.2020.09.015

25. Fleming SJ, Marioni JC, Babadi M. CellBender remove-background: a deep generative model for unsupervised removal of background noise from scRNA-seq datasets. *bioRxiv* (2019):791699. doi:10.1101/791699

26. Hao Y, Hao S, Andersen-Nissen E, Mauck WM, Zheng S, Butler A, et al. Integrated analysis of multimodal single-cell data. *Cell* (2021) **184**:3573–87.e29. doi:10.1016/j.cell.2021.04.048

27. McInnes L, Healy J, Melville J. UMAP: Uniform manifold approximation and projection for dimension reduction.

28. Simmons S. Cell type composition analysis: comparison of statistical methods. *bioRxiv* (2022) 2022. 02.04.479123. doi:10.1101/2022.02.04.479123

29. Villani AC, Satija R, Reynolds G, Sarkizova S, Shekhar K, Fletcher J, et al. Single-cell RNA-seq reveals new types of human blood dendritic cells, monocytes, and progenitors. *Science* (2017) **356**:eaah4573. doi:10.1126/science.aah4573

30. Amenga-Etego LN, Asoala V, Agongo G, Jacob C, Goncalves S, Awandare GA, et al. Temporal evolution of sulfadoxine-pyrimethamine resistance genotypes and genetic diversity in response to a decade of increased interventions against Plasmodium falciparum in northern Ghana. *Malar J* (2021) **20**:152. doi:10.1186/s12936-021-03693-3

31. Tusting LS, Bottomley C, Gibson H, Kleinschmidt I, Tatem AJ, Lindsay SW, et al. Housing improvements and malaria risk in Sub-Saharan Africa: a multi-country analysis of survey data. *PLoS Med* (2017) **14**:e1002234. doi:10.1371/journal.pmed.1002234

32. Awandare GA, Goka B, Boeuf P, Tetteh JKA, Kurtzhals JAL, Behr C, et al. Increased levels of inflammatory mediators in children with severe Plasmodium falciparum malaria with respiratory distress. *J Infect Dis* (2006) **194**:1438–46. doi:10.1086/508547

33. Cambier S, Gouwy M, Proost P. The chemokines CXCL8 and CXCL12: molecular and functional properties, role in disease and efforts towards pharmacological intervention. *Cell Mol Immunol* (2023) **20**:217–51. doi:10.1038/s41423-023-00974-6

34. Abrams ET, Brown H, Chensue SW, Turner GDH, Tadesse E, Lema VM, et al. Host response to malaria during pregnancy: placental monocyte recruitment is associated with elevated β chemokine expression. *J Immunol* (2003) **170**:2759–64. doi:10.4049/jimmunol.170.5.2759

35. Armah HB, Wilson NO, Sarfo BY, Powell MD, Bond VC, Anderson W, et al. Cerebrospinal fluid and serum biomarkers of cerebral malaria mortality in Ghanaian children. *Malar J* (2007) **6**:147–17. doi:10.1186/1475-2875-6-147

36. Ayimba E, Hegewald J, Ségbéna AY, Gantin RG, Lechner CJ, Agosssou A, et al. Proinflammatory and regulatory cytokines and chemokines in infants with uncomplicated and severe Plasmodium falciparum malaria. *Clin Exp Immunol* (2011) **166**:218–26. doi:10.1111/j.1365-2249.2011.04474.x

37. Nahrendorf W, Ivens A, Spence PJ. Inducible mechanisms of disease tolerance provide an alternative strategy of acquired immunity to malaria. *eLife* (2021) **10**: e63838. doi:10.7554/eLife.63838

38. Gazzinelli RT, Kalantari P, Fitzgerald KA, Golenbock DT. Innate sensing of malaria parasites. *Nat Rev Immunol* (2014) **14**:744–57. doi:10.1038/nri3742

39. Quin JE, Bujila I, Chérif M, Sanou GS, Qu Y, Vafa Homann M, et al. Major transcriptional changes observed in the Fulani, an ethnic group less susceptible to malaria. *eLife* (2017) **6**:e29156. doi:10.7554/ELIFE.29156

40. Gray JC, Corran PH, Mangia E, Gaunt MW, Li Q, Tetteh KKA, et al. Profiling the antibody immune response against blood stage malaria vaccine candidates. *Clin Chem* (2007) **53**:1244–53. doi:10.1373/clinchem.2006.081695

41. Spaulding E, Fooksman D, Moore JM, Saidi A, Feintuch CM, Reizis B, et al. STING-licensed macrophages prime type I IFN production by plasmacytoid dendritic cells in the bone marrow during severe plasmodium yoelii malaria. *PLoS Pathog* (2016) **12**:e1005975. doi:10.1371/journal.ppat.1005975

42. Awandare GA, Martinson JJ, Were T, Ouma C, Davenport GC, Ong'Echa JM, et al. MIF (Macrophage Migration Inhibitory Factor) promoter polymorphisms and susceptibility to severe malarial anemia. *J Infect Dis* (2009) **200**:629–37. doi:10.1086/600894

43. Hill AVS, Allsopp CEM, Kwiatkowski D, Anstey NM, Twumasi P, Rowe PA, et al. Common West African HLA antigens are associated with protection from severe malaria. *Nature* (1991) **352**:595–600. doi:10.1038/352595a0

44. Guermonprez P, Valladeau J, Zitvogel L, Théry C, Amigorena S. Antigen presentation and T cell stimulation by dendritic cells. *Annu Rev Immunol* (2002) **20**: 621–67. doi:10.1146/annurev.immunol.20.100301.064828

45. Rock KL, Reits E, Neefjes J. Present yourself! By MHC class I and MHC class II molecules. *Trends Immunol* (2016) **37**:724–37. doi:10.1016/j.it.2016.08.010

46. Kurup SP, Butler NS, Harty JT. T cell-mediated immunity to malaria. *Nat Rev Immunol* (2019) **19**:457–71. doi:10.1038/s41577-019-0158-z

47. Nideffer J, Ty M, Donato M, John R, Kajubi R, Ji X, et al. Disease tolerance acquired through repeated plasmodium infection involves epigenetic reprogramming of innate immune cells. *bioRxiv* (2023). 2023.04.19.537546. doi:10.1101/2023.04.19.537546

EBM Experimental Biology and Medicine

TYPE Brief Communication
PUBLISHED 29 January 2025
DOI 10.3389/ebm.2025.10308

*CORRESPONDENCE
Douglas D. Fraser,
✉ douglas.fraser@lhsc.on.ca

RECEIVED 06 July 2024
ACCEPTED 14 January 2025
PUBLISHED 29 January 2025

CITATION
Fraser DD, Roy S, Kuruc M, Quintero M, Van Nynatten LR, Cepinskas G, Zheng H, Soherwardy A and Roy D (2025) Functional mass spectrometry indicates anti-protease and complement activity increase with COVID-19 severity.
Exp. Biol. Med. 250:10308.
doi: 10.3389/ebm.2025.10308

Functional mass spectrometry indicates anti-protease and complement activity increase with COVID-19 severity

Douglas D. Fraser[1,2]*, Swapan Roy[3], Matt Kuruc[3], Maritza Quintero[2], Logan R. Van Nynatten[4], Gediminas Cepinskas[1,5], Haiyan Zheng[6], Amenah Soherwardy[6] and Devjit Roy[7]

[1]London Health Sciences Centre Research Institute, London, ON, Canada, [2]Pediatrics, Western University, London, ON, Canada, [3]Biotech Support Group LLC, Monmouth Junction, NJ, United States, [4]Medicine, Western University, London, ON, Canada, [5]Medical Biophysics, Western University, London, ON, Canada, [6]Rutgers Center for Integrative Proteomics, Rutgers University, Piscataway, NJ, United States, [7]Nathan Littauer Hospital, Gloversville, NY, United States

Abstract

Investigations on some innate immunity proteins can yield misleading information, as investigators often rely on static measurements and assume a direct correlation to function. As protein function is often not directly proportional to protein abundance, and mechanistic pathways are interconnected and under constant feedback regulatory control, functional analysis is required. In this study, we used functional mass spectrometry to measure anti-protease and complement activity in plasma obtained from coronavirus disease 2019 (COVID-19) patients. Our data suggests that within 48 h of hospital admission, COVID-19 patients undergo a protease storm with significantly elevated neutrophil elastase ($p < 0.001$) and lymphocyte granzyme B ($p < 0.01$), while, anti-protease activity is significantly increased, including alpha-1 antitrypsin (AAT; $p < 0.001$) and alpha-1-antichymotrypsin (ACT; $p < 0.001$). Concurrently, the ratio of C3a to C3beta activity significantly decreased with increasing COVID-19 severity, suggesting more complement activation (Mild COVID-19 $p < 0.05$; Severe COVID-19 $p < 0.001$). Activity levels of AAT, ACT and C3a/C3beta remained unchanged over 10 hospital days. Our data suggests that COVID-19 is associated with both a protease storm and complement activation, with the former somewhat balanced with increased anti-protease activity. Evaluation of the AAT/ACT ratio and C3a/C3beta ratio indicated that COVID-19 severity is associated with both neutrophil elastase neutralization and complement activation.

KEYWORDS

COVID-19, functional mass spectrometry, neutrophil elastase, lymphocyte granzyme B, complement

Impact statement

Our work is important as many investigations on innate immunity proteins can yield misleading information, as investigators often rely on static measurements. We used a novel approach which relies on functional mass spectrometry to measure the active site, thereby inferring function. We show that with increasing COVID-19 severity the anti-protease activity is significantly increased and that the ratio of C3a to C3beta activity significantly decreased. Our data is novel in that it shows COVID-19 severity is associated with both neutrophil elastase neutralization, together with complement activation.

Introduction

Coronavirus disease 2019 (COVID-19) is associated with a strong innate immune response [1], mediated by neutrophils, lymphocytes, and the complement system. Severe COVID-19 involves the acute replication of severe acute respiratory syndrome coronavirus 2 (SARS-CoV-2) that results in a strong innate inflammatory response associated with damage to the airways, hyperactivation of the complement system, and multiorgan failure [2–4]. This innate immune response is mediated by monocytes, macrophages and neutrophils and an elevation in serum chemokines.

Neutrophil elastase and granzyme B were previously identified as significantly elevated in severe COVID-19 [5]. Similarly, other studies have shown an upregulation of neutrophil degranulation proteins in SARS-CoV-2 positive nasal swabs [6] and that neutrophil serine proteases are key mediators in the innate and adaptive immune functions of immune cells [7] and inflammatory disease [8]. Dysregulated proteolysis is central to inflammatory disease and examining the anti-protease and complement responses could provide a better understanding of the disease process and aid the development of targeted therapies.

The anti-protease activities of serine protease inhibitors (serpins) have been identified as potential clinical biomarkers of COVID-19 severity [9]. Proteomic methods routinely use immunoassays and ligand binding assays to measure protein abundance, but these methods are designed to quantify total protein levels and not protein activity. Studying serpins poses a proteomic challenge as structural information is required to distinguish between active and inactive forms.

Quantifying protein activity would provide a more accurate measure to investigate the function of these factors in the innate immune response in COVID-19 [10, 11]. Mass spectrometry enables functional proteomics to inform on protein structure and functional status for select proteins. Additionally, mass spectrometry is a powerful proteomics tool because it requires small sample sizes, is quantitative, and is amenable to customizable sample preparation and enrichment techniques.

In this study, we aimed to examine differences in serum levels of neutrophil elastase and granzyme B proteases, and to examine the anti-protease activity of their associated serpins, alpha-1-antitrypsin (ATT) and alpha-1-antichymotrypsin (ACT) as well as complement activation activity of factor 3 (C3) and complement factor 3 a (C3a) in context of COVID-19 severity. We present a functional mass spectrometry approach that allows active protein to be distinguished from total protein for further investigation of these potential COVID-19 biomarkers.

Materials and methods

Study participants and clinical data

Patients were enrolled March-June 2000 after admission to our participating academic hospital, London Health Sciences Centre (London, Ontario). COVID-19 was first suspected based on standard hospital screening procedures, and then confirmed as part of standard hospital testing by detection of two SARS-CoV-2 viral genes using polymerase chain reaction (Dual target assay, specific target unique to SARS-Cov-2 along with a conserved region of the E-gene; Roche cobas® SARS-COV-2 Test). Patient baseline characteristics were recorded on admission and included age, sex, comorbidities, medications, hematologic labs, creatinine, arterial partial pressure to inspired oxygen (P/F) ratio, and chest x-ray findings. We calculated Multiple Organ Dysfunction Score (MODS) [12] and Sequential Organ Failure Assessment (SOFA) [13] score to illustrate their illness severity. We also recorded clinical interventions received during the observation period including use of antibiotics, anti-viral agents, systemic corticosteroids, vasoactive medications, venous thromboembolism (VTE) prophylaxis, anti-platelet or anti-coagulation treatment, renal replacement therapy, high flow oxygen therapy, and mechanical ventilation (invasive and non-invasive). For comparison to critically ill patients, we also included an age- and sex-matched non-critically ill COVID-19 patient cohort who were admitted to the hospital respiratory ward with moderate disease. All COVID-19 patients were non-vaccinated for SARS-CoV-2. Final participant groups contained were constructed by age- and sex-matching patient cohorts with healthy controls without disease, acute illness, or prescription medications (collected prior to the SARS-CoV-2 pandemic). Each of the three groups consisted of 15 participants.

Blood draws

Standard operating procedures were used to ensure all samples were treated rapidly and equally (available at[1]). The first blood sample was obtained within 48 h of hospital admission via indwelling catheters using vacuum serum separator tubes and placed immediately on ice. For ICU patients, additional blood samples were drawn at 4, 7, and 10 days. If venipuncture was required, research blood draws were coordinated with a clinically indicated blood draw. In keeping with accepted research phlebotomy protocols for adult patients, blood draws did not exceed maximal volumes. Once transferred to a negative pressure hood, blood was centrifuged and sera isolated, aliquoted at 250 μL and frozen at −80°C. All samples remained frozen until use and freeze/thaw cycles were avoided.

Protease measurements

The levels of serum neutrophil elastase and granzyme B, were determined using multiplexed biomarker immunoassay kits according to manufacturers' instructions (MilliporeSigma, 400 Summit Drive, Burlington, MA), as we have previously described [5]. Analytes were measured using a Bio-PlexTM 200 Suspension Array system (Bio-Rad Laboratories, Hercules, CA), which used Luminex xMAPTM fluorescent bead-based technology (Luminex Corp, Austin, TX). Bioanalyte concentrations were calculated from standard curves using five-parameter logistic regression in Bio-Plex Manager 6.1 software. Serum concentrations are reported as pg/mL.

Albumin and IgG depletion

A 60 mg aliquot of AlbuSorb™ PLUS beads (Biotech Support Group, Monmouth Junction NJ) was conditioned with 400 μL of Binding buffer (BB1), then the liquid was removed through a spin-filter by centrifugation for 2 min at 1000 × g, and repeated. A 25 μL aliquot of serum was diluted with 250 μL BB1 buffer, and clarified by passing through another spin-filter at 9,000 × g for 1 min. The clarified serum was loaded onto the conditioned AlbuSorb™ PLUS beads and incubated on a rotator at room temperature for 15 min then centrifuged for 4 min at 9,000 × g to collect the filtrate for further processing.

Reduction and digestion

After depletion, an equal volume of serum filtrate (~20 μg) was loaded onto SDS-PAGE as gel plug, and in-gel digested with a standard protocol; proteins in the gel bands were reduced with 10 mM dithiothreitol (DTT) for 30 min at 60°C, alkylated with 20 mM iodoacetamide for 45 min at room temperature in the dark, and digested overnight with 0.4 μg of trypsin (Pierce MS Grade (ThermoFisher) at 37°C. Peptides were extracted twice with 5% formic acid, 60% acetonitrile and dried under vacuum.

Target peptide selection

The target peptides were selected to report specific regions of the protein(s) that infer functionality (Table 1). For Complement C3, activation requires the proteolytic cleavage of the region C3a from the rest of the protein, generating Activated C3b. Two peptides were chosen from sequences of the C3 beta chain region – part of both the intact C3 and the Activated C3b subform (the C3 beta chain signal value was the average of the two peptides). One peptide was chosen from C3a sequence: the region proteolytically cleaved upon C3 Convertase activation [14]. As this method only considers observations at the protein level, less C3a relative to C3 beta would be indicative of proportionately more activated C3b subforms. For both Serpins (AAT and ACT), tryptic peptides which span the Reactive Center Loop (RCL) region were chosen, as these regions represent the proteins' potential function as an inhibitor, any loss of which would negate inhibitory potential [14]. Taken together, the peptides selected from these regions thus can serve as surrogates for reporting functional activity.

LC-MS/MS

0.2 μg of system-independent retention time (iRT) peptides (Biognosys) were added to each digested sample and 1% of the sample was analyzed by LC-MS/MS using a Dionex RSLC nano system coupled to an Orbitrap Eclipse Tribrid mass spectrometer (ThermoFisher). The peptides were loaded onto a fused silica trap column (Acclaim PepMap 100, 75 μm × 2 cm, ThermoFisher). After washing for 5 min at 5 μL/min with 0.1% trifluoroacetic acid (TFA), the trap column was brought in-line with an analytical column (Nanoease MZ peptide BEH C18, 130A, 1.7 μm, 75 μm × 250 mm, Waters) for LC-MS/MS. Peptides were fractionated at 300 nL/min using a segmented linear gradient 4–15% B in 5 min (where A: 0.2% formic acid, and B: 0.16% formic acid, 80% acetonitrile), 15–50% B in 50 min, and 50–90% B in 15 min. Parallel Reaction Monitoring (PRM) method template was used to target selected ions on the target list throughout the run (10–60 min). The target list is shown in Table 1. The isolation width was set at 1.6 Da. Automatic Gain Control (AGC) was set at 2E5 and max ion time set at 150 ms. Ions were fragmented by Higher Energy Collision Dissociation (HCD) using 30% relative collision energy and scanned in the Orbitrap with a resolution of 30,000 m/z. The data was analyzed using Skyline-daily (beta) [15] with a spectral library generated previously. Only peptides with

---

[1] https://translationalresearchcentre.com/

TABLE 1 PRM target peptides for LC-MS/MS.

Protein	Target peptide sequence
Complement C3a region	FISLGEAC [+57]K
Complement C3 beta chain region	FVTVQATFGTQVVEK
Complement C3 beta chain region	IPIEDGSGEVVLSR
Alpha-1-Antitrypsin RCL Spanning Intact Region	GTEAAGAMFLEAIPMSIPPEVK
Alpha-1-Antichymotrypsin RCL Spanning Intact Region	ITLLSALVETR

dotp > 0.8 were accepted. All fragmented ions from the mass spectrum that corresponded to the target peptides, generate an accumulated spectral intensity. Relative spectral intensity data is normalized to the average value of the iRT peptide ions for each individual run. Complement C3 beta was reported as an average value of the two C3 beta peptides.

Population statistics

Medians (IQRs) and frequencies (%) were used to report patient baseline characteristics for continuous and categorical variables, respectively; continuous variables were compared using Mann-Whitney U tests (and Kruskal-Wallis tests, as appropriate), and categorical variables were compared using Fisher's exact chi-square tests. p-values <0.05 (*) were considered statistically significant. All analyses were conducted using GraphPad Prism version 9.2.0 for Windows (GraphPad Software, California, United States) and SPSS version 27 (IBM Corp., Armonk, NY, United States).

Results

Participant demographics and clinical variables

We investigated a total of 45 age- and sex-matched subjects, including 15 severe COVID-19 ICU patients, 15 mild COVID-19 ward patients and 15 healthy subjects. The mean age and sex distribution were similar between groups. Subject demographics and clinical variables are presented in Table 2. COVID-19 patients were likely infected with wild-type SARS-CoV-2 (B.1 strain) given the dates of recruitment and sample collection.

Serine protease measurements

We observed increased levels of neutrophil elastase and granzyme B in patients hospitalized for severe COVID-19. Immunoassay quantification of these proteases in serum indicate that within 48 h of admission, severe COVID-19 patients had significantly higher levels of neutrophil elastase (median 71.8 pg/mL versus 2.8 pg/mL; p > 0.001) (Figure 1A) and granzyme B (median 8.0 pg/mL versus 2.3 pg/mL; p = 0.006) (Figure 1B).

Anti-protease activity

Functional mass spectrometry was used to quantify the level of active serpins AAT and ACT in serum. We observed that within 48 h of hospital admission, anti-protease activity in COVID-19 patient serum is significantly increased. AAT activity was highest in severe COVID-19 patients (median 57.3, p < 0.001; Figure 1C) and ACT activity (median 22.6, p < 0.001; Figure 1D) was significantly higher in mild compared to severe cases. These findings indicate that compared to healthy subjects, AAT may be correlated with COVID-19 disease severity. Interestingly, ACT activity was elevated in mild COVID-19 but decreased in severe COVID-19 serum (median 15.6, p < 0.001). Although ACT is significantly elevated in serum of both the mild and severe COVID-19 population, ACT may be relatively depleted in serum with a greater protease load. Neither AAT nor ACT changed significantly over 10 days of ICU admission (AAT, p = 0.082; ACT p = 0.059).

Complement activation

We observed that serum Complement activation was associated with COVID-19 severity within 48 h of hospital admission, as inversely measured by the C3a/C3beta ratio (median 0.12, p < 0.001) (Figure 2A). The C3a/C3beta ratio did not change significantly over 10 days of ICU admission (p = 0.447; data not shown).

Consequences of anti-protease activity versus complement activation

We compared anti-protease activity ratio (AAT/ACT) to complement activation (C3a/C3 beta) in both mild and severe COVID-19 cases. Our results indicate that milder COVID-19 cases cluster towards the lower right quadrant and associated with low anti-protease activity ratio and low complement activation (Figure 2B).

Discussion

In this study, we investigated two serine proteases, previously identified as elevated in the serum of COVID-19 ICU patients

TABLE 2 Subject demographics and clinical variables.

Clinical variable	Healthy subjects	Mild COVID-19	Severe COVID-19
Age in years, median (IQR)	61 (46–66)	59 (46–68)	60 (47–67)
Sex, female: male	7:8	7:8	7:8
Comorbidities, n (%)			
Diabetes		3 (20.0)	3 (20.0)
Hypertension		6 (40.0)	5 (33.3)
Coronary Artery Disease		0 (0)	0 (0)
Heart Failure		0 (0)	0 (0)
Chronic Kidney Disease		1 (6.6)	0 (0)
Cancer		1 (6.6)	1 (6.6)
COPD		0 (0)	0 (0)
MODS, median (IQR)		-	4.5 (4.0–5.0)
SOFA, median (IQR)		-	6.0 (2.0–7.0)
Presenting Symptoms, n (%)			
Fever		11 (73.3)	-
Cough		12 (80.0)	-
Anosmia/ageusia		3 (20.0)	-
Pharyngitis		3 (20.0)	-
Headache		2 (13.3)	-
Myalgias		9 (60.0)	-
Dyspnea		13 (86.6)	-
Chest Pain		0 (0)	-
Nausea/vomiting/diarrhea		6 (40.0)	-
Laboratory, median (IQR)			
Hemoglobin		137.0 (117.0–142.0)	121.0 (104.0–136.0)
White Blood Cell Count		7.5 (4.7–10.4)	8.2 (6.9–11.5)
Neutrophils		6.6 (3.5–8.4)	7.3 (5.5–9.7)
Lymphocytes		1.0 (0.5–1.2)	0.7 (0.4–1.0)
Platelets		236.0 (187.0–277.0)	210.0 (186.0–210.0)
Creatinine		70.0 (54.0–92.0)	81.0 (56.0–184.0)
INR		1.0 (1.0–1.1)	1.2 (1.1–1.3)
Lactate		1.5 (1.3–2.2)	1.2 (1.0–1.9)
CRP		90.6 (68.1–112.1)	133.9 (71.1–240.5)
D-Dimer		616.0 (441.0–3,367.0)	3,964.0 (1224.0–14725.0)
Albumin		34.0 (31.5–36.5)	30.0 (26.0–32.0)
Pulmonary Abnormalities, n (%)			
Bilateral Infiltrates		14 (93.3)	15 (100)
Unilateral Infiltrates		0 (0)	0 (0)
Normal		1 (6.6)	0 (0)
P/F Ratio, median (IQR)		-	93.0 (66.0–131.0)
Interventions, n (%)			
Antibiotics		14 (93.3)	15 (100)
Steroids		15 (100)	10 (66.6)
Remdesivir		4 (26.6)	0 (0)
Tocilizumab		1 (6.6)	0 (0)
Vasoactive medications		2 (13.3)	14 (93.3)
High Flow Nasal Cannula		7 (46.6)	10 (66.6)
Non-invasive MV		1 (6.6)	4 (26.6)
Invasive MV		2 (13.3)	14 (93.3)
Renal Replacement Therapy		0 (0)	3 (20.0)
ICU Days, median (IQR)		-	17.0 (10.0–26.0)
Hospital Days, median (IQR)		8.0 (6.0–16.0)	-
Outcome, n (%)			
Alive		15 (100)	8 (53.3)
Dead		0 (0)	7 (46.6)

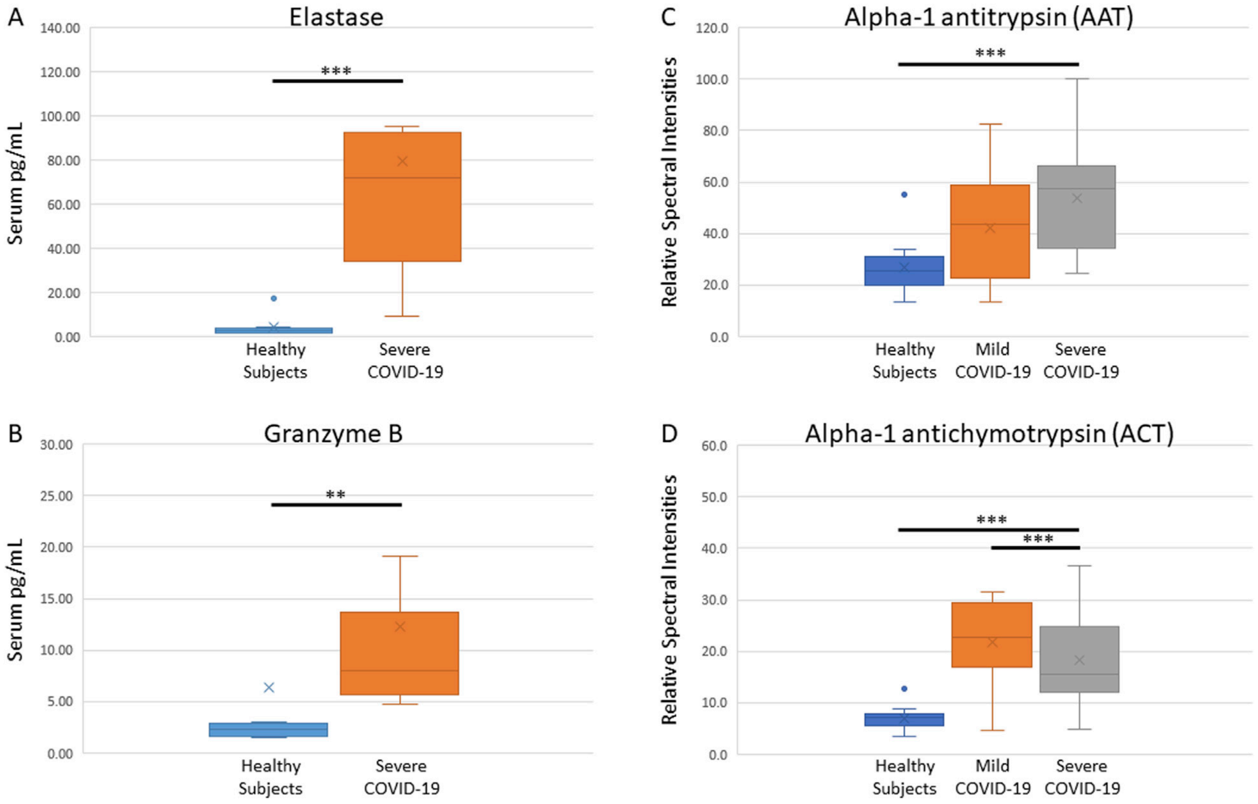

FIGURE 1
Measurements of serine proteases and functional analyses of their anti-proteases. Immunoassays show elevated levels of neutrophil elastase **(A)** and granzyme B **(B)**, and functional proteomic analysis indicate high activity of AAT **(C)** and ACT **(D)** anti-proteases, in serum of COVID-19 infected patients within 48 h of hospital admission.

[5], to assess their functional activity using mass spectrometry. We compared healthy controls to COVID-19 patients with mild or severe disease. Our results showed increased anti-protease activity with disease severity and decreased complement activity in COVID-19 patients.

Participants were classified as mild or severe based on PCR results and symptom severity, all infected with wild-type SARS-CoV-2. Blood samples were collected within 48 h of hospital admission. While all mild patients survived, 47% of severe patients died. Healthy controls were obtained prior to the pandemic.

Immunoassays showed significantly higher levels of neutrophil elastase and granzyme B in severe COVID-19 patients within 48 h of admission, compared to healthy controls. These proteases are crucial for immune regulation, but excessive activity can cause tissue damage, cytotoxicity, and inflammation [7, 16]. Protease-induced degradation of the extracellular matrix also damages blood vessels, increasing vascular permeability and causing hypotension, often necessitating vasoactive support. The elevated neutrophil elastase seen in COVID-19 may contribute to NETosis, where neutrophils release extracellular traps, further driving inflammation and tissue damage [17].

AAT is the primary inhibitor of neutrophil elastase, a serine protease released by neutrophils, monocytes, macrophages, and mast cells during immune responses to kill pathogens [18]. Neutrophil elastase activates receptors to increase chemokines and proinflammatory cytokines, promoting leukocyte recruitment [19, 20]. Elevated elastase contributes to cell death, inflammation, pulmonary vascular permeability, and injury [21] and is linked to conditions like chronic obstructive pulmonary disease [22], acute lung injury [23], and acute respiratory distress syndrome [24]. The D614G mutation in the SARS-CoV-2 spike protein created a cleavage site for elastase, enhancing viral spread, particularly in AAT-deficient individuals [25].

Granzyme B, a serine protease in cytotoxic T and natural killer cells, shares structural similarities with chymotrypsin and may be inhibited by AAT [16]. These cells release granzyme B via exocytosis to induce rapid cell death in infected cells [26]. Granzyme B can also function extracellularly, promoting proinflammatory cytokine responses and tissue remodeling

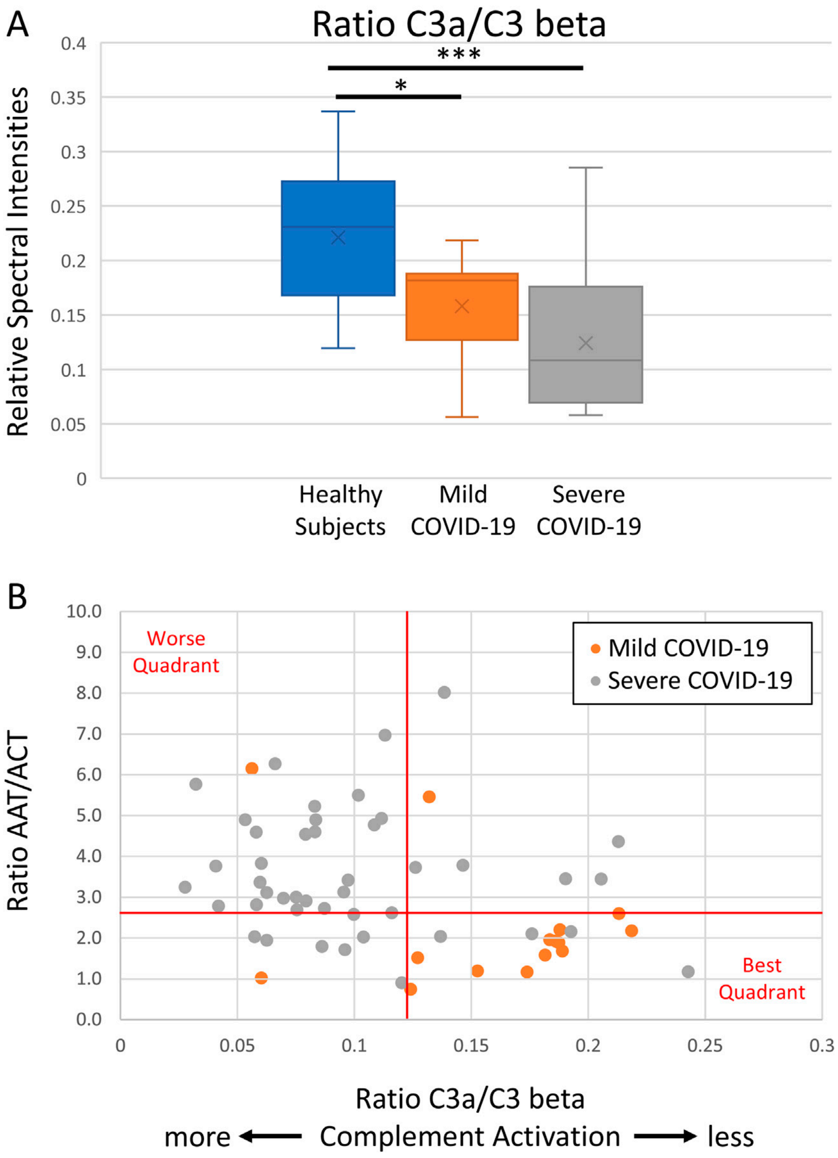

FIGURE 2
Functional analyses of complement activity and its role in COVID-19 severity. Functional proteomic analysis of serum complement activity indicates a decrease in C3a/C3 beta ratio **(A)**, which is a metric of relative C3 activation, and a comparison of anti-protease activity to complement activation indicates milder COVID-19 cases cluster toward low anti-protease activity ratio (AAT/ACT; the ratio of the RCL tryptic peptides) and less complement activation (C3a/C3 beta) **(B)**. The graphical line thresholds were chosen arbitrarily as an indicator for quadrant stratification. Severe COVID-19 data points were calculated from all ICU days.

that can lead to tissue destruction [27–30]. As a pro-apoptotic factor, granzyme B activates cytokines like Interleukin-18, which amplifies the innate immune response [31].

To evaluate the therapeutic potential of granzyme B and neutrophil elastase, we assessed their anti-protease and complement activity in COVID-19 severity using functional mass spectrometry. Serpin inhibition involves a 1:1 complex formation that irreversibly inactivates both the serpin and protease [32, 33]. The RCL of the serpin targets specific proteases, mimicking their substrate sequence, leading to cleavage, a conformational change, and the permanent deactivation of both proteins [34].

Immunoassays cannot differentiate between active and inactivated serpins, but functional mass spectrometry can detect peptide sequences and assess the state of the RCL region [35]. This study identified distinct peptide sequences in the RCL regions of AAT and ACT, associated with elastase and granzyme B, respectively. Intact peptide sequences in the RCL represent active anti-protease activity. Protein depletion beads were used to remove albumin and IgG from serum, enriching lower-abundance proteins for proteomic analysis.

Our results show that AAT significantly increases within 48 h of hospital admission in COVID-19 patients, correlating with disease severity and elevated neutrophil elastase levels. This aligns with previous studies showing increased serpins, including AAT, in COVID-19 sera, particularly in patients with high Interleukin-6 levels [36], and evidence suggesting that AAT deficiency increases the risk of severe COVID-19 [37].

The anti-protease and anti-inflammatory activity of AAT [38] may help mitigate COVID-19 and the hyperactive immune response. AAT inhibits SARS-CoV-2 entry by inactivating TMPRSS2, a serine protease that primes the spike protein for cell surface fusion [39]. AAT also protects against cytotoxicity by inhibiting inflammatory proteases, particularly neutrophil elastase [36]. Our results show that within 48 h of hospital admission, ACT activity increased with COVID-19 infection, peaking in mild cases. In severe COVID-19, ACT activity decreased, likely due to higher granzyme B and other proteases, leading to greater proteolysis that may inactivate ACT and compromise its regulatory function.

ACT is a serpin that inhibits chymotrypsin-like proteases, including neutrophil cathepsin G and mast cell chymases [40, 41]. Its concentration increases during acute inflammation and may protect tissues, such as the lower respiratory tract and brain, from proteolytic damage [42]. In cell culture, ACT-cathepsin G complexes signal acute phase protein synthesis and increase interleukin-6 production by fibroblasts [43]. Since ACT irreversibly forms complexes with cathepsin G, further research is needed to determine whether ACT activity protects against or contributes to severe COVID-19.

ACT is also a substrate for neutrophil elastase and other proteases [44]. In these cases, the protease cleaves ACT without forming an irreversible complex, rendering ACT inactive. Cleaved ACT products become potent chemoattractants at nanomolar concentrations [45], with slower serum clearance than ACT-cathepsin G complexes, suggesting prolonged neutrophil chemotaxis and potential interleukin-6 (IL-6) stimulation. Elevated IL-6 is linked to acute COVID-19 symptoms, including complement cascade upregulation, and current COVID-19 treatment regimens include the use of the IL-6 specific monoclonal antibody Tocilizumab [36].

C3a, a small complement fragment, is an anaphylatoxin that regulates inflammation with both pro- and anti-inflammatory effects [46]. It triggers chemokine release through mast cell degranulation and increased vascular permeability, but also helps regulate B-cell immune responses. C3 cleavage to form C3a is a key step in all complement pathways, necessary for C3 convertase to generate the membrane attack complex (C5b-9), which induces cell lysis and death. At sublytic levels, C5b-9 regulates tissue homeostasis by influencing cell cycle, proliferation, and differentiation [47]. C3 can also be cleaved by various serine proteases, including thrombin and cathepsin, at sites of inflammation [48]. As an anaphylatoxin, C3a increases vascular permeability and causes vasodilation, which can result in hypotension. The latter requires vasoactive support.

Multiple studies suggest that complement activation plays a key role in COVID-19 pathology [49], with C3 split products (e.g., C3a) often monitored by immunoassay [50, 51]. Using functional mass spectrometry, we distinguished cleaved C3b sequences from unprocessed C3 and examined the C3a/C3 beta; ratio as a relative metric for C3b activation, with lower ratios indicating greater activation. A limitation of this method is the use of a small 9-amino acid C3a peptide (FISLGEACK) compared to the full 77-amino acid C3a. Future studies are needed to confirm whether this peptide is sufficient for monitoring C3 subforms and to compare results with immunoassay measurements.

Our findings align with previous studies, showing an inverse relationship between the C3a/C3 beta ratio and COVID-19 severity. This suggests that anti-complement therapy may benefit severe COVID-19 patients. The mass spectrometry approach allows for efficient examination of functional characteristics, such as post-translational modifications and genetic variations, which are challenging for immunoassays. By comparing anti-protease activity (AAT/ACT ratio) to complement activation (C3a/C3 beta ratio), mild COVID-19 cases clustered in the lower right quadrant, indicating low anti-protease activity and minimal complement activation. These clusters may provide insights into disease severity and help predict disease progression and optimal interventions.

The COVID-19 pandemic and long COVID highlight the need for therapeutics that target viral infection and modulate immune responses. Serine proteases and serpins are promising drug targets for immunomodulation [52]. Future studies on the balance between protease and anti-protease activities, particularly AAT/ACT ratios, may reveal insights into enzyme regulation, complement activation, and clinical outcomes. The AAT/ACT ratio could serve as both a biomarker for COVID-19 severity and a potential therapeutic target.

Author contributions

Conceptualization, DF and MK; methodology, DF, SR, MK, LV, GC, HZ, AS, and DR; formal analysis, DF and MK; resources, DF; original draft preparation, DF, MK, and MQ; review and editing, SR, LV, GC, HZ, AS, and DR; funding acquisition, DF. All authors contributed to the article and approved the submitted version.

Data availability

The raw data supporting the conclusions of this article will be made available by the authors, without undue reservation.

Ethics statement

The studies involving humans were approved by Western University, Human Research Ethics Board. The studies were conducted in accordance with the local legislation and institutional requirements. Written informed consent for participation in this study was provided by the ' legal guardians/next of kin.

Funding

The author(s) declare that financial support was received for the research, authorship, and/or publication of this article. DF acknowledges funding from the London Health Sciences Foundation (https://lhsf.ca/) and the AMOSO Innovation Fund (INN20-029).

Acknowledgments

We thank the enthusiastic support of the frontline Nursing Staff and Research Assistants at London Health Sciences Centre.

Conflict of interest

Some authors (SR and MK) are employees of Biotech Support Group LLC, who provide proteomic and genomic sample prep and enrichment products and services.

The remaining authors declared no potential conflicts of interest with respect to the research, authorship, and/or publication of this article.

References

1. Diamond MS, Kanneganti T-D. Innate immunity: the first line of defense against SARS-CoV-2. *Nat Immunol* (2022) **23**(2):165–76. doi:10.1038/s41590-021-01091-0

2. Peiris JS, Chu C, Cheng V, Chan K, Hung I, Poon L, et al. Clinical progression and viral load in a community outbreak of coronavirus-associated SARS pneumonia: a prospective study. *The Lancet* (2003) **361**(9371):1767–72. doi:10.1016/s0140-6736(03)13412-5

3. Wong RSM. Haematological manifestations in patients with severe acute respiratory syndrome: retrospective analysis. *BMJ* (2003) **326**(7403):1358–62. doi:10.1136/bmj.326.7403.1358

4. Java A, Apicelli AJ, Liszewski MK, Coler-Reilly A, Atkinson JP, Kim AH, et al. The complement system in COVID-19: friend and foe? *JCI Insight* (2020) **5**(15): e140711. doi:10.1172/jci.insight.140711

5. Fraser DD, Cepinskas G, Slessarev M, Martin C, Daley M, Miller MR, et al. Inflammation profiling of critically ill coronavirus disease 2019 patients. *Crit Care Explorations* (2020) **2**(6):e0144. doi:10.1097/cce.0000000000000144

6. Akgun E, Tuzuner MB, Sahin B, Kilercik M, Kulah C, Cakiroglu HN, et al. Proteins associated with neutrophil degranulation are upregulated in nasopharyngeal swabs from SARS-CoV-2 patients. *PLOS ONE* (2020) **15**(10): e0240012. doi:10.1371/journal.pone.0240012

7. Meyer-Hoffert U, Wiedow O. Neutrophil serine proteases: mediators of innate immune responses. *Curr Opin Hematol* (2011) **18**(1):19–24. doi:10.1097/moh.0b013e32834115d1

8. Mantovani A, Cassatella MA, Costantini C, Jaillon S. Neutrophils in the activation and regulation of innate and adaptive immunity. *Nat Rev Immunol* (2011) **11**(8):519–31. doi:10.1038/nri3024

9. Medjeral-Thomas NR, Troldborg A, Hansen AG, Pihl R, Clarke CL, Peters JE, et al. Protease inhibitor plasma concentrations associate with COVID-19 infection. *Oxford Open Immunol* (2021) **2**(1):iqab014. doi:10.1093/oxfimm/iqab014

10. Mansouri V, Rezaiee Tavirani M, Okhovatian F, Allah Abbaszadeh H. Introducing markers which are involved in COVID-19 disease: severe condition versus mild state, a network analysis. *J Cell and Mol Anesth* (2022) **7**(2):109–15. doi:10.22037/jcma.v6i4.35656

11. Suvarna K, Biswas D, Pai MGJ, Acharjee A, Bankar R, Palanivel V, et al. Proteomics and machine learning approaches reveal a set of prognostic markers for COVID-19 severity with drug repurposing potential. *Front Physiol* (2021) **12**: 652799. doi:10.3389/fphys.2021.652799

12. Priestap F, Kao R, Martin CM. External validation of a prognostic model for intensive care unit mortality: a retrospective study using the ontario critical care information system. *Can J Anesthesia/Journal canadien d'anesthésie* (2020) **67**(8): 981–91. doi:10.1007/s12630-020-01686-5

13. Singer M, Deutschman CS, Seymour CW, Shankar-Hari M, Annane D, Bauer M, et al. The third international consensus definitions for sepsis and septic shock (Sepsis-3). *JAMA* (2016) **315**(8):801–10. doi:10.1001/jama.2016.0287

14. Zahn-Zabal M, Michel PA, Gateau A, Nikitin F, Schaeffer M, Audot E, et al. The neXtProt knowledgebase in 2020: data, tools and usability improvements. *Nucleic Acids Res* (2020) **48**(D1):D328–D334. doi:10.1093/nar/gkz995

15. Pino LK, Searle BC, Bollinger JG, Nunn B, MacLean B, MacCoss MJ. The skyline ecosystem: informatics for quantitative mass spectrometry proteomics. *Mass Spectrom Rev* (2020) **39**(3):229–44. doi:10.1002/mas.21540

16. Wowk ME, Trapani JA. Cytotoxic activity of the lymphocyte toxin granzyme B. *Microbes Infect* (2004) **6**(8):752–8. doi:10.1016/j.micinf.2004.03.008

17. Al-Kuraishy HM, Al-Gareeb AI, Al-hussaniy HA, Al-Harcan NAH, Alexiou A, Batiha GES. Neutrophil extracellular traps (NETs) and Covid-19: a new frontiers for therapeutic modality. *Int Immunopharmacology* (2022) **104**:108516. doi:10.1016/j.intimp.2021.108516

18. Korkmaz B, Horwitz MS, Jenne DE, Gauthier F, Sibley D. Neutrophil elastase, proteinase 3, and cathepsin G as therapeutic targets in human diseases. *Pharmacol Rev* (2010) **62**(4):726–59. doi:10.1124/pr.110.002733

19. Pham CT. Neutrophil serine proteases: specific regulators of inflammation. *Nat Rev Immunol* (2006) **6**(7):541–50. doi:10.1038/nri1841

20. Pham CT. Neutrophil serine proteases fine-tune the inflammatory response. *The Int J Biochem & Cell Biol* (2008) **40**(6-7):1317–33. doi:10.1016/j.biocel.2007.11.008

21. Voisin MB, Leoni G, Woodfin A, Loumagne L, Patel NS, Di Paola R, et al. Neutrophil elastase plays a non-redundant role in remodeling the venular basement membrane and neutrophil diapedesis post-ischemia/reperfusion injury. *The J Pathol* (2019) **248**(1):88–102. doi:10.1002/path.5234

22. Owen C. Roles for proteinases in the pathogenesis of chronic obstructive pulmonary disease. *Int J Chronic Obstructive Pulm Dis* (2008) **3**:253–68. doi:10.2147/copd.s2089

23. Lee WL, Downey GP. Leukocyte elastase: physiological functions and role in acute lung injury. *Am J Respir Crit Care Med* (2001) **164**(5):896–904. doi:10.1164/ajrccm.164.5.2103040

24. Moraes TJ, Chow CW, Downey GP. Proteases and lung injury. *Crit Care Med* (2003) **31**(4 Suppl. l):S189–94. doi:10.1097/01.ccm.0000057842.90746.1e

25. Bhattacharyya C, Das C, Ghosh A, Singh AK, Mukherjee S, Majumder PP, et al. SARS-CoV-2 mutation 614G creates an elastase cleavage site enhancing its spread in high AAT-deficient regions. *Infect Genet Evol* (2021) **90**:104760. doi:10.1016/j.meegid.2021.104760

26. Cullen SP, Martin SJ. Mechanisms of granule-dependent killing. *Cell Death & Differ* (2008) **15**(2):251–62. doi:10.1038/sj.cdd.4402244

27. Buzza MS, Zamurs L, Sun J, Bird CH, Smith AI, Trapani JA, et al. Extracellular matrix remodeling by human granzyme B via cleavage of vitronectin, fibronectin, and laminin. *J Biol Chem* (2005) **280**(25):23549–58. doi:10.1074/jbc.m412001200

28. Isaaz S, Baetz K, Olsen K, Podack E, Griffiths GM. Serial killing by cytotoxic T lymphocytes: T cell receptor triggers degranulation, re-filling of the lytic granules

and secretion of lytic proteins via a non-granule pathway. *Eur J Immunol* (1995) **25**(4):1071–9. doi:10.1002/eji.1830250432

29. Spaeny-Dekking EH, Hanna WL, Wolbink AM, Wever PC, Kummer AJ, Swaak AJG, et al. Extracellular granzymes A and B in humans: detection of native species during CTL responses *in vitro* and *in vivo*. *The J Immunol* (1998) **160**(7): 3610–6. doi:10.4049/jimmunol.160.7.3610

30. Wensink AC, Hack CE, Bovenschen N. Granzymes regulate proinflammatory cytokine responses. *The J Immunol* (2015) **194**(2):491–7. doi:10.4049/jimmunol.1401214

31. Akeda T, Yamanaka K, Tsuda K, Omoto Y, Gabazza EC, Mizutani H. CD8+ T cell granzyme B activates keratinocyte endogenous IL-18. *Arch Dermatol Res* (2014) **306**(2):125–30. doi:10.1007/s00403-013-1382-1

32. Huntington JA, Carrell RW. The serpins: nature's molecular mousetraps. *Sci Prog* (2001) **84**(Pt 2):125–36. doi:10.3184/003685001783239032

33. Khan MS, Singh P, Azhar A, Naseem A, Rashid Q, Kabir MA, et al. Serpin inhibition mechanism: a delicate balance between native metastable state and polymerization. *J Amino Acids* (2011) **2011**:1–10. doi:10.4061/2011/606797

34. Marijanovic EM, Fodor J, Riley BT, Porebski BT, Costa MGS, Kass I, et al. Reactive centre loop dynamics and serpin specificity. *Scientific Rep* (2019) **9**(1): 3870. doi:10.1038/s41598-019-40432-w

35. Tsutsui Y, Sarkar A, Wintrode PL. Probing serpin conformational change using mass spectrometry and related methods. *Methods Enzymol* (2011) **501**: 325–50. doi:10.1016/b978-0-12-385950-1.00015-8

36. D'Alessandro A, Thomas T, Dzieciatkowska M, Hill RC, Francis RO, Hudson KE, et al. Serum proteomics in COVID-19 patients: altered coagulation and complement status as a function of IL-6 level. *J Proteome Res* (2020) **19**(11): 4417–27. doi:10.1021/acs.jproteome.0c00365

37. Bai X, Schountz T, Buckle AM, Talbert JL, Sandhaus RA, Chan ED. Alpha-1-antitrypsin antagonizes COVID-19: a review of the epidemiology, molecular mechanisms, and clinical evidence. *Biochem Soc Trans* (2023) **51**(3):1361–75. doi:10.1042/bst20230078

38. Brantly ML, Paul LD, Miller BH, Falk RT, Wu M, Crystal RG. Clinical features and history of the destructive lung disease associated with alpha-1-antitrypsin deficiency of adults with pulmonary symptoms. *Am Rev Respir Dis* (1988) **138**(2): 327–36. doi:10.1164/ajrccm/138.2.327

39. Wettstein L, Weil T, Conzelmann C, Müller JA, Groß R, Hirschenberger M, et al. Alpha-1 antitrypsin inhibits TMPRSS2 protease activity and SARS-CoV-2 infection. *Nat Commun* (2021) **12**(1):1726. doi:10.1038/s41467-021-21972-0

40. Korkmaz B, Attucci S, Jourdan ML, Juliano L, Gauthier F. Inhibition of neutrophil elastase by α1-protease inhibitor at the surface of human polymorphonuclear neutrophils. *The J Immunol* (2005) **175**(5):3329–38. doi:10.4049/jimmunol.175.5.3329

41. Kalsheker NA. α1-antichymotrypsin. *The Int J Biochem & Cell Biol* (1996) **28**(9):961–4. doi:10.1016/1357-2725(96)00032-5

42. Calvin J, Price CP. Measurement of serum α_1-antichymotrypsin by immunoturbidimetry. *Ann Clin Biochem* (1986) **23**(Pt 2):206–9. doi:10.1177/000456328602300212

43. Kurdowska A, Travis J. Acute phase protein stimulation by alpha 1-antichymotrypsin-cathepsin G complexes. Evidence for the involvement of interleukin-6. *J Biol Chem* (1990) **265**(34):21023–6. doi:10.1016/s0021-9258(17)45321-x

44. Rubin H, Plotnick M, Wang Z, Liu X, Schechter NM, Zhong Q, et al. Conversion of.alpha.1-Antichymotrypsin into a human neutrophil elastase inhibitor: demonstration of variants with different association rate constants, stoichiometries of inhibition, and complex stabilities. *Biochemistry* (1994) **33**(24):7627–33. doi:10.1021/bi00190a016

45. Potempa J, Fedak D, Dubin A, Mast A, Travis J. Proteolytic inactivation of alpha-1-anti-chymotrypsin. Sites of cleavage and generation of chemotactic activity. *J Biol Chem* (1991) **266**(32):21482–7. doi:10.1016/s0021-9258(18)54664-0

46. Coulthard LG, Woodruff TM. Is the complement activation product C3a a proinflammatory molecule? Re-evaluating the evidence and the myth. *The J Immunol* (2015) **194**(8):3542–8. doi:10.4049/jimmunol.1403068

47. Tegla CA, Cudrici C, Patel S, Trippe R, III, Rus V, Niculescu F, et al. Membrane attack by complement: the assembly and biology of terminal complement complexes. *Immunol Res* (2011) **51**(1):45–60. doi:10.1007/s12026-011-8239-5

48. Markiewski MM, Nilsson B, Nilsson Ekdahl K, Mollnes TE, Lambris JD. Complement and coagulation: strangers or partners in crime? *Trends Immunol* (2007) **28**(4):184–92. doi:10.1016/j.it.2007.02.006

49. Zelek WM, Harrison RA. Complement and COVID-19: three years on, what we know, what we don't know, and what we ought to know. *Immunobiology* (2023) **228**(3):152393. doi:10.1016/j.imbio.2023.152393

50. Detsika MG, Diamanti E, Ampelakiotou K, Jahaj E, Tsipilis S, Athanasiou N, et al. C3a and C5b-9 differentially predict COVID-19 progression and outcome. *Life (Basel)* (2022) **12**(9):1335. doi:10.3390/life12091335

51. Ma L, Sahu SK, Cano M, Kuppuswamy V, Bajwa J, McPhatter J, et al. Increased complement activation is a distinctive feature of severe SARS-CoV-2 infection. *Sci Immunol* (2021) **6**(59):eabh2259. doi:10.1126/sciimmunol.abh2259

52. Lucas A, Liu L, Dai E, Bot I, Viswanathan K, Munuswamy-Ramunujam G, et al. The serpin saga; development of a new class of virus derived anti-inflammatory protein immunotherapeutics. *Adv Exp Med Biol* (2009) **666**: 132–56. doi:10.1007/978-1-4419-1601-3_11

EBM Experimental Biology and Medicine

TYPE Original Research
PUBLISHED 11 February 2025
DOI 10.3389/ebm.2025.10204

A study on the differences in the gut microbiota and metabolism between male and female mice in different stress periods

Yajun Qiao[1,2,3], Juan Guo[4], Qi Xiao[5], Jianv Wang[1,3], Xingfang Zhang[1,6], Xinxin Liang[1,3], Lixin Wei[1,3], Hongtao Bi[1]* and Tingting Gao[2,7]*

[1]Qinghai Provincial Key Laboratory of Tibetan Medicine Pharmacology and Safety Evaluation, Northwest Institute of Plateau Biology, Chinese Academy of Science, Xining, China, [2]School of Psychology, Chengdu Medical College, Chengdu, China, [3]CAS Key Laboratory of Tibetan Medicine Research, Northwest Institute of Plateau Biology, Chinese Academy of Sciences, Xining, China, [4]Qinghai Provincial Traffic Hospital, Xining, China, [5]Emergency Department, The First Hospital of Qinhuangdao, Qinhuangdao, China, [6]Medical College, Qinghai University, Xining, China, [7]Department of Psychiatry, The People's Hospital of Jiangmen, Southern Medical University, Jiangmen, China

OPEN ACCESS

*CORRESPONDENCE
Hongtao Bi,
✉ bihongtao@hotmail.com
Tingting Gao,
✉ gaott646@163.com

RECEIVED 18 April 2024
ACCEPTED 28 January 2025
PUBLISHED 11 February 2025

CITATION
Qiao Y, Guo J, Xiao Q, Wang J, Zhang X, Liang X, Wei L, Bi H and Gao T (2025) A study on the differences in the gut microbiota and metabolism between male and female mice in different stress periods.
Exp. Biol. Med. 250:10204.
doi: 10.3389/ebm.2025.10204

Abstract

The sex difference in depression has long been an unsolved issue. Women are twice as likely to suffer from depression as men. However, there were significant differences in the composition of gut microbiota between women and men. There is a lack of studies linking sex differences in depression to microbiota, and the specific mechanisms of this process have not been explained in detail. The main purpose of this study was to explore the gender differences in the intestinal tract of male and female depressed mice. In this study, chronic restraint stress (CRS) mouse models were used to simulate chronic stress, and behavioral tests were conducted, including the open field test (OFT), tail suspension test (TST) and forced swimming test (FST). Microbial diversity analysis and metabolomics were performed on collected mouse feces. The results showed that female mice were highly active and prone to anxious behavior before stress, and the levels of *f-Rikenellaceae, f-Ruminococcaceae* and 16α-hydroxyestrone were significantly different from those in male mice. After 21 days (Days) of stress, female mice showed depression-like behavior, and the levels of *f-Erysipelotrichaceae*, 5α-pregnane-3,20-dione, and 2-hydroxyestradiol were significantly different from those in male mice. After 14 days of stress withdrawal, the depression-like behavior continued to worsen in female mice, and the levels of 5α-pregnane-3,20-dione, estrone glucuronide and *f-Erysipelotrichaceae* were significantly different from those in male mice. In summary, female mice have stronger stress sensitivity and weaker resilience than male mice, which may be related to differences in bacterial diversity and estrogen metabolism disorders.

KEYWORDS

stress, sex differences, gut microbiota, gut metabolism, estrogen metabolism

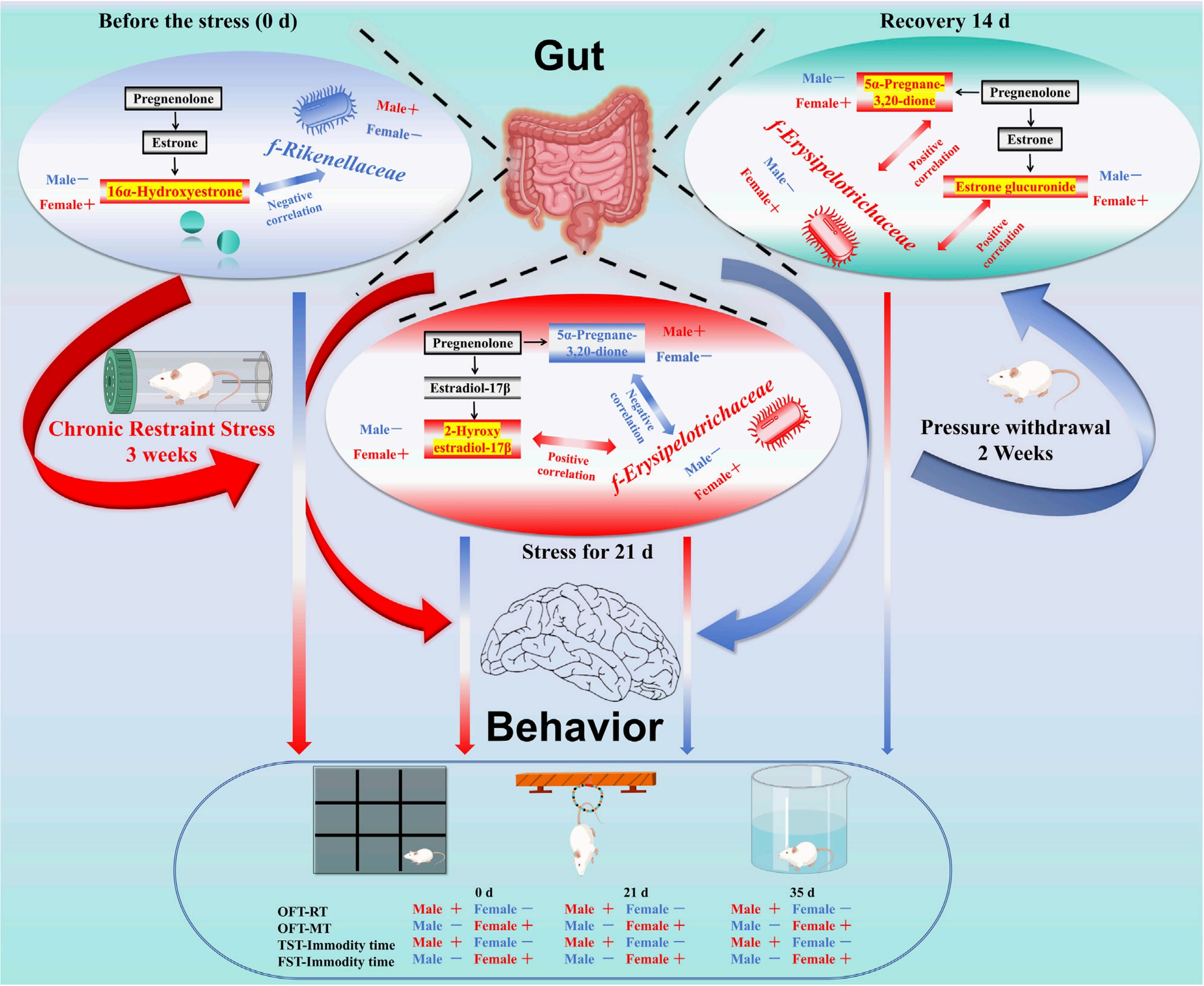

GRAPHICAL ABSTRACT

Note: Sex differences in depression have long been noted, with women being twice as likely to experience it compared to men. This study used chronic restraint stress (CRS) mouse models to investigate these differences, focusing on behavioral and microbial changes. Behavioral tests included the open field test (OFT), tail suspension test (TST), and forced swimming test (FST). Microbial diversity and metabolomics were analyzed from fecal samples. Results showed that female mice exhibited higher pre-stress activity and anxiety levels. Before stress, *f-Rikenellaceae*, *f-Ruminococcaceae*, and 16α-hydroxyestrone levels differed significantly between sexes. After 21 days of stress, female mice displayed depression-like behavior, with significant differences in *f-Erysipelotrichaceae*, 5α-pregnane-3,20-dione, and 2-hydroxyestradiol levels. Post-stress withdrawal for 14 days further exacerbated depression-like behavior in females, with continued differences in 5α-pregnane-3,20-dione, estrone glucuronide, and *f-Erysipelotrichaceae* levels. In summary, female mice show greater stress sensitivity and weaker resilience, potentially linked to bacterial diversity and estrogen metabolism differences.

Impact statement

In the present study, our experiments confirmed that prior to stress, females showed higher activity, despair and fight capacity, anxiety-like behaviour, gut flora (*f-Rikenellaceae* and *f-Ruminococcaceae*) and 16α-hydroxyestrone, significantly different from males; after 21 days of stress, females had worsened anxiety and depression-like behaviours, and gut metabolism and microbiota were disrupted, with significant differences in microbiota (*f-Erysipelotrichaceae*) and metabolites (5α-pregnane-3, 20-dione and 2-hydroxyestradiol); and after 14 days of stress relief, males began to recover from depression-like behaviours, whereas females showed deterioration. These results may provide new insights into gender-specific treatment and prevention of depression in patients with depression.

Introduction

Sex differences have consistently been a compelling area of scientific investigation. Notably, the divergence between males and females is particularly pronounced in both the prevalence and expression of depression. According to a 2021 study published in The Lancet, approximately 1 billion people worldwide are suffering from mental disorders [1]. The global burden of mental disorders has become heavier since the COVID-19 (coronavirus disease 2019) pandemic, with cases of major depression and anxiety increasing by 27.6% and 25.6%, respectively. The pressure of the epidemic has brought greater challenges to the diagnosis and treatment of depression [2]. Previous studies have shown that stress has the worst impact on women, with depression approximately twice as common in women as in men [3]. Currently, brain-gut axis communication is being studied as an important way to understand mental diseases, and gut microbes play an important role in brain and behavioral disorders [4–6].

Interestingly, there are also sex differences in the gut microbiota. B Flak, when commenting on the article published by JG Markle in Science in 2013, proposed the idea of sexual dimorphic microbiota and believed that there are differences in the microbiota of men and women [7, 8]. Li et al. found that 3β-hydroxysteroid dehydrogenase expressed by the gut microbiome can "eat" estradiol and is associated with depression in premenopausal women [9]. Estrogen also has physiological functions that interfere with pain regulation [10]. Existing studies have demonstrated a complex interaction between sex hormone signaling and stress responses in brain-gut axis function [11]. However, the specific mechanism of this process has not been elucidated in detail. Therefore, we used a CRS model to simulate stress in female and male mice and investigated the different behaviors of female and male mice in the face of stress through the differences in the gut microbiota and metabolites.

Materials and methods

Animals

Kunming (KM) mice (8 weeks of age) were obtained from Gansu University of Chinese Medicine, China [animal production license number: SCXK (Gan) 2015-0005]. Mice were housed in standard cages with wood shavings in a room with a carefully controlled ambient temperature (22 ± 1°C) and artificial lighting from 7:00 a.m. to 7:00 p.m. and were fed standard laboratory chow and provided distilled water *ad libitum*. All animal experiments were in compliance with the ARRIVE (Animal Research: Reporting of *In Vivo* Experiments) guidelines and were carried out in strict accordance with the National Institutes of Health Guide for the Care and Use of Laboratory Animals (NIH Publication No. 8023, revised 1978) and approved by the committee of the Northwest Plateau Institute of Biology, CAS, for animal experiments (allowance number: NWIPB20171106-01).

Stress stimuli and animal grouping

After an adjustment period (a week), 60 mice were randomly divided into 6 groups (n = 10): male control group, female control group, male stress group, female stress group, male stress recovery group, and female stress recovery group. Except for two control groups (Male and Female), mice were exposed to the chronic confining stressor of being bound to a 50 mL centrifuge tube for 6 h (8:30–14:30) per d for 3 weeks [12, 13]. Specifically, the weight of the mice in each group was measured weekly (Figure 1).

Behavioral tests

The behavioral tests consisted of the open field test (OFT), the tail suspension test (TST), and the forced swim test (FST), which were performed weekly during stress and recovery periods. The OFT followed the procedure described by Choleris et al. [14]. The TST and FST followed the procedures described by O'Leary (2009) and Porsolt (1977), respectively [15, 16]. Prior to the behavioral tests, test animals are allowed an acclimatization period of 1–2 h in the testing environment. Subsequently, the tests are conducted in ascending order of stimulus intensity (1. OFT; 2. TST; 3. FST). The specifics of the behavioral experiment are detailed in Supplementary Material S1.

Gut fecal metabolite analysis

Following the completion of behavioral testing, mice were euthanized via cervical dislocation. Fecal samples from both male and female mice were collected at three time points: prior to the experiment (0 days), during the experimental period (21 days), and during the stress recovery phase (14 days). Samples were immediately frozen in liquid nitrogen and stored at −80°C. Metabolomics analysis was conducted using LC-MS on 50 mg aliquots of freeze-dried fecal material [17–19]. See Supplementary Material S1 for details.

Gut microbial diversity analysis

The remaining samples in each group after the metabolomics analysis of the rectal contents were placed in a −80°C refrigerator for DNA extraction. The extracted DNA was used for the 16S

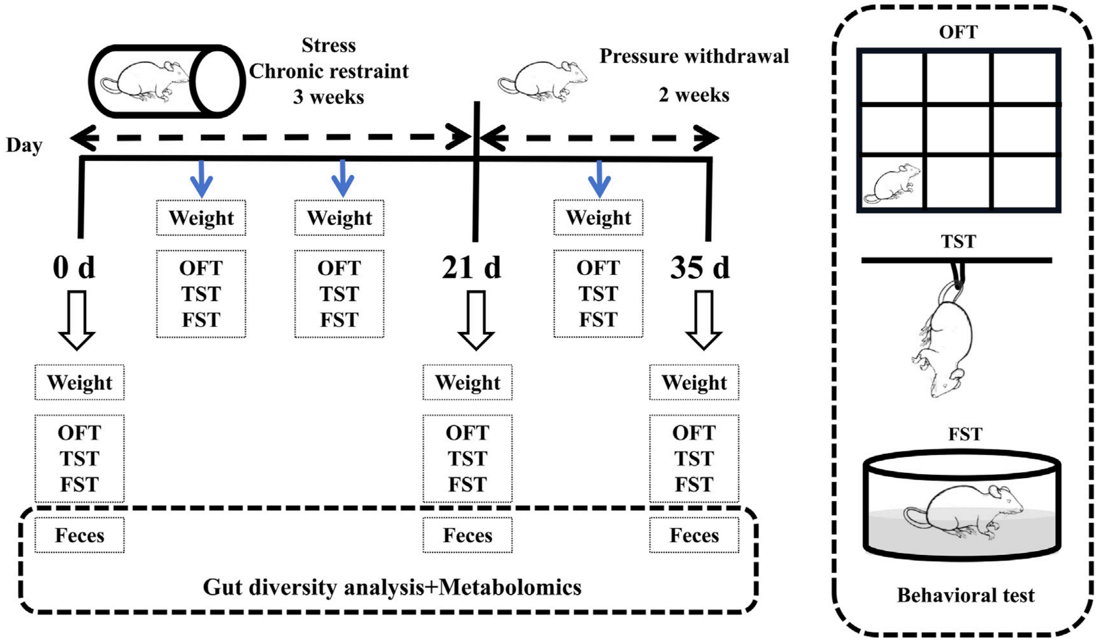

FIGURE 1
Flow chart of the experiment.

rRNA gene analysis of the bacterial population [16, 20]. See Supplementary Material S1 for details.

Statistical analyses

All data are expressed as the mean ± standard deviation (SD) of 10 or 6 replicates, and ANOVA was performed using a fully randomized trial design. SPSS 22.0 software was used for one-way ANOVA to determine differences between the means [without assuming consistent standard deviation (SD)] and Spearman correlation analysis. $P < 0.05$ was considered statistically significant. Graphs were drawn using Origin 2021 software.

Results

Stress-induced body weight loss is greater in female mice

To evaluate the weight alterations in mice elicited by stress stimuli, we conducted a study measuring the body weights of both male and female mice prior to and following exposure to stress. The weight of the mice was measured as shown in Figure 2A, and it was found that in the stress period (7 days, 14 days, and 21 days) and recovery period (28 days and 35 days), the body weight of the male control group mice was significantly lower than that of the male stress group mice (Figure 2A1: 7 days, $P < 0.05$; 14 days, $P < 0.01$; 21 days, $P < 0.01$; 28 days, $P < 0.01$; 35 days, $P < 0.05$). The weight change in female mice was similar to that in male mice, and compared with the female control group (Figure 2A2), the weight loss of female mice in the stress group was more significant (7 days, $P < 0.01$; 14 days, $P < 0.01$; 21 days, $P < 0.001$; 28 days, $P < 0.01$; 35 days, $P < 0.05$). The weight changes in male and female mice are illustrated in Figure 2A3. Compared to the male stress group mice, the female stress group mice exhibited lower weight changes before stress exposure, during the stress period (7 days, 14 days, and 21 days), and during the recovery period (28 days and 35 days). Notably, a significant difference was observed between male and female mice at 14 days ($P < 0.05$). Therefore, the observed weight changes prompted us to investigate the corresponding behavioral modifications in the mice.

Stress exerted a more pronounced influence on the behavior of female mice

To evaluate the impact of stress on mouse behavior, we employed the OFT, TST, and FST to detect behavioral changes in both male and female mice before and after exposure to stress. The OFT results showed that the rest time (RT) of male control group mice was significantly longer than that of male stress group mice during the stress period and recovery period (Figure 2B1: 7 days, $P < 0.01$; 14 days, $P < 0.001$; 21 days, $P <$

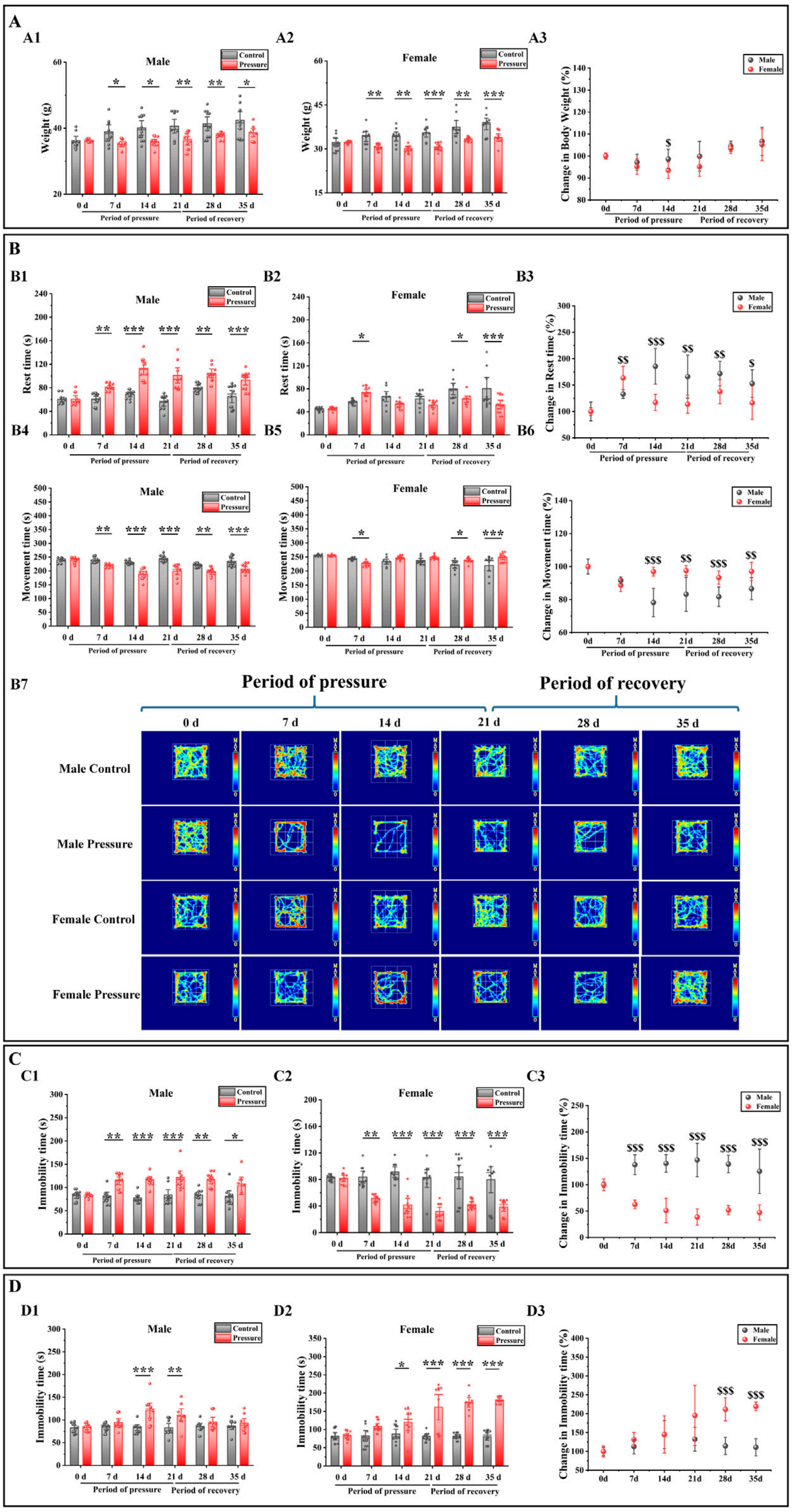

FIGURE 2
Effects of pressure simulation on mice in **(A)** Weight, **(B)** Rest time and Movement time in OFT, **(C)** TST-IT and **(D)** FST-IT. Note: **(A1, A2)** represent the initial weights of male and female mice, respectively, while **(A3)** denotes the changes in their weights. **(B1, B2)** indicate the RT of male and female mice, respectively, and **(B3)** represents the changes in RT. **(B4, B5)** refer to the MT of male and female mice, with **(B6)** indicating the changes in MT. **(B7)** Illustrates the movement tracks of the OFT for the mice. **(C1, C2)** denote the IT of male and female mice in the TST, with **(C3)**

(Continued)

FIGURE 2 (Continued)
representing the changes in TST-IT. **(D1, D2)** indicate the IT of male and female mice in the FST, and **(D3)** shows the changes in FST-IT. Data are presented as the mean ± SD ($n = 10$). $^{*}p < 0.05$, $^{**}p < 0.01$, and $^{***}p < 0.001$ indicate significant differences between the control group and the stress group. $^{\$\$}p < 0.01$ and $^{\$\$\$}p < 0.001$ indicate significant differences between the male stress group and the female stress group.

0.001; 28 days, $P < 0.01$; 35 days, $P < 0.001$), and the movement time (MT) was significantly decreased (Figure 2B4: 7 days, $P < 0.01$; 14 days, $P < 0.001$; 21 days, $P < 0.001$; 28 days, $P < 0.01$; 35 days, $P < 0.001$). Compared with the female stress group, the RT of the female control group was significantly increased (Figure 2B2: 7 days, $P < 0.05$; 28 days, $P < 0.05$; 35 days, $P < 0.001$), and the MT was significantly decreased (Figure 2B5: 7 days, $P < 0.05$; 28 days, $P < 0.05$; 35 days, $P < 0.001$). The female stress group was compared with the male stress group (Figure 2B3, B6); the RT change of male mice was significantly higher than that of female mice (14 days, $P < 0.001$; 21 days, $P < 0.01$; 28 days, $P < 0.01$; 35 days, $P < 0.05$), and the MT was significantly lower than that of female mice (14 days, $P < 0.001$; 21 days, $P < 0.01$; 28 days, $P < 0.001$; 35 days, $P < 0.01$). However, at 7 days, the RT changes in male mice were significantly lower compared to those in female mice ($P < 0.01$), while the MT changes were significantly higher. Figure 2B7 shows that the movement trajectory of male control mice increased with time, with little change. In the stress period, the range of motion of the mice tended to be around the periphery, and in the recovery period, the range of motion of the mice began to gradually shift to the center. The motion trajectory of female control mice was similar to that of male control mice. During the stress period, the activity of female stress mice tended to be around the periphery, but the activity of female stress mice was significantly stronger than that of male stress mice. During the recovery period, the activity of female stress mice began to gradually shift to the center, similar to that of male stress mice.

The TST and FST results showed that during the stress period and recovery period, compared with the male control group mice (Figures 2C1, D1), the IT (immobility time) of the male stress group mice in the TST and FST was significantly increased (7 days: $P < 0.01$; 14 days: $P < 0.001$, $P < 0.001$; 21 days: $P < 0.001$, $P < 0.01$; 28 days, $P < 0.01$; 35 days, $P < 0.05$). Compared with the female control group (Figures 2C2, D2), the TST-IT of female stress group mice was significantly decreased (7 days: $P < 0.01$; 14 days: $P < 0.001$; 21 days: $P < 0.001$; 28 days: $P < 0.001$; 35 days: $P < 0.001$), and the FST-IT increased significantly (14 days: $P < 0.05$; 21 days: $P < 0.001$; 28 days: $P < 0.001$; 35 days: $P < 0.001$). The female stress group was compared with the male stress group (Figures 2C3, D3); the TST-IT changes of male mice was significantly higher than that of female mice (7 days, $P < 0.001$; 14 days, $P < 0.001$; 21 days, $P < 0.001$; 28 days, $P < 0.001$; 35 days, $P < 0.001$), and the FST-IT changes was significantly lower than that of female mice (28 days, $P < 0.001$; 35 ays, $P < 0.001$). Therefore, based on the outcomes of the behavioral tests conducted on mice, we subsequently investigated the alterations in intestinal microbiota associated with these behaviors.

Effects of stress on the gut microbiota diversity and function prediction of mice

To evaluate the alterations in the gut microbiota of mice induced by stress, we initially examined the diversity of the gut microbiota in both male and female mice prior to and following the stress exposure. In the alpha diversity analysis (Figure 3A), including Simpson (male: 21 days vs. 0 days, $P < 0.01$; 35 days vs. 21 days, $P < 0.01$. Female: 21 days vs. 0 days, $P < 0.05$), Shannon (male: 21 days vs. 0 days, $P < 0.05$; 35 days vs. 0 days, $P < 0.05$. Female: 21 days vs. 0 days, $P < 0.05$), PD whole tree (male: 21 days vs. 0 days, $P < 0.01$; 35 days vs. 0 days, $P < 0.05$. Female: 21 days vs. 0 days, $P < 0.05$) and goods coverage (female: 21 days vs. 0 days, $P < 0.01$; 35 days vs. 0 days, $P < 0.05$. Male 0 days vs. female 0 days: $P < 0.05$), the differences between the index groups were statistically significant. Through β diversity analysis (Figure 3B) of the values calculated by Weighted UniFrac, it was found that the samples of each group had obvious differences. Subsequently, we employed LEfSe (Linear discriminant analysis Effect Size) analysis to identify significant differences in the gut microbiota of male and female mice before and after exposure to stress. The cladogram in Figure 4A shows that the study group played an important role in the microbiota. According to the statistical analysis at the species level, *f-Eggerthellaceae*, *f-Rikenellaceae* and *f-Saccharimonadaceae* were the main gut microbiota in the male 0 days group. *f-Tannerellaceae*, *f-Lactobacillaceae* and *f-Streptococcaceae* were the main gut microbiota in the male 21 days group. *f-Bacteroidaceae*, *f-Marinifilaceae*, *f-Prevotellaceae*, *f-Helicobacteraceae*, *f-Christensenellaceae*, *f-Family XIII* and *f-Peptostreptococcaceae* were the main gut microbiota in the male 35 days group. *f-Lachnospiraceae*, *f-Peptococcaceae*, *f-Ruminococcaceae*, and *f-Desulfovibrionaceae* were the main gut microbiota in the female 0 days group. *f-Bifdobacteriaceae*, *f-Erysipelotrichaceae* and *f-Burkholderiaceae* were the main gut microbiota in the female 21 days group. *f-Muribaculaceae* was the main gut microbiota in the female 35 days group. The histogram of the LDA (linear discriminant analysis) value distribution (Figure 4B) shows the species with LDA scores greater than the set value of 3 and $P < 0.05$. There were 3 species in males at 0 days, 3 species in males at 21 days and 6 species in males at 35 days. There were 4 species in

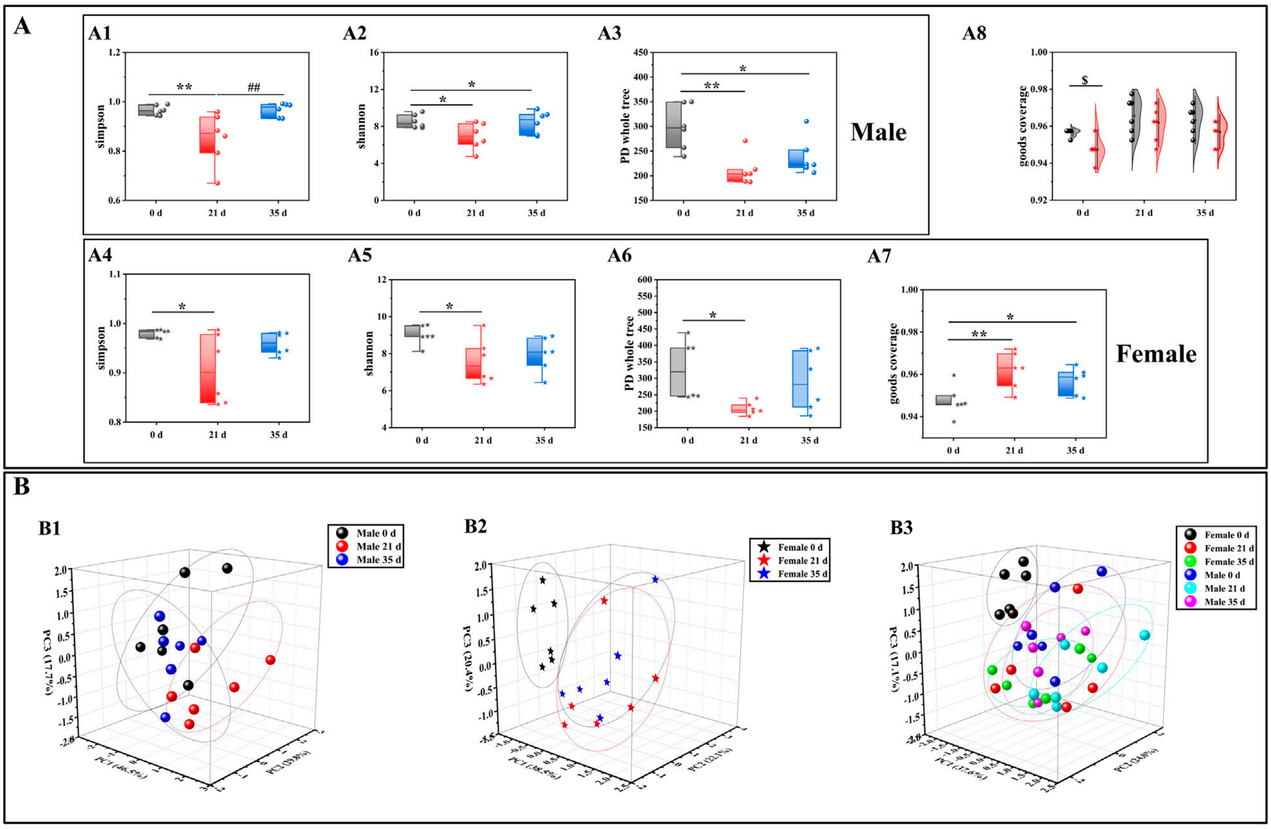

FIGURE 3
Effects of pressure simulation on the gut microbiota diversity of female and male mice. **(A)**: Alpha diversity analysis; **(B)**: Beta diversity analysis; **(C)**: Cladogram; **(D)**: LDA score; **(E)**: PICRUSt2 one-level pathway annotation results. Note: **(A1–A3)** denote the alpha diversity indices for male mice, while **(A4–A7)** indicate the alpha diversity indices for female mice. **(A8)** represents the combined alpha diversity index for both male and female mice, ensuring comprehensive coverage. **(B1)** refers to the beta diversity analysis for male mice, **(B2)** for female mice, and **(B3)** encompasses the beta diversity analysis for both sexes. Data are expressed as mean ± standard deviation (n = 6). *p < 0.05, **p < 0.01 indicates a significant difference compared with 0days $p < 0.05 indicates a difference between male and female mice.

females at 0 days, 3 species in females at 21 days, and 1 species in females at 35 days. Ultimately, we assessed the biological functional pathways associated with the differential microbiota observed in male and female mice. As shown in Figure 4C, the primary pathways that annotate the gut microbiota were mainly distributed in cellular processes, environmental information processing, genetic information processing, human diseases, metabolism, none, organismal systems, and unclassified. Based on these findings, we subsequently evaluated the alterations in the differential microbiota between male and female mice.

Stress had a more pronounced impact on the gut microbiota in female mice

To evaluate the impact of stress on the gut microbiota of male and female mice, we conducted a comparative analysis of the changes in gut microbiota both between and within the two groups, before and after exposure to stress. Figures 5A–C illustrates the variations in gut microbiota abundance between male and female mice before and after stress exposure at the family level, as determined by one-way ANOVA. For male mice (Figure 5A), intra-group analysis revealed a significant decrease in the relative abundance of *f-Rikenellaceae* ($P < 0.05$), *f-Lachnospiraceae* ($P < 0.001$), and *f-Marinifilaceae* ($P < 0.05$) at 21 days compared to 0 days. Conversely, the relative abundance of *f-Tannerellaceae* significantly increased ($P < 0.01$). Between 21 days and 35 days, the relative abundance of *f-Lachnospiraceae*, *f-Marinifilaceae*, and *f-Tannerellaceae* decreased, while that of *f-Lachnospiraceae* increased without reaching statistical significance. Over the entire period from 0 days to day 35 days, there was a significant reduction in the relative abundance of *f-Rikenellaceae* ($P < 0.01$), *f-Lachnospiraceae* ($P < 0.01$), and *f-Marinifilaceae* ($P < 0.05$), whereas the increase in *f-Tannerellaceae* did not reach statistical significance. For female mice (Figure 5B), intra-group analysis

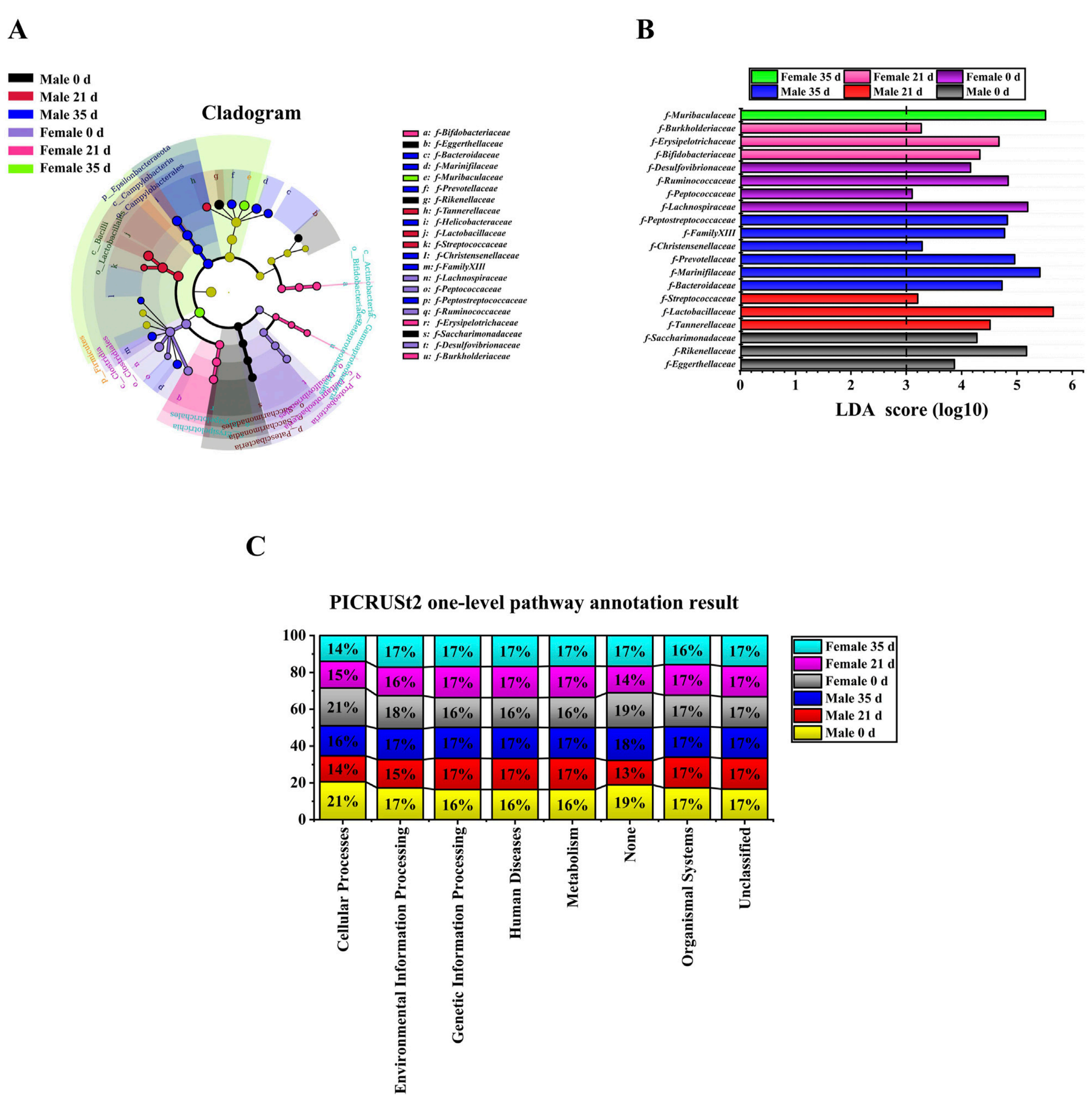

FIGURE 4
LEfSe analysis and functional prediction of gut microbiota in male and female Mice. **(A)**: Cladogram; **(B)**: LDA score (LDA score≥3); **(C)**: PICRUSt2 one-level pathway annotation results.

showed a significant increase in the relative abundance of *f-Erysipelotrichaceae* ($P < 0.05$) and *f-Lactobacillaceae* ($P < 0.01$) at 21 days compared to 0 days, while the relative abundance of f-Ruminococcaceae ($P < 0.01$) and f-Lachnospiraceae ($P < 0.01$) significantly decreased. From 21 days to 35 days, the relative abundance of *f-Erysipelotrichaceae*, *f-Lactobacillaceae*, and *f-Ruminococcaceae* decreased, although only *f-Lachnospiraceae* showed a significant increase ($P < 0.01$). Over the entire period from 0 days to 35 days, the relative abundance of *f-Erysipelotrichaceae* ($P < 0.05$) and *f-Lactobacillaceae* increased, while that of *f-Ruminococcaceae* ($P < 0.01$) and *f-Lachnospiraceae* ($P < 0.01$) significantly decreased.

Figure 5C shows the differences in the gut microbiota of mice before and after stress. At 0 days, the relative abundances of *f-Muribaculaceae* ($P < 0.05$), *f-Ruminococcaceae* ($P < 0.05$) and *f-Lachnospiraceae* ($P < 0.001$) decreased. The relative abundances of *f-Rikenellaceae* ($P < 0.001$), *f-Bacteroidaceae*,

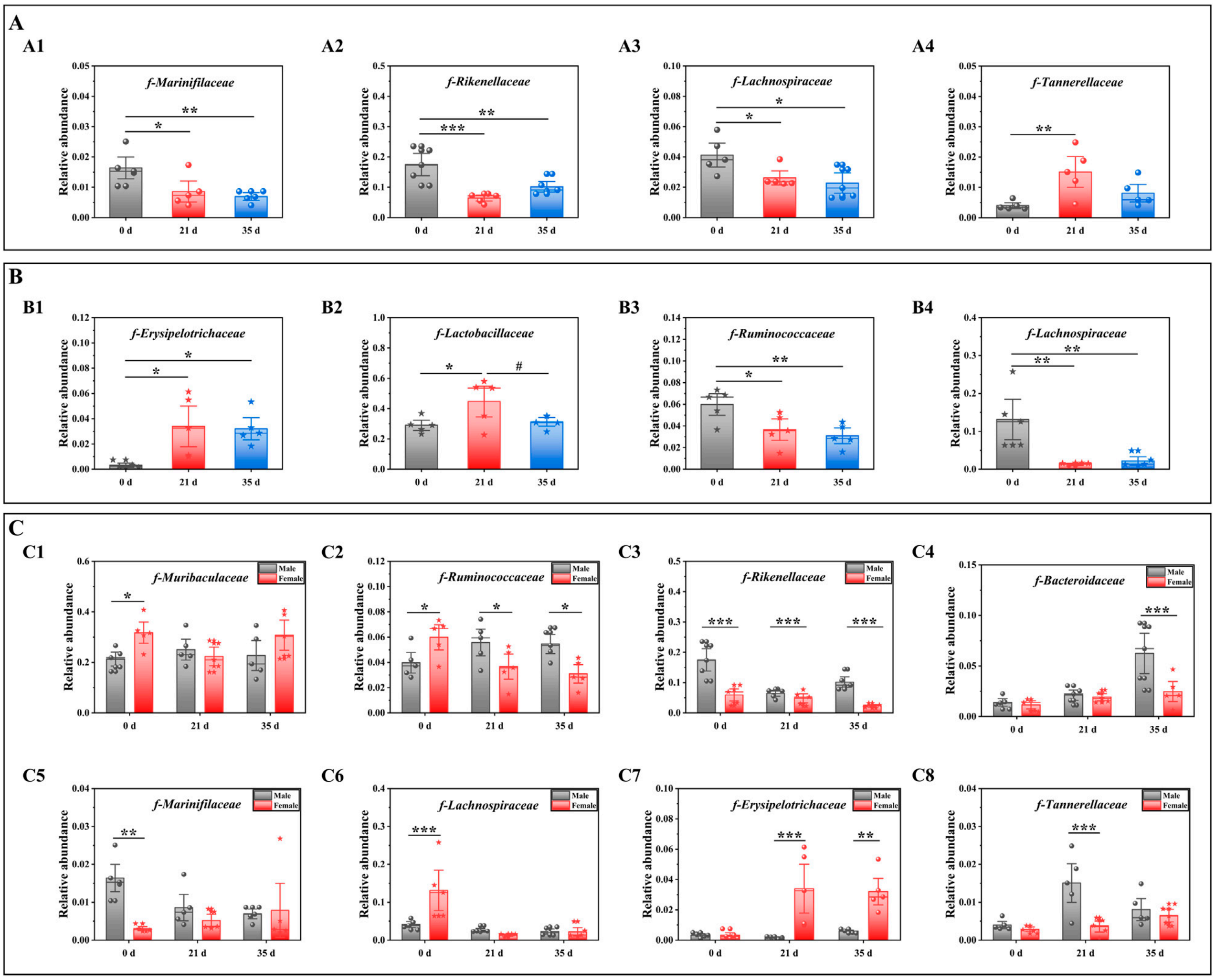

FIGURE 5
Effects of pressure on gut microbiota at the family level in mice. Note: **(A)** The gut microbiota composition of male mice before and after exposure to stress; A1–A4 denotes varying levels of microbial abundance. **(B)** Family-level comparison of the gut microbiota in female mice before and after exposure to stress; B1–B4 denotes different levels of microbiota abundance. **(C)** Comparative analysis of the gut microbiota between male and female mice before and after exposure to stress; C1–C8 denotes distinct levels of microbiota abundance. Data are expressed as mean ± standard deviation (n = 6). *p < 0.05, **p < 0.01 indicates a significant difference compared with 0 d. #p < 0.05 indicates a significant difference compared with 21 d. $p < 0.05 $$p < 0.01 and $$$p < 0.001 indicates a difference between male and female. Mice.

f-Erysipelotrichaceae, *f-Tannerellaceae* and *f-Marinifilaceae* ($P < 0.01$) increased. At 21 days, the relative abundances of *f-Muribaculaceae*, *f-Ruminococcaceae* ($P < 0.05$), *f-Rikenellaceae* ($P < 0.01$), *f-Bacteroidaceae*, *f-Tannerellaceae* ($P < 0.001$) and *f-Marinifilaceae* increased, while the relative abundance of *f-Erysipelotrichaceae* ($P < 0.001$) decreased. At 35 days, the relative abundances of *f-Ruminococcaceae* ($P < 0.05$), *f-Rikenellaceae* ($P < 0.001$), and *f-Tannerellaceae* increased, and the relative abundances of *f-Muribaculaceae*, *f-Marinifilaceae* and *f-Erysipelotrichaceae* decreased ($P < 0.01$). Based on the outcomes from the diverse flora, we subsequently conducted an analysis of the alterations in gut metabolites.

Effects of stress on gut metabolism in mice

To evaluate the impact of stress on intestinal metabolites in male and female mice, we performed a comparative analysis of the alterations in intestinal metabolites within each sex group, both before and after exposure to stress. The scatter plot of the OPLS-DA (orthogonal partial least squares discriminant analysis) model of mice in each group is shown in Figure 6A. The sample differentiation was very significant, and all samples were within the 95% confidence interval. The screening conditions for DMs (differential metabolites) were

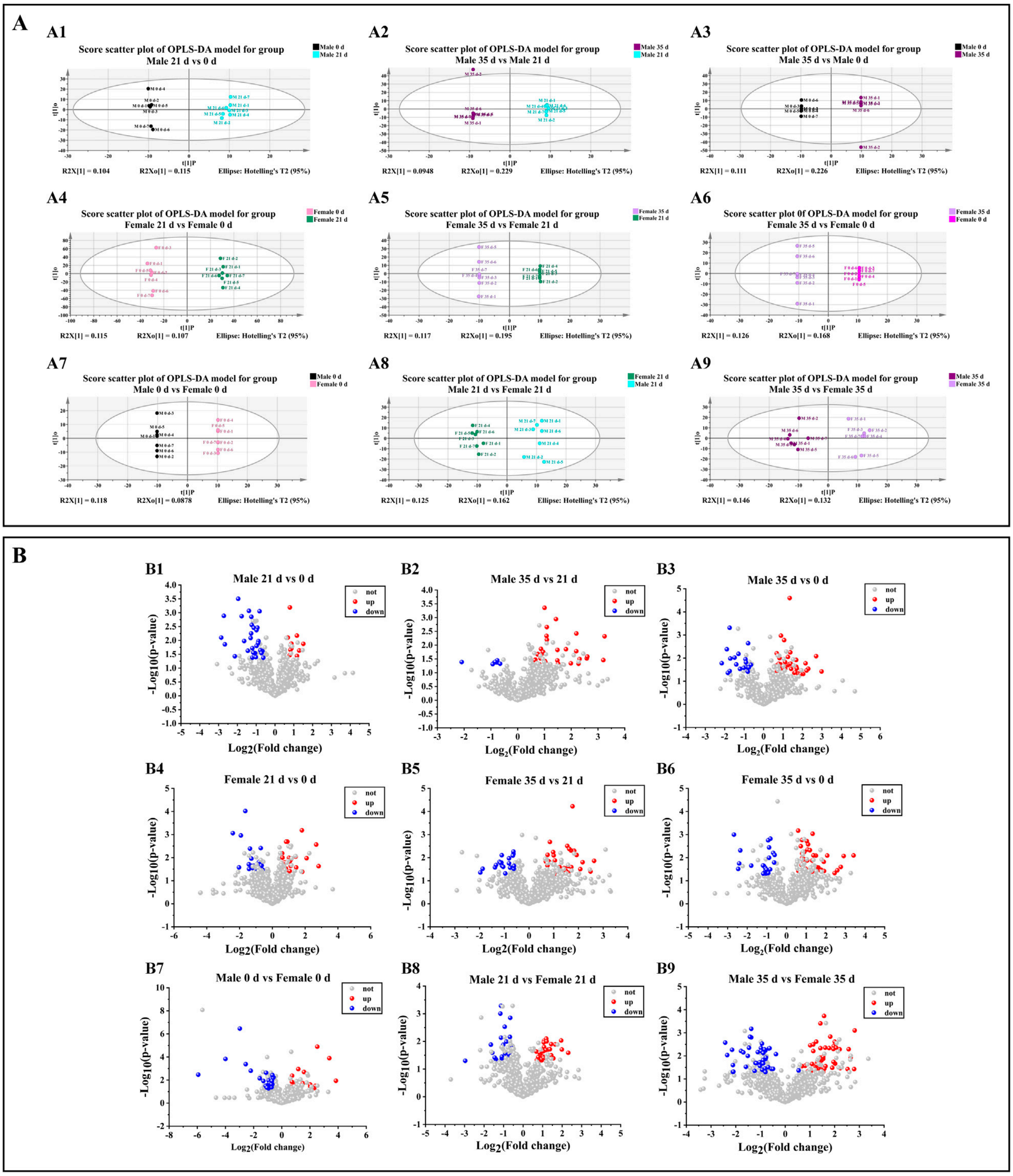

FIGURE 6
Effects of pressure on gut metabolism in mice. **(A)** Scatter plot of the OPLS-DA model. A1–A3 denotes the scatter plot of OPLS-DA model of metabolite comparison before and after stress in male mice. A4–A6 denotes the scatterplot of OPLS-DA model of metabolite comparison before and after stress in female mice. A7–A9 denotes a scatter plot of the OPLS-DA model in which metabolites in female and male mice are compared before and after stress. **(B)** Volcano map. B1–B3 denotes the volcanic map of metabolites before and after stress in male mice, B4–B6 denotes the volcanic map of metabolite comparison before and after stress in female mice, B7–B9 denotes the volcanic map of metabolites in female and male mice before and after stress (n = 6).

VIP >1 and P value <0.05. In addition, the results of screening upregulated DMs in each group of mice were visualized by a volcanic map (FC > 1.5; FC < 0.67, indicating downregulation). In male mice (Figures 6B1–3), compared to 0 days, 10 DMs were up-regulated and 30 DMs were down-regulated by 21 days. Between 21 days and 35 days, 29 DMs were up-regulated while 8 DMs were down-regulated. Over the entire period from 0 days to 35 days, 38 DMs were up-regulated and 18 DMs were down-regulated. In female mice (Figures 6B4–6), relative to 0 days, 21 DMs were up-regulated and 22 DMs were down-regulated by 21 days. From 21 days to 35 days, 32 DMs were up-regulated and 19 DMs were down-regulated. Overall, from 0 days to 35 days, 39 DMs were up-regulated and 22 DMs were down-regulated. When comparing male and female mice (Figures 5B7–9), at 0 days, 21 DMs were up-regulated and 28 DMs were down-regulated in males compared to females. By 21 days, 26 DMs metabolites were up-regulated and 26 DMs were down-regulated in males relative to females. At 35 days, this difference increased to 50 DMs up-regulated and 41 DMs down-regulated in males compared to females. Based on the findings from various gut metabolites, we subsequently conducted an in-depth analysis of the associated gut metabolic pathways.

Effects of stress on metabolic pathways and metabolites in mice

To evaluate the metabolic pathways involved in the stress response, the KEGG (Kyoto Encyclopedia of Genes and Genomes) was analyzed in male and female mice both before and after exposure to stress. The results of differential metabolite pathways were analyzed in a bar chart (Figure 7A). The DMs enrichment of male and female mice at three time points involved the same 16 pathways. DMs enrichment in both male and female mice at three time points (0 days, 21 days, and 35 days) involved the same 16 pathways, with a particular emphasis on the steroid hormone biosynthesis pathway. Due to the limited number of DMs (only 1-2) identified in the comparison between male and female mice, clustering analysis was not feasible. Consequently, we conducted inter-group comparisons between males and females and performed DM cluster analysis at the three specified time points (Figure 7B). Male mice were compared to female mice. On 0 days, 1 DM was up-regulated and 1 DM was down-regulated. By 21 days, 1 DM remained up-regulated while another DM was down-regulated. On 35 days, 1 DM was up-regulated and 3 DMs were down-regulated.

Correlation analysis of differential gut microbiota and DMs

To evaluate the association between metabolites and gut microbiota, Spearman correlation analysis was conducted to examine the relationship between the gut microbiota and DMs in male and female mice both before and after stress exposure. The results were subsequently compared between the sexes, as illustrated in Figure 8A. At 0 days, 16α-hydroxyestrone was negatively correlated with *f-Rikenellaceae* ($P < 0.05$) and positively correlated with *f-Muribaculaceae* ($P < 0.001$); cholesteryl sulfate was positively correlated with *f-Rikenellaceae* ($P < 0.01$) and negatively correlated with *f-Muribaculaceae* ($P < 0.05$). At 21 days, 2-hydroxyestradiol was positively correlated with *f-Erysipelotrichaceae* ($P < 0.05$); 5α-pregnane-3,20-dione was positively correlated with *f-Tannerellaceae* ($P < 0.01$) and negatively correlated with *f-Erysipelotrichaceae* ($P < 0.01$). At 35 days, 5α-pregnane-3,20-dione was positively correlated with *f-Erysipelotrichaceae* ($P < 0.01$) and negatively correlated with *f-Rikenellaceae* ($P < 0.01$) and *f-Bacteroidaceae* ($P < 0.05$); estrone glucuronide was negatively correlated with *f-Ruminococcaceae* ($P < 0.01$), *f-Rikenellaceae* ($P < 0.01$), and *f-Bacteroidaceae* ($P < 0.05$) and positively correlated with *f-Erysipelotrichaceae* ($P < 0.05$).

Correlation analysis of DMs and behavior

To evaluate the relationship between metabolites and behavior, Spearman correlation analysis was conducted on the behavioral data and DMs of both male and female mice before and after exposure to stress. The results were subsequently compared between the two sexes, as illustrated in Figure 8B. At 0 days, 16α-hydroxyestrone was negatively correlated with OFT-RT ($P < 0.05$) and positively correlated with OFT-MT ($P < 0.05$), and cholesteryl sulfate was positively correlated with OFT-RT ($P < 0.01$) and negatively correlated with OFT-MT ($P < 0.001$). At 21 days, 2-hydroxyestradiol was negatively correlated with OFT-RT ($P < 0.05$) and TST-IT ($P < 0.05$) and positively correlated with OFT-MT ($P < 0.01$); 5α-pregnane-3,20-dione was positively correlated with OFT-RT ($P < 0.01$) and TST-IT ($P < 0.05$) and negatively correlated with OFT-MT ($P < 0.05$) and FST-IT ($P < 0.05$). At 35 days, 5α-pregnane-3,20-dione and estrone glucuronide were positively correlated with OFT-RT ($P < 0.001$; $P < 0.01$), and TST-IT ($P < 0.05$; $P < 0.01$) and negatively correlated with OFT-MT ($P < 0.01$; $P < 0.01$) and FST-IT ($P < 0.05$; $P < 0.01$).

Discussion

Given the clinical phenomenon of sex differences in depression [21], this study explored the reasons for the differences in stress tolerance and recovery ability between male and female mice. We adopted the CRS model [22] and exposed mice to 21 days of continuous stress for 6 h to simulate a stressful environment. Clinically, weight loss is observed in depressed patients, and the degree of weight loss in women

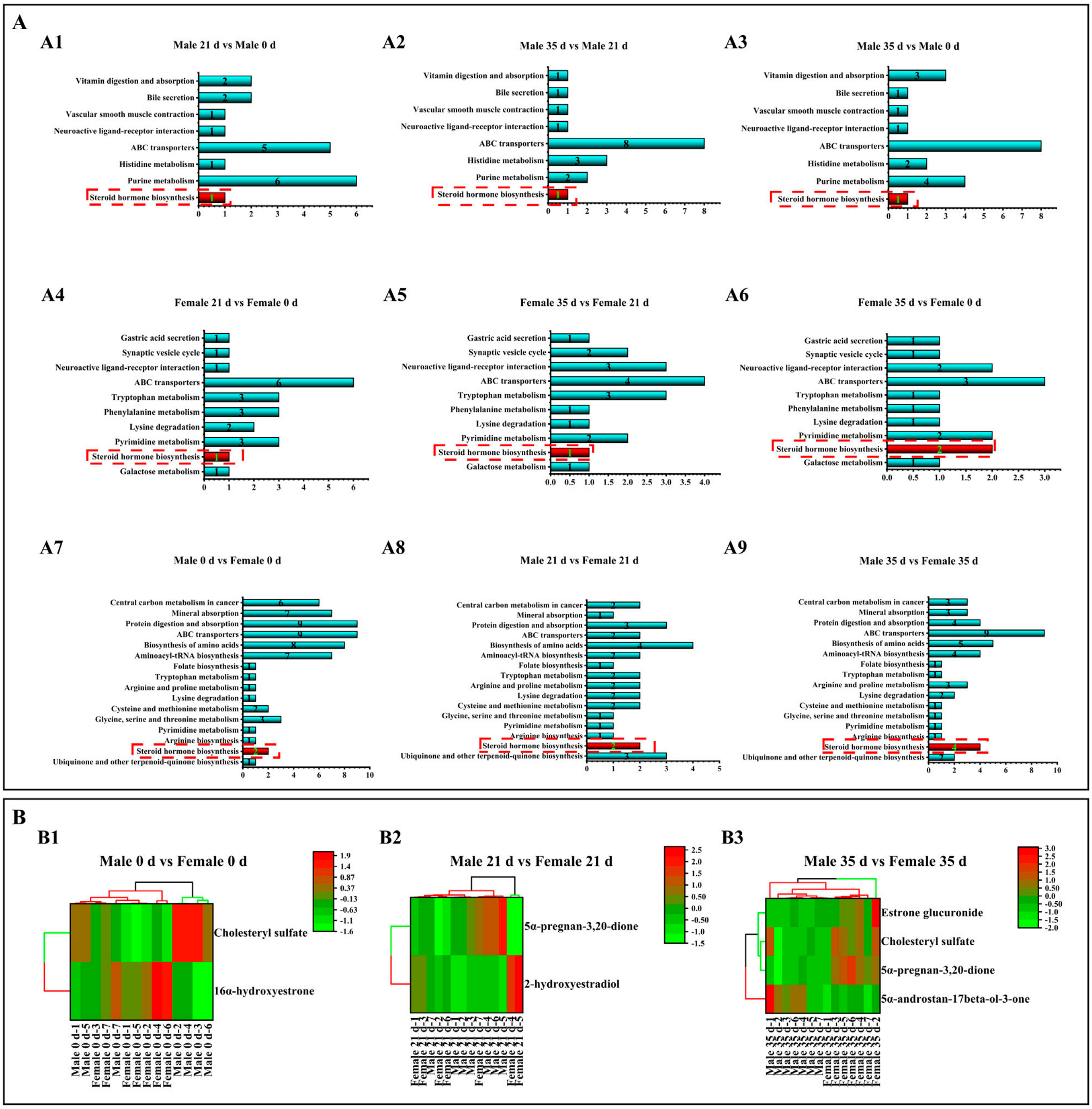

FIGURE 7
Effects of pressure on metabolic pathways and metabolites in mice. Note: **(A)** Metabolic pathways. A1–A3 denotes the metabolic pathways of male mice compared with DMs before and after stress. A4–A6 denotes the metabolic pathway of DMs compared before and after stress in male mice. A7–A9 denotes the metabolic pathway of DMs compared before and after stress in male and female mice. **(B)** DMs cluster analysis. B1 denotes DMs cluster analysis of male and female mice at 0 days; B1 denotes DMs cluster analysis of male and female mice at 21 days. B1 denotes DMs cluster analysis of male and female mice for 35 days (n = 6).

may be greater [23]. Our experimental results also showed this phenomenon. After 21 days of stress simulation, the weight change in female mice was similar to that in male mice, but the weight loss of female mice was more obvious. After 14 days of stress cessation, female mice also had lower weight recovery ability than male mice. The behavioral test results showed that male mice exhibited lower activity and increased resting time during stress compared to female mice. Interestingly, however, the female mice showed higher exercise time on the TST and lower IT on the FST. We speculate that female mice and male

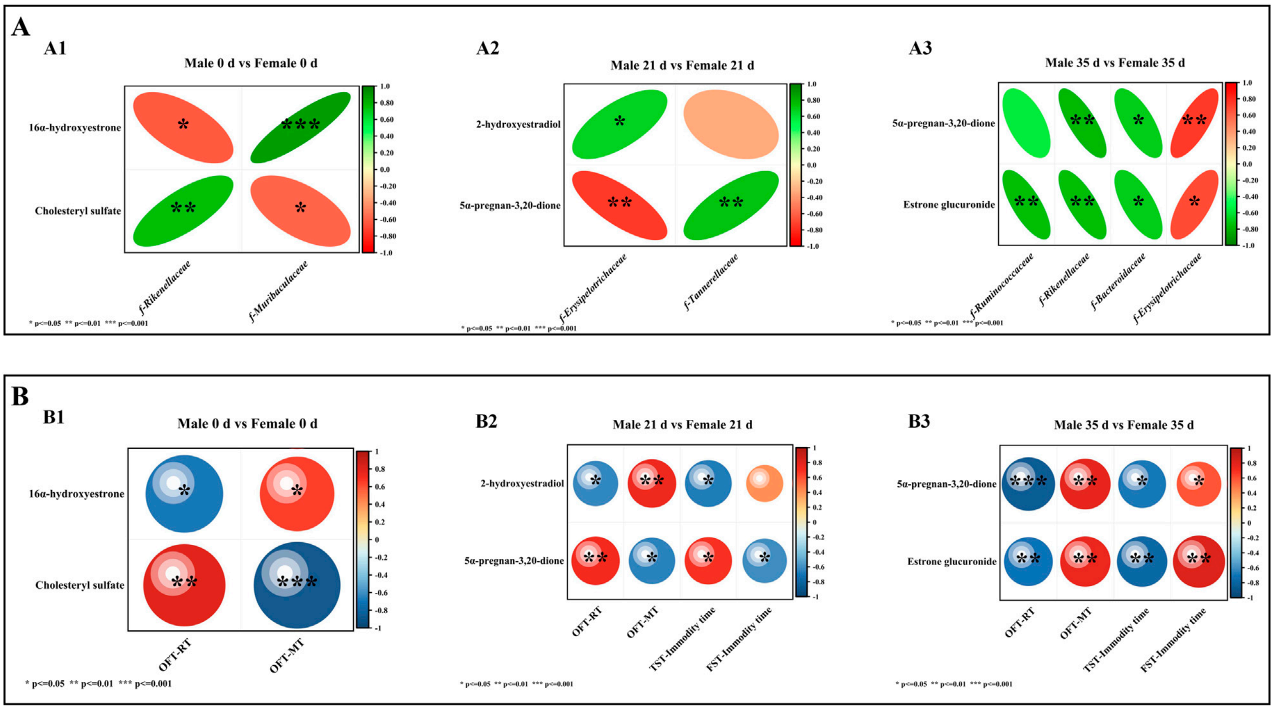

FIGURE 8
Spearman correlation analysis. Note **(A)** Correlation analysis between differential microbiota and DMs. A1 denotes the correlation analysis between 0 days of differential microbiota and DMs; A2 denotes the correlation analysis between 21 days of different microbiota and DMs; A3 denotes the correlation analysis between 35 days of different microbiota and DMs. **(B)** Correlation analysis between DMs and behavior. B1 denotes the correlation analysis between DMs and behavior at 0 days; B2 denotes the correlation analysis between DMs and behavior in 21 days; B3 denotes the correlation analysis between DMs and behavior in 35 days (n = 6).

mice exhibit different depressive phenotypes [24, 25] due to differences in sex personality and physiological metabolism [9, 26, 27] during stress and recovery, which may be the reason why female mice exhibited anxiety-like behaviors in the OFT and TST. Male mice began to return to desperate behavior, but female mice exhibited less recovery and increased depressive behavior. This is also similar to the clinical phenomenon that the recurrence rate of MDD in women is four times that of men [24].

The differences in depressive behavior and phenotype between female and male mice may be related to the regulation of sex hormones [9, 28]. Estradiol is a sex hormone that is crucial for regulating emotions. *Bacteroides thetaiotaomicron* and *Clostridia* can degrade estradiol through the metabolism of 3β-steroid dehydrogenase, which can induce depression in women [9]. Currently, behavioral differences caused by stress are known to be significantly related to the gut microbiota and its metabolites [29, 30]. At the same time, there are also significant sex differences in the composition of the microbiota. According to existing studies, men and women show differences in susceptibility, diagnosis, treatment and recovery of most diseases related to the microbiota [31]. The occurrence and development of depression cannot be separated from immunity and metabolism, and the microbiota plays an important role in immune metabolism [32]. However, we do not yet know what causes the behavioral differences between male and female mice during stress and recovery, or how the gut is involved in this process. Therefore, we performed microbiota 16S sequencing and metabolomics analysis of the gut contents.

Our results demonstrated that the relative abundance of *f-Ruminococcaceae* and *f-Lachnospiraceae* significantly decreased in both male and female mice during the 21 days stress period. This reduction may represent a common response of the murine gut microbiota to stress [33]. However, sex-specific differences in gut microbiota have been documented [34]. In our study, we observed distinct variations in the microbial composition between male and female mice. Prior to stress exposure (at 0 days), the relative abundance of *f-Rikenellaceae* was higher in male mice compared to females, whereas the relative abundance of f-Ruminococcaceae was lower in males than in females. Following 21 days of stress stimulation, the relative abundance of *f-Rikenellaceae* decreased, with a more pronounced reduction observed in female mice. Notably, the relative abundance of *f-Ruminococcaceae* exhibited opposite trends by sex, decreasing in females while increasing in males.

Two weeks after the cessation of stress, the relative abundance of *f-Rikenellaceae* and *f-Ruminococcaceae* began to recover in male mice, whereas it continued to decline in females. In 2015, a study from Ohio State University found that in boys, extroverted personality traits were associated with the abundance of *Rikenellaceae* and *Ruminococcaceae*. *Ruminococcaceae* is one of the main bacterial groups that produces butyric acid, an anti-inflammatory short-chain fatty acid that nourishes the gut mucosa. In girls, the abundance of *Rikenellaceae* seems to influence fear propensity [35]. This study is consistent with our findings of behavioral differences between females and males before stress, during stress, and during recovery. We speculate that the differences in the abundance of *Rikenellaceae* and *Ruminococcaceae* may be the reason for the different behaviors of female and male mice. Moreover, we found that the relative abundance of *f-Erysipelotrichaceae* in female mice began to increase after 21 days of stress and remained high after 14 days of recovery. Studies have found that *Erysipelotrichaceae* may be a driving factor in exercise performance [36], which is consistent with our behavioral results that female mice exhibit strong anxious exercise behaviors. Interestingly, several studies have demonstrated that supplementation with butyrate or butyrate-producing gut flora alleviates depressive symptoms in mice. Ari et al. [37] reported that long-term administration of β-hydroxybutyric acid (3HB) significantly reduced anxiety-like behavior in rats. An Italian research team observed in an autism model that maternal supplementation with butyrate during pregnancy and lactation increased butyrate levels in offspring and mitigated neuro developmental abnormalities and autism-like behaviors [38]. Furthermore, supplementation with certain butyrate-producing gut flora has been shown to improve depressive symptoms in women [33, 39, 40]. Consequently, we hypothesize that the disparity in the abundance of *Rikenellaceae* and *Ruminococcaceae* may influence butyrate metabolism, potentially contributing to differences in stress resilience between female and male mice. However, due to the limitations of our study, further research is required to substantiate this hypothesis.

Excitingly, in our gut metabolomics analysis, we found that the DMs between stress and recovery in male and female mice were concentrated in the steroid hormone biosynthesis pathway, which is involved in estrogen synthesis. Estrogen metabolism is closely related to the occurrence of MDD [9, 27]. Increasing research evidence shows that estrogen regulates neurotransmitters in the brain through estrogen receptor (GPER) signals, thereby affecting cognition, behavior, and emotion [41]. 16α-Hydroxyestrone is one of the metabolites of the female core hormone estradiol and a potent antioxidant [42, 43]. The relative content of 16 α-hydroxyestrone in female mice was higher than that in male mice at 0 days before stress. In Spearman association analysis, 16α-hydroxyestrone was positively correlated with *f-Ruminococcaceae* ($P < 0.001$) and OFT-MT and negatively correlated with OFT-RT. Therefore, we surmised that 16α-hydroxyestrone induced initial high motility in female mice, which may be related to the higher gut antioxidant and anti-inflammatory capacity of females than males.

Progesterone and estrogen jointly maintain the dynamic balance of the brain, and progesterone balances the excitatory effect of estrogen and plays a role in sedation and anti-anxiety [44, 45]. Progesterone has been shown to have anti-inflammatory effects in neuronal injury and infection models [46, 47]. In addition, many metabolites of progesterone have physiological activities and participate in human emotional regulation [48]. 5α-Pregnane-3,20-dione, a progesterone metabolite, induces increased activity in ovariectomized rats [49]. Estradiol-17β is hydroxylated to form 2-hydroxyestradiol-17β, a neuroprotective estrogen [50].

After 21 days of stress simulation, the relative content of 5α-pregnane-3,20-dione in female mice was lower than that in male mice, while 2-hydroxyestradiol-17β increased. Association analysis of DMs with microbiota and behavior showed that *f-Erysipelotrichaceae* was positively correlated with 2-hydroxyestradiol ($P < 0.05$) but negatively correlated with 5α-pregnane-3,20-dione ($P < 0.01$). Pregnane-3,20-dione was positively correlated with OFT RT ($P < 0.05$) and TST-IT ($P < 0.05$). 2-Hydroxyestradiol was negatively correlated with OFT RT ($P < 0.05$) and TST-IT ($P < 0.05$). Therefore, we speculate that an increase in the relative abundance of *f-Erysipelotrichaceae* in female mice drives stronger anxiety-like behavior and a decrease in 5α-pregnane-3,20-dione levels, resulting in increased FST-IT and increased depression-like behavior. The increase in 2-hydroxyestradiol-17β may reflect the resistance of female mice to stress. Interestingly, female mice performed differently in the two experiments that measured desperate behavior, showing greater struggle in the TST and greater desperation in the FST than male mice. We speculate that this may be related to the cognitive and physical differences between male and female mice. Female mice have lower physical capacity than male mice and are lighter in weight, so they are more likely to sway when suspended, while resistance in water consumes energy and induces females to be more likely to stay still. At the same time, females have stronger cognitive ability than males [51]. In our initial experiment, females had stronger exploration ability than males, and it was easier for females to understand despair in water. However, we cannot yet explain the biological mechanism of this phenomenon. After 2 weeks of stress withdrawal, male mice produced lower levels of 5α-pregnane-3,20-dione and estrone glucuronide than female mice. Estrone glucuronide is the downstream metabolite of estrone, which is also one of the indicators used to predict depression in women and is related to sensitivity to negative emotions [52]. In the association analysis, 5α-pregnane-3,20-dione and estrone glucuronide were positively correlated with *f-Erysipelotrichaceae*, OFT-RT ($P < 0.001$; $P < 0.01$) and TST-IT ($P < 0.05$; $P < 0.01$). The relative levels of 5α-pregnane-3,20-dione and *f-Erysipelotrichaceae* in female mice began to increase, which was consistent with increased anxious behavior in females. In addition, increased levels of estrone glucuronide may induce increased negative emotional sensitivity in female mice. We hypothesized that after stress withdrawal, the sex hormone metabolism of female mice continued to be disturbed, while depression and anxiety increased.

Conclusion

In mammals, there are significant sex differences in mental disorders such as depression, autism, and Alzheimer's disease. We used the CRS model to simulate the persistent stress in the environment that human beings have been exposed to for a long time and explored the differences between male and female mice at three time points (0 days before the stress, 21 days during the stress period, and 35 days during the recovery period) in behavior, gut microbiota, and gut metabolites to find biomarkers in different periods. The experimental results showed that before stress, females exhibited strong activity, a weak ability to despair and struggle, anxiety-prone behavior, *f-Rikenellaceae* and *f-Ruminococcaceae* gut microbiota and 16α-hydroxyestrone, which were significantly different from males. After 21 days of stress, female anxiety and depression-like behavior worsened, gut metabolism and microbiota were disrupted, and there were marked differences in the microbiota (*f-Erysipelotrichaceae*) and metabolites (5α-pregnane-3,20-dione and 2-hydroxyestradiol). After 14 days of stress relief, male depression-like behavior began to recover, while females exhibited exacerbated estrogen metabolism (5α-pregnane-3,20-dione and estrone glucuronide) and gut microbiota (*f-Erysipelotrichaceae*) disorders and aggravated depression-like and anxiety-like behaviors. We hope that this study can provide basic evidence for the phenomenon of sex differences in depression and target markers for the treatment of female depression.

Author contributions

All authors contributed a substantial workload of the research and writing of this article. The work of all authors is as follows: HB and TG designed the experimental study of this article; YQ, JG, QX, and JW conducted the overall experiment of this article; YQ, XL, and HB analyzed the experimental data and wrote the manuscript; XZ, QX, and LW interpret the experimental results and critically revise the manuscript. All authors contributed to the article and approved the submitted version.

Data availability

The datasets presented in this study can be found in online repositories. The names of the repository/repositories and accession number(s) can be found in the article/Supplementary Material.

Ethics statement

The animal study was approved by the Chinese Academy of Sciences Approved by the Northwest Plateau Institute of Biology Committee for use in animal experiments (lot number NWIPB20171106-01). The study was conducted in accordance with the local legislation and institutional requirements.

Funding

The author(s) declare that financial support was received for the research, authorship, and/or publication of this article. This work was supported by the Natural Science Foundation of China (Grant No. 82171863), the Innovation Platform Program of Qinghai Province (2021-ZJ-T02), the Key project of Basic and applied Basic Research of Jiangmen (2021030103000007455), the Major Science and Technology Project of Qinghai Province (2021-SF-A4), and the Key project of Chinese Academy of Sciences (Grant No. ZDRW-ZS-2020-2).

Acknowledgments

The authors acknowledge Xingang Lv (Shanghai Applied Protein Technology Co, Ltd., China) for the technical support.

Conflict of interest

The author(s) declared no potential conflicts of interest with respect to the research, authorship, and/or publication of this article.

Supplementary material

The Supplementary Material for this article can be found online at: https://www.ebm-journal.org/articles/10.3389/ebm.2025.10204/full#supplementary-material

References

1. Martin Ginis KA, van der Ploeg HP, Foster C, Lai B, McBride CB, Ng K, et al. Participation of people living with disabilities in physical activity: a global perspective. *The Lancet* (2021) **398**(10298):443–55. doi:10.1016/S0140-6736(21)01164-8

2. Santomauro DF, Mantilla Herrera AM, Shadid J, Zheng P, Ashbaugh C, Pigott DM, et al. Global prevalence and burden of depressive and anxiety disorders in 204 countries and territories in 2020 due to the COVID-19 pandemic. *The Lancet* (2021) **398**(10312):1700–12. doi:10.1016/S0140-6736(21)02143-7

3. Thapar A, Eyre O, Patel V, Brent D. Depression in young people. *The Lancet* (2022) **400**(10352):617–31. doi:10.1016/S0140-6736(22)01012-1

4. Agirman G, Hsiao EY. SnapShot: the microbiota-gut-brain axis. *Cell* (2021) **184**(9):2524–.e1. doi:10.1016/j.cell.2021.03.022

5. Socała K, Doboszewska U, Szopa A, Serefko A, Włodarczyk M, Zielińska A, et al. The role of microbiota-gut-brain axis in neuropsychiatric and neurological disorders. *Pharmacol Res* (2021) **172**(172):105840. doi:10.1016/j.phrs.2021.105840

6. Góralczyk-Bińkowska A, Szmajda-Krygier D, Kozłowska E. The microbiota-gut-brain Axis in psychiatric disorders. *Int J Mol Sci* (2022) **23**(19):11245. doi:10.3390/ijms231911245

7. Flak MB, Neves JF, Blumberg RS. Welcome to the microgenderome. *Science* (2013) **339**(6123):1044–5. doi:10.1126/science.1236226

8. Markle JG, Frank DN, Mortin-Toth S, Robertson CE, Feazel LM, Rolle-Kampczyk U, et al. Sex differences in the gut microbiome drive hormone-dependent regulation of autoimmunity. *Science* (2013) **339**(6123):1084–8. doi:10.1126/science.1233521

9. Li D, Sun T, Tong Y, Le J, Yao Q, Tao J, et al. Gut-microbiome-expressed 3β-hydroxysteroid dehydrogenase degrades estradiol and is linked to depression in premenopausal females. *Cell Metab* (2023) **35**(4):685–94.e5. doi:10.1016/j.cmet.2023.02.017

10. Calcaterra V, Rossi V, Massini G, Regalbuto C, Hruby C, Panelli S, et al. Precocious puberty and microbiota: the role of the sex hormone-gut microbiome axis. *Front Endocrinol (Lausanne)* (2022) **13**:1000919. doi:10.3389/fendo.2022.1000919

11. Jiang Y, Greenwood-Van Meerveld B, Johnson AC, Travagli RA. Role of estrogen and stress on the brain-gut axis. *Am J Physiol Gastrointest Liver Physiol* (2019) **317**(2):G203–G209. doi:10.1152/ajpgi.00144.2019

12. Ding Q, Li H, Tian X, Shen Z, Wang X, Mo F, et al. Zinc and imipramine reverse the depression-like behavior in mice induced by chronic restraint stress. *J Affective Disord* (2016) **197**(197):100–6. doi:10.1016/j.jad.2016.03.017

13. Qiao Y, Zhao J, Li C, Zhang M, Wei L, Zhang X, et al. Effect of combined chronic predictable and unpredictable stress on depression-like symptoms in mice. *Ann Transl Med* (2020) **8**(15):942. doi:10.21037/atm-20-5168

14. Choleris E, Thomas AW, Kavaliers M, Prato FS. A detailed ethological analysis of the mouse open field test: effects of diazepam, chlordiazepoxide and an extremely low frequency pulsed magnetic field. *Neurosci Biobehav Rev* (2001) **25**(3):235–60. doi:10.1016/s0149-7634(01)00011-2

15. Cryan JF, Mombereau C, Vassout A. The tail suspension test as a model for assessing antidepressant activity: review of pharmacological and genetic studies in mice. *Neurosci and Biobehavioral Rev* (2005) **29**(4-5):571–625. doi:10.1016/j.neubiorev.2005.03.009

16. Porsolt RD, Le Pichon M, Jalfre M. Depression: a new animal model sensitive to antidepressant treatments. *Nature* (1977) **266**(5604):730–2. doi:10.1038/266730a0

17. Zhou B, Xiao JF, Tuli L, Ressom HW. LC-MS-based metabolomics. *Mol Biosyst* (2012) **8**(2):470–81. doi:10.1039/c1mb05350g

18. Wiklund S, Johansson E, Sjöström L, Mellerowicz EJ, Edlund U, Shockcor JP, et al. Visualization of GC/TOF-MS-based metabolomics data for identification of biochemically interesting compounds using OPLS class models. *Anal Chem* (2008) **80**(1):115–22. doi:10.1021/ac0713510

19. Kanehisa M, Sato Y, Kawashima M, Furumichi M, Tanabe M. KEGG as a reference resource for gene and protein annotation. *Nucleic Acids Res* (2016) **44**(D1):D457–62. doi:10.1093/nar/gkv1070

20. Amato KR, Yeoman CJ, Kent A, Righini N, Carbonero F, Estrada A, et al. Habitat degradation impacts black howler monkey (*Alouatta pigra*) gastrointestinal microbiomes. *The ISME J* (2013) **7**(7):1344–53. doi:10.1038/ismej.2013.16

21. Alarcón G, Pfeifer JH, Fair DA, Nagel BJ. Adolescent gender differences in cognitive control performance and functional connectivity between default mode and fronto-parietal networks within a self-referential context. *Front Behav Neurosci* (2018) **12**:73. doi:10.3389/fnbeh.2018.00073

22. Campos AC, Fogaça MV, Aguiar DC, Guimarães FS. Animal models of anxiety disorders and stress. *Revista Brasileira de Psiquiatria* (2013) **35**(Suppl. 2):S101–11. doi:10.1590/1516-4446-2013-1139

23. Sala L, Mirabel-Sarron C, Gorwood P, Pham-Scottez A, Blanchet A, Rouillon F. The level of associated depression and anxiety traits improves during weight regain in eating disorder patients. *Eat Weight Disord* (2011) **16**(4):e280–4. doi:10.1007/BF03327473

24. Seney ML, Huo Z, Cahill K, French L, Puralewski R, Zhang J, et al. Opposite molecular signatures of depression in men and women. *Biol Psychiatry* (2018) **84**(1):18–27. doi:10.1016/j.biopsych.2018.01.017

25. Fried EI. The 52 symptoms of major depression: lack of content overlap among seven common depression scales. *J Affective Disord* (2017) **208**(208):191–7. doi:10.1016/j.jad.2016.10.019

26. Wang K, Lu H, Cheung EF, Neumann DL, Shum DH, Chan RC. Female preponderance of depression in non-clinical populations: a meta-analytic study. *Front Psychol* (2016) **7**(7):1398. doi:10.3389/fpsyg.2016.01398

27. Albert KM, Newhouse PA. Estrogen, stress, and depression: cognitive and biological interactions. *Annu Rev Clin Psychol* (2019) **15**(15):399–423. doi:10.1146/annurev-clinpsy-050718-095557

28. Thériault RK, Perreault ML. Hormonal regulation of circuit function: sex, systems and depression. *Biol Sex Differ* (2019) **10**(1):12. doi:10.1186/s13293-019-0226-x

29. Foster JA. Modulating brain function with microbiota. *Science* (2022) **376**:936–7. doi:10.1126/science.abo4220

30. Morais LH, Schreiber HL4th, Mazmanian SK. The gut microbiota-brain axis in behaviour and brain disorders. *Nat Rev Microbiol* (2021) **19**(4):241–55. doi:10.1038/s41579-020-00460-0

31. Ma ZS, Li W. How and why men and women differ in their microbiomes: medical ecology and network analyses of the microgenderome. *Adv Sci* (2019) **6**(23):1902054. doi:10.1002/advs.201902054

32. Michaudel C, Sokol H. The gut microbiota at the service of immunometabolism. *Cell Metab* (2020) **32**(4):514–23. doi:10.1016/j.cmet.2020.09.004

33. Wang M, Song Z, Lai S, Tang F, Dou L, Yang F. Depression-associated gut microbes, metabolites and clinical trials. *Front Microbiol* (2024) **15**:1292004. doi:10.3389/fmicb.2024.1292004

34. Kim YS, Unno T, Kim BY, Park MS. Sex differences in gut microbiota. *World J Mens Health* (2020) **38**(1):48–60. doi:10.5534/wjmh.190009

35. Kelsey CM, Prescott S, McCulloch JA, Trinchieri G, Valladares TL, Dreisbach C, et al. Gut microbiota composition is associated with newborn functional brain connectivity and behavioral temperament. *Brain Behav Immun* (2021) **91**:472–86. doi:10.1016/j.bbi.2020.11.003

36. Dohnalová L, Lundgren P, Carty JRE, Goldstein N, Wenski SL, Nanudorn P, et al. A microbiome-dependent gut-brain pathway regulates motivation for exercise. *Nature* (2022) **612**(7941):739–47. doi:10.1038/s41586-022-05525-z

37. Ari C, Kovács Z, Juhasz G, Murdun C, Goldhagen CR, Koutnik AP, et al. Exogenous ketone supplements reduce anxiety-related behavior in sprague-dawley and wistar albino glaxo/rijswijk rats. *Front Mol Neurosci* (2016) **9**(9):137. doi:10.3389/fnmol.2016.00137

38. Cristiano C, Hoxha E, Lippiello P, Balbo I, Russo R, Tempia F, et al. Maternal treatment with sodium butyrate reduces the development of autism-like traits in mice offspring. *Biomed and Pharmacother* (2022) **156**(156):113870. doi:10.1016/j.biopha.2022.113870

39. Singh V, Lee G, Son H, Koh H, Kim ES, Unno T, et al. The Sentinel of Gut: their intestinal significance with and beyond butyrate, and prospective use as microbial therapeutics. *Front Microbiol* (2023) **12**:1103836. doi:10.3389/fmicb.2022.1103836

40. Chen YH, Xue F, Yu SF, Li XS, Liu L, Jia YY, et al. Gut microbiota dysbiosis in depressed women: the association of symptom severity and microbiota function. *J Affective Disord* (2021) **282**(282):391–400. doi:10.1016/j.jad.2020.12.143

41. Colzato LS, Hommel B. Effects of estrogen on higher-order cognitive functions in unstressed human females may depend on individual variation in dopamine baseline levels. *Front Neurosci* (2014) **8**:65. doi:10.3389/fnins.2014.00065

42. Seeger H, Mueck AO, Lippert TH. Effect of estradiol metabolites on the susceptibility of low density lipoprotein to oxidation. *Life Sci* (1997) **61**(9):865–8. doi:10.1016/s0024-3205(97)00588-2

43. Patel S, Hawkley LC, Cacioppo JT, Masi CM. Dietary fiber and serum 16α-hydroxyestrone, an estrogen metabolite associated with lower systolic

blood pressure. *Nutrition* (2011) **27**(7-8):778–81. doi:10.1016/j.nut.2010.08.017

44. Toffoletto S, Lanzenberger R, Gingnell M, Sundström-Poromaa I, Comasco E. Emotional and cognitive functional imaging of estrogen and progesterone effects in the female human brain: a systematic review. *Psychoneuroendocrinology* (2014) **50**:28–52. doi:10.1016/j.psyneuen.2014.07.025

45. Sundström Poromaa I, Gingnell M. Menstrual cycle influence on cognitive function and emotion processing-from a reproductive perspective. *Front Neurosci* (2014) **8**:380. doi:10.3389/fnins.2014.00380

46. de Bie J, Lim CK, Guillemin GJ. Progesterone alters kynurenine pathway activation in IFN-γ-Activated macrophages-relevance for neuroinflammatory diseases. *Int J tryptophan Res : IJTR* (2016) **9**:89–93. doi:10.4137/IJTR.S40332

47. Sha Q, Achtyes E, Nagalla M, Keaton S, Smart L, Leach R, et al. Associations between estrogen and progesterone, the kynurenine pathway, and inflammation in the post-partum. *J Affective Disord* (2021) **281**:9–12. doi:10.1016/j.jad.2020.10.052

48. Osborne LM, Gispen F, Sanyal A, Yenokyan G, Meilman S, Payne JL. Lower allopregnanolone during pregnancy predicts postpartum depression: an exploratory study. *Psychoneuroendocrinology* (2017) **79**:116–21. doi:10.1016/j.psyneuen.2017.02.012

49. Dhar V, Stark R, Kraulis I, Murphy‡ B. Contrasting effects of 5α- and 5β-pregnane-3,20-dione on the motor activity of ovariectomized rats. *J Steroid Biochem* (1987) **26**(5):577–80. doi:10.1016/0022-4731(87)90010-0

50. Teepker M, Anthes N, Krieg JC, Vedder H. 2-OH-estradiol, an endogenous hormone with neuroprotective functions. *J Psychiatr Res* (2003) **37**(6):517–23. doi:10.1016/s0022-3956(03)00068-2

51. Reilly D. Gender, culture, and sex-typed cognitive abilities. *PLoS One* (2012) **7**(7):e39904. doi:10.1371/journal.pone.0039904

52. Gordon JL, Sander B, Eisenlohr-Moul TA, Sykes Tottenham L. Mood sensitivity to estradiol predicts depressive symptoms in the menopause transition. *Psychol Med* (2021) **51**(10):1733–41. doi:10.1017/S0033291720000483

EBM Experimental Biology and Medicine

TYPE Mini Review
PUBLISHED 04 February 2025
DOI 10.3389/ebm.2025.10390

Check for updates

OPEN ACCESS

*CORRESPONDENCE
Prakash Gangadaran,
prakashg@knu.ac.kr

RECEIVED 29 September 2024
ACCEPTED 16 January 2025
PUBLISHED 04 February 2025

CITATION
Muthu S, Viswanathan VK and Gangadaran P (2025) Is platelet-rich plasma better than steroids as epidural drug of choice in lumbar disc disease with radiculopathy? Meta-analysis of randomized controlled trials. *Exp. Biol. Med.* 250:10390. doi: 10.3389/ebm.2025.10390

Is platelet-rich plasma better than steroids as epidural drug of choice in lumbar disc disease with radiculopathy? Meta-analysis of randomized controlled trials

Sathish Muthu[1,2,3], Vibhu Krishnan Viswanathan[1,4] and Prakash Gangadaran[5,6,7]*

[1]Department of Spine Surgery, Orthopaedic Research Group, Coimbatore, India, [2]Department of Biotechnology, Faculty of Engineering, Karpagam Academy of Higher Education, Coimbatore, India, [3]Department of Orthopaedics, Government Medical College, Karur, India, [4]Department of Orthopaedics, Devadoss Hospital, Madurai, India, [5]Department of Nuclear Medicine, School of Medicine, Kyungpook National University, Daegu, Republic of Korea, [6]BK21 FOUR KNU Convergence Educational Program of Biomedical Sciences for Creative Future Talents, School of Medicine, Kyungpook National University, Daegu, Republic of Korea, [7]Cardiovascular Research Institute, Kyungpook National University, Daegu, Republic of Korea

The current meta-analysis was performed to analyze the efficacy and safety of platelet-rich plasma (PRP) as an epidural injectate, in comparison with steroids in the management of radiculopathy due to lumbar disc disease (LDD). We conducted independent and duplicate searches of the electronic databases (PubMed, Embase and Cochrane Library) in March 2024 to identify randomized controlled trials (RCTs) analyzing the efficacy of epidural PRP for pain relief in the management of LDD. Animal or *in vitro* studies, clinical studies without a comparator group, and retrospective or non-randomised clinical studies were excluded. Diverse post-intervention pain scores [visual analog score (VAS)] and functional scores [Oswestry Disability Index (ODI), SF-36], as reported in the reviewed studies, were evaluated. Statistical analysis was performed using STATA 17 software. 5 RCTs including 310 patients (PRP/Steroids = 153/157) were included in the analysis. The included studies compared the efficacy and safety of epidural PRP and steroids at various time-points including 1, 3, 6, 12, 24, and 48 weeks. Epidural PRP injection was found to offer comparable pain relief (VAS; WMD = –0.09, 95% CI [–0.66, 0.47], $p = 0.641$; $I^2 = 96.72\%$, $p < 0.001$), functional improvement (ODI; WMD = 0.72, 95% CI [-6.81, 8.25], $p = 0.524$; $I^2 = 98.73\%$, $p < 0.001$), and overall health improvement (SF-36; WMD = 1.01, 95% CI [–1.14, 3.17], $p = 0.224$; $I^2 = 0.0\%$, $p = 0.36$) as epidural steroid injection (ESI) at all the observed time points in the included studies without any increase in adverse events or complications. Epidural administration of PRP offers comparable benefit as epidural steroid injection (ESI) in the management of radiculopathy due to LDD. The safety profile of the epidural PRP is also similar to ESI.

KEYWORDS

PRP, epidural steroid, degenerative disc disease, pain relief, biologics

Impact statement

This manuscript makes an important contribution to the field by providing a comprehensive meta-analysis on the use of platelet-rich plasma (PRP) as an alternative to steroids for epidural injections in managing radiculopathy caused by lumbar disc disease (LDD). By comparing PRP and steroids across multiple randomized controlled trials, this work advances the field by offering robust evidence that PRP provides similar pain relief, functional improvement, and overall health benefits as steroids, without increased risk of adverse events. This new information introduces a potential treatment option that could reduce dependency on steroids, thus having significant implications for patient care. The findings are timely and relevant, as they highlight PRP's comparable efficacy and safety, potentially shifting clinical practice toward non-steroid-based interventions for managing LDD-related radiculopathy.

Introduction

Lumbar radicular pain is a well-known cause for spinal disability secondary to mechanical compression of the nerve roots or inflammatory responses to the inciting stimuli [1, 2]. Conservative measures like bed rest, anti-inflammatory medications and physical therapy constitute the first line of management in these patients [3]. However, 20% of patients have recurrent or recalcitrant pain or symptoms despite such non-surgical measures [4].

Interlaminar or transforaminal epidural steroid injections (ESIs) have been acknowledged as interventions short of surgery, which may mitigate the symptoms and reduce the radicular pain [5, 6]. Traditionally, triamcinolone has remained the therapeutic drug utilized for epidural injections, in view of its excellent anti-inflammatory property and relatively low adverse events [7, 8]. While a majority of studies have reported substantial pain relief during the initial 3 months following ESI; the evidence in the current literature on the long-term outcome including need for surgical intervention at the end of 1 year is still largely unclear [9, 10]. In addition, certain studies have reported severe complications including allergic reactions, sepsis and chronic adrenal suppression [11, 12].

Platelet-rich plasma (PRP) is growingly recognized as an important adjuvant component in the field of orthopedic surgery, whose properties depend on the platelet and white blood cell (WBC) concentrations. Numerous cytokines within PRP like transforming growth factor (TGF) -β1, interleukin-1 receptor antagonist (IL-1RA), insulin-like growth factor (IGF-1) and platelet-derived growth factor (PDGF) form the basis for their regenerative and anti-inflammatory actions in the healing of various pathologies [13, 14]. In addition, in view of the autologous and antimicrobial nature of PRP, studies have indicated relatively lower concerns with regard to the infective and immunogenic complications following its use [15, 16]. Over the recent years, diverse studies have evaluated the role of PRP in the management of different degenerative, neuropathic and inflammatory pathologies of the spine [10, 17–19]. Even though meta-analyses have been published on the role of PRPs in spinal conditions, a majority of these reviews have followed inconsistent strategies for study inclusion; and have considered evidence from retrospective and non-randomized studies too [20–30]. In addition, may studies have also reviewed the role of PRP administration through different routes for a wide variety of spinal pathologies [16, 20]. As a result of such heterogeneity in the methodological quality and evidence available in the existing literature; diverse issues regarding the status of epidural administration of PRP in the management of lumbar radiculopathy, including its safety and efficacy (based on outcome measures like functional scores, improvement of pain scores, incidence of treatment failure and complication rates) are still largely controversial. The current meta-analysis was thus planned to comprehensively evaluate only the randomized controlled trials (RCTs) in available literature; and compare the safety profile and efficacy of epidural PRP injections with traditional ESIs.

Materials and methods

This meta-analysis was performed in compliance with the recommendations of the Back Review Group of Cochrane Collaboration [25] and presented in adherence to the Preferred Reporting Items for Systematic Reviews and Meta-Analyses (PRISMA) statement [31].

Search strategy

Two reviewers were involved in making an independent electronic literature search for RCTs evaluating the efficacy

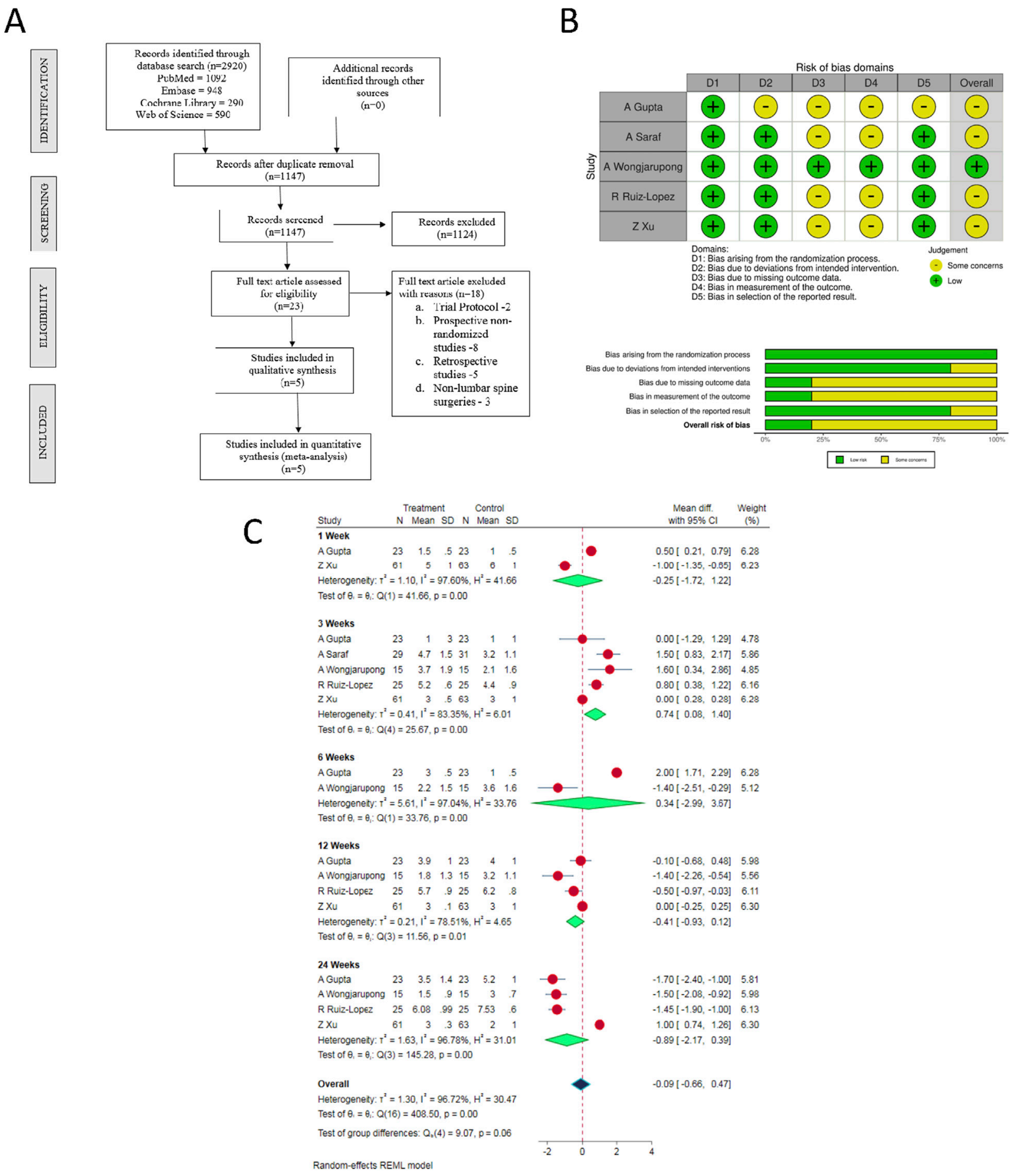

FIGURE 1
(A) PRISMA flow diagram of the included studies. **(B)** Quality and risk of bias assessment of all the included studies. **(C)** Forest plot of the included studies comparing post-operative pain score at various time points.

of PRP, as compared to steroids in the management of degenerative lumbar disc disease (LLD). The databases namely, PubMed, Embase and the Cochrane Library, were searched to identify all the relevant studies published until March 2024 (no specific date restrictions were applied to the search query).

We used the following keywords in the database search: "Platelet-rich Plasma," "Epidural steroid," "Lumbar degenerative disc disease." We also went through the references of the articles shortlisted from preliminary screening to identify studies missed in the preliminary search. Studies were then selected for the meta-analysis based on the specific inclusion and exclusion criteria, mentioned vide-infra. In case of any discrepancy in selecting the article, the final decision was made based on the consensus achieved through mutual discussions. The sequence of selecting the studies for the analysis has been shown in the PRISMA flow diagram (Figure 1A).

Inclusion criteria

We included studies for analysis based on the PICOS criteria:

Population: Patients with lumbar disc disease with radicular pain.
Intervention: Epidural PRP.
Comparator: Epidural steroids.
Outcomes: Post-operative pain scores, functional scores, complications.
Study Design: Randomized controlled trials (RCTs).

Exclusion criteria

Studies were excluded from the review based upon the following criteria:

1. Animal studies involving PRP in disc disease conditions.
2. *In vitro* studies on PRP in disc disease models.
3. Studies without a comparator group such as case series and case reports.

Data extraction

Two reviewers independently retrieved relevant data from the articles included for analysis. The following data were extracted from the reviewed studies:

1. *Study characteristics*: Year of publication, authors, country, number of patients enrolled.
2. *Baseline characteristics*: Mean age, gender proportions, levels involved, route of administration.
3. *Primary Outcomes*: Post-operative pain scores
   Secondary Outcomes: Functional scores and overall health related scores.
   Other Outcomes: Adverse events and complications.

If any data was found missing from the included study, we contacted the corresponding authors of the study for necessary clarifications. All discrepancies were resolved through mutual discussions among the authors.

Risk of bias and quality assessment

Two reviewers independently assessed the methodological quality of the included studies with the help of Cochrane Collaboration's RoB 2 tool for RCTs with five domains of bias assessment included in them [32].

Statistical analysis

We performed the meta-analysis of the pooled data in Stata software Version 17. In case of dichotomous variables, we utilised odds ratio (OR) with 95% Confidence Interval (CI). For analysing continuous variables, we used weighted mean difference (WMD) with 95% CI. We evaluated the heterogeneity of the pooled data using I^2 statistics [33]. If $I^2 < 50\%$ and $p > 0.1$, a fixed-effects model was employed in meta-analysis. On the other hand, if $I^2 > 50\%$ and $p < 0.1$, random-effects model was utilised. Publication bias was evaluated with funnel plots and egger regression test. Heterogeneity was explored with galbraith plot. Further, subgroup and sensitivity analyses were performed to examine the causes of heterogeneity. A p-value of less than 0.05 was considered significant.

Results

Search results

Electronic database search resulted in 2,920 articles, which after initial screening through de-duplication, revealed a total of 1,147 articles. After title and abstract screening of these articles, 1,124 were excluded. 23 articles qualified for full-text review; among which, 18 were excluded. Finally, 5 RCTs [34, 35, 37, 38] involving a total of 310 patients (ESPB group/Control group = 153/157) were included in our meta-analysis. PRISMA flow diagram of study selection is given in Figure 1A. The general characteristics of the RCTs included in our analysis have been shown in Supplementary Table S1. PRP protocols of the included studies are shown in Supplementary Table S2.

Quality assessment

The methodological quality of the included studies is depicted in Figure 1B. Based on the available data, none of

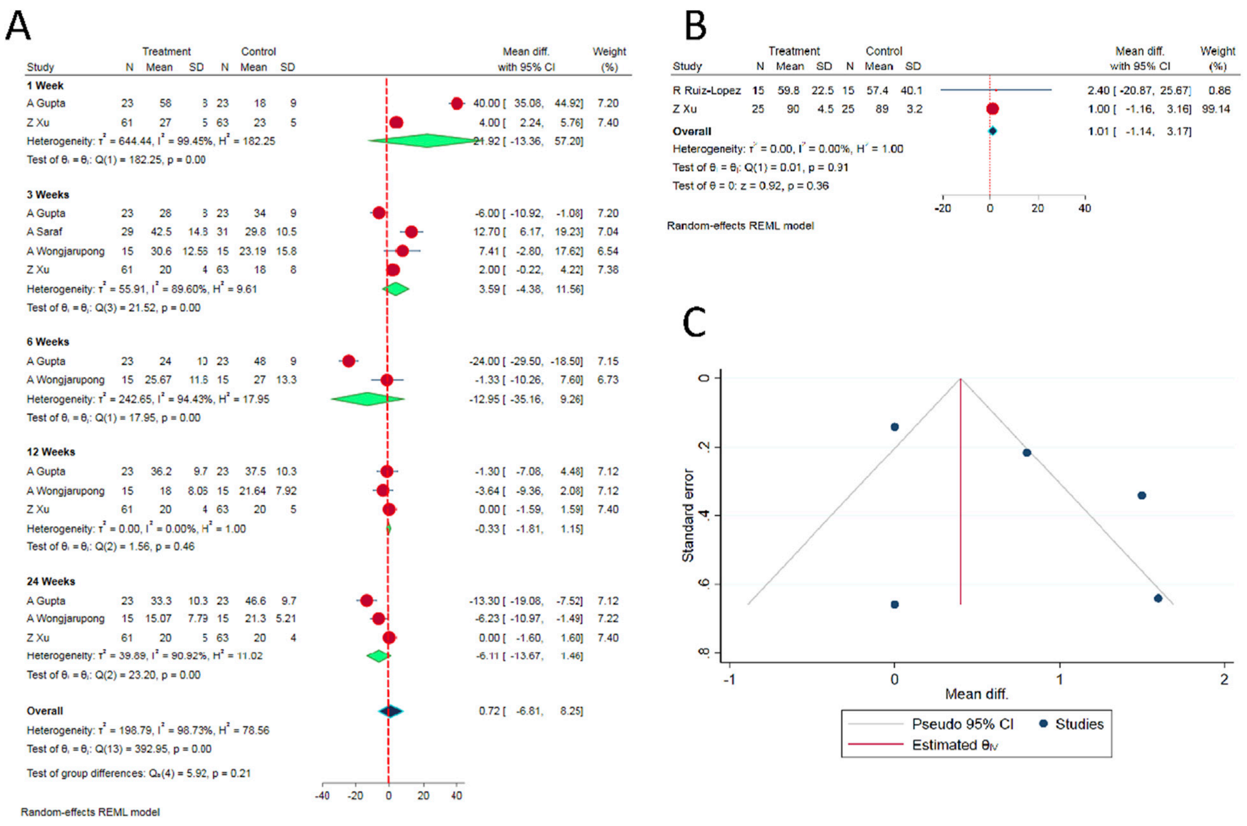

FIGURE 2

(A) Forest plot of the included studies comparing functional score at various time points. **(B)** Forest plot of the included studies comparing overall health score SF-36 at 6 months. **(C)** Funnel plot estimation of the publication bias in the included studies for analysis.

the included studies had an overall high risk of bias which necessitated an exclusion from the analysis.

Primary outcomes

VAS (visual analog scale) score

There were substantial variations in the time points at which the post-operative pain scores were evaluated in the included studies. Therefore, we considered only the post-operative pain score measurements at 1-, 3-, 6-, 12- and 24-week time points for our analysis (as reported in the individual studies). In view of the significant heterogeneity among the reviewed studies, random-effects model was utilized for analysis. Epidural PRP was shown to be comparable to the epidural steroid in relieving pain at all the observed time points with the overall [WMD = −0.09, 95% CI (−0.66, 0.47), $p = 0.641$; $I^2 = 96.72\%$, $p < 0.001$; as shown in Figure 1C].

ODI (oswestry disability index) score

Similar to the VAS, there was substantial heterogeneity in the time points at which the ODI scores were measured in the included studies. Hence, we analyzed post-operative ODI scores reported at 1-, 3-, 6-, 12- and 24-week time points in the reviewed studies. There was no significant difference between the epidural PRP and epidural steroid injections with regard to the ODI scores at all the aforementioned time points [WMD = 0.72, 95% CI (−6.81, 8.25), $p = 0.524$; $I^2 = 98.73\%$, $p < 0.001$; as shown in Figure 2A].

SF-36 score

Based on our comparison of SF-36 scores between the epidural PRP and epidural steroid injections, there was no significant difference between the intervention groups at 6th month time point [WMD = 1.01, 95% CI (−1.14, 3.17), $p = 0.224$; $I^2 = 0.0\%$, $p = 0.36$; as shown in Figure 2B].

Complications

Based on our analysis of 3 studies, we could not observe any significant difference in the incidence of adverse events or complications between the epidural PRP and epidural steroid injection groups ($p > 0.05$) [34, 37, 38].

Publication bias analysis

Given the limited number of RCTs on the subject, estimating publication bias and sensitivity analysis to explore into the heterogeneity in the results among the included studies would not yield meaningful results. Nevertheless, funnel plot was generated for the VAS score for pain relief. We did not observe significant asymmetry as shown in Figure 2C. In addition, Egger's regression test did not show significant publication bias (p = 0.274).

Discussion

The overall prevalence of symptomatic low back pain (LBP) is approximately 1–3%; while the prevalence of lumbar radicular pain is reportedly around 0.98% [30, 35, 36]. Administration of medications through epidural route has been traditionally practised as an intervention short of surgery in patients with radicular symptoms secondary to lumbar spine pathologies like lumbar disc herniation (LDH) or canal stenosis [37]. Corticosteroids (especially triamcinolone) have quintessentially remained the drug of choice for epidural administration, although recent studies have demonstrated a lack of clear evidence regarding its superiority over placebo agents in improving function, obviating surgery or mitigating disability [12]. In addition, some researchers have also underscored the need to consider the numerous adverse events associated with steroid use, including its impact over diverse bodily functions [38]. It is well established that cytokine production from macrophages or disc cells play an important role in pain generation in patients with degenerative disc disease. In this context, the role of cell-based biological therapies such as autologous bone marrow concentrate (BMC), platelet rich plasma (PRP), mesenchymal stem cells (MSC), autologous conditioned serum (ACS) and platelet lysate in diverse spinal pathologies have been widely discussed [17, 19, 39, 40]. The current meta-analysis of RCTs was performed to comprehensively examine the role of PRP as an epidural injectate in mitigating LBP and lumbar radiculopathy.

Rationale of biological agents in chronic LBP

The nucleus pulposus (NP) consists of diverse inflammatory cytokines and pain mediators including phospholipase A2, nitric oxide, prostaglandin E, and IL-1 [41, 42]. Studies have also demonstrated that disc material through inflammatory mediators produces direct chemical injury to the nerve root; and enhances the intra- and extra-neural inflammation, venous congestion as well as conduction block [43]. Among all the aforementioned mediators, IL-1 has been acknowledged to play a special role in the development of low back pain. Among the biological agents inhibiting IL-1, IL-1 receptor antagonist (IL-1RA), soluble IL-1 receptors, and type-1 cytokines like IL-4, IL-10, and IL-13 have been examined for their therapeutic efficacy.

With progressive developments in the biological agents, PRP and its derivatives, mesenchymal stem cells (MSC), plasma lysate, plasma rich in growth factors (PRGF-Endoret) and ACS have been proposed as biologics amenable to delivery through epidural route. ACS is a rich source of anti-inflammatory cytokines like IL-4, IL-10, IL-13, IL-1RA, fibroblast growth factor-2 (FGF-2), hepatocyte growth factor (HGF), and transforming growth factor-β (TGF-β) [39, 44]. Being an IL-1 receptor antagonist, ACS has been growing in popularity as an epidural treatment option in the form of a "biochemical sensitiser" of inflamed nerve roots [30, 40].

The platelet concentration within PRP is 3–8 times higher than the serum level, which facilitates its anti-inflammatory, angiogenic, cell-migration enhancing and anabolic potential for tissue regeneration. The activated platelets release diverse growth factors like TGF-β, insulin-like growth factor (IGF), platelet-derived growth factor (PDGF), vascular endothelial growth factor (VEGF) and fibroblast growth factor (FGF), which in turn, enable tissue healing through stimulation of chondrocytes, collagen synthesis, inhibition of cell apoptosis and regulation or catabolic cytokines. In addition, PRP has been shown to play a vital role in the healing of connective tissues like Sox9, AGN, COL I and COL II [23, 45].

Preparations of PRP

The purification processes for PRP have broadly been categorised into open and closed techniques [20]. Diverse systems for centrifugation and concentration of platelets have been described in the literature; and different classification systems for such PRP preparations have been described. Certain basic and clinical studies have shown that high concentrations of leucocytes can negatively impact the PRP efficacy; however, the issue is still controversial across various indications [14, 46]. Dohan et al. [47] classified PRP preparations into pure-PRP (P-PRP), leucocyte-rich PRP (L-PRP) and pure platelet-rich fibrin (P-PRF), based on the relative concentrations of the components. Mishra et al. [48] further categorised PRP preparations in 8 categories based on leucocyte concentration, activation of leucocytes and platelet concentrations.

Injection strategies in the published literature

Based on the review by Kawabata et al. [20], the role of PRP in the repair of degenerated disc, promotion of spinal fusion and enhancing neurological recovery after spinal cord injury (SCI) were discussed in detail. Studies have evaluated epidural injections through interlaminar (IL), transforaminal (TF) and caudal routes. Some studies also evaluated the role of PRP injections into paraspinal musculature (intra-muscular), facet joints, intravertebral disc space, sacroiliitis, and spinal ligaments [20, 26]. In a majority of the published studies, the injection was administered under fluoroscopic guidance, while ultrasound- and computed tomography (CT)-guided approaches were utilised in certain studies. A majority of the reviewed studies evaluated outcome following single-time PRP injection [14, 20].

Results of our meta-analysis

Our meta-analysis is the first study to only evaluate all the RCTs hitherto published comparing the efficacy and safety of epidural corticosteroid and PRP injections for lumbar radiculopathy. All the previous systematic reviews or meta-analyses have included retrospective, non-randomised studies, studies involving other control arms for comparative analysis; or included studies evaluating different types of injections for LBP secondary to multiple spinal pathologies [20, 23, 26, 29, 30]. In view of such wide variations in the study designs and analysis, there is still substantial ambiguity in our knowledge regarding this subject and heterogeneity in the available results. Our meta-analysis was thus planned to examine the true role of this modality in the context of lumbar radiculopathy.

Evidence from available RCTs

In the RCT by Ruiz-Lopez and Tsai (2020) [21], caudal injection of PRP in 50 patients with LBP provided substantial improvement in pain and disability during the immediate post-intervention period. The procedure also resulted in superior outcome than corticosteroids at the 6th month followup time point [49]. In recent double-blind, prospective, randomised controlled study (involving 46 patients) comparing transforaminal epidural PRP and corticosteroid injections, Gupta et al. [25] concluded that transforaminally-administered epidural PRP injection had significantly better outcome than steroid injection at the 6th week and 6th month time points; however, the outcome at the end of 1 year was comparable between the two groups.

In another recently-published RCT by Saraf et al. [24], substantially better outcome was observed in the steroid group at the end of 1 month ($p < 0.001$ for both VAS and modified ODI scores); although, PRP showed sustained minimal clinically important benefit (MCID) at 6 months ($p < 0.001$). In the RCT published by Wongjarupong et al. [18], it was demonstrated that transforaminal epidural injection of PRP demonstrated clinical meaningful improvements (significant MCID) in leg VAS score at 6, 12, and 24 weeks; and in ODI at 24 weeks. They concluded that epidural, double-spin PRP provided significantly better results in comparison with triamcinolone administration.

On the other hand, in the RCT by Xu et al. [22], among 124 patients treated with USG-guided TF epidural injections using steroid or PRP, similar outcome was observed between the two patient groups in terms of VAS, ODI, and SF-36 (physical function and bodily pain) and complications at various time points (1 week, 1 month, 3 months, 6 months, and 1 year). Thus, based on the previously published RCTs, the reporting of the improvement in pain and disability is substantially varied across different time points [18, 21, 22, 24, 25]. While some studies have reported better early or more consistent outcome with PRP, others have observed no significant differences between the two approaches.

Corroborative evidence from our meta-analysis

For our analysis, we compared the outcome and complications reported at 1-, 3-, 6-, 12- and 24-week time points in the reviewed articles. We compared the outcome based on the VAS, ODI and SF-36 scores, as reported in the reviewed RCTs. Based on our analysis, we did not observe any significant difference between the two groups (ESI vs. epidural PRPs) at all the time points for all the aforementioned outcome measurements. Thus, the current evidence does not demonstrate a substantial superiority of PRP injections over ESI, in terms of clinical effectiveness or efficacy (either during the early or delayed post-intervention time points). Among the studies, only Saraf et al. [24] included a clinical parameter (straight leg raising test - SLR) for evaluating the outcome during the followup assessments. In this study, at the end of 6 months, 90% and 62% of patients were SLR (straight leg raising) test negative in the PRP and steroid groups, respectively.

Complication rates

Among the reviewed RCTs, only 2 major complications were directly attributed to the medications. In the study by Ruiz Lopez et al. [21], one male patient in the leucocyte-rich PRP group experienced itching in the pelvic area, which was relieved following treatment with antihistaminics. In the another RCT [18], 2 patients in the triamcinolone injection group required to undergo surgery within 6 weeks in view of treatment failure. Our metaanalysis also (similar to other previous reviews [22–24, 30, 49, 50]) did not reveal any statistical difference in the complication or adverse event rates between the two interventions.

In the RCT by Gupta et al. [25], they concluded that since PRPs are autologous components, multiple injections could be safely administered (with minimal added complications), as compared to corticosteroids. Thus, based on the available literature, there is significant evidence to support the safety of epidural PRP injections in patients with lumbar radiculopathy.

Evidence based on other systematic reviews on PRP

Overall, pain intensity has been variously evaluated in the literature using different parameters including VAS score, numerical pain score (NPS), Lattinen index, COMI pain score (CPS) and Oswestry pain score (OPS); functional outcome by Oswestry Disability Index (ODI), functional rating index (FRI), single assessment numerical evaluation (SANE), MacNab criteria, Modified Oswestry Disability Questionnaire (MODQ), physical performance test (PPT), SF-36 with subscores for bodily pain and physical functioning, COMI disability score (CDS) and Rolland Morris Disability Questionnaire (MODQ) [21, 28, 29, 45].

Although a majority of the systematic reviews hitherto published [23, 28, 29], all the studies have highlighted on the lack of high quality and reliable evidence on this subject. In a recent systematic review, Machado et al. [29] concluded that a majority of published studies have revealed positive results regarding the effectiveness of PRP, with a relatively low risk of overall bias. The quality of evidence supporting PRP in LBP was graded as level-II (defined as "moderate evidence from at least one relevant high-quality RCT or multiple relevant moderate-/lower-quality RCTs). They emphasized on the need for large-scale, multi-centered RCT on this subject to further substantiate their observations.

In another systematic review by Kubrova et al. [28], 12 studies (3 RCTs and 9 observational studies) were considered. While pain intensity was the primary outcome evaluated; functional improvement, radiological findings and complications were the secondary outcome parameters considered. They also demonstrated that PRP was associated with similar or longer pain relief, with effects extending up to 12 or 24 months. The Grading of Recommendations Assessment, Development and Evaluation (GRADE) analysis showed very low certainty of available evidence owing to the risk of bias and imprecision. We therefore conducted a meta-analysis including only RCTs (2 additional RCTs have been published since the last review) in order to provide a more definite verdict on this subject.

Limitations of our study

Only 5 RCTs have been published on this subject hitherto, with relatively small sample size. Although a wide variety of outcome measures have been examined in the literature heretofore; only certain parameters (VAS, ODI and SF-36) were amenable to meta-analysis. There are variations in the PRP preparations, techniques for injections, post-intervention protocols and follow-up strategies employed in the individual studies. Nevertheless, our study is the only meta-analysis to provide the highest quality evidence, based only upon the updated RCTs published till date on this issue.

Conclusion

Epidural administration of PRP offers comparable (and not superior) benefit as ESI in the management of radiculopathy due to LDD. The safety profile of the epidural PRP is also similar to ESI. Nevertheless, large-scale, multi-centric RCTs involving larger sample population, and longer follow-up are necessary to further validate our observations.

Author contributions

Conception and design: SM, VV, and PG; administrative support: SM, VV, and PG; provision of study materials SM and VV; collection and assembly of data: SM and VV; data analysis and interpretation: SM, VV, and PG; manuscript writing: All authors; and funding acquisition: PG. All authors contributed to the article and approved the submitted version.

Funding

The author(s) declare that financial support was received for the research, authorship, and/or publication of this article. This research was supported by Basic Science Research Program through the National Research Foundation of Korea (NRF) funded by the Ministry of Education (NRF-2022R1I1A1A01068652).

Conflict of interest

The author(s) declared no potential conflicts of interest with respect to the research, authorship, and/or publication of this article.

Generative AI statement

The author(s) declare that no Generative AI was used in the creation of this manuscript.

Supplementary material

The Supplementary Material for this article can be found online at: https://www.ebm-journal.org/articles/10.3389/ebm.2025.10390/full#supplementary-material

References

1. Bogduk N. On the definitions and physiology of back pain, referred pain, and radicular pain. *Pain* (2009) **147**(1–3):17–9. doi:10.1016/j.pain.2009.08.020

2. Peng B, Wu W, Li Z, Guo J, Wang X. Chemical radiculitis. *Pain* (2007) **127**(1–2):11–6. doi:10.1016/j.pain.2006.06.034

3. Slipman CW, Isaac Z, Lenrow DA, Chou LH, Gilchrist RV, Vresilovic EJ. Clinical evidence of chemical radiculopathy. *Pain Physician* (2002) **5**(3):260–5.

4. Weber H, Holme I, Amlie E. The natural course of acute sciatica with nerve root symptoms in a double-blind placebo-controlled trial evaluating the effect of piroxicam. *Spine (Phila Pa 1976)* (1993) **18**(11):1433–8. doi:10.1097/00007632-199318110-00006

5. Liu J, Zhou H, Lu L, Li X, Jia J, Shi Z, et al. The effectiveness of transforaminal versus caudal routes for epidural steroid injections in managing lumbosacral radicular pain: a systematic review and meta-analysis. *Medicine (Baltimore)* (2016) **95**(18):e3373. doi:10.1097/MD.0000000000003373

6. Saal JA, Saal JS. Nonoperative treatment of herniated lumbar intervertebral disc with radiculopathy. An outcome study. *Spine (Phila Pa 1976)* (1989) **14**(4):431–7. doi:10.1097/00007632-198904000-00018

7. Yang S, Kim W, Kong HH, Do KH, Choi KH. Epidural steroid injection versus conservative treatment for patients with lumbosacral radicular pain: a meta-analysis of randomized controlled trials. *Medicine (Baltimore)* (2020) **99**(30):e21283. doi:10.1097/MD.0000000000021283

8. Wilson-MacDonald J, Burt G, Griffin D, Glynn C. Epidural steroid injection for nerve root compression. A randomised, controlled trial. *The J Bone Joint Surg Br volume* (2005) **87-B**(3):352–5. doi:10.1302/0301-620x.87b3.15338

9. Koes BW, Scholten RJPM, Mens JMA, Bouter LM. Efficacy of epidural steroid injections for low-back pain and sciatica: a systematic review of randomized clinical trials. *Pain* (1995) **63**(3):279–88. doi:10.1016/0304-3959(95)00124-7

10. Bhatia A, Flamer D, Shah PS, Cohen SP. Transforaminal epidural steroid injections for treating lumbosacral radicular pain from herniated intervertebral discs: a systematic review and meta-analysis. *Anesth & Analgesia* (2016) **122**(3):857–70. doi:10.1213/ANE.0000000000001155

11. Manchikanti L, Falco FJE. Safeguards to prevent neurologic complications after epidural steroid injections: analysis of evidence and lack of applicability of controversial policies. *Pain Physician* (2015) **18**(2):E129–138.

12. Knezevic NN, Jovanovic F, Voronov D, Candido KD. Do corticosteroids still have a place in the treatment of chronic pain? *Front Pharmacol* (2018) **9**:1229. doi:10.3389/fphar.2018.01229

13. Padilla S, Sánchez M, Orive G, Anitua E. Human-based biological and biomimetic autologous therapies for musculoskeletal tissue regeneration. *Trends Biotechnol* (2017) **35**(3):192–202. doi:10.1016/j.tibtech.2016.09.008

14. DeLong JM, Russell RP, Mazzocca AD. Platelet-rich plasma: the PAW classification system. *Arthroscopy* (2012) **28**(7):998–1009. doi:10.1016/j.arthro.2012.04.148

15. Fabbro MD, Bortolin M, Taschieri S, Ceci C, Weinstein RL. Antimicrobial properties of platelet-rich preparations. A systematic review of the current pre-clinical evidence. *Platelets* (2016) **27**(4):276–85. doi:10.3109/09537104.2015.1116686

16. Anitua E, Padilla S. Biologic therapies to enhance intervertebral disc repair. *Regen Med* (2018) **13**(1):55–72. doi:10.2217/rme-2017-0111

17. Bhatia R, Chopra G. Efficacy of platelet rich plasma via lumbar epidural route in chronic prolapsed intervertebral disc patients-A pilot study. *J Clin Diagn Res* (2016) **10**(9):UC05–UC07. doi:10.7860/JCDR/2016/21863.8482

18. Wongjarupong A, Pairuchvej S, Laohapornsvan P, Kotheeranurak V, Jitpakdee K, Yeekian C, et al. "Platelet-Rich Plasma" epidural injection an emerging strategy in lumbar disc herniation: a Randomized Controlled Trial. *BMC Musculoskelet Disord* (2023) **24**:335. doi:10.1186/s12891-023-06429-3

19. Centeno C, Markle J, Dodson E, Stemper I, Hyzy M, Williams C, et al. The use of lumbar epidural injection of platelet lysate for treatment of radicular pain. *J Exp Orthopaedics* (2017) **4**(1):38. doi:10.1186/s40634-017-0113-5

20. Kawabata S, Akeda K, Yamada J, Takegami N, Fujiwara T, Fujita N, et al. Advances in platelet-rich plasma treatment for spinal diseases: a systematic review. *Int J Mol Sci* (2023) **24**(8):7677. doi:10.3390/ijms24087677

21. Ruiz-Lopez R, Tsai YC. A randomized double-blind controlled pilot study comparing leucocyte-rich platelet-rich plasma and corticosteroid in caudal epidural injection for complex chronic degenerative spinal pain. *Pain Pract* (2020) **20**(6):639–46. doi:10.1111/papr.12893

22. Xu Z, Wu S, Li X, Liu C, Fan S, Ma C. Ultrasound-guided transforaminal injections of platelet-rich plasma compared with steroid in lumbar disc herniation: a prospective, randomized, controlled study. *Neural Plasticity* (2021) **2021**:1–11. doi:10.1155/2021/5558138

23. Singjie LC, Kusuma SA, Saleh I, Kholinne E. The potency of platelet-rich plasma for chronic low back pain: a systematic review and metaanalysis of randomized controlled trial. *Asian Spine J* (2023) **17**(4):782–9. doi:10.31616/asj.2022.0209

24. Saraf A, Hussain A, Sandhu AS, Bishnoi S, Arora V. Transforaminal injections of platelet-rich plasma compared with steroid in lumbar radiculopathy: a prospective, double-blind randomized study. *Indian J Orthopaedics* (2023) **57**(7):1126–33. doi:10.1007/s43465-023-00898-3

25. Gupta A, Chhabra HS, Singh V, Nagarjuna D. Lumbar transforaminal injection of steroids versus platelet-rich plasma for prolapse lumbar intervertebral disc with radiculopathy: a randomized double-blind controlled pilot study. *Asian Spine J* (2024) **18**(1):58–65. doi:10.31616/asj.2023.0115

26. Urits I, Viswanath O, Galasso AC, Sottosani ER, Mahan KM, Aiudi CM, et al. Platelet-rich plasma for the treatment of low back pain: a comprehensive review. *Curr Pain Headache Rep* (2019) **23**(7):52. doi:10.1007/s11916-019-0797-6

27. Patel A, Koushik S, Schwartz R, Gritsenko K, Farah F, Urits I, et al. Platelet-rich plasma in the treatment of facet mediated low back pain: a comprehensive review. *Orthop Rev* (2022) **14**(4):37076. doi:10.52965/001c.37076

28. Kubrova E, Martinez Alvarez GA, Her YF, Pagan-Rosado R, Qu W, D'Souza RS. Platelet rich plasma and platelet-related products in the treatment of radiculopathy-A systematic review of the literature. *Biomedicines* (2022) **10**(11):2813. doi:10.3390/biomedicines10112813

29. Machado ES, Soares FP, Vianna de Abreu E, de Souza TAC, Meves R, Grohs H, et al. Systematic review of platelet-rich plasma for low back pain. *Biomedicines* (2023) **11**(9):2404. doi:10.3390/biomedicines11092404

30. Sanapati J, Manchikanti L, Atluri S, Jordan S, Albers SL, Pappolla MA, et al. Do regenerative medicine therapies provide long-term relief in chronic low back pain: a systematic review and metaanalysis. *Pain Physician* (2018) **21**(6):515–40.

31. Page MJ, McKenzie JE, Bossuyt PM, Boutron I, Hoffmann TC, Mulrow CD, et al. The PRISMA 2020 statement: an updated guideline for reporting systematic reviews. *BMJ* (2021) **372**:n71. doi:10.1136/bmj.n71

32. Sterne JAC, Savović J, Page MJ, Elbers RG, Blencowe NS, Boutron I, et al. RoB 2: a revised tool for assessing risk of bias in randomised trials. *BMJ* (2019) **366**:l4898. doi:10.1136/bmj.l4898

33. Higgins JPT, Thompson SG, Deeks JJ, Altman DG. Measuring inconsistency in meta-analyses. *BMJ* (2003) **327**(7414):557–60. doi:10.1136/bmj.327.7414.557

34. Wongjarupong A, Pairuchvej S, Laohapornsvan P, Kotheeranurak V, Jitpakdee K, Yeekian C, et al. "Platelet-Rich Plasma" epidural injection an emerging strategy in lumbar disc herniation: a Randomized Controlled Trial. *BMC Musculoskelet Disord* (2023) **24**(1):335. doi:10.1186/s12891-023-06429-3

35. Manchikanti L, Soin A, Benyamin RM, Singh V, Falco FJ, Calodney AK, et al. An update of the systematic appraisal of the accuracy and utility of discography in chronic spinal pain. *Pain Physician* (2018) **21**(2):91–110.

36. Savettieri G, Salemi G, Rocca WA, Meneghini F, D'Arpa A, Morgante L, et al. Prevalence of lumbosacral radiculopathy in two Sicilian municipalities. *Acta Neurol Scand* (2009) **93**(6):464–9. doi:10.1111/j.1600-0404.1996.tb00027.x

37. Rivera CE. Lumbar epidural steroid injections. *Phys Med Rehabil Clin North America* (2018) **29**(1):73–92. doi:10.1016/j.pmr.2017.08.007

38. Knezevic NN, Manchikanti L, Urits I, Orhurhu V, Vangala BP, Vanaparthy R, et al. Lack of superiority of epidural injections with lidocaine with steroids compared to without steroids in spinal pain: a systematic review and meta-analysis. *Pain Physician* (2020) **23**(4S):S239–S270.

39. Becker C, Heidersdorf S, Drewlo S, de Rodriguez SZ, Krämer J, Willburger RE. Efficacy of epidural perineural injections with autologous conditioned serum for lumbar radicular compression: an investigator-initiated, prospective, double-blind, reference-controlled study. *Spine (Phila Pa 1976)* (2007) **32**(17):1803–8. doi:10.1097/BRS.0b013e3181076514

40. H SRK, Goni VG, Y KB. Autologous conditioned serum as a novel alternative option in the treatment of unilateral lumbar radiculopathy: a prospective study. *Asian Spine J* (2015) **9**(6):916–22. doi:10.4184/asj.2015.9.6.916

41. Hirsch JA, Harvey HB, Barr RM, Donovan W, Duszak R, Jr, Nicola G, et al. Sustainable growth rate repealed, MACRA revealed: historical context and analysis of recent changes in medicare physician payment methodologies. *AJNR Am J Neuroradiol* (2016) **37**(2):210–4. doi:10.3174/ajnr.A4522

42. Basso M, Cavagnaro L, Zanirato A, Divano S, Formica C, Formica M, et al. What is the clinical evidence on regenerative medicine in intervertebral disc

degeneration? *Musculoskelet Surg* (2017) **101**(2):93–104. doi:10.1007/s12306-017-0462-3

43. Saal JA. Natural history and nonoperative treatment of lumbar disc herniation. *Spine (Phila Pa 1976)* (1996) **21**(24 Suppl. l):2S–9S. doi:10.1097/00007632-199612151-00002

44. Wright-Carpenter T, Klein P, Schäferhoff P, Appell HJ, Mir LM, Wehling P. Treatment of muscle injuries by local administration of autologous conditioned serum: a pilot study on sportsmen with muscle strains. *Int J Sports Med* (2004) **25**(8):588–93. doi:10.1055/s-2004-821304

45. Akeda K, Ohishi K, Takegami N, Sudo T, Yamada J, Fujiwara T, et al. Platelet-rich plasma releasate versus corticosteroid for the treatment of discogenic low back pain: a double-blind randomized controlled trial. *J Clin Med* (2022) **11**(2):304. doi:10.3390/jcm11020304

46. Muthu S, Patel S, Selvaraj P, Jeyaraman M. Comparative analysis of leucocyte poor vs leucocyte rich platelet-rich plasma in the management of lateral epicondylitis: systematic review & meta-analysis of randomised controlled trials. *J Clin Orthopaedics Trauma* (2021) **19**:96–107. doi:10.1016/j.jcot.2021.05.020

47. Dohan Ehrenfest DM, Andia I, Zumstein MA, Zhang CQ, Pinto NR, Bielecki T. Classification of platelet concentrates (Platelet-Rich Plasma-PRP, Platelet-Rich Fibrin-PRF) for topical and infiltrative use in orthopedic and sports medicine: current consensus, clinical implications and perspectives. *Muscles Ligaments Tendons J* (2014) **4**(1):3–9.

48. Mishra A, Harmon K, Woodall J, Vieira A. Sports medicine applications of platelet rich plasma. *Curr Pharm Biotechnol* (2012) **13**(7):1185–95. doi:10.2174/138920112800624283

49. Núñez PPB, Cedeño JLH, Oliver TG. Efficacy of parasargital translaminar epidural application of growth factors derived from Platelet Rich Plasma as a treatment for unilateral root pain caused by multisegmental disc disease. *Invest Medicoquir* (2021) **13**(1). Available from: https://www.medigraphic.com/cgi-bin/new/resumenI.cgi?IDARTICULO=106940 (Accessed May 1, 2024).

50. Spangfort EV. The lumbar disc herniation. A computer-aided analysis of 2,504 operations. *Acta Orthopaedica Scand* (1972) **43**:1–99. doi:10.3109/ort.1972.43.suppl-142.01

Experimental Biology and Medicine

TYPE Correction
PUBLISHED 13 December 2024
DOI 10.3389/ebm.2024.10419

Check for updates

OPEN ACCESS

*CORRESPONDENCE
Feng Suo,
suofeng163@163.com

RECEIVED 31 October 2024
ACCEPTED 25 November 2024
PUBLISHED 13 December 2024

CITATION
Shi H, Kong R, Miao X, Gou L, Yin X, Ding Y, Cao X, Meng Q, Gu M and Suo F (2024) Corrigendum: Decreased PPP1R3G in pre-eclampsia impairs human trophoblast invasion and migration via Akt/MMP-9 signaling pathway.
Exp. Biol. Med. 249:10419.
doi: 10.3389/ebm.2024.10419

Corrigendum: Decreased PPP1R3G in pre-eclampsia impairs human trophoblast invasion and migration via Akt/MMP-9 signaling pathway

Huimin Shi[1], Renyu Kong[2], Xu Miao[2], Lingshan Gou[3], Xin Yin[3], Yuning Ding[2], Xiliang Cao[4], Qingyong Meng[5], Maosheng Gu[3] and Feng Suo[3]*

[1]Department of Obstetrics, Xuzhou Cancer Hospital, Xuzhou, Jiangsu, China, [2]Department of Cell Biology and Neurobiology, Xuzhou Key Laboratory of Neurobiology, Xuzhou Medical University, Xuzhou, China, [3]Center for Genetic Medicine, Maternity and Child Health Care Hospital Affiliated to Xuzhou Medical University, Xuzhou, Jiangsu, China, [4]Department of Urology, Xuzhou No. 1 People's Hospital, The Affiliated Xuzhou Municipal Hospital of Xuzhou Medical University, Xuzhou, Jiangsu, China, [5]Department of Obstetrics, Xuzhou Maternal and Child Health Hospital Affiliated to Xuzhou Medical University, Xuzhou, Jiangsu, China

KEYWORDS

MMP-9, PE, PPP1R3G, trophoblast invasion

A Corrigendum on
Decreased PPP1R3G in pre-eclampsia impairs human trophoblast invasion and migration via Akt/MMP-9 signaling pathway

by Shi H, Kong R, Miao X, Gou L, Yin X, Ding Y, Cao X, Meng Q, Gu M and Suo F (2023). Exp Biol Med (Maywood). 248(16):1373-1382. doi: 10.1177/15353702231182214

In the original article, there was an error in Figure 3, where the image for the sh-NC group at 12 h was mistakenly duplicated with the image for the sh-PPP1R3G group at 24 h. The corrected Figure 3 is provided below.

The authors apologize for this error and state that this does not change the scientific conclusions of the article in any way.

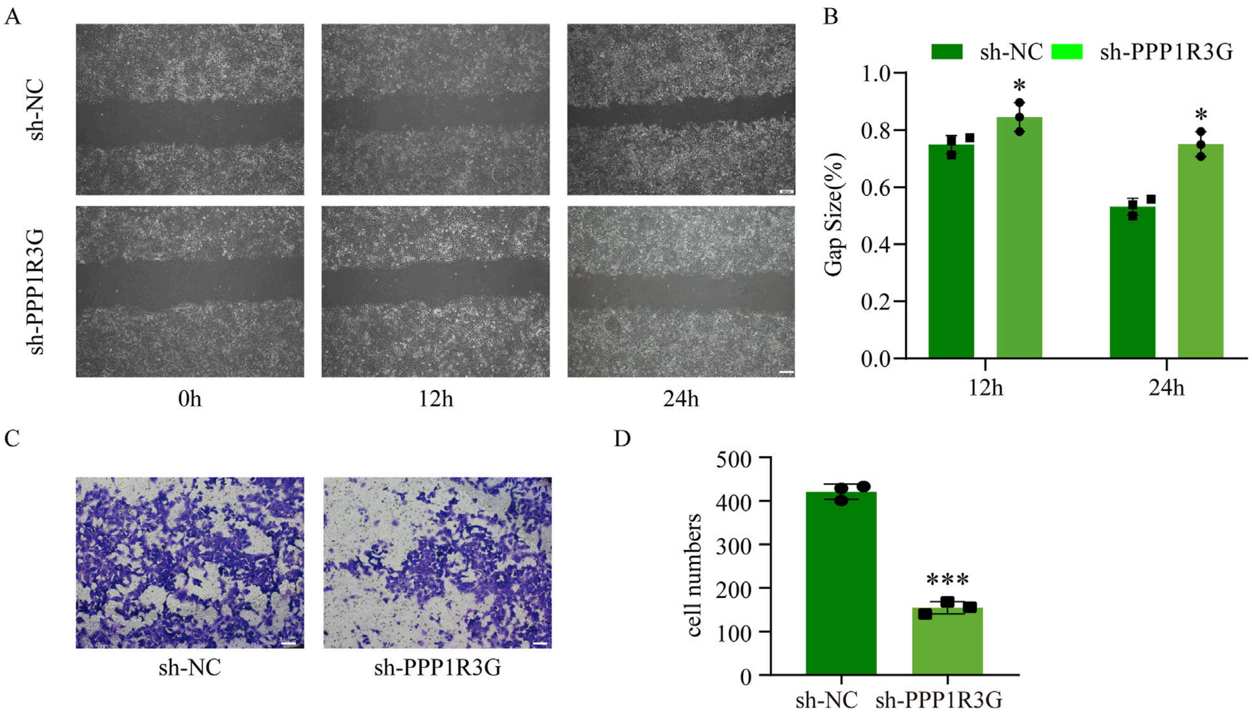

FIGURE 3
PPP1R3G knockdown significantly inhibits trophoblast invasion and migration. **(A, B)** Representative images of wound-healing assay and quantitative analysis of HTR-8/SVneo cells transfected with sh-PPP1R3G or sh-NC at 0, 12, and 24 h **(C, D)** Representative images of transwell assay and quantitative analysis of HTR-8/SVneo cells transfected with sh-PPP1R3G or sh-NC. Bar = 50 μm. Data are expressed as means ± SEM (n = 3), Student's t-test, *P < 0.05, ***P < 0.001 versus sh-NC group.

Scope

Experimental Biology and Medicine (EBM) is a global, peer-reviewed journal dedicated to the publication of multidisciplinary and interdisciplinary research in the biomedical sciences. The journal covers the spectrum of translational research from T0, basic research, to T4, population health. Articles in EBM represent cutting edge research at the overlapping junctions of the biological, physical and engineering sciences that impact upon the health and welfare of the world's population. EBM is particularly appropriate for publication of papers that are multidisciplinary in nature, are of potential interest to a wide audience, and represent experimental medicine in the broadest sense of the term. However, manuscripts reporting novel findings on any topic in the realm of experimental biology and medicine are most welcome.

EBM publishes Research, Reviews, Mini Reviews, and Brief Communications in the following categories.

- Anatomy/Pathology
- Artificial Intelligence/ Machine Learning Applications to Biomedical Research
- Biochemistry and Molecular Biology
- Bioimaging
- Biomedical Engineering
- Bionanoscience
- Cell and Developmental Biology
- Clinical Trials
- Endocrinology and Nutrition
- Environmental Health/Biomarkers/ Precision Medicine
- Genomics, Proteomics, and Bioinformatics
- Immunology/Microbiology/Virology
- Mechanisms of Aging
- Neuroscience
- Pharmacology and Toxicology
- Physiology and Pathophysiology
- Population Health
- Stem Cell Biology
- Structural Biology
- Synthetic Biology
- Systems Biology and Microphysiological Systems
- Translational Research

Submit your work to Experimental Biology and Medicine at
ebm-journal.org/submission

More information
ebm-journal.org/journals/experimental-biology-and-medicine

EBM Experimental Biology and Medicine

EBM is the official journal of the Society for Experimental Biology and Medicine

Led by Dr Steven Goodman, Experimental Biology and Medicine (EBM) is a global, peer-reviewed journal dedicated to the publication of multidisciplinary and interdisciplinary research in the biomedical sciences.

Discover more of our Special Issues

See more →

EBM Experimental Biology and Medicine

The official journal of the Society for Experimental Biology and Medicine

CHIEF EDITOR

Dr. Steven R Goodman

University of Tennessee Health Science Center, Memphis, TN, USA

frontiers | Publishing Partnerships

Contact

development@ebm-journal.org

See more

ebm-journal.org
publishingpartnerships.frontiersin.org/our-partners

frontiers | Publishing Partnerships